Aerodynamic Analysis for Hybrid Electric Distributed Propulsion Aircraft

Tianyi Pan
MSc, BEng Hons.

Submitted in accordance with the requirements for the degree of
Doctor of Philosophy

The University of Leeds
Institute of Thermofluids
School of Mechanical Engineering

September 2020

Publications & Copyright

The candidate confirms that the work submitted is his own and that appropriate credit has been given where reference has been made to the work of others.

Acknowledgement

I would like to thank my supervisors, Dr. Andrew Shires and Dr. Carl Gilkeson, for their patient guidance, encouragement and advice they have provided throughout my time as a PhD student. I have been lucky to have supervisors who cared so much about my work, and who responded to my questions promptly. I would also like to thank all the members of staff at School of Mechanical Engineering.

I must express my gratitude to my parents for their continued support and encouragement. I was continually amazed by the patience from them who experienced all of the ups and downs of my research. Completing this work would have been the most difficult one without the support and friendship provided by my friends from home.

Last and by no means least I would like to thank my girlfriend, Wan Jin, who has been there from the very beginning of my PhD study and is still somehow putting up with me now. I am thankful for your support on a daily basis encouraging me to be the best as I could be. This work is dedicated to my newborn baby, Zhongqi Pan. You have made me stronger, better and more fulfilled than I could have ever imagined. I love you to the moon and back.

This work was undertaken on Men-Comp2 and ARC3, part of the High Performance Computing facilities at School of Mechanical Engineering and the University of Leeds, UK.

Abstract

In a bid to meet the requirements on drag reduction, consumer demands and the latest regulations on carbon emissions and noise, aircraft manufacturers are continually looking at new technologies to improve performance. The aerospace industry is also looking to achieve the mutual benefit of combining existing technologies with new concepts to enhance transonic aerodynamic performance. With the power of modern computing, scientists and engineers can conduct Computational Fluid Dynamics (CFD) simulations for various aircraft configurations to test potential improvements by saving both prototyping and experimental costs.

This research project considers the Hybrid Electric Distributed Propulsion (HEDP) concept with under (UWN) and over-wing nacelle (OWN) configurations for large transonic transport aircraft. It examines the potential benefits of integrated UWN and OWN configurations including: (1) the effect of the fan in controlling rear adverse pressure gradients to maintain a safe operating margin between cruise and buffet, (2) providing Mach flexibility, and (3) potential performance benefits of an integrated fan design compared with traditional under-wing podded engines that can generate strong shock waves in gully regions at off-design conditions. The research also considers a design approach to improve the drag standard of a typical supercritical aerofoil by optimising its shape to minimise/eliminate the strength of shock waves. This was achieved by combining the well-known CST aerofoil parametrisation method and a four-dimensional Optimal Latin Hypercube Design of Experiments.

This research project relies on numerical analysis to investigate the flow mechanism associated with the aerodynamic performance of HEDP for both nacelle configurations. Through this research project, the distributed UWN configuration provides 87.46% in sectional drag reduction compared to the conventional podded engine configuration. Similarly, drag is reduced by 40.96% for the OWN configuration. However, it should be noted that the two-dimensional (2D) analysis of the conventional podded engine configuration is not truly representative of a three-dimensional (3D) flow field. Both of these results are achieved with an increase in aerofoil thickness which would be expected to also contribute to a wing weight reduction.

Further 3D computational research, and experimental verification is recommended for future research activities. The scope of this study was largely two-dimensional but it will be important for next steps in this research direction to account for more complex 3D effects, such as cross-flow and swirl; these considerations will be important to fully exploit potential improvements in aerodynamic performance for transonic wing designs.

Contents

List of Figures

List of Tables

Nomenclature

Roman & Greek Symbols

Symbol	Units	Description
A	m^2	Area
c	m	Chord length
C_D	-	Coefficient of drag
C_L	-	Coefficient of lift
C_P	-	Coefficient of pressure
c_t	-	Thrust specific fuel consumption
$\dot{m}$	kg/s	Mass flow rate
M	-	Mach number
P_s	Pa	Static pressure
P_t	Pa	Total pressure
Re	-	Reynolds number
T	K	Temperature
t	s	Time
T_s	K	Static temperature
t_s	-	Structural thickness
T_t	K	Total temperature
ε	-	Dissipation of turbulence kinetic energy
ρ	kg/m^3	Density
μ		Dynamic viscosity
τ		Shear stress
ϕ		Scalar transport variable
Γ		Diffusion coefficient
Γ_M		Fluid viscosity
Γ_S		Species diffusion coefficient
Γ_T		Thermal conductivity of fluid

Abbreviations

AoA	Angle of attack
BC	Boundary condition
BL	Boundary layer
BPR	Bypass ratio
CAD	Computer aided design
CFD	Computational fluid dynamics
DLR	German Aerospace Centre
DNS	Direct numerical simulation
DoE	Design of Experiments
DPW	Drag Prediction Workshop
DRAGON	Distributed fans Research Aircraft with electric Generators by ONERA
ESDU	Engineering Sciences Data Unit
FEM	Finite element method
FVM	Finite volume method
FPR	Fan pressure ratio
GCI	Grid Convergence Index
HEDP	Hybrid Electric Distributed Propulsion
LES	Large eddy simulation
LHS	Latin Hypercube Sampling
OLH	Optimal Latin Hypercube
ONERA	French National Aerospace Research Centre
OWN	Over-wing nacelle
PDE	Partial differential equation
RANS	Reynolds averaged Navier Stokes
SA	Spalart Allmaras turbulence model

Chapter 1

Introduction

1.1 Introduction

Nowadays, almost all large civil transport aircraft have the requirement to fly at transonic speeds for greater range. However, the design of transonic aircraft faces several crucial challenges and aerodynamic drags is a central issue. Moreover, the development of the aerospace industry comes with increasing concerns about climate change. The UK government recently announced the "net zero emission" target for the aviation industry (*Climate Change Act*, 2008). Aircraft manufacturers and commercial airlines are seeking more ways to obtain economic and environmental benefits for transonic airliners. In recent decades, the concept of hybrid propulsion technology is well-known for its advantages in fuel consumption, carbon emissions, and noise abatement. Therefore, it is desirable to investigate the potential benefits in reducing aerodynamic drag and thus carbon emissions by incorporating hybrid propulsion technology to improve aircraft flight performance (Isikveren et al., 2015).

Hybrid propulsion technology has been developed within the automotive industry since the 1900s, and the concept has been taken forward into aircraft design in the 21^{st} century. At the 2013 Paris Air Show, Airbus proposed a hybrid "E-Thrust" propulsion concept using several electrically-powered fans distributed in clusters along the wingspan for propulsion, with one advanced gas power unit providing the electrical power for these distributed electric fans, and re-charging of an energy storage system. This hybrid architecture offered the potential of improving overall efficiency by allowing the separate optimisation of the thermal efficiency of the gas turbine unit and the propulsive efficiency of the electric fans.

A fundamental aspect of optimising the propulsive efficiency and reducing the specific fuel consumption is to increase the bypass ratio of turbofan engines (Sforza, 2014). Large transonic airliners are commonly equipped with two or four high bypass ratio turbofan engines configured in under-wing podded nacelles. However, as the constraint of ground clearance for commercial aircraft exists, turbofan engine sizes cannot be increased beyond this constraint if further improvements of efficiency are needed. Consequently, the over wing nacelle (OWN) configuration was seen as an opportunity to allow even larger turbofan engines to be installed above the wing, but Wick et al. (2015) has shown that the supersonic region on the upper wing is very sensitive to any obstructions (including engines) in transonic flight conditions. Fortunately, the distributed electric propulsion system offers the opportunity for both UWN and OWN configurations, by connecting fans to electric motors, to either (i) eliminate the limitation of reducing efficiency from scaling down the fan size (Moore, 2012) or (ii) mitigate the strong shock waves on the upper surface. Furthermore, with advanced distributed propulsion technology, future aircraft could see significant reductions in fuel consumption, carbon emissions and total propulsion system noise to meet the stricter emission and noise regulations.

This research will develop a thorough understanding of a supercritical aerofoil with the aerodynamic performance improvement studied at transonic speeds and coupling it with both distributed UWN and OWN propulsion concepts. The main method used in this research investigation will be high fidelity Computational Fluid Dynamics (CFD) analysis for aerodynamic simulation of active distributed electric fans. This allows the potential of utilising aerofoil parametrisation and a Design of Experiments (DoE) to improve overall aerodynamic performance.

1.2 Scope of the Research

The scope of this research is to develop a computational approach in a commercial CFD environment to simulate distributed electric fans, and provide design recommendations for supercritical aerofoils and for coupling them with distributed electric propulsion concepts to reduce aerodynamic drag. In this research project, CFD techniques applied in conjunction with DoE allow to consider the trade-offs in terms of the aerofoil parametrisation and the selection of UWN and OWN configurations, in order to achieve a low-drag design and maintain a lighter wing structural weight (through an increase in section thickness). Conclusions are drawn from the research, and provide a direction for future work.

1.2.1 Novel contributions

The most important novel aspects in this research work can be identified as:

- Conception of a method to investigate the mutual benefits between UWN/OWN configurations and the hybrid electric distributed propulsion concept.
- Identification of which combination of boundary condition types are suitable for simulating working electric fans for high-speed distributed aircraft propulsion; very limited guidance currently exists in the literature.
- Combining an existing and sophisticated aerofoil parametrisation method with a DoE to explore the potential benefits of drag and weight reduction.
- Insights are formed from the improved aerofoil and conventional podded nacelle configurations to find out where future improvements may be possible.
- Insights are gained into the potential of using an aft distributed propulsion concept to mitigate buffet onset for a supercritical aerofoil at transonic speeds.

1.3 Thesis Outline

This thesis is organised as follows:

- Chapter 2 - An extended review into fundamental aerodynamics, transonic wing design, wing configuration, and distributed electric propulsion.
- Chapter 3 - This chapter describes the methods underpinning CFD, Design of Experiments, and aerofoil parametrisation that will be used for this research study. It covers detailed applications of CFD methodology and techniques which are required for examining aircraft aerodynamic performance and potential improvements in reducing aerodynamic drag and structural weight.
- Chapter 4 - The focus of this chapter is the verification and validation of a CFD approach using existing research geometries, the DLR-F6 and NASA Common Research Model. It also includes the simulation of a low interference drag belly-fairing to mitigate wing root separation and the influence of propulsive nacelles.
- Chapter 5 - Exploration of an appropriate combination of boundary conditions to simulate distributed electric propulsion systems is established in this chapter. It also includes a sensitivity study to investigate the uncertainties of the established method in the next chapter.

- Chapter 6 - An aerodynamic performance study for a typical supercritical aerofoil is conducted to consider employing distributed under and over-wing nacelle configurations for reducing aerodynamic drag and structural weight. CFD automation and Design of Experiments are applied along with a sophisticated aerofoil parametrisation method in the sensitivity and parametric study. Discussion of the opportunities to mitigate transonic buffet onset and engineering insight are also made.
- Chapter 7 - Important conclusions drawn from the investigations into aerofoil performance improvement by coupling with distributed under and over-wing nacelle concepts are discussed. Suggestions for future work to improve the methodology, as well as aerofoil drag reduction research are put forward.

Chapter 2

Literature Review

Modern transonic aircraft design is strongly influenced by aerodynamics, economic and environmental aspects. This project involves the research of methods to improve aircraft performance at transonic speeds through advances in aircraft design and optimisation processes by considering the relevant fields, including the fundamental aerodynamics, transonic aerofoil design and wing-nacelle configurations, as well as novel hybrid distributed propulsion concepts. This chapter focuses on the exploration of gaps in knowledge through a comprehensive literature review.

2.1 Background

This section of the literature review considers fundamental concepts in aerodynamics and aspects of aircraft design including environmental, economic and general design considerations.

2.1.1 Aerodynamic Forces

When a civil transport aircraft is in cruise, there are four main forces existing on it, i.e. lift, drag, thrust and weight. The lift and drag can be classified as aerodynamic forces whilst thrust and weight are mechanical forces. The lift is perpendicular to the direction of oncoming airflow while the drag force is parallel to the free air stream (Anderson, 2005). Figure 2.1 illustrates the simplified components of forces on an Airbus A380 in cruise.

For fixed-wing aircraft, the aerodynamic lift requires relative motion between the

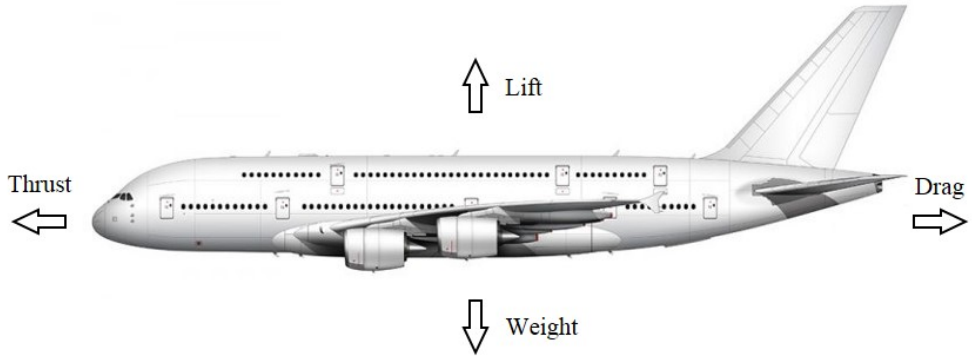

Figure 2.1: Components of forces on the aircraft in cruise modified from (Airbus Group, 2014).

aircraft and the surrounding fluid. According to Clancy (1975), the streamlined-shape of an aerofoil generates more lift than drag. Lift is generated by an aerofoil turning the flow around it and adding circulation, Γ, which is the line integral of the velocity field around the aerofoil (Anderson, 2011). The lift per unit span, L', can be determined by the Kutta-Joukowski theorem, see Eq. 2.1 (Anderson, 2011).

$$L' = \rho V \Gamma \tag{2.1}$$

where, ρ is the fluid density, V is the speed of the moving object relative to the freestream velocity, and Γ is the circulation around the object.

Lift can also be determined from the difference in pressure around its surface, which is caused by the difference in velocity of airflow across upper and lower surfaces of the aerofoil which is explained by the Bernoulli principle.

In terms of aerodynamics, drag is a type of frictional force opposing the motion in a surrounding fluid. Generally, the drag is divided into viscous drag, lift-induced drag, interference drag, wave drag, and parasitic drag (Batchelor, 2000).

The engine on an aircraft provides thrust which is an important parameter in the selection of a propulsion system, e.g. engine types, location of engine, and the number of engines to be installed. The thrust provided by the engines must satisfy the design and flight requirements. However, the number of engines is not in direct proportion to the maximum flight distance as it is only associated with the thrust requirements during flight; the flight distance is associated with the following three aspects, i.e. aerodynamics, propulsion, and weight (Chaudhry and Ahmed, 2014), which will be explained later with the Breguet range equation (2.6).

2.1.2 Environmental and Economic Influence

With the increasing concerns regarding environmental protection, a growing number of laws and regulations have been established regarding the restriction of carbon emission, air pollution and noise control for aircraft.

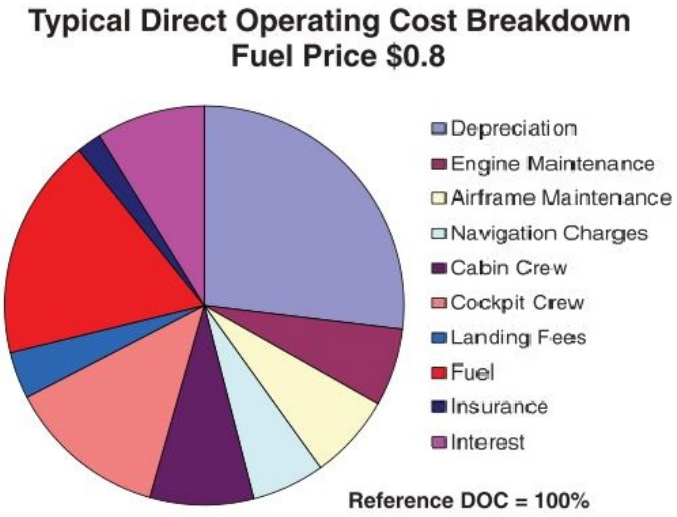

(a)

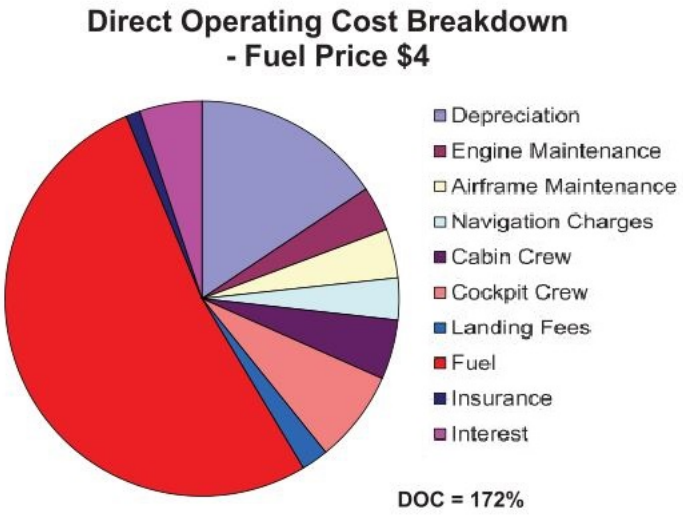

(b)

Figure 2.2: Illustration showing the comparison of Direct Operating Cost breakdown with different fuel prices (a) 0.8 USD per gallon and (b) 4 USD per gallon (Jupp, 2016).

In 2001, the European Union established European Aeronautics: A Vision for 2020, which set ambitious targets of a 50% reduction in fuel consumption and carbon emission, 80% reduction of NO_x emission, 50% reduction of perceived external noise, and a reduction in impaction for the environment during aircraft manufacturing, maintenance and operation by 2020 (Argüelles et al., 2001). Additionally, the fuel

cost has an important aspect in the airline direct operating costs and is highly dependent on fluctuations in oil prices. Figure 2.2 shows the proportions of fuel and other costs with two different oil prices. It can be seen that when the oil price was 80 US cents per gallon, the fuel cost accounted for around 18% of the total airlines direct operating costs. However, when it increased to 400 US cents per gallon, this increased to more than 50%, becoming the largest part in the total cost for airlines. Over the past twelve months the Jet Fuel Spot Price published by IATA has been around 230 US-ct/US-gallon and so there is also a strong incentive to reduce drag for economic as well as environmental reasons.

Therefore it is desirable to investigate and develop new technologies to improve both aircraft performance and environmental impact, which can be achieved by using novel approaches during aircraft design and flight operation.

2.1.3 General Aircraft Design

Aircraft design is a complex subject, which includes numerous considerations and trade-off studies. Generally speaking, general aircraft design can be divided into three main stages, i.e. conceptual design, preliminary design, and detail design (Raymer, 1989). In conceptual and preliminary design, aircraft design constraints need to be considered including the intended design purpose, aircraft regulations, financial factors, marketing, environmental factors, and safety issues (Munjulury et al., 2016). For example, the Airbus A380 could in theory have a longer wingspan but its size would cause operational trouble in some airports because the maximum wingspan allowed for a conventional aircraft is 80 meters to prevent collisions between aircraft while taxiing (ICAO, 1999).

Conceptual design is the first design step and it involves the selection of a variety of possible aircraft configurations that meet the required design specifications, including the consideration of several important factors such as aerodynamics, propulsion, flight performance, structural and control systems (Roskam, 1997). With the development of aerospace engineering, some unconventional aircraft configurations have also been designed in order to improve aircraft performance, such as canard and tandem wings, flying wings, closed and joined wings (Amadori, Jouannet and Krus, 2008). At this stage, the fundamental elements of the design of aircraft components, for example, fuselage shape, wing configuration and location, engine type, are determined. The design constraints, which are relevant to the design specifications, are taken into consideration. The main outcome of the aircraft conceptual design process is the identification of the layout of the aircraft for the preliminary design phase (Raymer, 1989).

Preliminary design is the design process which considers most of the major design parameters. Here, wind tunnel testing and numerical analysis of the aerodynamics (e.g. Computational Fluid Dynamics) will typically be implemented as well as major structural and control analysis (Ghoreyshi and Cummings, 2014). Then after the finalisation of the design lies the key decision with the manufacturer or individual designing it whether to actually go ahead with the production of the aircraft (Raymer, 1989).

In detail design, the main purpose is to deal with the fabrication and manufacturing aspect of the aircraft. It determines the number, design and location of ribs, spars, including other functional elements, for instance, the flight control system, avionics, landing gear, cabin doors and seats, etc. (Raymer, 1989). As this research focuses on the transonic aircraft design, the benefits and challenges of flying at transonic speeds will be discussed in Section 2.3.2.

2.2 Fundamental Aerodynamics

Aerodynamics is a branch of fluid dynamics focused on the interaction of moving air and solid objects. It is a very important aspect of aeronautical engineering as it deals with the characteristics of airflow, including velocity, pressure, temperature, compressibility and viscosity. In terms of compressibility, aerodynamic flows can be categorised as either incompressible or compressible according to whether the density will change with the pressure (Anderson, 2011). In this research project, the focus is an aircraft geometry designed for high cruise speed, which is in the transonic regime, therefore fluid compressibility is considered. This and other important concepts in aerodynamics are discussed.

2.2.1 Turbulence

In fluid mechanics, fluid flows can be classified into three flow regimes, i.e. laminar, turbulent, and transitional (Tennekes and Lumley, 1972). Laminar flow occurs when the fluid flows in parallel layers without eddies or swirls between them (Batchelor, 2000); the particles of the fluid move in an orderly and structured pattern. Turbulent flow, which occurs in most aerodynamic applications, involves the fluid flowing in a disorderly fashion with unsteady vortices observed. In turbulence, the fluid flow is not as predictable as that in laminar flow due to the occurrence of eddies and swirls. The transitional status in between laminar flow and turbulence is named transitional flow.

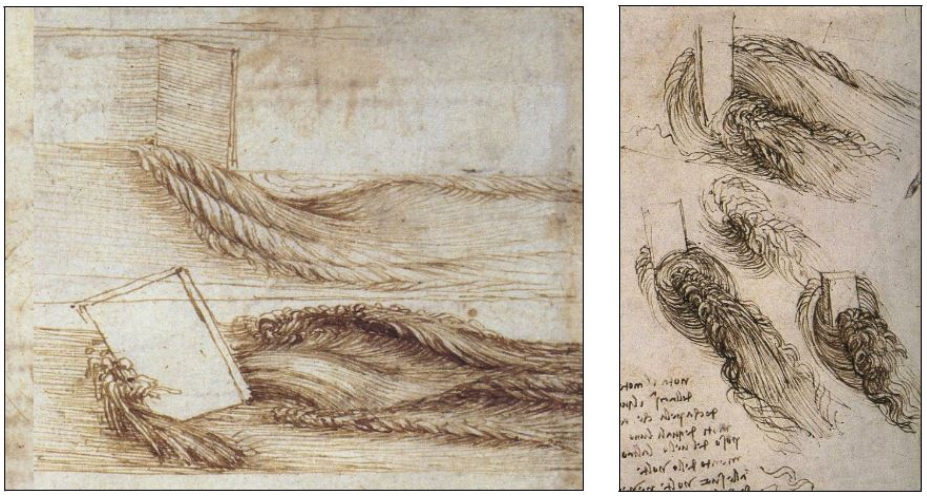

(a) (b)

Figure 2.3: Illustrations showing turbulent flow behind objects placed in river streams by Leonardo Da Vinci (a) from (Kemp, 2006) and (b) from (Roberts, 1989).

In late 15^{th} and early 16^{th} centuries, Italian polymath Leonardo da Vinci recorded some of the earliest observations of turbulence in his experiments by placing different shapes in river streams to produce swirls, his sketches are shown in Figure 2.3. Da Vinci's understanding of turbulence were novel at that time, however, it was limited to qualitative observations of external flow patterns of water.

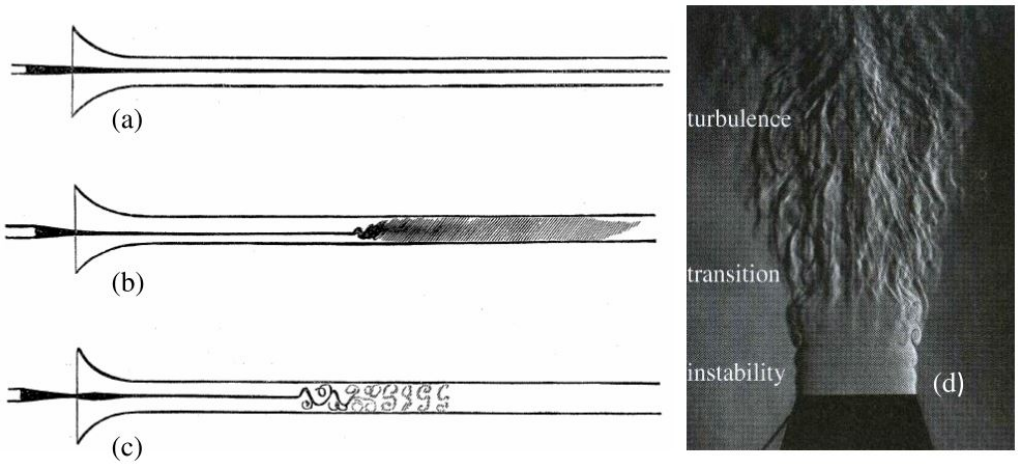

Figure 2.4: Illustrations of three flow regimes in pipe flow: (a) laminar, (b) turbulent, and (c) transitional flow (Reynolds, 1883) and (d) shows all three jet flow regimes (Durbin and Medic, 2007).

In the 18^{th} century, Osborne Reynolds conducted his well-known experiment when he claimed the transparency of water causes difficulty to observe fluid movement inside it. He injected dye into a column of water inside a glass tube to investigate the flow regimes in pipe flow. Figure 2.4 shows the observations of dye when Reynolds gradually increased the flow velocity. It can be seen that the dye follows

an orderly and continuous path in the water at low speed, Fig. 2.4 (a). When the velocity increased, the dye started to mix downstream to exhibit the instability of transitional flow, Fig. 2.4 (c). Above a certain value of velocity, the dye became turbulent and produced eddies, Fig. 2.4 (b). Figure 2.4 (d) presents the transition of three flow regimes in a single free jet (Durbin and Medic, 2007).

The significance of laminar and turbulent regimes is not only related to the flow patterns. Figure 2.5 shows the comparison of the velocity profile away from a plate for laminar and turbulent flow, together with a simplified visualisation of laminar and turbulent flow patterns in the boundary layer. It can be seen that turbulence exhibits a higher velocity gradient than laminar flow near walls, which means that turbulence produces more shear stress, according to the shear stress equation (2.2).

$$\tau = \mu \frac{du}{dy} \tag{2.2}$$

where τ is the shear stress, μ is the fluid viscosity, and $\frac{du}{dy}$ is the velocity gradient.

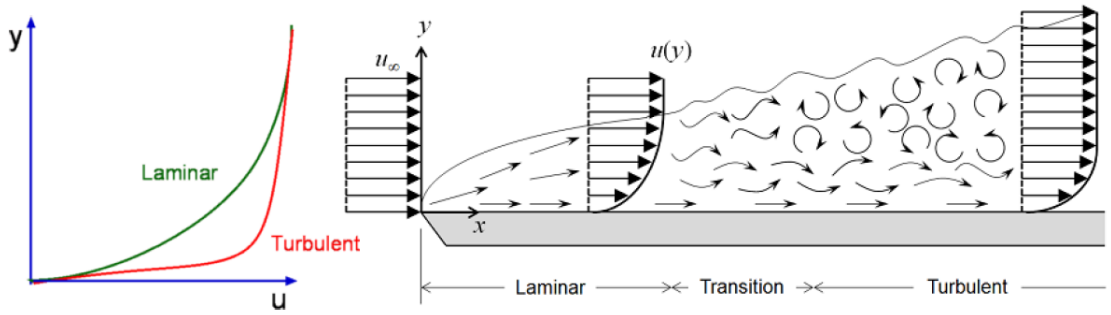

Figure 2.5: Laminar and turbulent flow velocity profiles and flat plate boundary layer development modified from (Anderson, 2011).

In terms of the definition of the flow regimes in pipe flow, the Reynolds number, Re, which is a dimensionless quantity, was introduced by Reynolds (1883) to quantify whether the flow is laminar or turbulent. By calculating the Reynolds number, the flow regime is characterised by the value obtained. Re is normally low for pipe flow, however, it can be extremely high in aircraft aerodynamics because inertial forces dominate (Tennekes and Lumley, 1972). Re is defined as:

$$Re = \frac{\text{Inertial Forces}}{\text{Viscous Force}} = \frac{\rho u L}{\mu} \tag{2.3}$$

where u is the velocity of the fluid, L is the characteristic length, ρ is the density, and μ is the dynamic viscosity.

The Reynolds number is also important in aerodynamics and Computational

Fluid Dynamics (CFD) because it will influence the thickness and state of the boundary layer (Schlichting and Gersten, 2000). Therefore, it is necessary to match the Reynolds numbers before comparing CFD results with experimental data to ensure the CFD simulation has the same flow conditions to allow a fair comparison.

2.2.2 Drag Breakdown

The overall aerodynamic forces acting on an aircraft were briefly introduced in the beginning of this chapter. Focusing on drag forces, there are different types and it is important to appreciate how these contributions may impact an aircraft during flight. Figure 2.6 shows the breakdown of drag for a typical civil aircraft, the Airbus A320, in cruise, as well as the potential drag reduction with possible technology improvements. Drag on an aircraft can be sub-divided into pressure drag and skin friction drag, however, specifically for a civil aircraft, drag can be further classified into five types, i.e. viscous drag, lift-induced drag, interference drag, wave drag, and parasitic drag (Anderson, 2011).

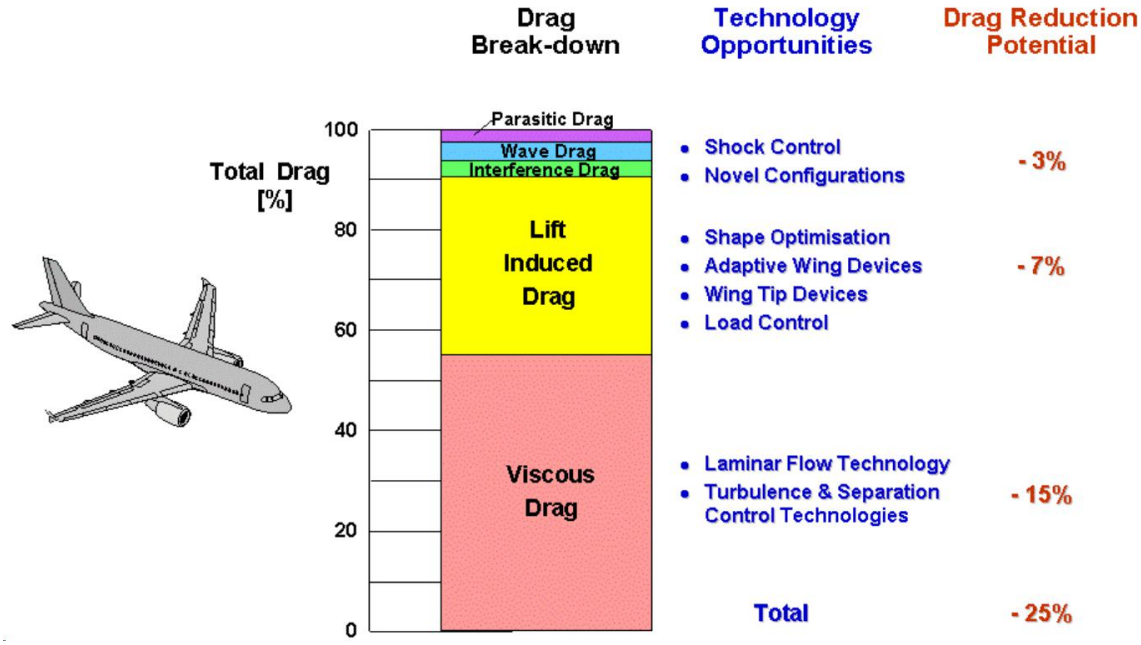

Figure 2.6: Breakdown of the drag and technology opportunities for drag reduction (Schrauf, 2006).

Viscous drag is a pressure drag resulting from the presence of boundary layers on the surface. Lift-induced drag is a pressure drag produced by the induced down-wash while the aircraft is in motion. The lift-induced drag increases with the increase of angle of attack (AoA) if other parameters remain unchanged (Clancy, 1975). Interference drag is an additional pressure drag resulting from the mutual interaction

of flows which can be seen at the intersection of aircraft components, e.g. wing-fuselage junction (Anderson, 2005). Wave drag is associated with the effect of fluid compressibility, for instance, shock wave formation in transonic or supersonic flight. Parasitic drag is associated with both pressure and skin friction drag when flow separation occurs (Clancy, 1975).

Based on the result provided by Schrauf (2006), it can be seen that the viscous drag and lift-induced drag contribute the majority proportions, approximately 50% and 35%, respectively. While the total proportion of parasitic drag, wave drag, and interference drag are only around 10%. With the technology development opportunities mentioned by Schrauf (2006) (Figure 2.6), Schrauf estimates that a 15% reduction in viscous drag could potentially be achieved by laminar flow technology as well as turbulence and separation control technologies. Schrauf also estimates that shape optimisation, adaptive wing devices, wing tip devices, and load control could contribute a 7% potential reduction of lift-induced drag. Additionally, a 3% potential reduction in parasitic drag, wave drag, and interference drag could be achieved with effective shock wave control and novel configuration design (Schrauf, 2006). The total potential drag reduction is 25% plus 25% reduction in weight, which projects a 50% total reduction in fuel consumption to meet the European Union ACARE Target (Argüelles et al., 2001).

2.2.3 Boundary Layer

The molecules of a fluid such as air will be disturbed when an object moves in the fluid or the fluid flows past a solid object. The resulting aerodynamic forces occur mainly because of the viscosity of the fluid (Schlichting and Gersten, 2000). The viscosity creates a thin layer, termed the boundary layer, close to the solid object where the velocity of the fluid varies from zero at the wall to the value of the freestream velocity in a perpendicular direction away from the object; i.e. no-slip condition (Massey, 1998). In fluid mechanics, the boundary layer is the region of fluid where the effect of viscosity is significant (Anderson, 2011). Similar to the basic flow regimes, boundary layers can be classified as either laminar or turbulent depending on the Reynolds number. Figure 2.7 illustrates the structure of a developing boundary layer of a fluid moving past a flat plate. The thickness of the turbulent boundary layer is greater than the laminar portion because turbulent flow produces more shear stress near the wall resulting in the reduction of the velocity around the bounding surface (Schlichting and Gersten, 2000). A viscous sub-layer beneath the turbulent region is always essentially laminar as the eddies within the turbulent boundary will disappear close to the surface. The boundary layer thickness, δ, is

typically defined as $0.99U_\infty$ (freestream velocity). Normally, the maximum boundary layer thickness is smaller than 20 mm for an aircraft wing in cruise(Barnard, 2001), but this is very dependent on Reynolds number.

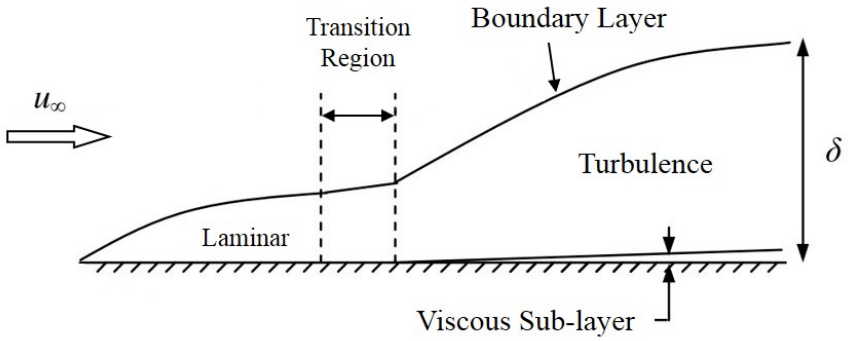

Figure 2.7: Illustration of the structure of the boundary layer modified from (Massey, 1998).

A typical example of the boundary layer development over a conventional aerofoil is shown in Figure 2.8. It can be seen that on the upper surface, the thickness grows from the leading edge and after a small transition region due to the rapid development of turbulent eddies, the boundary layer changes from laminar to turbulent where eventually it will usually lead to separation (Prandtl, 1952). An important property of a turbulent boundary layer is that it accommodates more kinetic energy because the fast-moving fluid molecules are drawn in by turbulent eddies from the freestream.

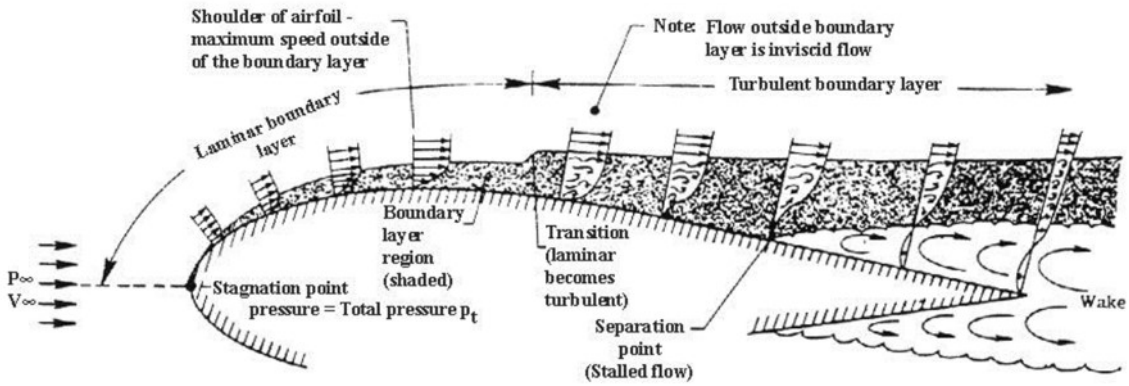

Figure 2.8: Development of boundary layer over an aerofoil (Prandtl, 1952).

Figure 2.8 illustrates how the boundary layer thickens as it moves downstream along the aerofoil until the wake forms at the trailing edge after the separation point. As the laminar flow portion produces less skin friction than the turbulent flow region, it is desirable to control the flow type over the aerofoil; i.e. to increase the extent of the laminar boundary layer (Joslin and Miller, 2009). An approach to this concept

was developed in the 1930s, called Laminar Flow Control (LFC) technology, aimed to maintain the extent of laminar flow over the wing (Green, 2008).

2.2.4 Pressure Distribution

One of the most convenient ways to interpret the local flow mechanisms at various points in a given flow field is by observing the pressure distribution. The non-dimensional coefficient of pressure, C_P, is a very useful indicator to characterise flow features and to compare different aerofoils in a fair way. C_P is given by:

$$C_P = \frac{p - p_\infty}{\frac{1}{2}\rho U_\infty^2} \tag{2.4}$$

where, p is the local static pressure, P_∞ is the freestream static pressure, ρ is the local air density, and U_∞ is the freestream air velocity, which is equivalent to the vehicle speed in still air (Barnard, 2000).

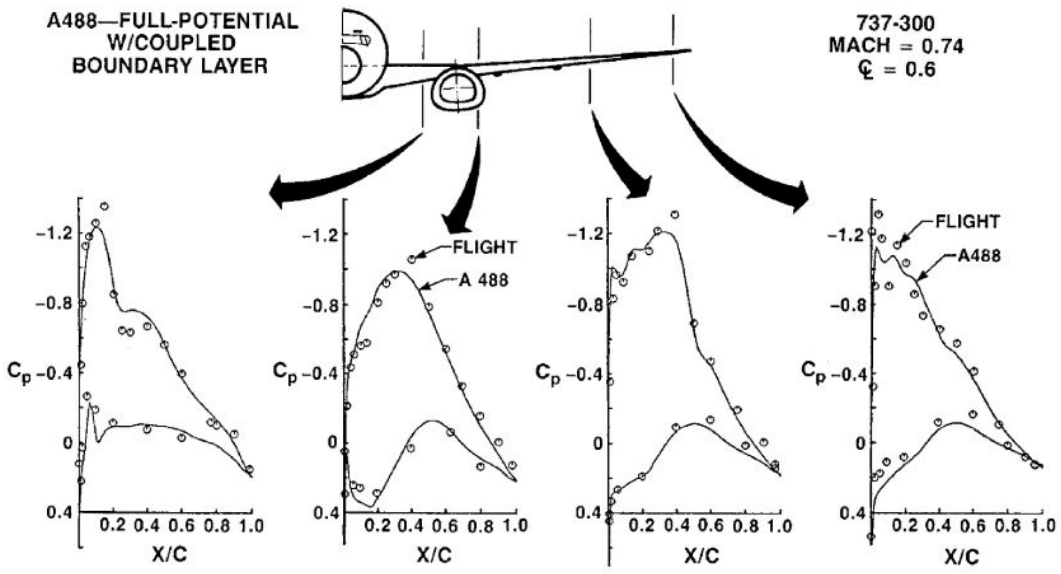

Figure 2.9: Illustration showing the wing surface pressure distribution at different stations on a Boeing 737 (Tinoco, 1991).

At a given angle of attack, the pressure around an aerofoil will form a pressure distribution. In aeronautical engineering, pressure distribution is typically drawn with a flipped y-axis, as the C_P for the upper (suction) surface of an aerofoil is usually negative and hence becomes the top line in the pressure distribution plot. Figure 2.9 shows the pressure distribution plots of four different stations across the wing of a Boeing 737 during a flight test.

As the aircraft moves in the air, the flow stagnates and rests at the leading edge, where $C_P = 1$. After the stagnation point, the air is rapidly accelerated on the upper surface to a suction peak (highest point on a C_P plot) where the pressure is the lowest. Pressure recovery starts after the suction peak and local pressure gradually increases to the ambient pressure prior to reaching the trailing edge. At the rear of the aerofoil, the adverse pressure gradient occurs, $dp/dx > 0$, reducing the kinetic energy and inducing an extensive region of separated flow.

2.2.5 Separation and Pressure Gradient

In fluid dynamics, the pressure gradient, dp/dx, where x increases in the direction of flow, is a primary factor to determine whether the flow is attached or separated from the surface when it passes an object. When $dp/dx < 0$, the flow is accelerating (static pressure is therefore reducing) and is referred to as a favourable pressure gradient. This occurs when the air accelerates from the high pressure stagnation point at the leading edge of the aerofoil to the low-pressure suction peaks on both upper and lower surfaces. A boundary-layer will remain attached to the surface of the solid body and follows its contours, when subjected to a favourable pressure gradient. When the static pressure increases in the direction of the flow, an adverse pressure gradient occurs (Anderson, 2011), where $dp/dx > 0$, as the flow decelerates. In this circumstance, the boundary layer, either laminar or turbulent, may not be able to maintain sufficient energy to stay alongside the body contour and it detaches from the surface. Typically, this flow regime occurs at the rear half of an aerofoil where pressure recovery starts aft of the suction peak and increases towards the ambient pressure at the trailing edge.

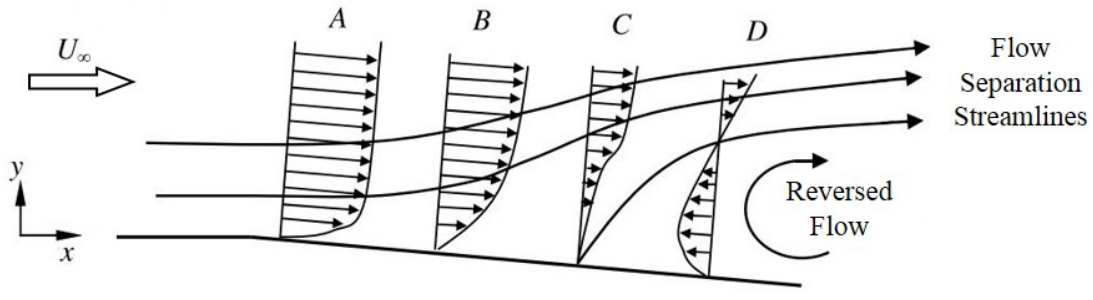

Figure 2.10: Schematic of a velocity profile of separation modified from (Binder, 1958).

In Figure 2.10, the schematic of the velocity profile over a sloping diffuser is shown. At position A, a fully developed velocity profile exists and, the pressure gradient is zero. Thus, the external flow is neither accelerating nor decelerating.

When the pressure increases this means the velocity of the internal boundary layer decreases, at position B. The external flow could have enough momentum to overcome the deceleration, as at position B. However, eventually the velocity and shear stress of the boundary layer becomes zero at the wall, which is shown in position C. If the pressure continues to increase, at position D, the local flow reverses against the freestream direction, which leads to detachment of the boundary layer away from the surface. For an aerofoil, the favourable pressure gradient, (pressure decrease), produces a growing and stable boundary layer whilst adverse pressure gradients produce an unstable boundary layer increasing the risk of flow separation if it is very large (Schlichting and Gersten, 2000). If the pressure gradient increases rapidly, for example in a shock wave, it can immediately cause the detachment of the flow from the wall, which is named shock-induced separation and is discussed later.

Compared to a laminar boundary layer, turbulent boundary layers have better capability to sustain an adverse pressure gradient, i.e. to prevent the separation under the same flow conditions (Schlichting and Gersten, 2000), which is also the most difficult challenge facing Laminar Flow Control.

2.2.6 CFD Background

Before the development of transistors, obtaining the solution for fluid problems mainly relied on hand calculations by discretising the fluid domain and applying the numerical method. English mathematician Lewis F. Richardson was one of the pioneers using hand calculations to numerically solve the governing equations; his numerical approach to solve the fluid problem was then applied to the structural analysis of weather prediction. In the 1930s, Thom (1933) applied the principles of numerical analysis to the flow around a cylinder with a very low Reynolds number, 10 to 20. Thom commented that the flow field should be divided into squares of any desired size, where a finer grid results in a better solution if the flow gradient is large between each grid point, an example of a uniform grid is shown in Figure 2.11. His comment also initiated the discussion of the balance between grid size discretising the fluid domain and the solution accuracy, stability, and computational capability. Figure 2.12 shows the streamlines of flow past a cylinder plotted by Thom (1933) after 5 to 50 iterations of hand calculation per grid cell for Re=10.

After Thom's attempt to solve flow problems by hand calculation, Kawaguti (1953) extended the numerical simulation for the same geometry with a larger grid size of 232 grid points and a higher Reynolds number of 40, while the final solution took totally 1560 hours for 65 iterations of calculations. It is clear that the manual approach is not practical and feasible for complex three dimensional scenarios. For-

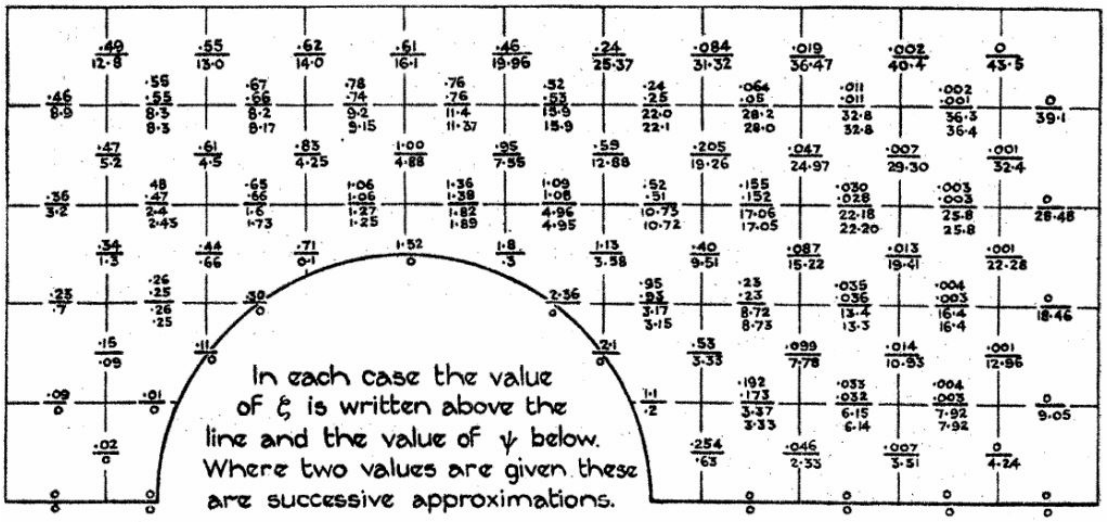

Figure 2.11: One of the first grids used for numerical calculations of the fluid flow around a cylinder with overlaid calculations at each boundary of cell (Thom, 1933).

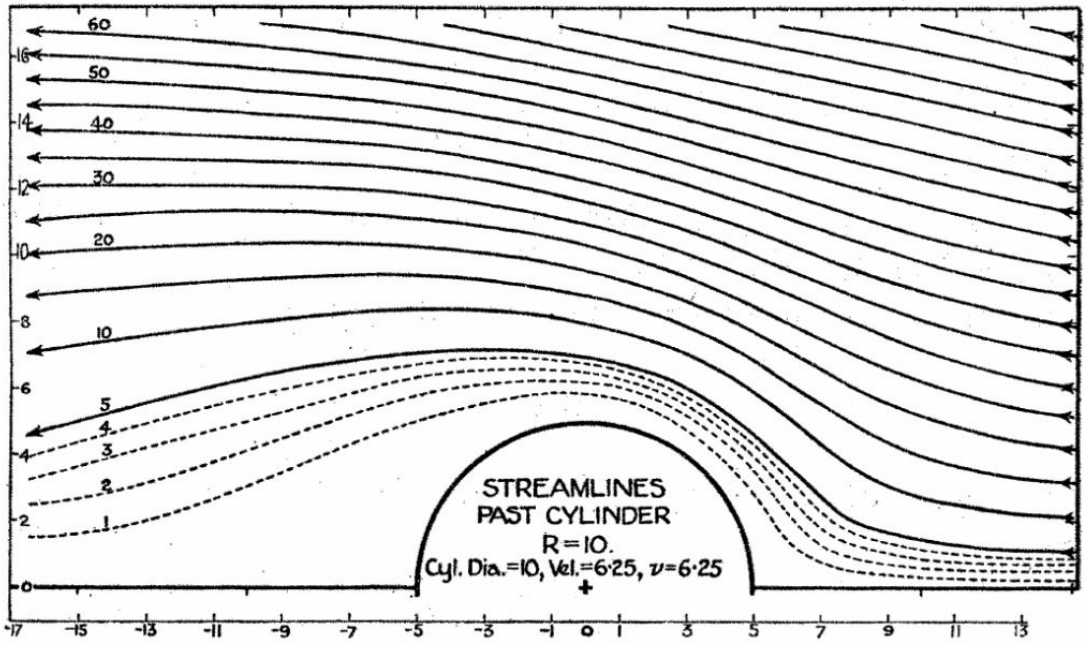

Figure 2.12: Streamlines of flow past a cylinder for Re=10 drawn by Thom (1933).

tunately, in the second half of 20^{th} century, thanks to the development of transistors, modern high performance computers can handle extremely high-speed calculation with reliable solutions, which makes computational approaches a popular tool. Figure 2.13 shows the evolution of Airbus's first 40 years of CFD applications from the early 2D potential flows to full 3D Navier-Stokes solutions for large commercial airliners.

The advancement in computing is the key factor to realise greater complexity of computational simulations, other factors such as development and implementation of algorithms and CFD codes utilises even greater ability and capability. CFD is

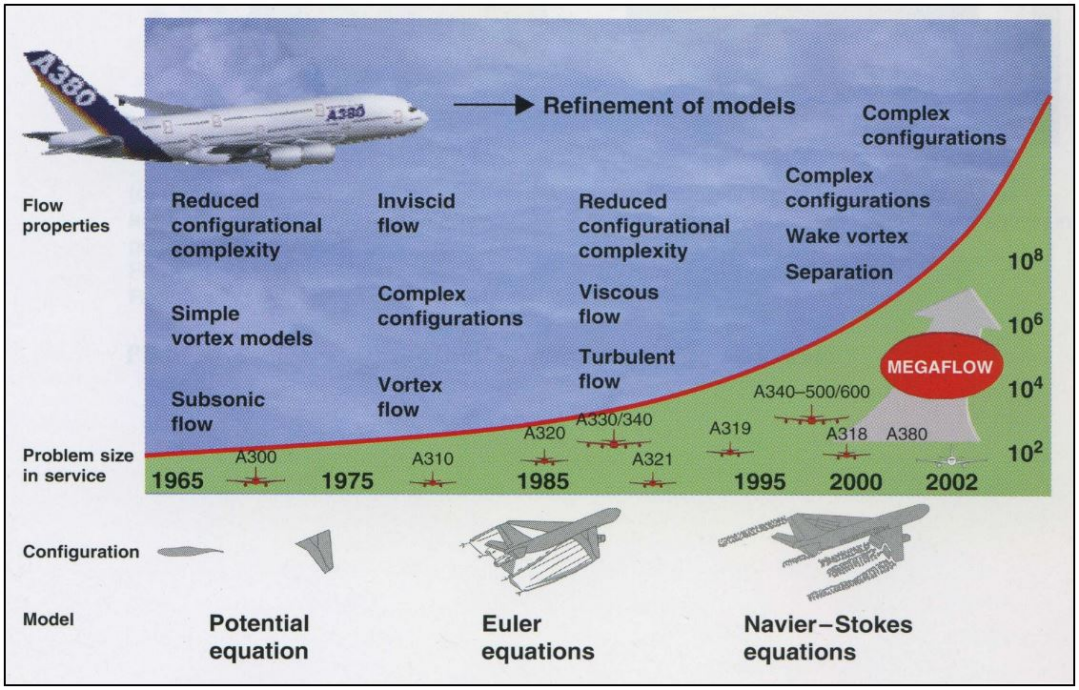

Figure 2.13: Timeline showing the evolution of the CFD methods employed by Airbus between 1965 and 2002 (Becker, 2003).

now widely used to undertake many aspects of problems including diverse subjects including aircraft aerodynamics (Johnson, Tinoco and Yu, 2005) amongst many other fields. The sophistication of commercial CFD codes manage to deal with majority of fluid problems and also avoid the requirements of creating bespoke codes for a narrow focus. These commercial CFD packages, such as Star CCM+ and ANSYS Fluent, consist of Computer Aided Design (CAD) and mesh generation tools (pre-processor), which synchronise with all the essential packages for CFD calculations (solver) and eventually the analysis of solutions (post-processor).

In summary, CFD is a branch of fluid mechanics, which uses numerical methods and algorithms to solve the governing Navier-Stokes equations for various fluid flow problems. It is also an established practice widely used and embedded within the design cycle of many engineering applications. Inevitably, the quality of CFD simulations is dependent on the skill of the user and performance of computers. The more powerful the computer is, the faster the simulation of the interactions of fluids with defined boundary conditions is. With the development of commercial CFD packages, the results and accuracy have been improved for complex flow situations, e.g. transonic or supersonic flight simulations. The applications of CFD will be introduced in Chapter 3.

2.2.7 Experimental Techniques

For all their advantages, computational approaches are purely simulation methods and they cannot replace research with the actual fluid itself. In order to judge and prove the degree of credibility of numerical simulations, they are required to be validated against real experimental data.

2.2.7.1 Wind Tunnel Testing

Wind tunnel testing is widely used in aerodynamic research. In 1901, the Wright brothers built one of the first wind tunnels for aerodynamic testing aerofoil sections, which led to the success of the Wright brothers' first powered and heavier-than air flight in 1903 (Anderson, 2004). Their wind tunnel used a straightforward principle to study the flow behaviour of a column of moving air past an object of interest (the aerofoil) which is fixed in the wind tunnel. By fixing the object, it is easier and more accurate to measure the lift and drag forces than analysing the object moving through the air. Figure 2.14 shows the structure of the most widespread open-circuit wind tunnel.

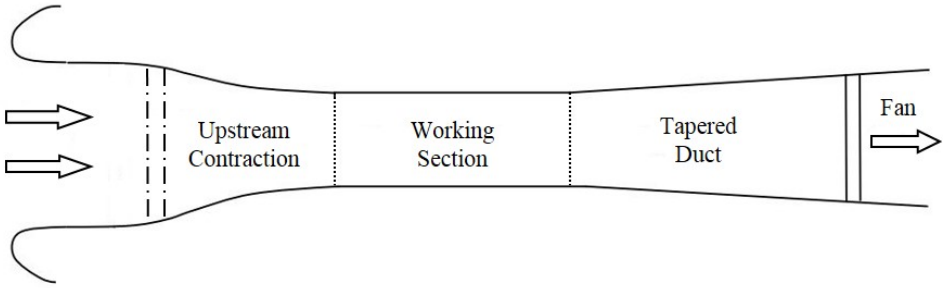

Figure 2.14: An example of low-speed open-circuit wing tunnel modified from (Bradshaw, 1964).

This simple wind tunnel consists of an intake equipped with a flow-straightening device and a screen (dash-dot lines) to reduce both the turbulence of incoming freestream flow and the chances of ingesting foreign objects. A contraction region upstream of the working section is designed to accelerate the air flow by the ratio of cross-sectional area before and after the contraction region. The working section is where the research object and other test instrumentation is installed, for instance, force balance, etc. The fan installed at the tapered duct downstream is assigned to provide the power to pull the air through the tunnel.

Wind tunnel testing has the advantages of being able to adjust the flow conditions, i.e. the air velocity and temperature, which makes it a useful approach for

acquiring reliable experiment data on aerodynamic flows. Conversely, wind tunnel testing also has its shortcomings, such as blockage effects, and it is difficult to produce flows with extremely high Reynolds number, which makes it easy to cause significant errors without appropriate calibration procedures (Barlow, Rae Jr. and Pope, 1999). In Figure 2.15, the problem of confining an object in a wind tunnel is revealed by superimposing the equivalent free-flight streamlines (dash line) over wind tunnel flow streamlines in a wind tunnel. If the wind tunnel is too small or the research object is too large, blockage effects lead to streamline curvature, adversely affecting the accuracy of final results.

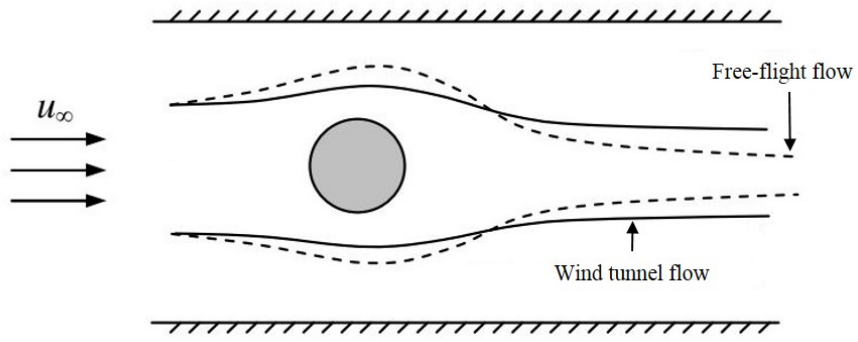

Figure 2.15: Schematic showing the effects of streamline curvature modified from (Bradshaw, 1964).

As most designs of transonic aircraft involve extremely high Reynolds numbers of 50 million or higher, the usefulness of low speed wind tunnel are limited to low test Reynolds numbers. One solution for the difficulty of simulating high Re conditions is the cryogenic wind tunnel. Cryogenic wind tunnels have relative larger working section size ($2 \times 2 \times 2$ m or even larger) with a relatively high pressure (up to 5 bar) and a cryogenic temperature using nitrogen as the test gas (Goodyer, 1992). From equation (2.3), cooling the test gas increases its density and decreases its viscosity, which both contribute to raising the Re, as desired.

The scale effect in wind tunnel testing is also crucial when dealing with curved surfaces, for example, an aerofoil. The problem of scale effect is demonstrated by Barnard (2001), shown in Figure 2.16. It highlights a vast difference in boundary layer form if the Reynolds number remains unchanged when scaling up the geometry. In small-scale geometry, the laminar boundary layer dominates the body surface before detaching at the rear, whereas the flow regimes are completely different in full-scale geometry. It can be seen in Figure 2.16 that the length of the laminar boundary layer is much less. However, with the implementation of wind tunnel correction factors, the experimental data can be modified to neutralise this negative effect (Barlow, Rae Jr. and Pope, 1999).

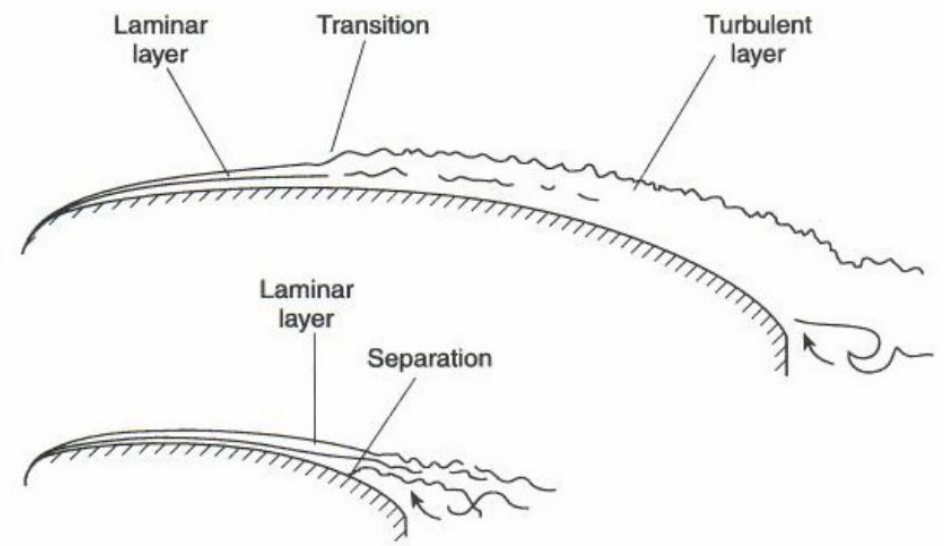

Figure 2.16: Schematic showing the scale effect on a curved surface in aerodynamics (Barnard, 2001).

2.2.7.2 Flow Measurement and Visualisation

In wind tunnel testing, the forces and moments on the research object are accurately measured as well as velocity, pressure and temperature. Typically, a six-component balance connected to the object via a "sting" measures the components of forces and moments (Barlow, Rae Jr. and Pope, 1999). The local and freestream static pressure are normally obtained by differential pressure transducers to calculate the pressure coefficient while the dynamic pressure is recorded using a pitot tube installed upstream of the working section.

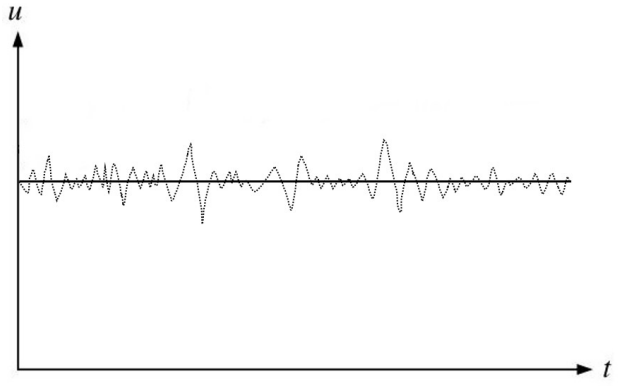

Figure 2.17: Plot of time history versus velocity of a point modified from (Tu, Yeoh and Liu, 2018).

The difficulty of accurately measuring local velocity is greater because of turbulence. Figure 2.17 shows an example by considering the local velocity at a single point as a function of time. The mean component of air velocity, $\overline{u}$ (the straight

line), and the fluctuating component of velocity, u' (the oscillating dotted line), are used to determine the levels of turbulence, i.e. turbulence intensity, I_u (Tu, Yeoh and Liu, 2018). The turbulence intensity is defined as the ratio of the standard deviation of $\overline{u}$ to u':

$$I_u = \frac{\sqrt{\overline{u}}}{u'} \tag{2.5}$$

Flow visualisation can be usually achieved with two methods, surface flow visualisation and off-surface flow field visualisation. Surface flow visualisation applies oil or other viscous fluids over the object surface to show flow separation and vortex structures, see Fig. 2.18a. Flow field visualisation typically uses downstream tufts which are freely directed by aerodynamic flows, see Fig. 2.18b, and smoke traces to display the movement of the flow field. With more sophisticated Schlieren photography, the changes of fluid density can also be monitored at high Mach number (Barlow, Rae Jr. and Pope, 1999).

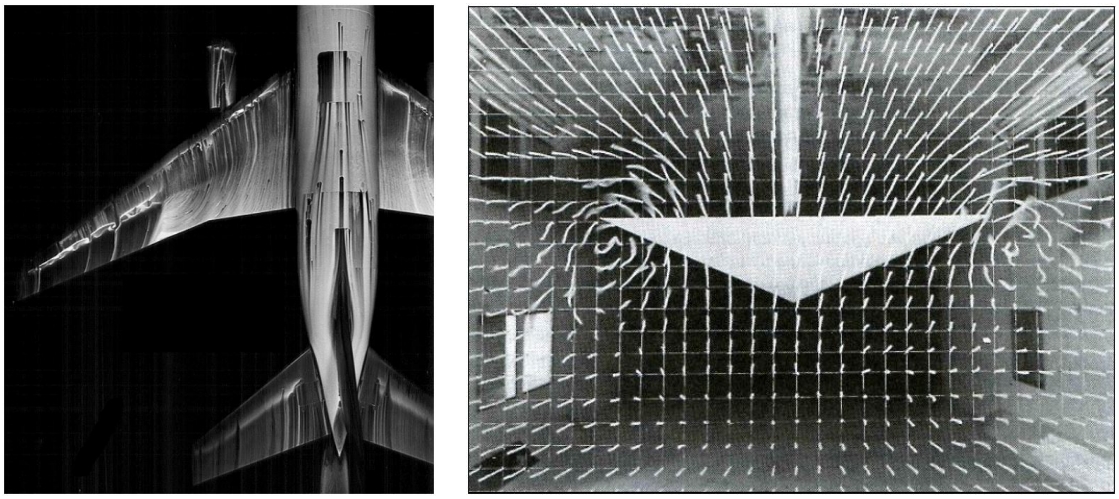

(a) (b)

Figure 2.18: Wind tunnel flow visualisation techniques showing (a) surface oil flow over an aircraft (Vos and Farokhi, 2015) and (b) a tuft grid behind a delta wing (Barlow, Rae Jr. and Pope, 1999).

2.3 Transonic Wing Design and Configuration

The design of modern aircraft involves numerous wing configurations for different purposes. Examples include the conventional wing planform, delta wing, canard, tandem wing, and the joined wing, etc. Structurally, the wing consists of numbers of sections of aerofoils, where aerofoils are twisted with reducing angles of incidence

to control the spanwise lift distribution from wing root to wing tip. This design characteristic is named as "washout" and is aimed at minimising the wing induced drag and to avoid wing-tip stall. This section will cover the background of aerofoil design, main considerations for design and engine integration at transonic speeds, characteristics of supercritical aerofoils, and a trade-off of under and over-wing nacelle configurations.

2.3.1 Aerofoil Parameter

In aeronautical engineering, a subsonic or transonic aerofoil is shaped with a rounded leading edge and a sharp or relatively blunt trailing edge. The working principle of an aerofoil is to generate lift based on the pressure difference on the upper and lower surfaces. Lift generation from an aerofoil primarily depends on the angle of attack and its shape. At an appropriate angle of attack, the aerofoil deflects the oncoming air and creates curved streamlines around it, resulting in the velocity difference between the upper and lower surfaces. This leads to the pressure difference, which produces lift. A symmetric aerofoil requires a positive angle of attack to generate lift, however, a cambered aerofoil, which is mostly employed in modern commercial aircraft, can generate lift at a zero angle of attack.

Generally speaking, an aerofoil is defined by several parameters, i.e. thickness distribution, camber distribution, leading edge radius. Figure 2.19 illustrates the aerofoil terminology for a typical aerofoil.

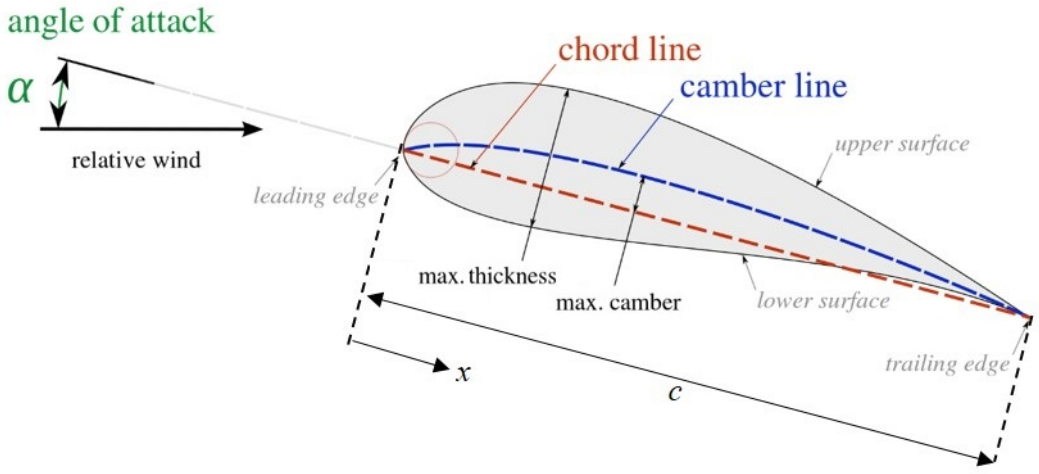

Figure 2.19: Schematics showing fundamental aerofoil parameters modified from (Birajdar and Kale, 2015).

Here, the upper surface, also named as the suction surface, is associated with higher velocity and lower static pressure, while the lower surface, also named as

the pressure surface, typically experiences slower, higher pressure conditions. The leading edge is the point at the front with maximum curvature, and the trailing edge is at the rear. The chord line is the line connecting the leading edge and trailing edge, which is also the reference dimension of aerofoil sections; normalised chordwise position is represented by x/c. The camber line is the locus of points midway between the upper and lower surface (Anderson, 2011). The combination of camber and thickness distributions determines the final shape of an aerofoil. Note that thickness is measured perpendicular to the chord line.

Simply changing a single parameter of an aerofoil affects its general aerodynamic performance and even the structural weight of the wing. For example, an increase of thickness typically lowers the maximum lift coefficient, however, it improves the internal space for the wing spars allowing fewer spars to support the aircraft and a reduction in overall wing weight (Vos and Farokhi, 2015). On the other hand, for aerofoil optimisation, it is desirable to achieve a higher maximum lift coefficient without thinning the aerofoil. With the increase of leading edge radius, the aerodynamic performance of the aerofoil decreases, however, the aerofoil gains broader performance range (Birajdar and Kale, 2015).

2.3.2 Transonic Design Consideration

Although there are different aircraft design methods, the range and endurance is always a major design consideration for civil transport aircraft (Torenbeek, 1997), and so the Breguet range equation is particularly important. This has formations for both jet and propeller aircraft configurations, however, only the equation for jet aircraft will be introduced here because it is relevant to this thesis. The Breguet range equation for jet aircraft is shown below (Randle, Hall and Vera-Morales, 2011):

$$Range_{Jet} = \frac{V}{c_t}\frac{C_L}{C_D}\ln\frac{W_0}{W_1} \tag{2.6}$$

where V is the cruise flight speed, c_t is the thrust specific fuel consumption, C_L is the cruise lift coefficient, C_D is the cruise drag coefficient, W_0 is the initial (take-off) aircraft weight and W_1 is the final aircraft weight.

The Breguet range equation contains three parts, i.e. $\frac{C_L}{C_D}$ refers to the aerodynamics, $\frac{1}{c_t}$ refers to the propulsion system, and $\ln\frac{W_0}{W_1}$ refers to the aircraft structure. It can be seen that, to maximise the range and economic performance of a civil transport aircraft, the most practical way is to reduce the thrust specific fuel consumption (c_t) and/or the cruise drag coefficient (C_D), i.e. to increase fuel efficiency and/or

reduce the aerodynamic drag and structural weight (Sun, 2014). On the other hand, the Breguet range equation also indicates that a maximum ML/D can also benefit the range and economic performance for steady cruise, where M is the cruise Mach number, L is the lift, and D is the drag. Figure 2.20 illustrates the ML/D variation for a typical transonic aircraft with different freestream Mach numbers, M_0.

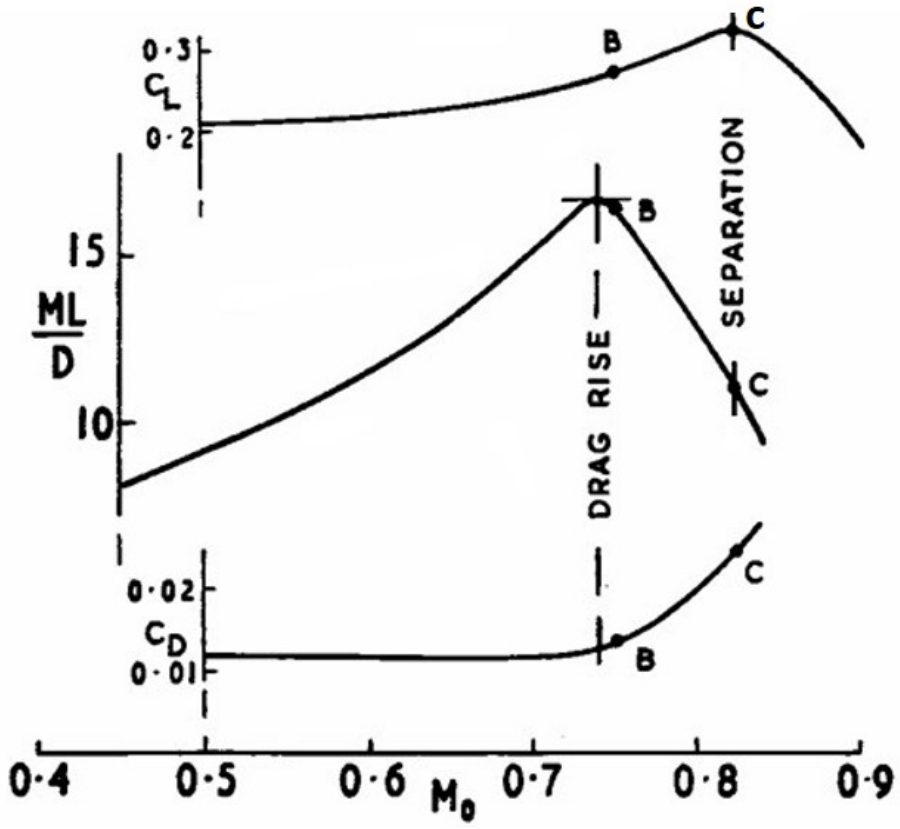

Figure 2.20: Plot illustrating the variation of two-dimensional ML/D at different Mach numbers for a typical civil aircraft (Ashill, 1995).

It can be seen that the maximum ML/D is achieved in the transonic speed regime ($0.7<M_0<0.8$) just ahead of the point B, which implies that flying at transonic speeds are suitable for most large civil transport aircraft to maximise range and economic performance, where C_L and C_D remain in an appropriate level. However, the ML/D decreases at higher Mach numbers, between the points B and C, due to the rapid drag rise encountered at high transonic Mach numbers as shock waves develop and become stronger with increasing M. It can be found that the C_L reaches its highest value at point C. Beyond this point there is a rapid reduction in lift due to shock-induced boundary-layer separation. Between points B and C, although the C_L increases, any advantage is removed by the significant increase in drag. In this range, a supersonic flow region will exist on a part of the wing surface that is terminated by a shock wave, which produces a significant drag, called wave drag. An empirical relationship for wave drag was derived by Lock (1945) implying the

dramatic increase in drag when $M > M_{crit}$, namely:

$$C_{D_{\text{wave}}} \approx 20(M - M_{crit})^4 \tag{2.7}$$

where M_{crit} represents the freestream Mach number at which the flow just becomes sonic at a point on the wing surface.

Figure 2.21 shows the drag rise of the NACA 66-210 sub-critical aerofoil with various angles of incidence and Mach numbers. It can be seen that the significant drag rise commonly occurs in the transonic speed regime ($0.7<M_0<0.8$), except that at extreme AoAs (-6 and 8°), drag starts to increase at a relative lower Mach ($M_0 \approx 0.65$), because flow acceleration is more pronounced. Sub-critical aerofoils were developed for relatively low speed applications and before the effects of compressibility at high speeds were fully know.

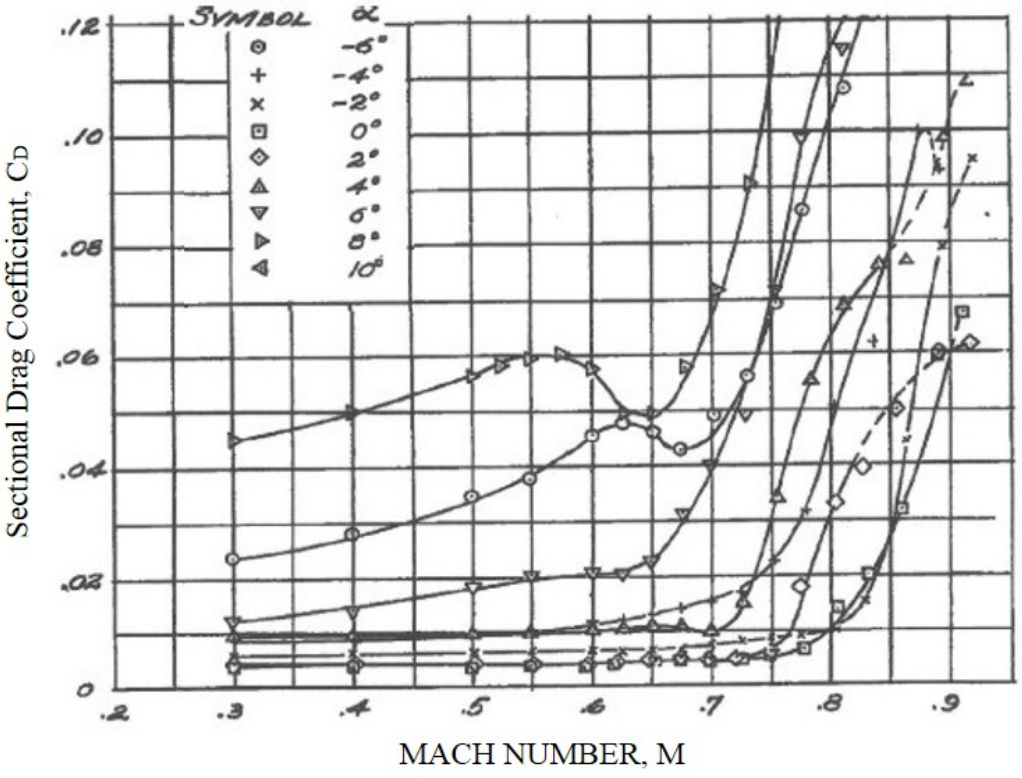

Figure 2.21: Plot showing the variation of section drag coefficient of the NACA 66-210 aerofoil with Mach number at various angles of attack (Graham, 1947).

It is important to mitigate the transonic drag rise in order to enable a higher M_{crit} and therefore a higher ML/D for improving aircraft performance. The empirical equation derived by Korn (1968), the Korn equation, can provide a simple means of estimating the possible combination of Mach number, wing thickness (t/c), sweep (Λ), and lift that can be obtained using a specific aerofoil design standard (κ_A),

shown below:

$$M_{crit} \approx \frac{\kappa_A}{\cos \Lambda} - \frac{(t/c)}{\cos \Lambda^2} - \frac{C_L}{10\cos \Lambda^3} - \left(\frac{0.1}{80}\right)^{\frac{1}{3}} \tag{2.8}$$

Here, κ_A is an aerofoil technology factor with a typical value of 0.95 for a supercritical aerofoil section (this will be introduced in Section 2.3.3) and 0.87 for a sub-critical NACA 6-series aerofoil which is not optimised for transonic flow. This relationship shows that the drag rise can be delayed by; (1) reducing lift (which reduces payload), (2) reducing wing thickness (which tends to increase structural weight), and (3) increasing wing sweep (which also tends to increase structural weight and likelihood of tip stall due to higher wing tip loading). Additionally, almost all large commercial aircraft comprise of the swept wing, where the wing normally sweeps backward. The swept wing has the advantage of delaying shock wave formation and the accompanying increase of wave drag during transonic flight (Obert, 2009).

Hence, it is desirable to improve the aerofoil drag standard (i.e. κ_A) by optimising the aerofoil shape to minimise the strength of shock waves at the desired lift condition (typically C_L=0.5) for cruise. However, aircraft inevitably have to operate off-design, for instance, instructions from air traffic control or during gusts, potentially resulting in an increased M_∞ and C_L. Therefore, wing designs need to consider "Mach flexibility", i.e. providing a good compromise of aerodynamic performance over a range of M_∞ and C_L, which is relatively difficult to achieve. If either M_∞ or C_L (or both) increase, the strength of shock wave on the upper surface is very likely to increase. The pressure increase across a shock wave results in a local increase in the boundary layer thickness. For strong shock waves scenario, this phenomenon can lead to a shock-induced separation of the boundary layer (see Fig. 2.23). To avoid this shock-induced separation, it is recommended that the M_{local} should not exceed a value of 1.3 (Obert, 2009). All of these considerations for design at transonic speeds led to the development of the supercritical aerofoil design philosophy.

2.3.3 Supercritical Aerofoil Design

In the 1960s, supercritical aerofoils were developed by Whitcomb and Clark (1965) primarily to confront the negative effect of wave drag for transonic aircraft. This was achieved with flatter suction surfaces, larger leading edge radii, and adverse pressure gradient control of the aft section (Harris, 1990). Supercritical aerofoils have three main aerodynamic benefits: (1) higher drag divergence Mach numbers, where the drag divergence Mach number is a critical value at which the aerodynamic drag

dramatically increases with the increase of Mach number, this increase can lead to a ten-fold increase of C_D than at low speeds (Anderson, 2011); (2) delay shock waves so they occur further aft than on conventional aerofoils by using a low-curvature design along the upper surface; and (3) reduce shock-induced boundary layer separation with a larger amount of aft camber (Harris, 1990). Figure 2.22 shows the comparison of flow features between a conventional aerofoil and a typical supercritical one.

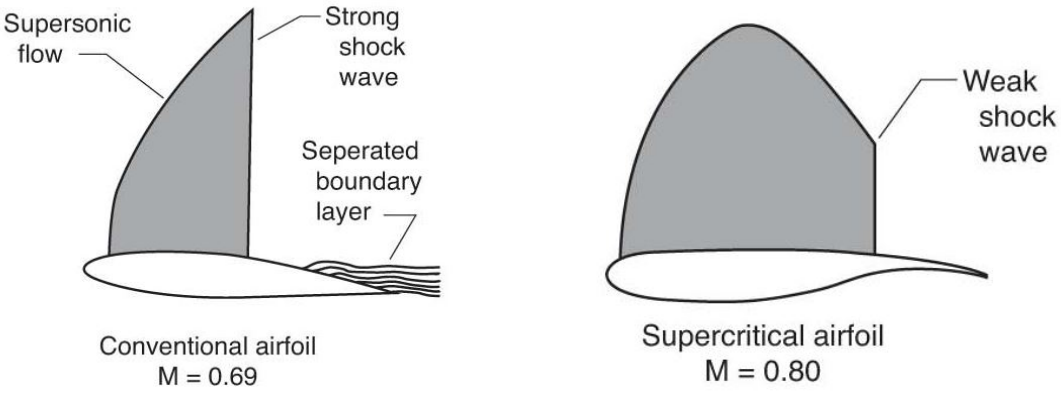

(a) (b)

Figure 2.22: Illustration showing the difference of flow features between (a) a conventional and (b) a supercritical aerofoil at different designed Mach numbers (NASA, 2014).

Here, with the conventional aerofoil, a strong shock wave occurs after the suction peak around the mid-chord followed by severe separation at a freestream Mach number of 0.69. While the supercritical aerofoil has a more gradual adverse pressure gradient after the suction peak (compared to a conventional aerofoil), the result is a weak shock wave and (ideally) no shock-induced separation. With the development of the supercritical aerofoil, aeronautical engineers were able to consider transonic design for commercial aircraft with better performance and economy (Whitcomb and Clark, 1965).

In terms of pressure distributions, the supercritical aerofoil design philosophy results in a relatively high "rear loading", compared to a sub-critical designs, see Fig. 2.24, where the shock wave is stronger and separation starts earlier than supercritical aerofoil. Therefore, it is important to control these adverse pressure gradients by careful design to avoid boundary layer separation at the trailing edge, which is different from shock-induced separation. This condition is referred to as "buffet", which is crucial to ensure a safe operating margin between the cruise and buffet conditions for transonic aircraft design.

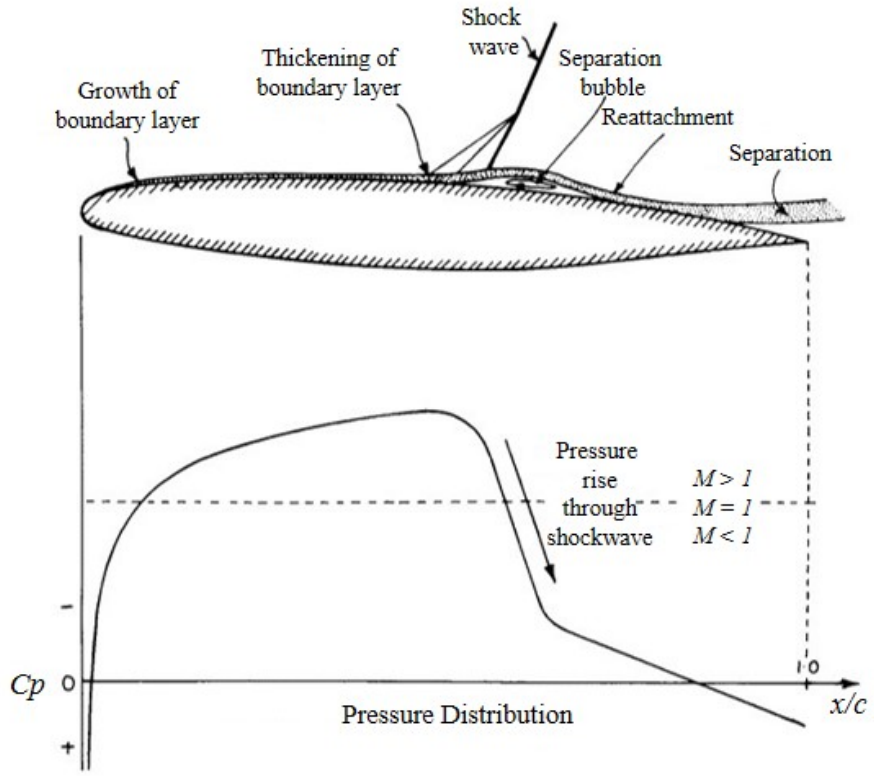

Figure 2.23: Plot showing the pressure distribution for a typical supercritical aerofoil modified from (Ashill, 1995).

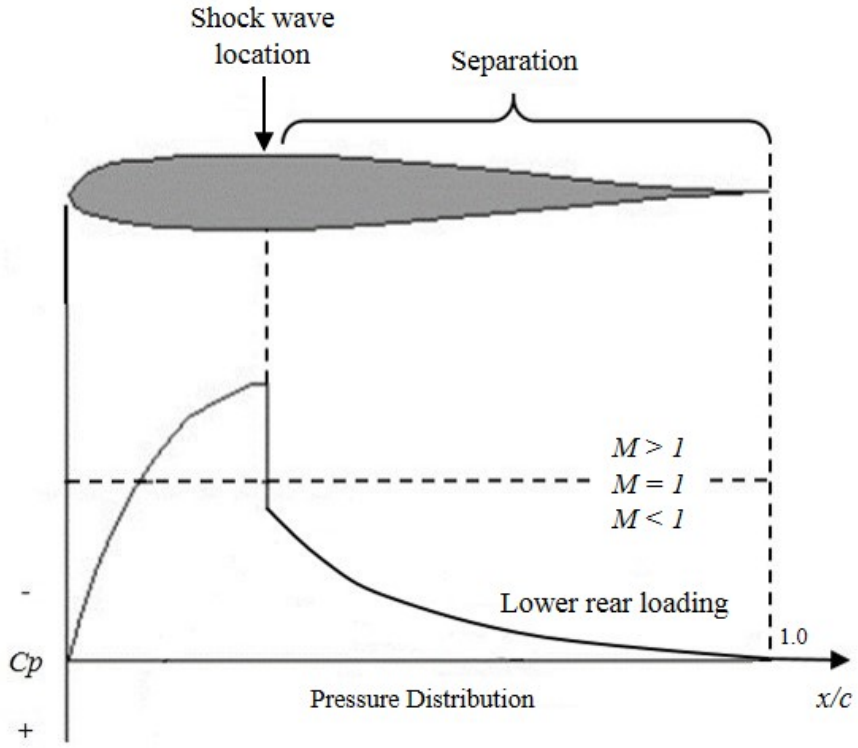

Figure 2.24: Plot showing the pressure distribution for a typical sub-critical aerofoil modified from (Bertin and Smith, 1989).

2.3.4 Under Wing Nacelle Configuration

In most commercial aircraft, the podded under-wing nacelle (UWN) configuration is the most commonly used. Under-wing mounted nacelles are generally placed ahead of the front spar of the wing to minimise wing structural damage in the event of a disk or blade failure (Obert, 2009). By installing a podded engine underneath the wing connected with a pylon, the UWN configuration offers beneficial wing bending relief during flight, the avoidance of wing flutter allowing a lighter wing structure, convenient maintenance and better cabin noise control (Obert, 2009).

The UWN configuration also places the nacelle inlet well ahead of the wing leading edge and away from the upwash flow from the wing leading edge, which minimises the risk of inlet distortion because the angle of attack at the nacelle inlet is reduced and no wakes are ingested (i.e. minimal interference from the airframe) (Obert, 2009). However, careful design is required to reduce interference effects between the nacelle, pylon, wing and fuselage as there is an increasing trend to install the nacelle closer to the wing for larger bypass ratio engines. It is widely known that high bypass ratio engines have a significantly improved fuel efficiency for the same thrust by reducing the fan pressure ratio (Sforza, 2014). However, the increased level of interference could result in higher airframe drag, reduced $C_{L_{max}}$ and potential flow separation.

In addition, at high-speed or off-design conditions, the high M_{local} on the lower surface could form shocks in the region of the pylon. For close-coupled UWN configurations, the contraction or "gully" between the wing, pylon and nacelle may result in shock waves, "gully shocks", at high-speed conditions, which can generate a significant amount of wave drag and lead to shock-induced separation. Furthermore, the limited space between the wing and the ground cannot allow larger bypass ratio engines to be conveniently installed and safely operated; very careful consideration of the position of nacelle must therefore be applied.

2.3.4.1 Under Wing Nacelle Integration

The coupling of under-wing podded engines and the wing is a complicated trade-off study in aircraft design. Commercial aircraft can benefit from the closely coupled engine to further increase turbofan diameter, see Fig. 2.25a. The aerodynamic effects of under wing nacelle position can be summarised as:

- Moving the nacelle close to the wing (decreasing x) will result in a drag penalty because of the formation of a gully shock between them which strengthens

when increasing the Mach number.

- Moving the nacelle forward (increasing x) leads to a small drag reduction, but is possibly outweighed by a weight increase of the pylon.
- Moving the nacelle upward (decreasing h) can increase wave drag due to gully shock formation, but it potentially reduces the weight with a shorter pylon structure and undercarriage leg length.

(a)

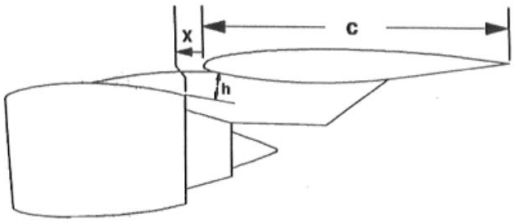

(b)

Figure 2.25: Illustration showing (a) limited margins for further increase of turbofan size on A320neo (Schmollgruber et al., 2019) and (b) typical engine position parameters.

2.3.5 Over Wing Nacelle Configuration

Despite the under-wing nacelle configuration offering substantial benefits, the ground clearance constrains the future development of UWN configurations. The over-wing nacelle (OWN) configuration, which is rarely adopted by commercial aircraft, allows the engine to be mounted over the wing, which eliminates the constraint of ground clearance allowing more space for even higher bypass ratio engines. Figure 2.26 shows historical OWN designs and concepts in recent decades. Additionally, the OWN offers the opportunity for free landing gear design, reduction of community noise by wind shielding (Berton, 2002), reduced foreign object damage risk, and the possibility of short take-off and landing due to power lift.

Here, the Boeing YC14 is a military experimental cargo aircraft designed for shorter take-off and landing in battle zones, which other heavy cargo aircraft is not capable of. Its over-wing nacelle featured Upper Surface Blowing technology, which uses blown air through a nozzle to shape the airflow over the rear wing, allowing a higher lift coefficient at low speed. The Fokker VFW 614 is the first OWN transport designed for the commercial market with a shorter robust landing gear and easier payload access. It was designed with a subsonic cruise Mach number of 0.65

Figure 2.26: Historical OWN designs and concepts (Berguin et al., 2018).

(Green, 1976), which is a safe cruise speed to avoid transonic wave drag. The NASA QSRA and NAL ASKA were four-engine research aircraft both featuring Upper Surface Blowing technology as well to improve low speed performance and enable the capability of short take-off and landing by taking advantage of the Coanda effect, in which deflecting the exhaust flow downwards with a curved flap at the trailing edge, converting a portion of thrust to lift (Birckelbaw, 1992). Lockheed HWB is a large military airlifter which is still under development. HondaJet is a successful small business jet integrating OWN configuration, natural laminar flow (NLF) wing, and a NLF fuselage nose, designed for Mach 0.72 with a longer range than any other small business jet (Fujino, 2005).

On the other hand, OWN configurations have historically warranted concerns over high drag levels at the upper surface for transonic conditions, however, the recent studies by Fujino and Kawamura (2003) and Hooker and Wick (2014) have disproved this preconception, resulting in renewed interest in the OWN concept. Results from the computational studies by Hooker et al. (2013) and Hooker and Wick (2014) demonstrated that a 5% improvement in aerodynamic efficiency can be realised from optimal OWN installation locations and wing shape optimisation with an additional reduction of wing weight and community noise levels compared to a representative baseline of UWN configurations.

2.3.5.1 Over Wing Nacelle Integration

Similar to the under-wing nacelle coupling concept, an optimum position for over-wing engine configuration is also crucial to aerodynamic performance. The research conducted by Berguin et al. (2018) from Georgia Institute of Technology using CFD gives an outline of the aerodynamic effect of locating powered engines at various positions on a typical commercial aircraft geometry equipped with a supercritical wing in real cruise conditions. The mid-chord position was eliminated as it produces unacceptably large shock-induced separation between the nacelle and wing, see Fig. 2.27, which severely deteriorates the aerodynamic performance.

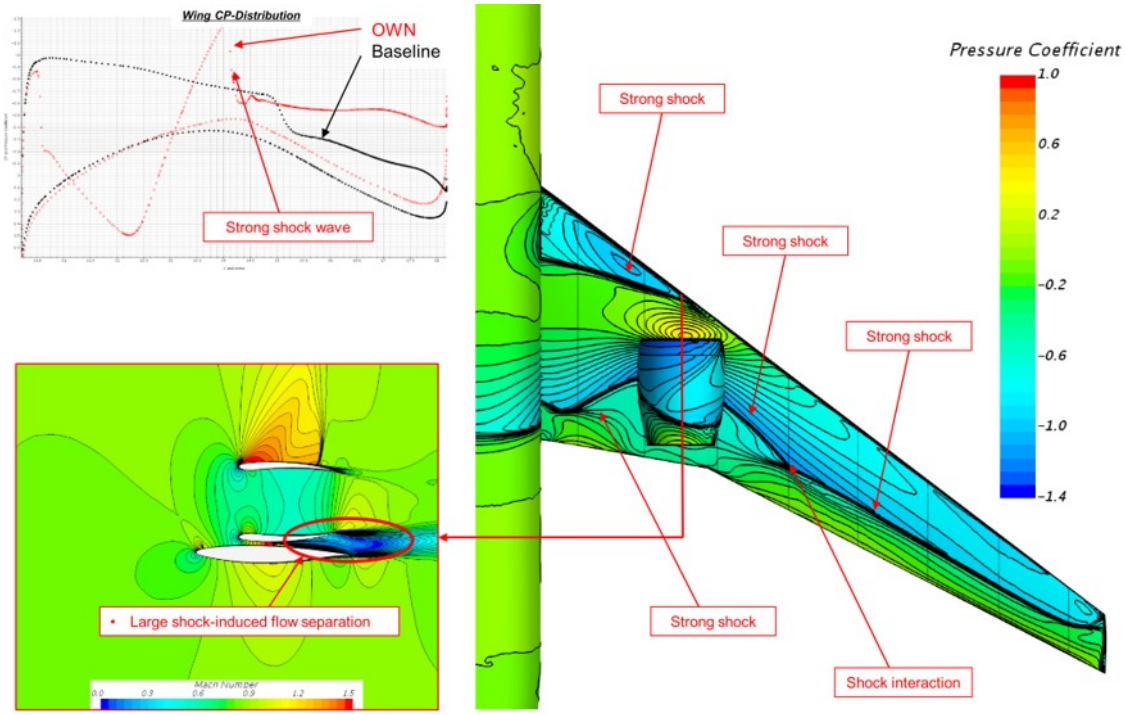

Figure 2.27: Detailed flow analysis of mid-wing positioned nacelle (Berguin et al., 2018)

Figure 2.28 illustrates the Mach contours and pressure distribution of leading edge (LE) and trailing edge (TE) positioned configurations compared to the clean wing. The LE and TE OWN configurations both gain greater flow acceleration between nacelle and wing. The LE position has a fairly large suction peak at the leading edge, which is potentially beneficial, followed by a weak shock, and the appearance of another strong gully shock wake at around 30% chord. The TE position presents a strong shock wave caused by the higher back pressure because of the presence of the nacelle slowing down the flow. Additionally, a second shock on the outboard wing is also observed (Berguin et al., 2018). The improved suction peak of LE position may somewhat counteract the extra drag penalty, however, it requires substantial improvement to achieve the same lift condition compared with

the clean baseline wing. The TE position is more promising if the strong shock can be mitigated via optimisation which was explored by Fujino and Kawamura (2003) using aft nacelle locations for optimum wave drag level; the existence of a strong shock can negatively affect flow into the engine and the pressure recovery at the engine intake.

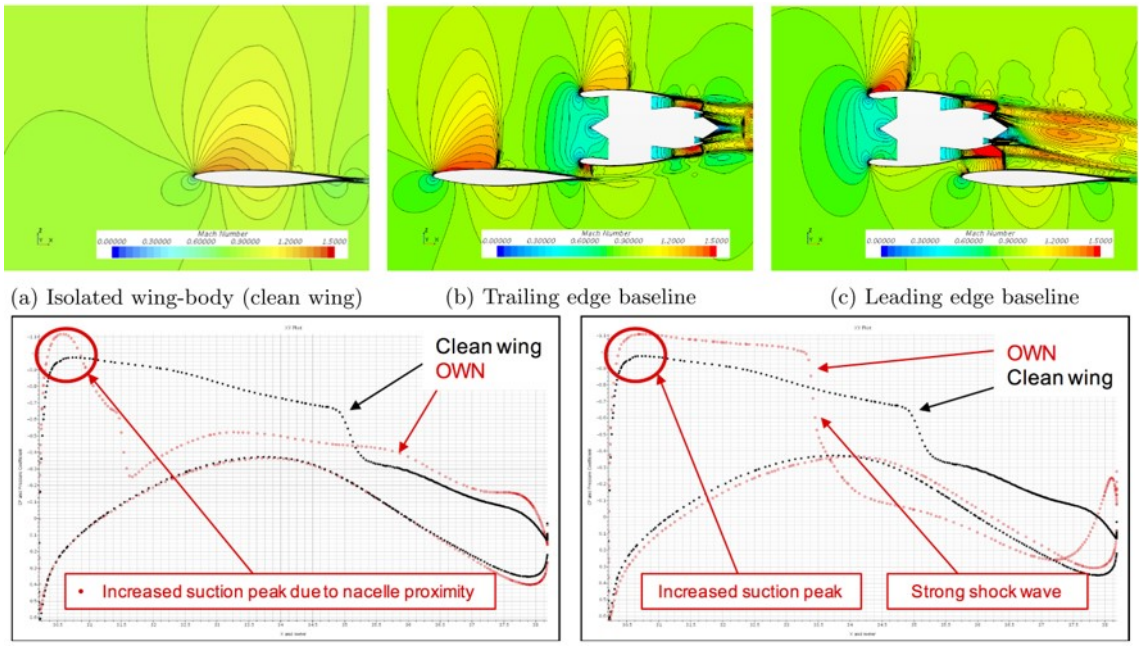

Figure 2.28: Historical OWN designs and concepts (Berguin et al., 2018).

The limitation of this study is that it only suggested a higher mounted nacelle to minimise the negative influence of any shock wave on the flow entering the engine intake. It is still possible to investigate an embedded OWN configuration by sacrificing the lift from the areas occupied by the nacelle but minimising the complexity of engine-wing coupling.

	EDS	CFD
Inlet mass flow rate (kg/s)	610.48	681.65
Fan exit mass flow rate (kg/s)	607.40	587.12
Error (%)	0.5	13.9

Table 2.1: Comparison of mass flow rate values at engine intake and exit for EDS and CFD results modified from (Berguin et al., 2018)

Another limitation of GeorgiaTech's report is that the fan intake and exit mass flow rate were not matched during their study (Berguin et al., 2018). Table 2.1 shows mass flow rate values for fan intake and exit from Environmental Design Space (EDS) and CFD in their study, where the EDS is a rigorous multi-design point vehicle sizing process (Kirby and Mavris, 2008). Although the mass of fuel is

added to the turbofan exit mass flow rate, it is still a fraction of the mass flow rate of air moving through the engine. It can be seen that the actual CFD exit mass flow rate is almost 14% smaller than the intake value, which is an important aspect in modelling engines, particularly for electric fans as no mass of fuel will be added into the exit mass flow.

2.4 Hybrid Distributed Propulsion

Aircraft propulsion systems generate thrust to propel an aircraft. From the traditional propeller to the modern turbofan engine, overall propulsive efficiency has significantly improved over past decades. The most well-known and effective improvement in propulsive efficiency comes from the increased bypass ratio of engines designed for commercial aircraft. The overall propulsive efficiency is mathematically defined as the product of propulsive efficiency and cycle efficiency. Propulsive efficiency is the proportion of mechanical energy propelling the aircraft and thermal efficiency is the proportion of chemical energy converted to mechanical energy (Loftin, 1985). By using combustion engines on an aircraft, during the conversion from thermal energy to mechanical energy, the loss of heat and kinetic energy is inevitable due to the lack of the energy storage and backup system. By considering the combination of two types of propulsion system on a single aircraft, the loss of energy can be reduced by utilising an energy storage unit when one of the propulsion units is not working at its maximum working rate; this is the fundamental idea of the hybrid propulsion system. Distributed propulsion is a type of propulsion system for fixed-wing aircraft accomplished by partially or fully span-wise distributed engines. It is a promising solution to maintain a bypass ratio without the negative effect of scaling down the engine size when incorporating such a propulsion system.

2.4.1 Background

Hybrid propulsion technology implies that vehicles employ more than one distinct type of power to drive them, for instance, the internal combustion engine plus electrical motors (Chau and Wong, 2002). The hybrid propulsion concept was initially established in the automotive industry. In 1901, Ferdinand Porsche developed the Lohner-Porsche, the first gasoline-electric hybrid vehicle in the world (Miller, 2008). The concept was criticised as unnecessary because of the low cost of fuel in that era. However, this criticism had turned to praise in the late 2000s due to the worldwide increases in fuel prices. Many auto-makers started to develop and release hybrid

propulsion vehicles at that time and since. Nowadays, hybrid propulsion technology is becoming increasingly important and necessary with concerns regarding fuel consumption, carbon emission and noise control. Furthermore, hybrid propulsion technology is not only available in the automotive industry, but also, it has drawn the attention of the aviation industry.

In aviation, hybrid propulsion technology can be incorporated with distributed propulsion, which can be defined as an aircraft propelled using multiple distributed propulsive actuators driven by an internal combustion engine with an additional power storage system (Kim, 2010). Some designs of hybrid propulsion systems for aircraft involve a clutch to individually or jointly drive the propellers (Schoemann and Hornung, 2013) in a parallel system (Schoemann, 2012) or a planetary gear system for a more optimum and efficient operation range (Lieh et al., 2011). Figure 2.29 shows a simplified example of a hybrid propulsion system for an aircraft.The combustion engine drives the power generator to charge the energy backup system and drive the propulsion actuator simultaneously.

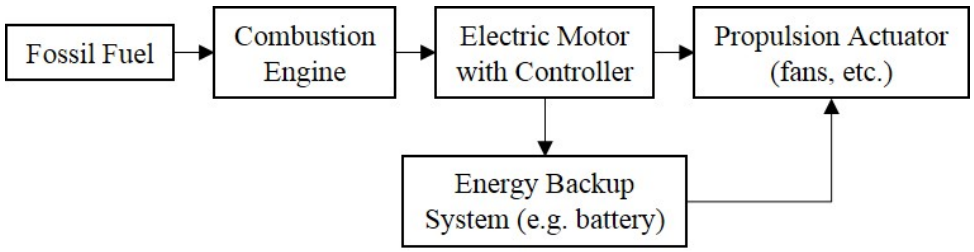

Figure 2.29: Simplified hybrid propulsion system modified from (Hung and Gonzalez, 2012).

2.4.2 Advantage in Aerospace Engineering

As already stated, hybrid propulsion technology has three main advantages: significant reduction in fuel consumption, carbon emission, and flight noise. The energy storage system can store and reuse excess power, which means that less fuel consumption can be achieved than the conventional propulsion system during cruise because the maximum power is only required during take-off and landing. Less fuel consumption can obviously lead to reduced carbon emission. The research of a hybrid propulsion system implemented on an Unmanned Aerial Vehicle (UAV) by Bagassi et al. (2012) showed that a hybrid configuration has an advantage in efficiency comparing with traditional diesel configurations. They found that hybrid propulsion can reach up to 92% efficiency using electric power whereas the efficiency of diesel was only 40%.

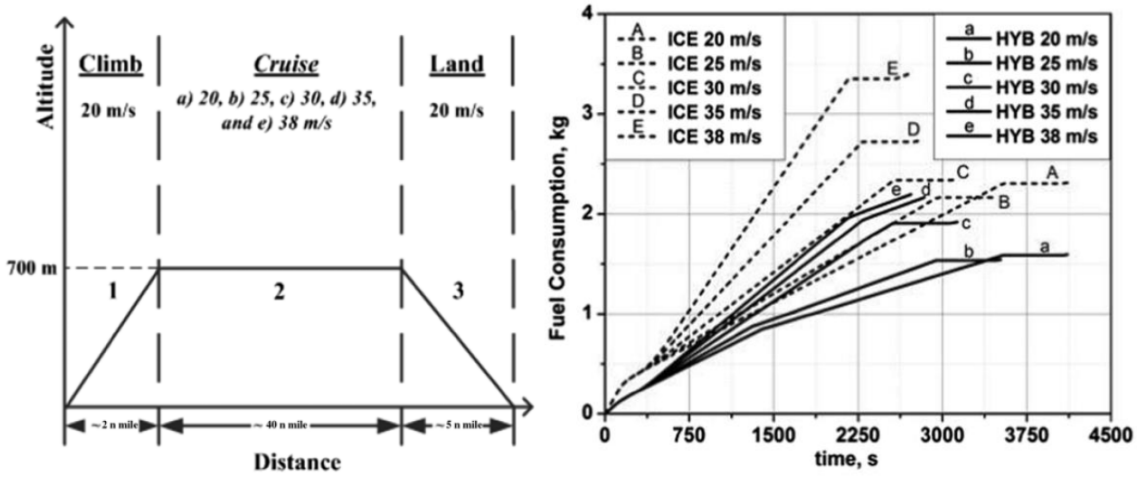

Figure 2.30: Fuel consumption in different airspeeds over flight times in simple flight mission profiles (Friedrich and Robertson, 2015).

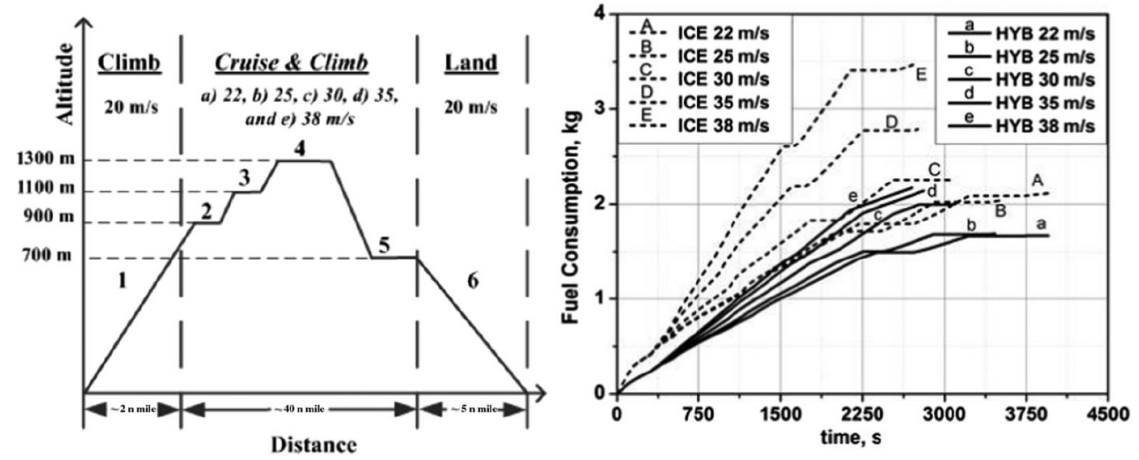

Figure 2.31: Fuel consumption in different airspeeds over flight times in complex flight mission profiles (Friedrich and Robertson, 2015).

Other research conducted by Friedrich and Robertson (2015) shows that the hybrid-electric configuration was able to save up to 37% fuel and 30% energy in a simulated flight mission profile. Figures 2.30 and 2.31 show the comparison of the fuel consumption between the hybrid configuration (HYB) and internal combustion engine (ICE) for different airspeeds and flight mission profiles. It is clear that the fuel consumption of HYB is lower than that in the ICE configuration under the same conditions.

Another convincing method to improve fuel efficiency is to decrease the fan pressure ratio (Sforza, 2014), by increasing the bypass ratios for modern turbofan engines. However, increasing the bypass ratio inevitably results in a larger turbofan size, which all turbofan engines have. As it has been discussed in the under wing nacelle configuration section, this idea of continuously increasing the size of the turbofan for future improvement is jeopardised due to ground clearance restric-

tions. For a given thrust, by multiplying the number of fans, previous solutions cannot be applied to maintain a low fan pressure ratio as well as a smaller fan size because the fans associated with engine cores are less effective when they are scaled down (Schmollgruber et al., 2019). With electric distributed propulsion, the negative scale effects will disappear if the fans are connected to electric motors that makes the electric distributed propulsion a potential approach for further increase of propulsive efficiency. Furthermore, distributed electric propulsion can improve the propulsive efficiency and reduce turbulent kinetic energy losses in the wake by utilising boundary layer ingestion (Felder, Kim, Brown and Chu, 2011), which has the advantage of generating thrust by re-accelerating the air (slow moving boundary layer). This uses less power rather than accelerating the same amount of air from the freestream to a higher velocity to provide the same level of thrust (Rolt and Whurr, 2015). However, the disadvantage of utilising boundary layer ingestion is that the boundary layer airflow can highly distort the conditions on the fan face when the fan is closely coupled with either the wing or the fuselage, of a typical aircraft. A common solution to this in scenarios where close coupling is required is to lift the engine nacelle slightly away from the wing/fuselage surface, to ensure free-air (and not the boundary layer) approaches the fan face. Without interventions, intake distortion effects due to boundary layer ingestion can produce a non-uniform total pressure distribution on the fan blade, whilst the unsteady loading of fan blades can lead to vibration and potential fatigue failure (Longley and Greitzer, 1992). Effectively employing boundary layer ingestion on a distributed propulsion system requires a stronger fan which has the disadvantage of increasing the structural weight and design complexity.

In addition to improving the propulsive efficiency, distributed propulsion also offers a greater flexibility for aircraft design to reduce structural weight and aerodynamic drag (Dehpanah and Nejat, 2015). For example, a smaller vertical tail control surface rather than a large traditional empennage can be achieved by relaxed engine-out design constraints and propulsion based control (Kim, Perry and Ansell, 2018). Moreover, a downsized power unit requires less power for cruise, additional power for climb can be provided by the energy storage system, and there are possibilities to distribute the weight of the propulsion system components across the wing and employ better flow control technologies for improving aerodynamic performance (Ko, Schetz and Manson, 2003).

Another advantage of hybrid propulsion is less noise. It is widely known that conventional aircraft flight causes serious noise problems to the ground even at a very high altitude. Cabin noise can be reduced by clever airframe design, but the noise experienced at the ground is a serious issue and it actually affects more people

(Kroo and Antoine, 2005). Commercial aircraft noise in cruise mainly comes from engine noise, which can be split to fan noise and jet noise. With the introduction of high bypass ratio (BPR) engines in the 1960s, engine-induced noise was significantly reduced by lowering the jet velocity (Keith, 1975). With high BPR design, the engine takes in a large mass of air and exhausts a small mass of air, which lowers exhaust jet velocity to reduce jet noise during cruise. Distributed propulsion aircraft uses multiple small and low-power fans in a row instead of a few large turbofans to be the propulsive means. With modern technology, bypass ratios of over 20 could be achievable in the future for distributed fan modules (Airbus Group Innovations and Rolls-Royce, 2014), which is higher than the values of BPR=12 achieved by today's most efficient turbofans, allowing the possibility for distributed propulsion to produce less noise than conventional jet engines.

2.4.3 NASA Distributed Propulsion Concept

Under the Environmentally Responsible Aviation N+ target, NASA has conducted research on distributed propulsion concepts under the Subsonic Fixed Wing Project (Pornet and Isikveren, 2015). The NASA N3-X concept, see Fig. 2.32, is based on the blended wing body airframe with electrically driven fans distributed on the upper surface aft fuselage.

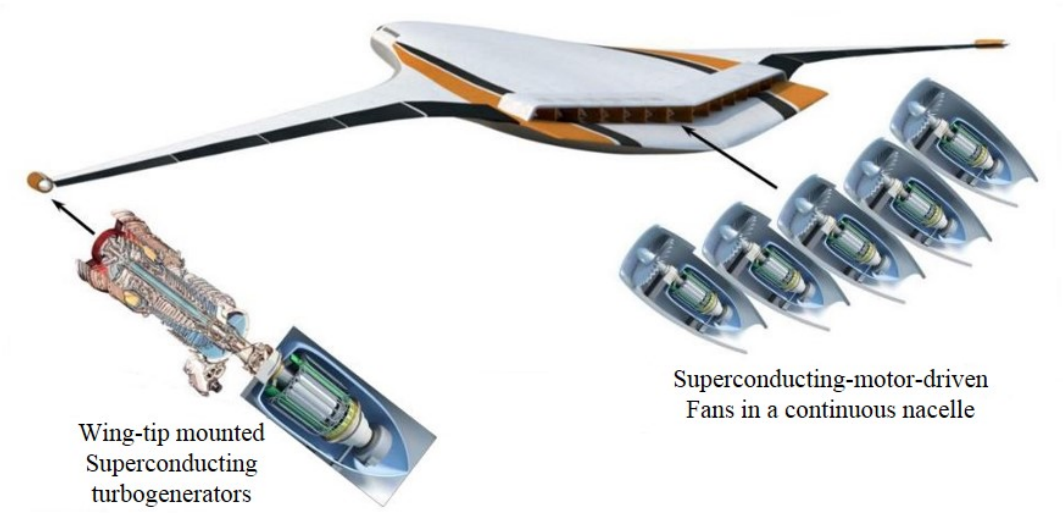

Figure 2.32: NASA Hybrid Wing Body N3-X concept with a Turboelectric Distributed Propulsion (TeDP) system (Felder, Brown, Kim and Chu, 2011).

The electric fans are powered by an advanced electric power generation and transfer system, which was also called turbo-electric distributed propulsion (TeDP), shown in Figure 2.33. The propulsion system adopted a high-speed generator to produce the electricity with a high-temperature superconductor (HTS) electrical

bus and a power converter to run the distributed fans with the power provided by the turbo-shaft engine (Felder, Kim and Brown, 2009). The fan module was installed in a continuous fan nacelle near the rear fuselage, where the thick boundary-layer flow exists. Then, the fan module was able to ingest that flow in order to fill the wake, therefore, the thrust required by the aircraft can be reduced by boundary layer ingestion (Felder, Kim, Brown and Chu, 2011; Kim, 2010). The N3-X also benefits from further development of a turbo-electric distributed propulsion system which is able to reduce the mission fuel burn by 70%-72% compared to the Boeing 777-200LR without compromising payload, range and cruise speed (Felder, Brown, Kim and Chu, 2011).

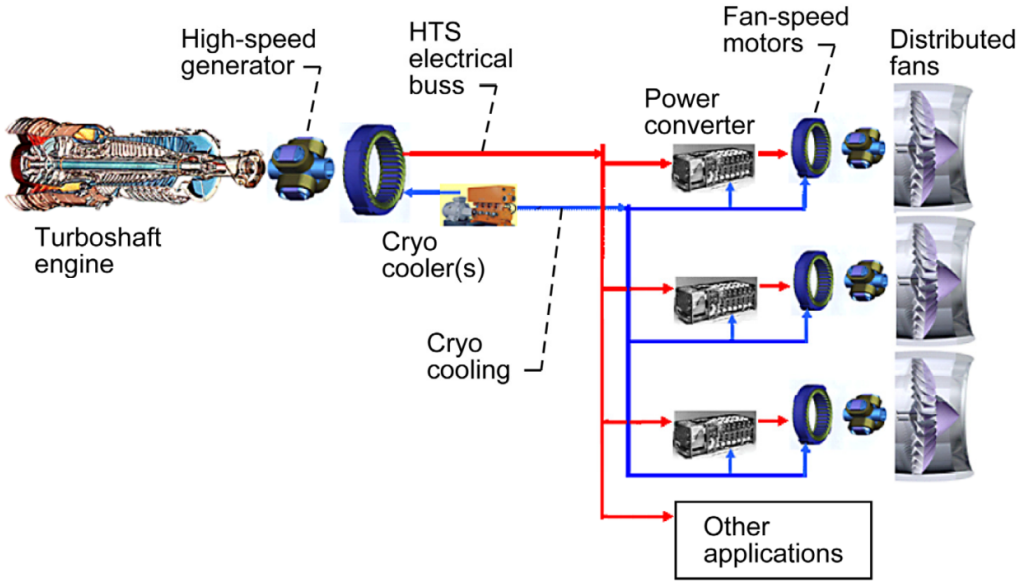

Figure 2.33: Illustration of Turboelectric Distributed Propulsion (TeDP) systems (Felder, Kim and Brown, 2009).

2.4.4 E-Thrust Concept

The E-Thrust concept is an electrical distributed propulsion system concept under the Distributed Electrical Aerospace Propulsion (DEAP) project, which is an international collaboration program launched by Airbus and Rolls-Royce focused on integrating distributed propulsion into future aircraft design to improve fuel economy, carbon emissions, and noise control (Botti, 2016). Figure 2.34 shows this wing-mounted distributed propulsion aircraft. This concept can be considered as a serial hybrid propulsion system.

In this design concept, the gas turbine will only be fully working during take-off and climb to provide peak power with the support of an electrical energy storage system in case of failure of the gas turbine during this phase. During cruise, the

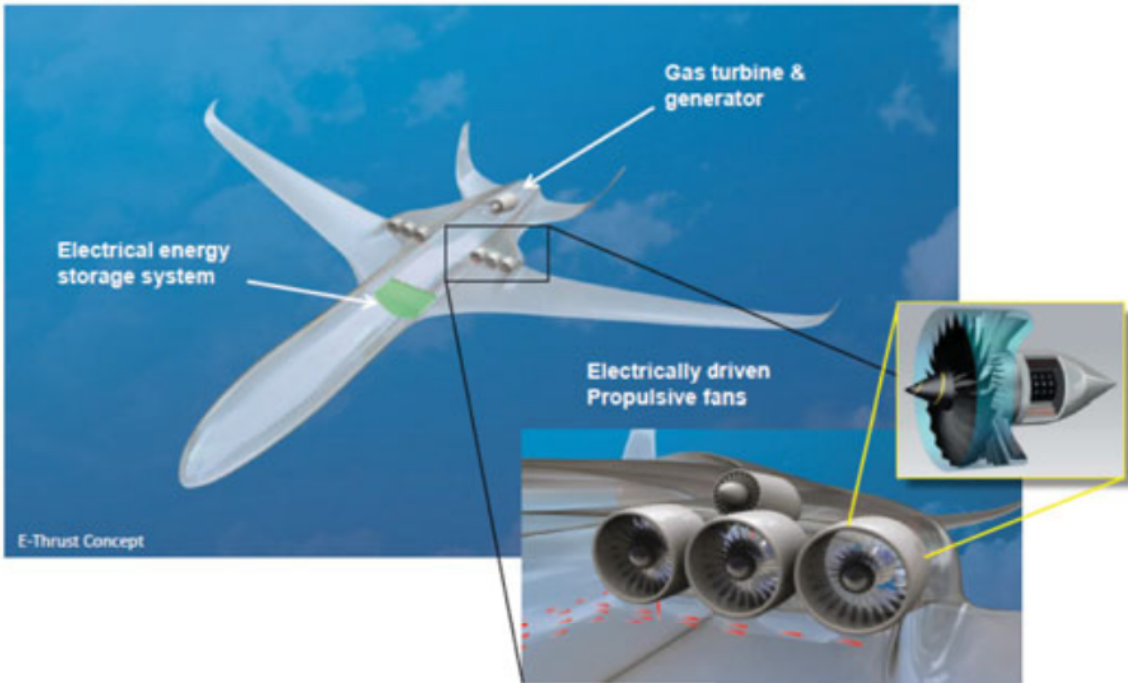

Figure 2.34: E-Thrust concept by Airbus and Rolls-Royce (Jupp, 2016).

gas turbine will provide cruise power as well as re-charge the energy storage system. During descent and landing, only low power is needed from the gas turbine, as the fan module can be wind-milling, rotating in the opposite direction, to charge the electrical energy storage system during descent while the gas turbine will provide low power for propulsion for final landing (Airbus Group Innovations and Rolls-Royce, 2014).

However, there are still some challenges which need to be dealt with, i.e. high bypass ratio fans, superconductivity, and the capacity of energy storage systems. Having high bypass ratio fans is a fundamental requirement to improve propulsive efficiency in distributed propulsion technology. As distributed propulsion requires a megawatt level working electrical network, design and validation of new high-voltage superconducting systems are necessary to reduce loss of electrical energy (Isikveren et al., 2015). Energy storage is a crucial aspect as distributed propulsion aircraft primarily rely on the stored energy when the gas turbine is not fully working. It is expected that a sufficient energy density for energy storage systems for the E-Thrust concept can be achieved before 2035 (Airbus Group Innovations and Rolls-Royce, 2014).

2.4.5 ONERA DRAGON Concept

Within the European Program Clean Sky2, the largest European research programme funded by EU's Horizon 2020, French National Aerospace Lab (ONERA) have recently developed a Hybrid Electric Distributed Propulsion test-bed "DRAGON", Distributed Fans Research Aircraft with electric Generators, which aims to carry 150 passengers at a cruise Mach number of 0.78 with a range of 1200 nautical miles to satisfy the flexibility requirement for airlines (Schmollgruber et al., 2019). Figure 2.35 shows the DRAGON concept with distributed fans located all along the wing span on the lower surface at the rear position of the wing for maximum aerofoil-propulsive effect and the opportunity of investigating span-wise effects of lift.

Figure 2.35: ORENA's distributed electric propulsion concept, "DRAGON" (Schmollgruber et al., 2019).

The DRAGON concept selects the under-wing nacelle configuration rather than the over-wing type, based on the research carried out by Isikveren et al. (2015) and Wick et al. (2015); the transonic regions of flow on the upper surface are extremely sensitive to any obstacles, for example, the OWN configuration could trigger buffet onset. While the compression zone on the lower surface naturally helps the flow slowing down for a downstream engine intake.

2.5 Synthesis

2.5.1 Summary of the Literature Review

This literature review served to explain the benefits and challenges of transonic aircraft designs and that the idea of placing the engines under or over the wing are not novel for transonic aircraft. However, incorporating these with the hybrid electric distributed propulsion concept has great potential. Employing smaller distributed electric fans can maintain relatively high energy and propulsive efficiency and it is possible that they could simultaneously improve wing pressure distributions. Computational simulation tools have been developed to be highly versatile and powerful. It is worth implementing conceptual analysis on the existing UWN's benefits and the OWN's design driver (energy efficiency), with Computational Fluid Dynamics and powerful aerofoil parametrisation methods, to explore the aerodynamic performance improvement for supercritical aerofoils in the transonic regime. The future of developing an optimised aerofoil for either UWN or OWN still remains if the potential benefits of incorporating them with the novel hybrid electric distributed propulsion concept can be translated into commercial aviation. Thereafter, a proof-of-concept is necessary.

2.5.2 Gaps in Knowledge and Research Objectives

From this literature review, the gaps in knowledge can be summarised as follows:

- Using a generic method, the combination of suitable boundary conditions in commercial CFD packages to simulate electric ducted fans, is not well posed in previous studies due to the discrepancy of intake and exit mass flow rates. Therefore, it is worthwhile to establish a suitable combination of boundary conditions to address in this gap.
- There is numerous research focusing on under and over-wing nacelle configurations, but the research combining these two configurations with distributed propulsion is limited, which is a notable gap in knowledge.
- Many methods have been developed for improving the aerodynamic performance of the supercritical aerofoil. However, for the distributed propulsion concept, there are few studies which couple it to under and over-wing nacelle configurations.
- To mitigate the challenges of transonic supercritical aerofoil design, research

has not been carried out in detail in this field, while a lot of research regarding boundary layer ingestion has been implemented. To investigate the potential "flow entrainment" offered by under and over-wing nacelle configurations, it is still necessary to cope with boundary layer separation when buffet onset occurs.

Based on the gaps in knowledge found in the literature, this study will consider the aerodynamic performance improvement on a supercritical aerofoil by incorporating the UWN and OWN configurations at transonic speeds. The research objectives are:

1) Develop a method to simulate an electric ducted fan in a commercial CFD package.

2) Improve the aerodynamic performance of a supercritical aerofoil by combining a Design of Experiments (DoE), CST parametrisation (Kulfan, 2007), and CFD automation for the distributed propulsion concept.

3) Conduct numerical analysis of distributed UWN and OWN propulsion concepts to investigate their advantages and disadvantages.

4) Mitigate buffet onset with the distributed propulsion concept at transonic speeds.

5) Determine design recommendations and highlight areas of future investigation which offer greater promise for new wing design and distributed propulsion integration.

Chapter 3

Research Methodology

As described in Chapter 2, experimental methods provides a controlled testing environment to analyse and visualise the flow field. However, the complexity of flow structures around any aircraft at transonic speeds, especially the region where separation occurs, makes the testing of scale models inadequate and insufficient in wind tunnels. In addition to solving fluid dynamics problems with theoretical and experimental approaches, the maturity of Computational Fluid Dynamics (CFD) has dramatically improved in recent decades, offering enhanced capability to handle huge amounts of calculations for producing numerical solutions for the governing equations. In this research project, CFD is the main research tool to conduct aerodynamic analysis on a representative aircraft geometry and to explore the benefits of both under and over-wing nacelle configurations with the distributed propulsion concept. In this chapter, a comprehensive description of CFD applications followed by the introduction of aerofoil parametrisation methods and Design of Experiments (DoE) are presented; these will be used in subsequent chapters.

3.1 Computational Fluid Dynamics

In CFD applications, conducting the analysis of fluid behaviour involves three key steps, i.e. pre-processing, solving, and post-processing. In pre-processing, a grid must be generated before the definition of physical properties and boundary conditions are made. The accuracy of CFD depends on the quality of the grid and the number of cells in the domain. Grid independence must be investigated to ensure the solution is independent from the grid size (Roache, 1994). However, excessive number of cells will significantly reduce the time efficiency, as the computing needs

extra processing power and time. Therefore, it is necessary and important to decide an appropriate number of cells in the grid to balance accuracy and time efficiency.

During the solving process, the numerical methods will be used to obtain a solution. There are two popular numerical methods in which the governing partial differential equations (PDEs) can be discretised, finite volume method (FVM) and finite element method (FEM) (Versteeg and Malalasekera, 2007). FVM divides the fluid domain into finite set of cells (control volumes), and fluxes are calculated by integration through control volumes with continuity, momentum and energy conserved (Versteeg and Malalasekera, 2007). By comparing FVM with FEM, FVM requires more time and effort to solve irregular geometries (Versteeg and Malalasekera, 2007). The principles of FEM and FVM will be introduced and discussed in later subsections. The operations in the solving process include the definition of unknown flow variables, selection of governing equations, mathematical manipulations, and solution of algebraic equations (Versteeg and Malalasekera, 2007).

Post-processing involves extracting the information of interest from the fluid flow solutions, which is normally covered by the post-processing tools in all commercial CFD packages. Some key features in CFD applications, including governing equations, the Finite Element Method, and the Finite Volume Method are introduced in the following subsections.

3.1.1 Governing Equations

The underlying physics of fluid flows is based on three fundamental conservation laws; the conservation of mass, momentum and energy (Anderson, 1995). To describe these three principles, Claude Navier and George Stokes derived a set of equations, the Navier-Stokes equations, by introducing the variable, ϕ, which can be any scalar quantity (Durbin and Medic, 2007). Hence, the conservative form of the general transport equations utilised in CFD implementation (Versteeg and Malalasekera, 2007) is expressed by:

$$\underbrace{\frac{\partial(\rho\phi)}{\partial t}}_{\substack{\text{Rate of increase}\\ \text{of } \phi \text{ of fluid}\\ \text{element}}} + \underbrace{\nabla.(\rho\phi\vec{u})}_{\substack{\text{Net rate of flow}\\ \text{of } \phi \text{ out of fluid}\\ \text{element}}} = \underbrace{\nabla.(\Gamma\nabla\phi)}_{\substack{\text{Rate of increase}\\ \text{of } \phi \text{ due to}\\ \text{diffusion}}} + \underbrace{S_\phi}_{\substack{\text{Rate of increase}\\ \text{of } \phi \text{ due to}\\ \text{sources}}} \tag{3.1}$$

where the fluid element in this equation refers to a small arbitrary control volume, $\vec{u}$ is the velocity vector, Γ is the diffusion coefficient, and S_ϕ is the source term. Given appropriate values of Γ and S_ϕ, for ϕ=1, that gives the continuity

equation (3.2). Using velocity components u, ν, and w in place of ϕ yields the momentum equations (3.4)(3.5)(3.6). For $\phi = T$, the temperature, that produces the energy equation(3.7). Considering other types of fluid problems, the general transport equation (3.1) can also be derived into other governing equations, for example, the species transport equation(3.7) (Versteeg and Malalasekera, 2007).

$$\frac{\partial \rho}{\partial t} + \nabla.(\rho \vec{u}) = 0 \tag{3.2}$$

$$\frac{\partial \rho u}{\partial t} + \nabla.(\rho u \vec{u}) = \nabla.(\Gamma_M \nabla u) + S_{Mx} \tag{3.3}$$

$$\frac{\partial \rho v}{\partial t} + \nabla.(\rho \nu \vec{u}) = \nabla.(\Gamma_M \nabla v) + S_{My} \tag{3.4}$$

$$\frac{\partial \rho w}{\partial t} + \nabla.(\rho w \vec{u}) = \nabla.(\Gamma_M \nabla w) + S_{Mz} \tag{3.5}$$

$$\frac{\partial \rho T}{\partial t} + \nabla.(\rho T \vec{u}) = \nabla.(\Gamma_T \nabla T) + S_T \tag{3.6}$$

$$\frac{\partial \rho Y}{\partial t} + \nabla.(\rho Y \vec{u}) = \nabla.(\Gamma_S \nabla Y) + S_S \tag{3.7}$$

where Γ_M, Γ_T and Γ_S represent fluid viscosity (Pa.s), thermal conductivity ($W^{\circ}K^{-1}m^{-1}$) and species diffusion coefficient ($m^2 s^{-1}$) respectively. S_{Mx}, S_{My}, S_{Mz}, S_T and S_S are the source terms for XYZ coordinate directions of the momentum equation, the temperature equation, and the species transport equation. (Versteeg and Malalasekera, 2007).

3.1.2 Discretisation and FEM/FVM

Unlike the geometrically simple problem that can be solved by simplified governing equations in analytical solutions, for geometrically complex domains, a process of deriving a system of algebraic equations to represent the general governing partial differential equations (PDE) shown in previous section is required. There are a number of discretisation methods and two common methods employed in commercial CFD solvers are introduced here, i.e. finite element method (FEM) and finite volume method (FVM).

The principle of FEM is to discretise a large domain into smaller and simpler elements, namely finite elements, by a particular spatial discretisation in the domain. Consequently, the results from each element are reassembled to provide a final solution for the entire problem. FEM is widely and typically used in structural analysis, heat transfer, fluid flow problems, and mass transport. This method originated from the need to solve unstructured triangular elements allowing an appropriate numerical approach for fluid mechanics (Hirsch, 2007). After its formulation, FEM became practical for any continuously shaped space. One of the greatest advantages of FEM is that it is able to discretise a fluid domain with irregular curvilinear elements by filling the domain space with any shapes (Patankar, 1980). In the derivation of its discretised equations, an interpolation function (often low-order polynomial) describes the way dependent variables, ϕ, vary across each individual element as a function of the values of ϕ at the nodes of each individual element. Thus the basis of FEM is to approximate the solution rather than the equations (Patankar, 1980). Eventually, the final solution is represented by a set of algebraic equations to determine the nodal values of ϕ.

FVM is another well-established fluid dynamics technique which has been incorporated by many commercial CFD packages, e.g. Star CCM+ and ANSYS Fluent. This method uses a technique that divides the fluid domain into a finite set of non-overlapping cells, also known as control volumes. The computational node lies at the centre and this is where the solution variables are stored after discretising the fluid domain. Figure 3.1 shows a comparison between FVM and FEM, the latter has computational nodes lying at boundaries.

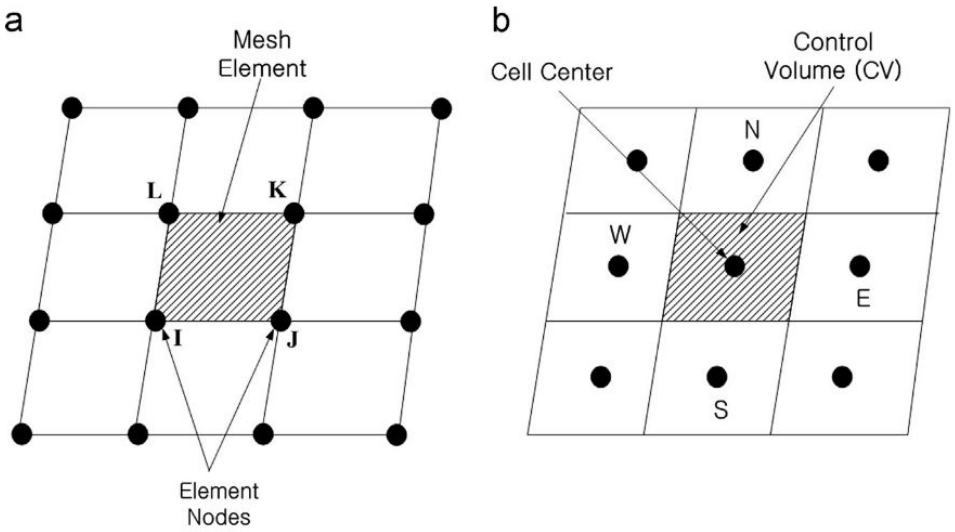

Figure 3.1: A representation of a structured mesh for the two discretisation methods analysed by (a) FEM and (b) FVM (Jeong and Seong, 2014).

Then, the differential equations describing the flow properties are solved and

integrated over each of all individual control volumes to evaluate the fluxes through each of the cell faces with the governing equations (Patankar, 1980). For example, the integration process produces solution variable fluxes through Control Volume N, S, W and E for the shaded control volume in Figure 3.1. Therefore, this is the major advantage FVM has over FEM that integration of the conservation quantities ensures that momentum, mass and energy are locally conserved to each control volume (Versteeg and Malalasekera, 2007). This also ensures global conservation whether the grid is coarse or fine as it produces the solutions exhibiting exact integral balances (Patankar, 1980). Table 3.1 shows the comparison of advantages and disadvantages between FEM and FVM. The FVM discretisation method utilised in the Star CCM+'s solver is the primary research tool used in this thesis.

Methods	Advantages	Disadvantages
FEM	Natural boundary conditions for fluxes	Less physics involved
	More Mathematics involved	Less physical significance
	Any shaped geometry can be modelled with the same amount of effort	Cannot tell with conservation of flow properties
	Master element formulation	
FVM	Fluxes have more physical significance	Irregular geometry requires more time and effort
	More Physics involved	

Table 3.1: Advantages and Disadvantages of FEM and FVM.

3.1.3 Grid Representation

One of the most time consuming and difficult stages in CFD application is the discretisation of the domain through grid generation, which is also known as meshing. A mesh is the discretised representation of the computational domain where the solvers provide a numerical solution (CD-adapco, 2016). High quality CFD solutions depend on quality grid in both two and three-dimensional problems. In order to increase the complexity of the grid for solutions in complicated flow conditions, two main grid strategies are commonly utilised (i.e. structured and unstructured).

3.1.3.1 Structured Grid

Before the development of structured grids, body-fitted grids used simple shapes to map the flow domain into a computational domain (Versteeg and Malalasekera, 2007). Figure 3.2 illustrates an example of the body-fitted grid for flow past

cylinders and the equivalent Cartesian computational grid. This strategy avoids time-consuming and complicated conversion by adopting simple matrices. However, in complex fluid domains, a body-fitted grid will produce unreliable solutions due to the simple matrices resulting in poor cell quality in the grid.

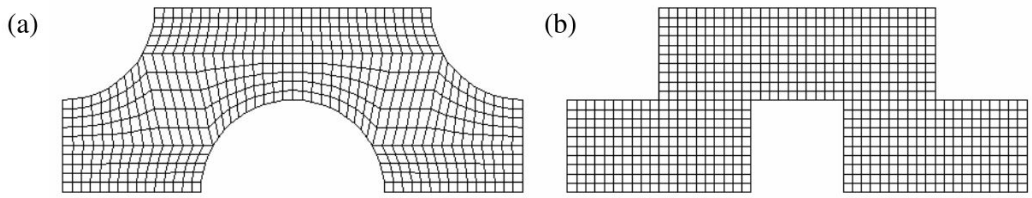

Figure 3.2: Schematics showing (a) the simple body-fitted grid and (b) the mapped computational grid (Versteeg and Malalasekera, 2007).

The structured grid is an appropriate method, identified by regular connectivity, to discretise the domain normally into quadrilateral and hexahedral elements in 2D and 3D respectively, which can be easily meshed without degenerate regions of the grid. Figure 3.3 shows two examples representing a 2D quadrilateral grid for an aerofoil and a 3D multi-block grid for a "pipe" shape geometry. This method also allows dense elements to be positioned in the locations where large flow gradients are expected.

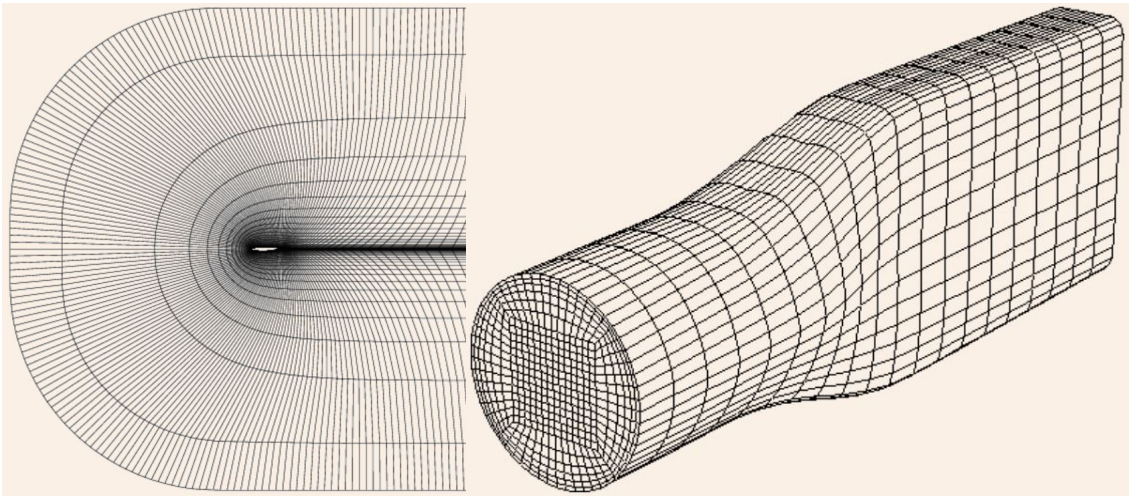

(a) (b)

Figure 3.3: Example of (a) a 2D structured quadrilateral grid for an aerofoil and (b) a 3D hexahedral structured grid (ANSYS Fluent, 2018).

3.1.3.2 Unstructured Grid

The unstructured grid, in contrast to the regular connectivity of a structured grid, identifies each cell to be an individual block in its own right (Versteeg and Malalasek-

era, 2007). This method allows the ability to deal with the issue from sudden geometrical change in the domain. It also benefits from reduced time consumption as structured method requires a suitable arrangement of elements before decomposing the domain. Unstructured grids typically employ triangular cells in 2D and tetrahedral cells in 3D. Two examples of unstructured grids are shown in Figure 3.4.

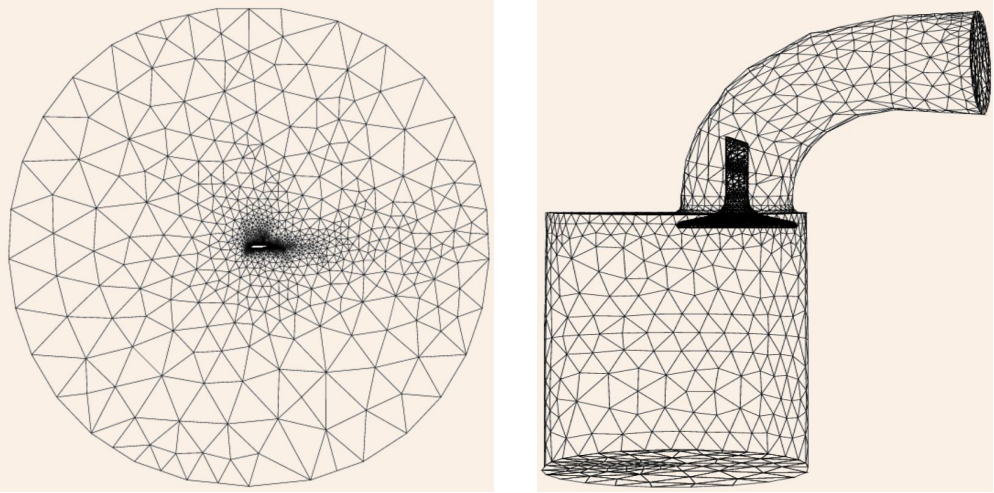

(a) (b)

Figure 3.4: Example of (a) a 2D unstructured triangular grid for an aerofoil and (b) a 3D hexahedral unstructured tetrahedral grid (ANSYS Fluent, 2018).

3.1.3.3 Grid Quality

Examining and verifying the cell quality relies on a number of geometrical properties, such as aspect ratio, volume ratio, and skewness angle. An often used criterion is equiangular skew, Q_{SK}, which a measure of the level of distortion or "skewness" in the grid (ANSYS Fluent, 2018). The maximum skewness of each element is determined from the following expression:

$$Q_{SK} = max\left(\frac{\theta_{\max} - \theta_{eq}}{180 - \theta_{eq}}, \frac{\theta_{eq} - \theta_{min}}{\theta_{eq}}\right) \tag{3.8}$$

where θ_{max} and θ_{min} are the maximum and minimum internal angles of a given cell. θ_{eq} is the angle corresponding to a perfect cell without distortion i.e. $\theta_{eq} = 60°$ for triangular and tetrahedral elements, and $\theta_{eq} = 90°$ for quadrilateral and hexahedral elements ANSYS Fluent (2018). Table 3.2 summarises the classification of cell quality corresponding to various ranges of Q_{SK}, where Q_{SK} is normalised between 0 and 1. Both ANSYS Fluent (2018) and CD-adapco (2016) recommend that the maximum skewness does not exceed 0.85.

Cell Quality	Classification
$Q_{SK} = 0.00$	Perfect
$0.00 < Q_{SK} < 0.25$	Excellent
$0.25 < Q_{SK} < 0.50$	Good
$0.50 < Q_{SK} < 0.75$	Fair
$0.75 < Q_{SK} < 0.90$	Poor
$0.90 < Q_{SK} < 1.00$	Very Poor
$Q_{SK} = 1.00$	Degenerate

Table 3.2: Classification of cell quality by Q_{SK} (ANSYS Fluent, 2018).

3.1.4 Turbulence Modelling

Due to the nature of turbulence, containing complex and non-linear behaviour, accurately and efficiently capturing salient features of fluid flows in turbulence is one of the most challenging parts in CFD simulations. However, the difficulty lies with sufficient iterations of calculations rather than mathematical complexity. The necessity to solve turbulence problems results in the development of turbulence modelling. An appropriate turbulence model is able to accurately simulate and predict the physical effects of turbulent flow (Wilcox, 1998). In fluid flow, the velocity and pressure are governed by Navier-Stokes equations, whilst velocity and pressure can be decomposed into mean and fluctuating parts in turbulent flow. By averaging the governing equations, Reynolds-averaged Navier-Stokes (RANS) equations, these are able to govern the mean flow in order to solve the large-scale and non-fluctuating features (Wilcox, 1998). By comparing with Direct Numerical Simulation (DNS) and Large Eddy Simulation (LES), RANS has the advantage in time efficiency because DNS and LES are both computationally far more expensive due to their inherently transient nature (Wilcox, 1998). The following sections will briefly introduce the DNS and LES, and the details of three commonly used turbulence models based on RANS equations in aerospace engineering applications: k-ω, k-ε, and Spalart-Allmaras turbulence models.

3.1.4.1 Direct Numerical Simulation

The principle of Direct Numerical Simulation (DNS) is to directly solve all of the turbulent length and time scales, including the smallest eddies, with an adequately fine grid, which demands numerous computing resources(Wolfshtein, 2009). Figure 3.5 shows a DNS result of the flow through a rectangular duct at $Re = 47,500$ (Hirsch, 2007).

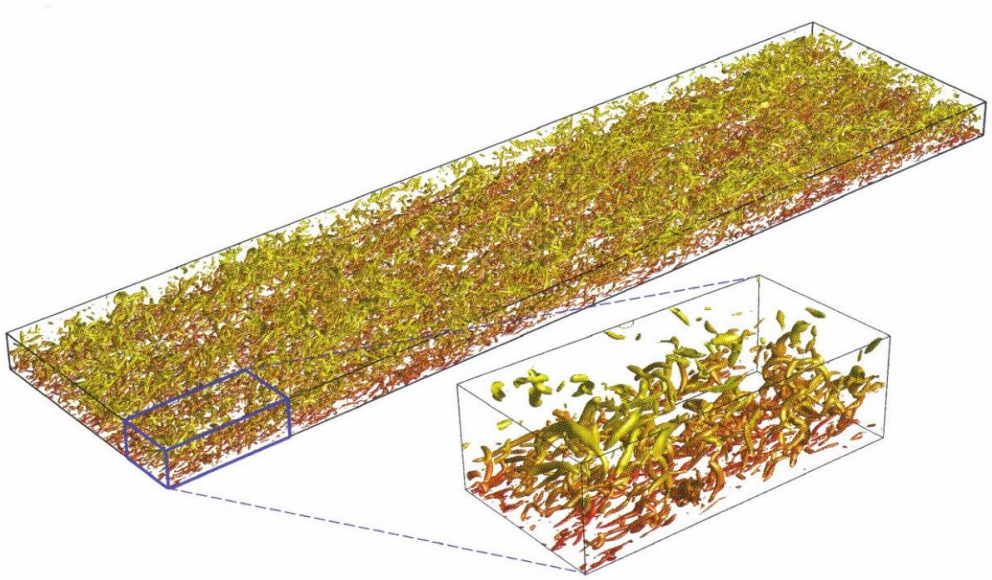

Figure 3.5: DNS results showing turbulent vortices throughout a rectangular duct (orange colours represent near-wall vortices) (Hirsch, 2007).

In Hirsch's research, the full range of turbulent length scales were directly resolved, resulting in a extremely high number of cells in total (i.e. 1.226×10^9), which took 106 processing hours running on 384 processors (Hirsch, 2007). Additionally, sufficient temporal discretisation was required to capture the fastest movement in this fine grid, leading to a frequency on the order of 10kHz and a time steps of $100\mu s$ (Tu, Yeoh and Liu, 2018). Due to tremendous computational demands, DNS is only suitable to solve low Re flow problems or a small flow domain, whereas most aerodynamic research involve large domains and flow with a high Re (Spalart, 2000).

3.1.4.2 Large Eddy Simulation

Large Eddy Simulation (LES) is a compromise between the accuracy of DNS, directly computing large scale turbulent fluctuations in space and time, and the computational efficiency, using semi-empirical laws in the form of a sub-grid scale (SGS) to model filtered turbulent eddies below the cut-off width, Δ (Versteeg and Malalasekera, 2007). Comparing to DNS, LES only requires a fine grid as long as it is enough to model larger eddies, while the SGS model can manage to deal with other smaller eddies due to the isotropic structure of micro-scales. However, for high Re conditions, LES also requires plenty of computing resources because of its time-dependent nature, which is still infeasible for aerodynamic study (Spalart et al., 1997). Krajnovic (2009) also commented that LES requires approximately 600 million cells solely in the near-wall region of $y^+ < 20$ for the simulation of wall bounded flow around a simple vehicle. Additionally, LES requires accurate turbulence levels at the

domain inlet including fluctuations (Krajnovic, 2009) and structured grids strictly on cell stretching to reduce numerical diffusion (Hutton, 2009).

3.1.4.3 Reynolds Averaged Navier-Stokes

Reynolds Averaged Navier-Stokes (RANS) is the most used approach for turbulence simulations, which is inherently steady-state and only computes largest turbulent scales (Hirsch, 2007). Normally, RANS models employ wall functions to represent near-wall turbulence (Versteeg and Malalasekera, 2007). It is known that the process of Reynolds averaging suppresses some vital information in a given flow field. However, the averaging process considerably simplifies the problem and avoids time-averaging (Spalart, 2000). Some of commonly used types can be classified as:

- Spalart-Allmaras model (one transport equation) (Spalart and Allmaras, 1992)
- k-ε model (two transport equations) (Launder and Spalding, 1974)
- k-ω model (two transport equations) (Wilcox, 1998)

3.1.4.4 *k*-*ε* Model

The standard k-ε turbulence model is one of the earliest developed turbulence models, being used for nearly 50 years, for non-trivial Re flows (Launder and Spalding, 1974), which includes two extra transport equations to represent two turbulence variables, i.e. turbulence energy, k, and the dissipation rate of turbulence energy, ε (Wilcox, 1998). These two transport equations are given below (Versteeg and Malalasekera, 2007):

$$\frac{\partial(\rho k)}{\partial t} + \nabla.(\rho k\vec{u}) = \nabla.\left(\frac{\mu_t}{\sigma_k}\nabla k\right) + 2\mu_t S_{ij}.S_{ij} - \rho\varepsilon \tag{3.9}$$

$$\frac{\partial(\rho\varepsilon)}{\partial t} + \nabla.(\rho\varepsilon\vec{u}) = \nabla.\left(\frac{\mu_t}{\sigma_\varepsilon}\nabla\varepsilon) + C_{1\varepsilon}\frac{\varepsilon}{k}2\mu_t S_{ij}.S_{ij} - +C_{2\varepsilon}\rho\frac{\varepsilon^2}{k}\right. \tag{3.10}$$

where the five adjustable constants are given the following values by default:

$$C_\mu = 0.09;\ \sigma_k = 1.00;\ \sigma_\varepsilon = 1.30;\ C_{1\varepsilon} = 1.44;\ C_{2\varepsilon} = 1.92$$

The term S_{ij} is the mean rate of deformation of a fluid and the eddy viscosity, μ_t is given by:

$$\mu_t = \rho C_\mu \frac{k^2}{\varepsilon} \tag{3.11}$$

The standard k-ε model is widely used to solve free-shear layer flow with relatively small pressure gradients. If the pressure gradient is high, the accuracy of results from the k-ε model will be deteriorated (Bardina, Huang and Coakley, 1997). Moreover, the k-ε model has poor performance in certain unconfined flows such as flows with large extra strains (e.g. where there are curved boundary layers in swirling flows), rotating flows, and flows driven by anisotropy of the normal Reynolds stresses (e.g. fully developed flows in non-circular ducts) (Wilcox, 1998). Therefore, the standard k-ε model is an appropriate model to solve the problem related to internal flow.

3.1.4.5 *k*-*ω* Model

k-ω turbulence model is a two-equation model, which includes two partial differential equations to represent two variables of turbulence, i.e. turbulence kinetic energy, k, and specific rate of dissipation, ω, also referred to the mean frequency of turbulence (Wilcox, 1998). Here ω is given by:

$$\omega = \frac{\varepsilon}{k} \tag{3.12}$$

The eddy viscosity is defined as:

$$\mu_t = \rho \frac{k}{\omega} \tag{3.13}$$

Transport equations for k and ω are given by:

$$\frac{\partial(\rho k)}{\partial t} + \nabla.(\rho k \vec{u}) = \nabla.\left(\left(\mu + \frac{\mu_t}{\sigma_k}\right)\nabla\omega\right) + \left(2\mu_t S_{ij}.S_{ij} - \frac{2}{3}\rho k \frac{\partial U_i}{\partial x_j}\delta_{ij}\right) - \beta^* \rho k \omega \tag{3.14}$$

$$\frac{\partial(\rho \omega)}{\partial t} + \nabla.(\rho \omega \vec{u}) = \nabla.\left(\left(\mu + \frac{\mu_t}{\sigma_\omega}\right)\nabla k\right) + \gamma_1\left(2\rho S_{ij}.S_{ij} - \frac{2}{3}\rho\omega \frac{\partial U_i}{\partial x_j}\delta_{ij}\right) - \beta_1 \rho \omega^2 \tag{3.15}$$

With constants:

$$\sigma_k = 2.00;\ \sigma_\omega = 2.00;\ \gamma_1 = 0.553;\ \beta_1 = 0.075;\ \beta^* = 0.09$$

Menter's Shear Stress Transport k-ω turbulence model, SST k-ω, is a combination of standard k-ω and SST models (Menter, 1994). It was developed to neutralise the problem that the standard k-ω model is too sensitive to simulate the characteristics of turbulence of inlet freestream (Menter, 1993). SST k-ω uses kinetic energy dissipation to model the freestream and turbulence frequency to model the turbulence in the boundary layer, which is particularly suitable for the simulation of aerodynamics due to its ability to solve viscous flow and turbulence in the boundary layer as well as the far-field regions (Menter, 1994).

In addition, the SST k-ω model has good performance in the prediction of adverse pressure gradients and separating flows, although it produces larger turbulence levels in regions with large normal strain, e.g. stagnation points or area with strong acceleration, than the standard k-ω model (Menter, 1994). In CFD simulations, k-ω models require proper resolution at the viscosity-affected region of the boundary, i.e. the y^+ value should approximately be 1.

3.1.4.6 Spalart Allmaras model

The Spalart-Allmaras (SA) turbulence model is a one-equation model specifically designed to solve external flow problems encountered in aerospace applications (Spalart and Allmaras, 1992). It is based on a single transport equation for the eddy viscosity, ν, (Versteeg and Malalasekera, 2007) given by:

$$\underbrace{\frac{\partial(\rho\nu)}{\partial t}}_{\text{Rate of Change of } \nu} + \underbrace{\nabla.(\rho\nu\vec{u})}_{\text{Transport of } \nu \text{ by convection}} =$$
$$\underbrace{\frac{1}{\sigma_\nu}\nabla.[(\mu_t + \rho\nu)\nabla\nu] + C_{b2}\rho\frac{\partial\nu}{\partial x_k}\frac{\partial\nu}{\partial x_k}}_{\text{Transport of } \nu \text{ by turbulent diffusion}} + \underbrace{C_{b1}\rho\nu\widetilde{\Omega}}_{\text{Rate of production of } \nu} + \underbrace{C_{w1}\rho\left(\frac{\nu}{ky}\right)^2 f_w}_{\text{Rate of dissipation of } \nu} \tag{3.16}$$

where:

$$\widetilde{\Omega} = \Omega + \left(\frac{\nu}{ky^2} f_{\nu 2}\right) \tag{3.17}$$

where f_w and f_{v2} are wall damping functions and the model constants are given

by:

$$\sigma_\nu = \frac{2}{3}; C_{b1} = 0.1355; C_{b2} = 0.622 \ and \ C_{w1} = C_{b1} + k^2 \frac{1 + C_2}{\sigma_\nu}$$

The Spalart-Allmaras model is good at producing the results for boundary layers subjected to adverse pressure gradient, which is suitable for predicting aerofoil performance as it involves flow separations (Spalart and Allmaras, 1992). The SA model requires a similar y^+ value similar to the SST k-ω model (i.e. approximately y^+=1). The disadvantage of the SA model is that it produces relatively large errors for free-shear layer flows, and Spalart and Allmaras (1992) suggested its unreliability on predicting the decay of homogeneous isotropic turbulence.

3.1.5 Boundary Conditions

CFD simulation requires a suitable combination of boundaries to represent the fluid domain of interest for a well-posed problem. Some of the boundary conditions available in the CD-adapco (2016) package, Star CCM+, are listed below:

- Inlets (e.g. velocity inlet, mass flow inlet, stagnation inlet)
- Interface (e.g. fan interface, momentum source)
- Outlets (e.g. pressure outlet)
- Symmetry plane
- Wall

3.1.5.1 Inlet and Outlet

Conducting the aerodynamic analysis of aircraft in CFD is similar to the equipment set-up in a wind tunnel test. The aircraft is placed in a large duct, but there are no limits for the external boundaries, where the full-slip condition can be assigned to the tunnel walls to avoid unrealistic boundary layers. The distance between inlet/outlet and aircraft should be far enough allowing the flow to be fully developed, which can be demonstrated by the flow past a backward-facing step with outlet positioned with increasing distance in Figure 3.6 (Tu, Yeoh and Liu, 2018).

As it can be seen placing the outlet at Position 1 results in unrealistic underdeveloped flow, while at Position 2, the flow is still developing with poor accuracy. The flow is fully developed at Position 3, where the outlet is located more than 10 times of inlet height ($L \gg 10h$) from the step. For external flow around aircraft, the

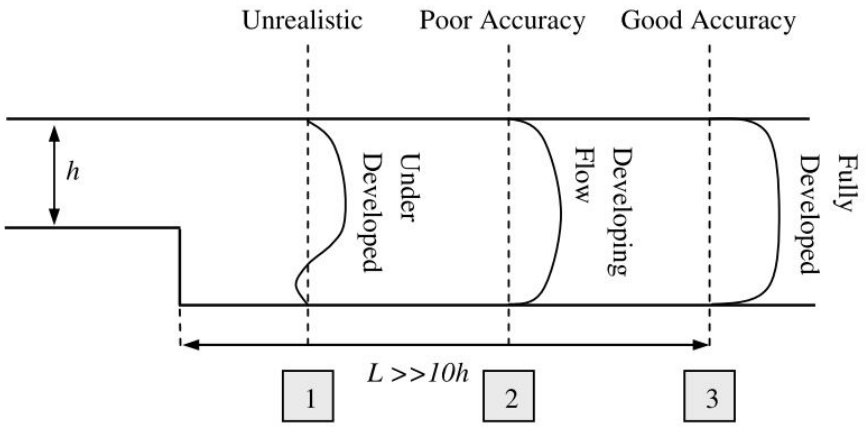

Figure 3.6: Illustration showing the effect of outlet placement on the flow past a backward- facing step (Tu, Yeoh and Liu, 2018).

effect of positioning the inlet is similar, as high pressure areas such as stagnation points at the leading edge of an aerofoil has a significant impact on the flow upstream. Therefore, it is important to leave plenty of space for the inlet and outlet in relation to the aircraft, which allows the static pressure on the inlet to be close to atmospheric pressure while the wake can be fully developed.

3.1.5.2 Wall and Symmetry Plane

The wall is the most common boundary condition to represent solid bodies. Grid cells closest to the wall are defined with a velocity of zero from the no-slip condition (CD-adapco, 2016). As the growth and development of boundary layers produce small and intermediate scale turbulence, two approaches are established to simulate the near-wall turbulence. The first approach is to solve all the way from the wall to the freestream, which requires a highly dense boundary layer grid adjacent to the wall. The second one is to apply a wall function to model the mean velocity profile close to the wall (Launder and Spalding, 1974; Wilcox, 1998), which allows a coarse grid to be used filling the gap between the computational nodes on the wall surface and those in the turbulence cores. Two variables, time-averaged dimensionless velocity parallel to the wall, u^+, and dimensionless normal distance away from the wall, y^+, are used to characterise the wall functions (Tu, Yeoh and Liu, 2018).

Figure 3.7 demonstrates two distinct regions established from experimental results by plotting the logarithm of y^+ against u^+ (Versteeg and Malalasekera, 2007). Here, the shear stress of the fluid within the linear sub-layer, τ, is assumed to be equal to the wall shear stress, τ_w, which results in the following relation in this region of $0 < y^+ < 5$ (Versteeg and Malalasekera, 2007).

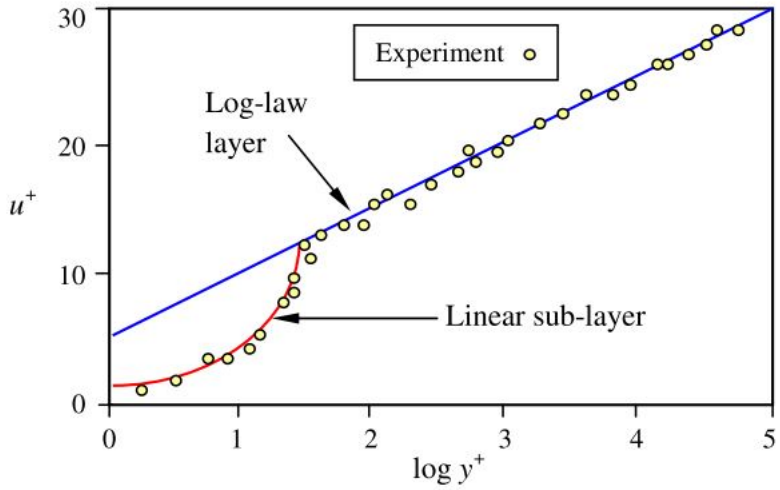

Figure 3.7: Dimensionless velocity distribution inside a boundary layer close to the wall (Versteeg and Malalasekera, 2007).

$$u^+ = y^+ \tag{3.18}$$

The log-law layer exists for the region of $30 < y^+ < 500$ further away from the wall, which provides the following relationship (Versteeg and Malalasekera, 2007).

$$u^+ = \frac{1}{\kappa} \ln(E_c y^+) \tag{3.19}$$

where the Von Karman's constant $\kappa \approx 0.4$ and universal constant $E_c \approx 9.8$ are valid for all high Re turbulence over smooth walls (Tu, Yeoh and Liu, 2018).

Tu, Yeoh and Liu (2018) also pointed out that the relationships given by Eq. (3.18) and (3.19) were experimentally derived from an attached two-dimensional Couette flow, based on the assumption of the local equilibrium of turbulence, smallness of pressure gradients, and the constant existence of near wall stress layer. This drawback typically affects the applications involving highly separated flow, however, non-equilibrium or enhanced wall treatments can minimise the error by accounting for the pressure gradient and the non-equilibrium of turbulence (Tu, Yeoh and Liu, 2018)

Another advantage making the wall functions widely used for three-dimensional turbulence applications is the reduction in grid size. The structure of the boundary layer grid needs to be well-constructed to satisfy the recommendation that the first cell height should produce the value of $20 < y^+ < 30$ and further 8 to 10 grid cells should be retained in the log-law layer with an upper limit of $y^+ \approx 500$ (Tu, Yeoh and Liu, 2018). This guarantees the adequate treatment of near-wall turbulence

without using a large grid size.

Symmetry boundaries assume the flow is tangential to the boundary with zero transverse velocity components, zero shear stress, and zero heat flux (Versteeg and Malalasekera, 2007). This boundary condition suits steady flow past a symmetrical object, for instance, it significantly reduces the grid size and processing time to efficiently simulate an aircraft.

3.1.6 Error and Uncertainty

AIAA (1998) defines the error as "*A recognisable deficiency in any phase or activity of modelling and simulation that is not due to lack of knowledge*", and the uncertainty as "*A potential deficiency in any phase or activity of the modelling process that is due to the lack of knowledge*". The key phrase differentiating the definitions is literally, "*lack of knowledge*". Errors can be mainly categorised as: (1) Coding error, (2) user errors, and (3) Numerical errors including round-off error, convergence error and discretisation error (Versteeg and Malalasekera, 2007).

Coding errors mainly arise by human mistakes during the development of a CFD code and its implementation. It is impossible to eliminate all the coding errors because of the sheer size and complexity of modern CFD applications. In this case, careful and systematic validations are required to minimise the impact of coding errors.

Incorrect or inaccurate definitions of geometry, boundary conditions, and solvers by CFD users are classified as user errors. User errors can be controllable through proper training and accumulation of experience.

Round-off errors develop with the representation of floating point numbers and the accuracy at which numbers are stored as advanced computers store the number with 16, 32, or 64 bits (AIAA, 1998). A higher precision solver is recommended to reduce the round-off errors as the processor stores the floating point number with more significant figures.

Convergence errors exist because the iterative method used in CFD simulations requires sufficient iterations of calculations. Analysing the solution before it is converged would mislead the final result. In the commercial CFD package which will be used in this thesis, CD-adapco (2016), qualitative solution convergence is established with a maximum residual of 10^{-5}. However, for more complex high-Re simulations, solutions with converged (level) residuals of 10^{-3} can be sufficiently accurate, in qualitative terms. Generally speaking, lower residual errors generally imply that

the resulting solution is more accurate.

Discretisation errors occur from discretising the continuous representation of governing equations and solving other physical models as algebraic expressions in a discrete domain space (either finite volume or finite element) and time (either steady or unsteady simulation) (Oberkampf and Trucano, 2002), which is the most significant error in CFD application as it is dependent on the accuracy of the grid. Discretisation errors also develop due to discontinuities, such as shock, slip surface, and interface in a grid. When the grid quality improves, the solution will be less sensitive to the grid spacing and approach the continuum solution (AIAA, 1998), leading to the concept of "*grid convergence*" which will be discussed in the next section. The grid convergence study is an important procedure to determine the level of discretisation error in CFD solutions.

3.1.7 Verification and Validation

In CFD applications, verification and validation are two fundamental principles to ensure the accuracy of solving the mathematical representation of a physical system and examine whether the actual problem is correctly solved (AIAA, 1998). Roache (1994) described verification as the process of "*solving the governing equations right*" and validation as "*solving the right governing equations*". Verification and validation are absolutely crucial and must be addressed in any CFD applications.

Validation is a process to validate the numerical solutions by comparing with either an accurately obtained analytical solution or a high quality experimental result for non-trivial problems. Verification is a relatively complicated process due to the inevitably induced numerical errors when discretising the governing equations. As grid convergence has been mentioned with discretisation errors in the previous section, Roache (1994) developed the Grid Convergence Index (GCI), which is a uniform method to quantify the grid convergence in order to determine the level of discretisation error. The GCI is based on Richardson's Extrapolation to use two or three solutions generated from different grid sizes to estimate the discretisation error (Roache, 1994). The solution error, e, of two solutions derived from two different grids is given by:

$$e = \frac{f_2 - f_1}{f_1} \tag{3.20}$$

where f_1 and f_2 are solutions from fine and coarse grids respectively, and e is a measure of the difference in solution variables related to the coarse and fine grids.

To consider the formal order of accuracy, p, and the grid refinement ratio, r, a more appropriate approach to measure the discretisation error is given by:

$$r = \frac{h_2}{h_1} \tag{3.21}$$

$$E = \frac{e}{r^p - 1} \tag{3.22}$$

where h_1 and h_2 are the fine and coarse grid element edge lengths respectively. However, exclusively using e will potentially induce errors with lower order discretisation schemes. Here, an example is used for illustration of the potential error. Given $f_1 = 0.98$ and $f_2 = 0.99$, the error calculated by Eq (3.20) is very small, $e = 1.02\%$. The problem is that the difference of how f_1 and f_2 are computed by two different grids are not taken into account. Roache (1998) suggested to use grid doubling or grid halving for all three coordinates, for example, a 2^{nd} order discretisation scheme produces a more accurate solution than 1^{st} order discretisation. If applying 2^{nd} order discretisation and grid doubling to the previous solutions, the error is $E = 0.34\%$ (highly accurate). When using 1^{st} order discretisation scheme and a grid refinement ratio of 20% (i.e. $r = 1.2$), the error is therefore $E = 5.10\%$, which shows the poor performance of estimator e. This example demonstrates that even though the solutions from different grids are seemingly close, the actual accuracy may be worse. Roache (1998) improved Richardson's estimator, E, by adding a safety factor, F_s. The GCI for a fine grid is expressed as:

$$GCI_{Fine\,Grid} = \frac{F_s|e|}{r^p - 1} \tag{3.23}$$

F_s is recommended to be $F_s = 3$ for comparisons of two grids (Roache, 1998), which is taken from the denominator of Eq. (3.22) when $r = 2$ and $p = 2$, representing a good example of grid independence. To avoid the increasing conservatism of $F_s = 3$ in more rigorous studies over three or more grids, a typical value of $F_s = 1.25$ is also suggested by Roache (1998). Using GCI has the distinct advantage to apply the error estimation to global solutions, e.g. C_L and C_D (Roache, 1998).

In three-dimensional problems, grid doubling is often infeasible as it increases the total grid size by a factor of eight. For this reason, the grid refinement ratio for 3D problems is usually smaller. Roache (1994) recommended a minimum refinement ratio of $r = 1.1$ (i.e. 10%) as either increasing or decreasing this limit by 1% will generate skewed solutions due to convergence and round-off errors. Using larger grid refinement ratios not only dramatically increases the grid size, but also produces a

coarse grid which is too far away from the ideal zero grid spacing. This implies that the solutions used in error estimation should be in the asymptotic range of convergence, in another words, all solutions should be able to adequately solve the problems.

The discussion of grid refinement above is based on structured grids. For unstructured grid, where triangular elements are commonly used, r is still valid. However, it is impossible to consistently have a grid refinement ratio. Hence, an alternative approach to describe the effective grid refinement ratio as:

$$r_{effective} = \left(\frac{N_1}{N_2}\right)^{\frac{1}{D}} \tag{3.24}$$

where N_1 and N_2 are the total number of elements in the fine and coarse grids respectively and D is the dimension of the flow domain. The $r_{effective}$ can be directly used in Eq. (3.23) but it is less accurate in predicting discretisation error, and lacks robustness (Roache, 1994).

Versteeg and Malalasekera (2007) commented that a minor deficiency in the numerical method and skewness in unstructured grid cells may cause the discrepancy between formal order of accuracy, p, of the numerical solutions and the observed order. In this case, Roache (1998) used three grids and the effective order of the solution, $p_{effective}$ to minimise the risks, given by:

$$p_{effective} = \frac{\ln\left(\frac{f_3 - f_2}{f_2 - f_1}\right)}{\ln(r)} \tag{3.25}$$

where, f_1, f_2 and f_3 are the solutions from fine, medium and coarse grids respectively. Due to the nature of CFD simulation, the difficulty of estimating the discretisation error is greater than predicting the coding, usage, round-off and convergence errors. All the procedures discussed in this section were designed to overcome the difficulty of consistently estimating and reporting the discretisation errors.

3.2 Aerofoil Parametrisation Method

Modifying single or multiple aerofoil parameters, such as using XFoil, does not give sophisticated control over aerofoil design. With this in mind, it is desirable to employ an established aerofoil parametrisation method with full control of all aerofoil parameters and to a sufficiently large the design space.

One of the most powerful aerofoil parametrisation methods was developed by Sobieczky (1999), namely PARSEC, to analytically define aerofoils based on twelve equations representing twelve parameters, such as upper/lower crest position, maximum thickness, leading edge radius, and boat-tail angle. The parameters used in this method is shown in Figure 3.8 and the definitions are given in Table 3.3. The basis of PARSEC is that the upper and lower surfaces are defined by the following 6^{th} order polynomials (Masters et al., 2015):

$$z_{up}(x) = \sum_{i=1}^{6} a_i x^{i-0.5} \tag{3.26}$$

and,

$$z_{lo}(x) = \sum_{i=1}^{6} b_i x^{i-0.5} \tag{3.27}$$

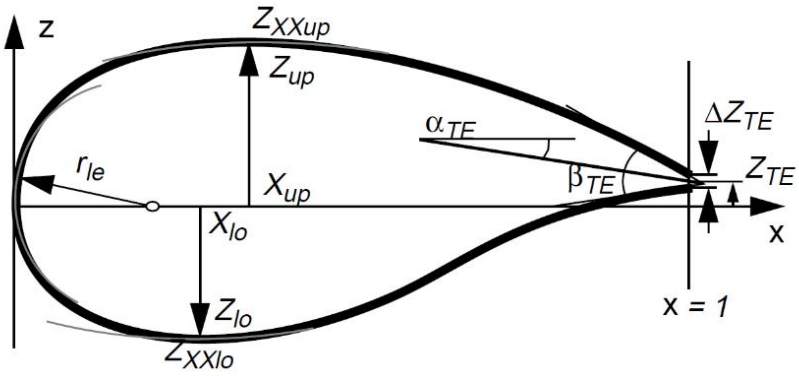

Figure 3.8: A geometric representation of aerofoil parameters using PARSEC (Sobieczky, 1999).

Sasaki and Nakahashi (2011) applied PARSEC to an aerodynamic optimisation for an over-wing-nacelle-mount configuration, achieving an optimum L/D value of 35.5 over the baseline's L/D value of 31.7 after hundreds of iterations of optimising both wing and pylon. This research demonstrated the capability and flexibility of using PARSEC in aerodynamic optimisation. However, the difficulty of using this method is that the amount of parameters employed is numerous, although the total amount will reduce to ten if the trailing edge is fixed. Even so, exploring a 10-dimensional design space is extremely time-consuming and very challenging to do. The aerofoil shape optimisation carried out by Della Vecchia, Daniele and D'Amato (2014) also faced huge demand of computational time and convergence issues while using PARSEC coupled to a genetic algorithm.

Parameter	Definition
Upper leading edge radius (r_{leu})	$r_{leu} = a_1$
Lower leading edge radius (r_{lel})	$r_{lel} = b_1$
Upper crest point (Z_{up})	$Z_{up} = z_{up}(X_{up})$
Lower crest point (Z_{lo})	$Z_{lo} = z_{lo}(X_{lo})$
Position of upper crest (X_{up})	$z'_{up}(X_{up}) = 0$
Position of lower crest (X_{lo})	$z'_{lo}(X_{lo}) = 0$
Upper crest curvature (Z_{XXup})	$z''_{up}(X_{up}) = Z_{XXup}$
Lower crest curvature (Z_{XXlo})	$z''_{lo}(X_{lo}) = Z_{XXlo}$
Trailing edge offset (Z_{TE})	$z_{lo}(1) = Z_{TE}$
Trailing edge thickness (ΔZ_{TE})	$z_{up}(1) = Z_{TE} + \Delta Z_{TE}$
Trailing edge angle (α_{TE})	$z'_{up}(1) = -tan(\alpha_{TE} + \frac{\beta_{TE}}{2})$
Boat-tail angle (β_{TE})	$z'_{lo}(1) = -tan(\alpha_{TE} - \frac{\beta_{TE}}{2})$

Table 3.3: Definitions of parameters used in PARSEC (Sobieczky, 1999).

Another powerful and sophisticated aerofoil parametrisation method developed by Kulfan and Bussoletti (2006), Class/Shape Transformation (CST), employs class and shape functions to define all classes of geometries with easily observed features. The significance is that the CST method does not require specific definitions for each aerofoil parameter, which offers the possibility of simplified program scripts for automatic parametrisation. Studies completed by Lane and Marshall (2009, 2010) demonstrated the substantial capability of the CST method for optimising a circulation control wing (CCW) with high lift devices and implementing an inverse aerofoil design for RAE2822. The general mathematical expression of CST in two-dimensions is given by (Kulfan, 2007):

$$\frac{z}{c} = \sqrt{\frac{x}{c}} \cdot \left(1 - \frac{x}{c}\right) \cdot \sum_{i=0}^{N} \left[A_i \cdot \left(\frac{x}{c}\right)^i\right] + \frac{x}{c} \cdot \frac{\Delta z_{te}}{c} \tag{3.28}$$

This form can be rewritten as:

$$\xi(\psi) = C_{N_1}^{N_2}(\psi) \cdot S(\psi) + \psi \cdot \Delta\xi_{te} \tag{3.29}$$

where:

$$C_{N_1}^{N_2}(\psi) = \psi^{N_1} \cdot (1 - \psi)^{N_2} \tag{3.30}$$

and,

$$S(\psi) = \sum_{i=0}^{N} \left[A_i \cdot \left(\frac{x}{c} \right)^i \right] \tag{3.31}$$

where $C_{N_1}^{N_2}(\psi)$ is the class function, $S(\psi)$ is the shape function, and Δz_{te} is the trailing-edge thickness ratio (Kulfan, 2007). For a typical aerofoil shape, with a round nose and sharp trailing edge, the class parameters N_1 and N_2 are set to 0.5 and 1.0 respectively. With CST, an aerofoil is defined by a set of coefficients, while higher order will give a more accurate shape.

Masters et al. (2017) analysed several aerofoil parametrisation methods, including PARSEC and CST, by considering efficiency, geometric error and convergence based on three aerofoils, i.e. NACA4412, RAE2822 and ONERA M6, over 2000 aerofoils using a range of design variables. They found that the CST method gives a fast convergence rate and minimal errors. Another research study conducted by Zhu and Qin (2014) proved that a 12^{th}-order CST, consisting 14 coefficients for both upper and lower surfaces, can accurately fit to a series of well-known aerofoils including RAE2822, RAE5214, NASA SC-20714, and NASA Natural Laminar Flow (NLF) designs, with better performance compared to the PARSEC method. Considering the relative simplicity of the CST method and its sophistication in shape control, it is therefore chosen to be the aerofoil parametrisation tool that will be used in Chapter 6.

3.3 Design of Experiments

This research involves an improvement study for the aerodynamic performance of a supercritical aerofoil. Since the CST method has been selected as the aerofoil parametrisation method, due to its simplicity of using coefficients to control the shape of the aerofoil, it is necessary to select a suitable method to explore the potential aerodynamic benefit from sufficient random designs.

To explore the design space, a Design of Experiments (DoE) is a sampling plan, which is capable of determining the number and distribution of all design points, as required for comprehensive analysis (Queipo et al., 2005). Optimum Latin Hypercube (OLH) sampling is a method to equally sample all design variables with n points ($n \geqslant 10$), which was an improvement over the Latin Hypercube Sampling (LHS) method (Narayanan et al., 2007). It incorporates the optimisation of a spreading measure, thereby avoiding the possibility of LHS to under or over sample some regions of the design space from one DoE to another, resulting in significant

improvement for the quality of the DoE (Queipo et al., 2005). Figure 3.9 shows an example of a 40 point DoE generated with 2 and 3 design variables by OLH sampling (Narayanan et al., 2007), where all design variables are normalised between 0 and 1. This method is used in later chapters in this thesis.

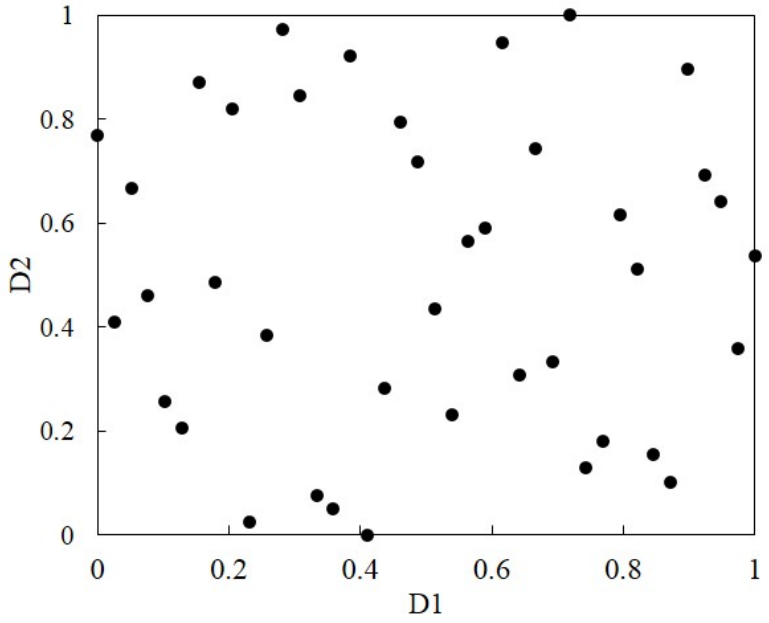

(a)

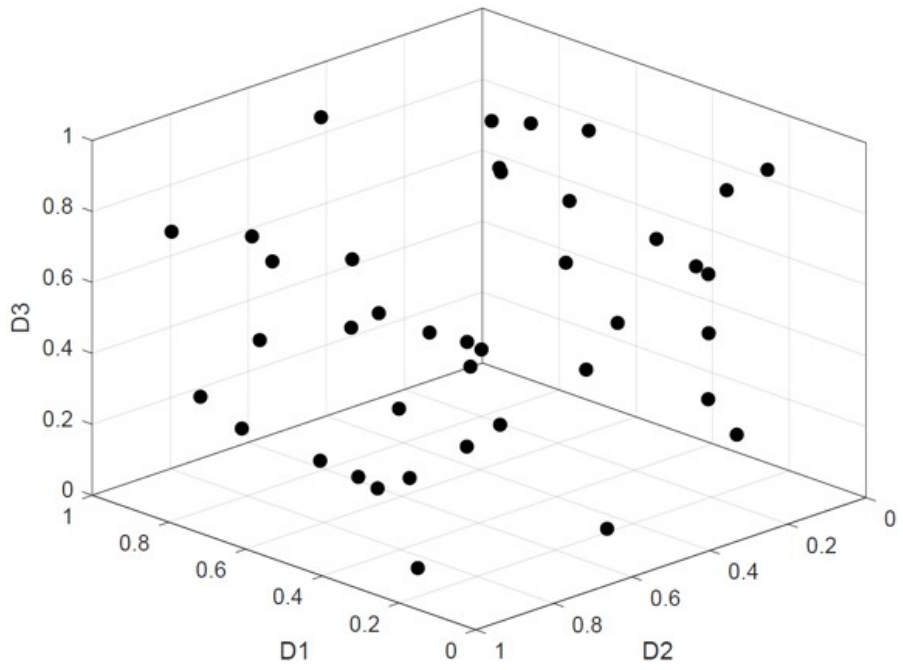

(b)

Figure 3.9: Plots showing the distributions of 40 design point generated by (a) 2 design variables (D1 and D2) and (b) 3 design variables (D1, D2, and D3), with Optimum Latin Hypercube sampling (Narayanan et al., 2007).

Chapter 4

CFD Verification and Validation

The previous chapter introduced important concepts of CFD methodology and highlighted the importance of verification and validation. In this chapter, these principles are applied to two generic aircraft geometries, the DLR-F6 and the NASA Common Research Model, which have been widely researched using wind tunnel testing. This chapter also considers some important factors, including the selection of turbulence models and the impact of propulsion on pressure distributions on a representative aircraft wing, which are essential for subsequent research. These findings form the basis of the studies in Chapter 5 and 6, with the focus being to identify the most appropriate combination of turbulence model, and mesh and solver settings for effective and reliable aerodynamic analysis.

4.1 DLR-F6

In this CFD case study, the DLR-F6 wing-body-nacelle-pylon (WBNP) geometry, available at the second AIAA Drag Prediction Workshop (DPW) (Frink, 2003), was used as a representative geometry of a typical medium-sized civil airliner, e.g. Airbus A320. The geometry was based on a wind tunnel model with a length of 1.19 m, the mean aerodynamic chord (MAC) was 0.1412 m, and the wing reference area was 0.0727 m^2. The WBNP geometry used in the ONERA wind tunnel was a symmetric model, which allowed a symmetry plane to be used in order to reduce the computational cost in CFD.

The CAD geometry was firstly extruded from an initial domain to a solid entity by Dassault Systems Solidworks 2016, then, it was imported and cleaned up in Star

CCM+ 11.04.012, while a large domain was created to model the ONERA's wind tunnel condition. The size of the domain was 8.75m × 4.5m × 2m, which allows at least $5L$ (L is the length of the aircraft) to the pressure outlet of the domain, and $3L$ for the velocity inlet and the symmetry planes of the domain. Additionally, the width of the domain was also wide enough to adequately capture the effect of the wing tip vortex. Then, the WBNP configuration was subtracted from the domain volume to produce the required air volume. Figure 4.1 shows the detailed DLR-F6 WBNP configuration inside the domain.

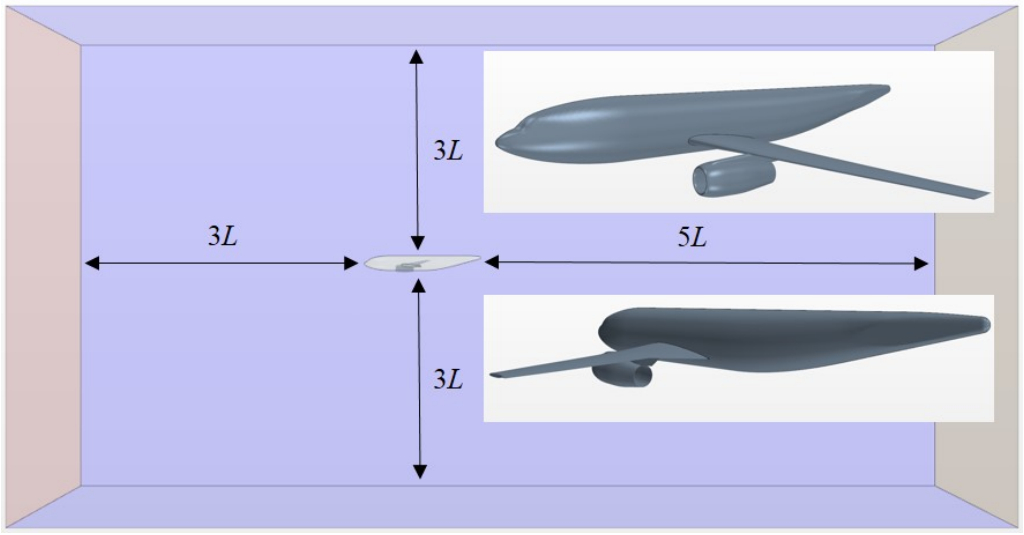

Figure 4.1: Detailed DLR-F6 WBNP configuration inside the solution domain.

The FX2B fairing, designed to mitigate boundary layer separation at the wing root, was also considered in this case study, and will be presented in Section 4.1.6.

4.1.1 Meshing

After creating the domain, there were three sequential methods selected for the meshing process, i.e. Surface Remesher, Prism Layer Mesher, and Trimmer. The Surface Remesher was used, rather than Surface Wrapper, to discretise the surface into a fine and uniform grid because the Surface Wrapper is only used to provide a closed, manifold, non-intersecting surface when starting from poor quality CAD (CD-adapco, 2016).

The Prism Layer Mesher was used to create the cells close to the surface of the geometry, which enables accurate modelling of the boundary layers by setting an appropriate thickness (0.001 m) and number of prism layers (20 layers) (CD-adapco, 2016). In this CFD case, the prism layers were only applied to the wing area to limit the total number of cells saving computational time. Figure 4.2 shows the prism

layer surrounding the leading edge and trailing edge of the wing.

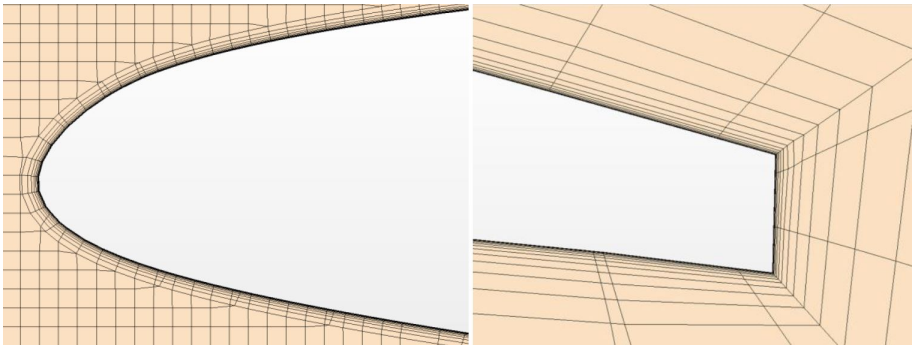

Figure 4.2: Figure showing the prism layers around the leading edge and the trailing edge at different scales.

The Trimmer was set to control the cells size of the surface and volume mesh in proportion to the globally defined base size. By decreasing the global base size, the mesh became finer, and vice versa. The Trimmer can be applied to specific areas, such as the leading edge, wing tip, and wake, allowing the possibility to obtain a custom mesh in different regions, with suitable refinement.

The initial mesh did not have a sufficient quality for the solving process to ensure the accuracy of the final results, as certain areas of the WBNP configuration needed to be refined, for instance, the leading and trailing edges of the wing, the wing tip, and wake regions, etc.

The surface mesh size on the wing was set to be finer than that on the fuselage as the wing contributes most of the lift, and accurately capturing this is a priority. By setting suitable values in the surface curvature function, more cells were added to the curved surfaces such as the leading edge and fuselage nose.

The volume meshing method employed an unstructured hybrid grid, where cells of different shapes are placed in different regions in the domain. With this volume meshing method, more cells were clustered into the areas of high curvature. By adding volumetric controls the mesh was customised with three extra-fine cell clustering regions applied to the inner and outer wing, nacelle and pylon, and the leading edge respectively, while medium-fine cells were set to cover the wake region. Figure 4.3 shows the cylinder-shaped volumetric control placed along the leading edge. The reason for utilising the volumetric controls was to balance the total number of cells in the mesh, as simply decreasing the global base size will result in a larger number of cells in the final mesh, which can be prohibitively large.

Figure 4.4 shows two examples of sectional views of the final mesh around the aerofoil at the inner and outer wing stations. It can be seen that the mesh is denser when close to the surface, especially at the leading edge, which results from the

Figure 4.3: Illustration of an example of cylinder-shaped mesh refinement zone (purple) across the leading edge.

volumetric control applied in the wing area and the leading edge.

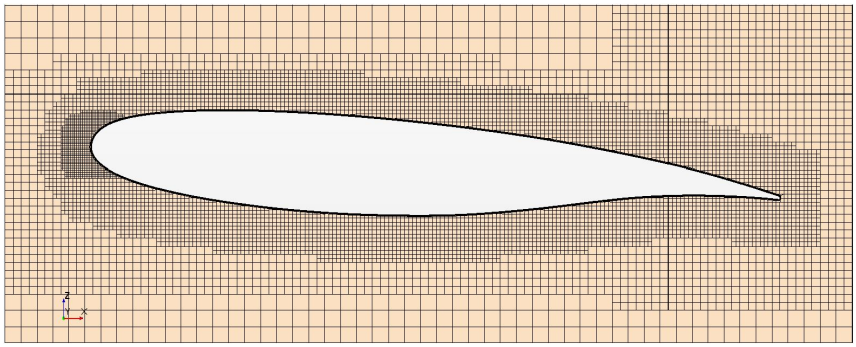

(a) Inner wing aerofoil

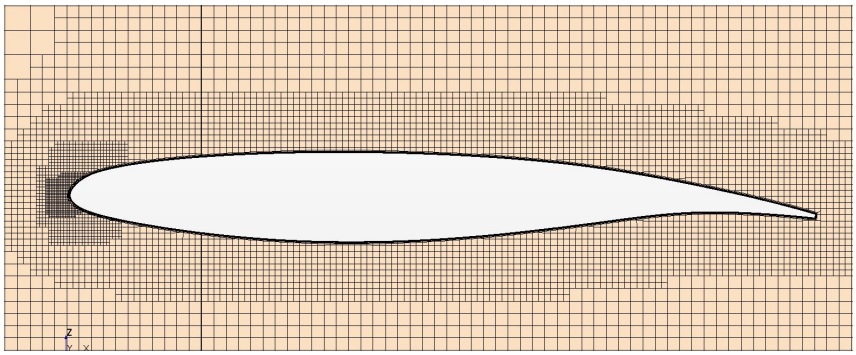

(b) Outer wing aerofoil

Figure 4.4: Examples of sectional view of refined mesh for (a) inner wing and (b) outer wing.

Furthermore, in other far-field areas, such as the velocity inlet and pressure outlets, these were left unrefined as detailed computation is not necessary at these locations. The fully refined mesh, shown in Figure 4.5, contains 9.42 million cells. As every surface and volume mesh setting was relative to a global base size (except

the setting for prism layers), this made the grid independence study simpler by only changing the base size to obtain differently sized meshes. The reason to retain prism layer settings was that the y^+ value should be fixed to meet the requirement of certain turbulence models, i.e. SST k-ω and Spalart Allmaras variants.

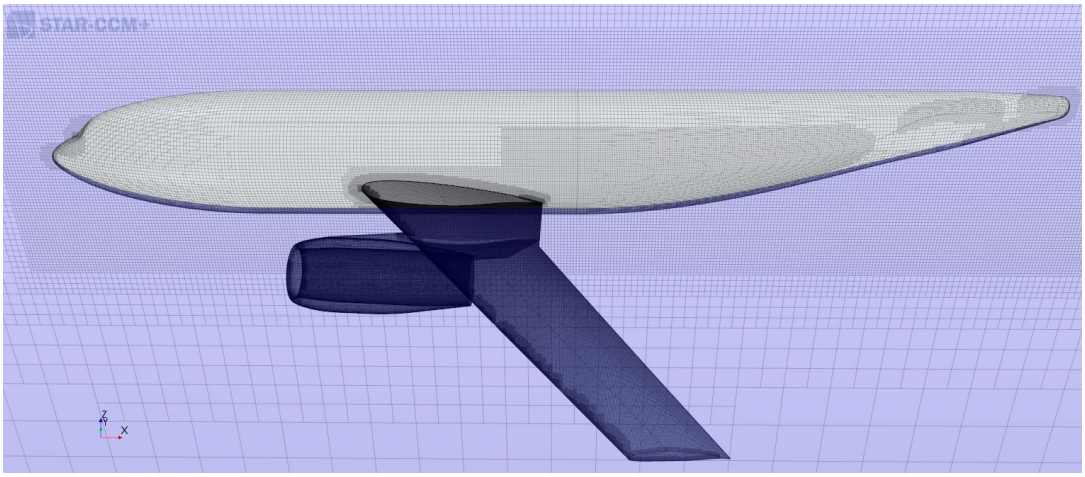

Figure 4.5: Fully refined mesh of DLR-F6 wing-body-nacelle-pylon configuration.

4.1.2 Physics and Boundary Conditions

After the meshing stage, each surface of the configuration were assigned to different boundary types for different purposes with certain conditions. To match the ONERA wind tunnel test, the freestream velocity at the domain inlet was set to Mach 0.75, with an ambient static pressure of P_{static} = 101325.0 Pa for the domain (Frink, 2003). The side surfaces of the domain were set as symmetry planes because these surfaces would not affect the flow inside the domain in the case of zero yaw, where shear stresses on the symmetry plane are zero (CD-adapco, 2016).

This three-dimensional simulation was set as steady-state, utilising the ideal gas law and a coupled flow solver with a turbulence model to simulate the same flow conditions in ONERA's wind tunnel test. The coupled flow solver was considered to be the most suitable option to solve the compressible flow rather than segregated flow solver by dealing with mass, energy, and momentum conservation equations together, because the segregated flow solver assumes constant density which is not valid in this case; the density of air changes during transonic condition (CD-adapco, 2016). Considering the limited capability of k-ε turbulence models to deal with boundary layers, requiring coarser meshing criteria to resolve boundary layers, both the SST k-ω and Spalart-Allmaras turbulence models were chosen in this case study to identify a suitable turbulence model for subsequent simulations (Cummings et al., 2015).

Thereafter, simulations were submitted to High Performance Computing (HPC) facilities at the University of Leeds. For a typical simulation, after 2200 iterations, all residuals were converged with the maximum value of 10^{-4}, which was found to be acceptable as fully converged solutions for solving the flow field.

4.1.3 Mesh Verification

The mesh verification is an essential part of the post-processing step. Firstly, the y^+ value should be checked to meet the requirements for different turbulence models and whether the grid can accurately represent boundary layers. It is necessary to check the y^+ value to match the requirement restricted by k-ω and Spalart-Allmaras turbulence models, which is $y^+ \approx 1$. The y^+ is defined as a dimensionless wall distance for a wall-bounded flow and it is used to describe how coarse or fine a mesh is for a particular flow pattern (Schlichting and Gersten, 2000). The equation for calculating y^+ is shown below.

$$y^+ = \frac{yu^*}{\nu} \tag{4.1}$$

where y is the distance to the nearest wall (i.e. first cell height), u^* is the friction velocity at the wall, and ν is the local kinematic viscosity of the fluid (Schlichting and Gersten, 2000). The y^+ value can be calculated in Star CCM+ by creating a surface report in certain regions after several hundred iterations, which is useful to adjust the y^+ value prior to full convergence. Three stations across the wing and the whole wing surface were chosen to export the average y^+ value, see Table 4.1.

Region	y/b=0.239	y/b=0.411	y/b=638	Whole Wing Area
Average y^+	0.5418	0.5543	0.5632	0.5544

Table 4.1: Wall y^+ values at three stations and average value for whole wing area.

It can be seen that the average y^+ values at every position met the approximate requirement of k-ω and Spalart-Allmaras turbulence models. Figure 4.6 shows a plot of y^+ values along the chord for the upper and lower surfaces over the wing at three typical stations, i.e. y/b=0.239 (inner wing), y/b=0.411 (middle wing), and y/b=0.638 (outer wing), where y is the spanwise distance and b is the wing semi-span.

After checking y^+ values, the next step is to zoom into the prism layers to examine whether there is an adequate number of grid layers to fully capture boundary layers. The grid layers (i.e. prism layers) in this mesh were defined to ensure that at least 10

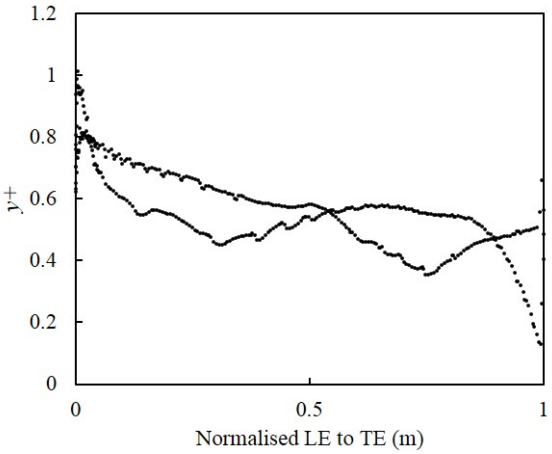

(a) y/b=0.239 (inner wing)

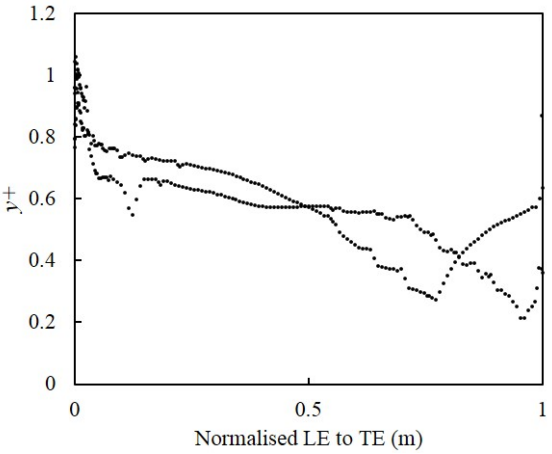

(b) y/b=0.411 (middle wing)

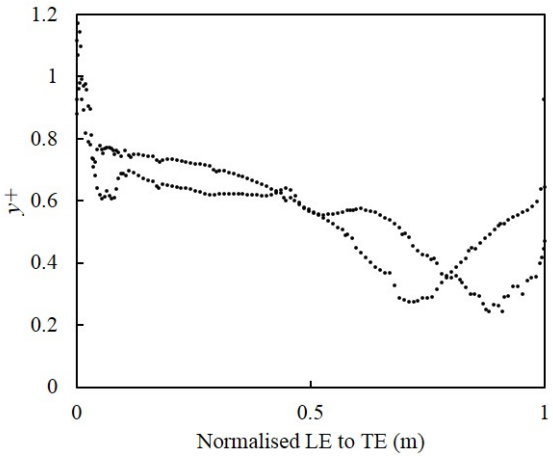

(c) y/b=0.638 (outer wing)

Figure 4.6: Plot showing the y^+ values at (a) y/b=0.239 (inner wing), (b) y/b=0.411 (middle wing), and (c) y/b=0.638 (outer wing).

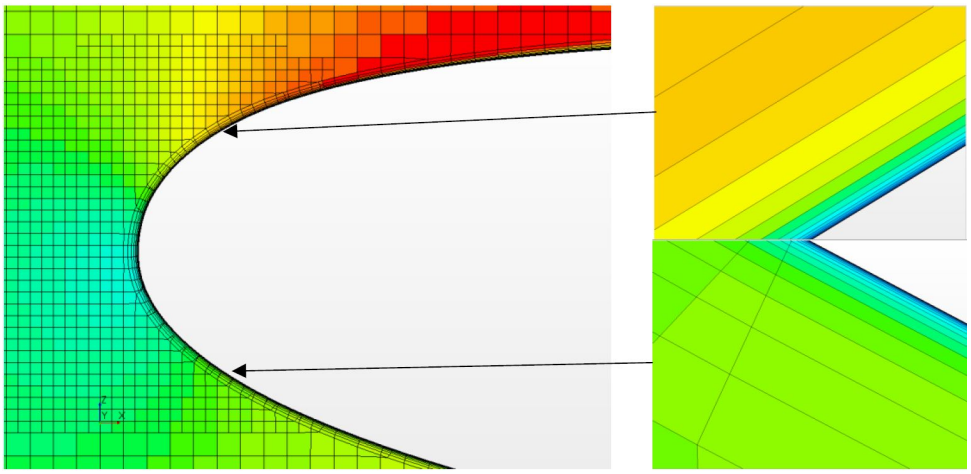

Figure 4.7: Zoom-in of velocity magnitude at grid layers at the leading edge (y/b=0.239).

cells fully capture the boundary layer with velocity varying from zero at the wall to the freestream velocity. Figure 4.7 shows an example of the zoom-in in grid layers at

the leading edge (y/b=0.239), where it can be observed that the velocity magnitude changes from dark blue (zero velocity) to the same colour of the freestream.

4.1.4 Grid Independence Study

The grid independence study aims to examine whether the solutions are independent of the grid density. As the settings of the mesh size were relative to the global base size, (except the settings for prism layers), the grid independence study was carried out by varying the global base size proportionally from 0.9 m (+10%) to 1.2 m (-20%) at zero angle of incidence.

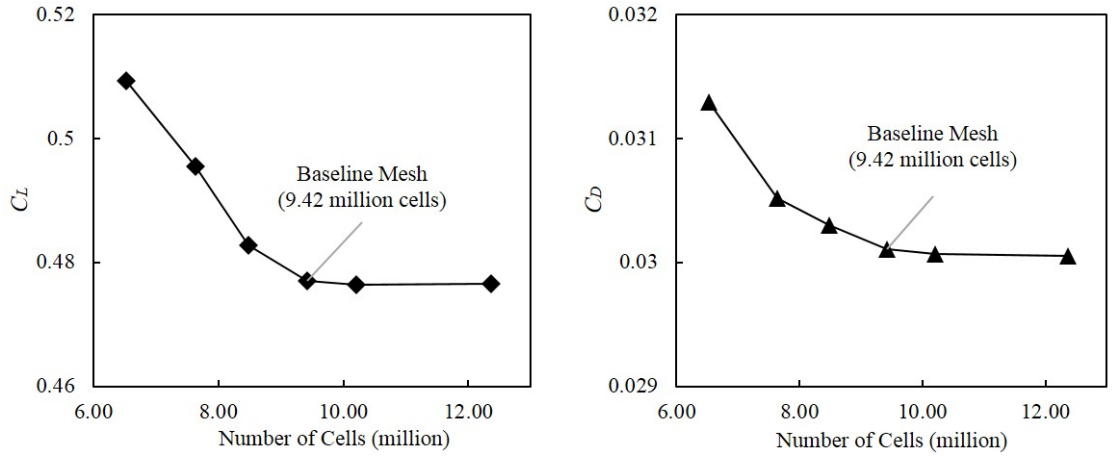

Figure 4.8: Plot showing grid independence study by (a) predicted coefficient of lift and (b) predicted coefficient of drag.

As it can be found from Figure 4.8, the predicted coefficient of lift (C_L) and coefficient of drag (C_D) were used as the parameters in this grid independence study. When the numbers of cells in the mesh increased to 9.42 million, the predicted C_L is approximately maintained, see Fig. 4.8a. In Figure 4.8b, the plot of C_D values shows the same pattern, which suggests that the baseline mesh of 9.42 million cells is adequately fine, and the effect of a finer mesh for the lift and drag is unnecessary.

4.1.5 Pressure Distributions Comparison

Due to the nature of CFD simulations, the results are mathematical and computational. Although the latest CFD solver is accurately designed and optimised, the validation between the computational result and experimental data from wind tunnel tests is still imperative. The validation process was implemented by selecting three stations at the inner wing, wing crank and outer wing respectively to compare

with the wind tunnel test data at the same stations. The coefficient of pressure, C_P, was used as the parameter in this validation because the C_P is independent of the body size, therefore, it is very useful to determine the accuracy of the CFD results against experimental data. Furthermore, the C_P distribution can be used for predicting the actual pressure distribution around a full-sized research object (Frink, 2003).

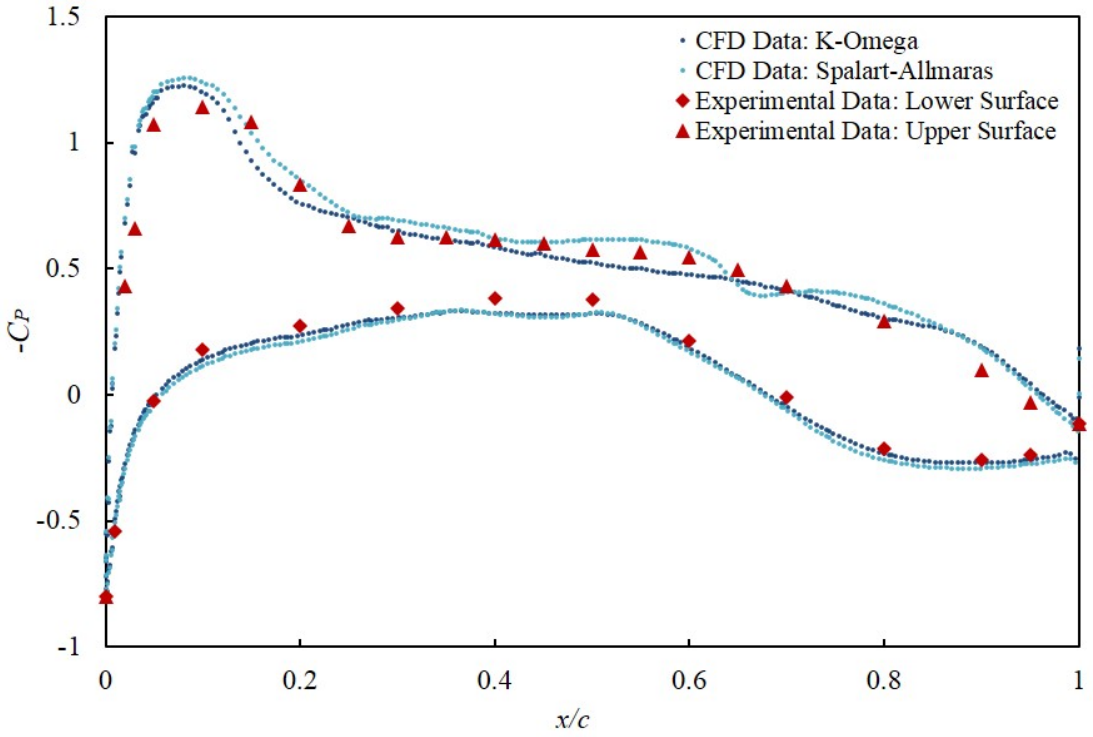

Figure 4.9: Plot showing a comparison of pressure distributions at y/b=0.239 between two CFD results and experimental data. (Experimental error bars were determined to be $\Delta C_{P_{\text{exp}}}$=± 0.01)

Figures 4.9 - 4.11 show the comparisons of pressure distributions simulated by the SST k-ω and Spalart-Allmaras turbulence models and experimental data, obtained from AIAA DWP2 (Frink, 2003), at y/b=0.239, y/b=0.411, and y/b=0.638 respectively. The Re and C_L values for both CFD and experimental results were matched before the pressure distribution comparison, C_L (wind tunnel)=0.4981 at AoA=1.003° and C_L (CFD)=0.4935 at AoA=0°. The same lift condition must be ensured to allow a consistent comparison of the pressure distribution between CFD and wind tunnel tests. Furthermore, the focus of the work in this thesis is on cruise conditions whereby lift must be equal to weight; there cannot be discrepancies in lift. Also, C_L-matching is used more than alpha matching because CFD and experiments rarely produce the same lift coefficient for the same offset angle. One contributing factor behind this discrepancy is likely to be caused by numerical diffusion, which always exists.

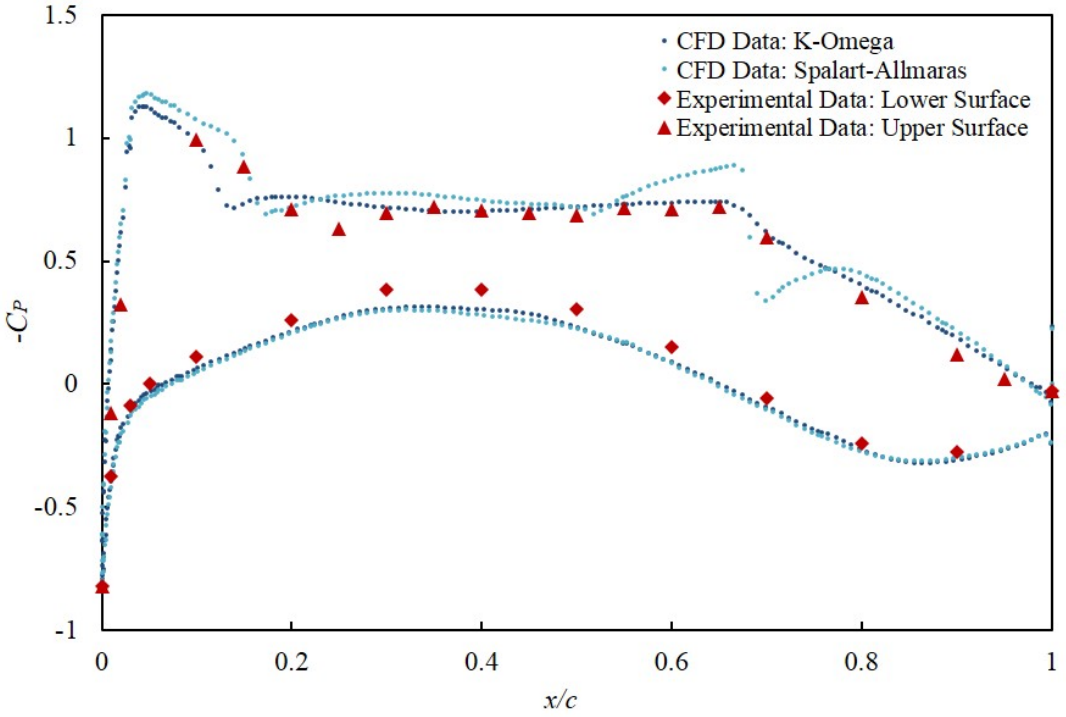

Figure 4.10: Plot showing a comparison of pressure distribution at y/b=0.411 between two CFD results and experimental data. (Experimental error bars were determined to be $\Delta C_{P_{\text{exp}}}$=± 0.01)

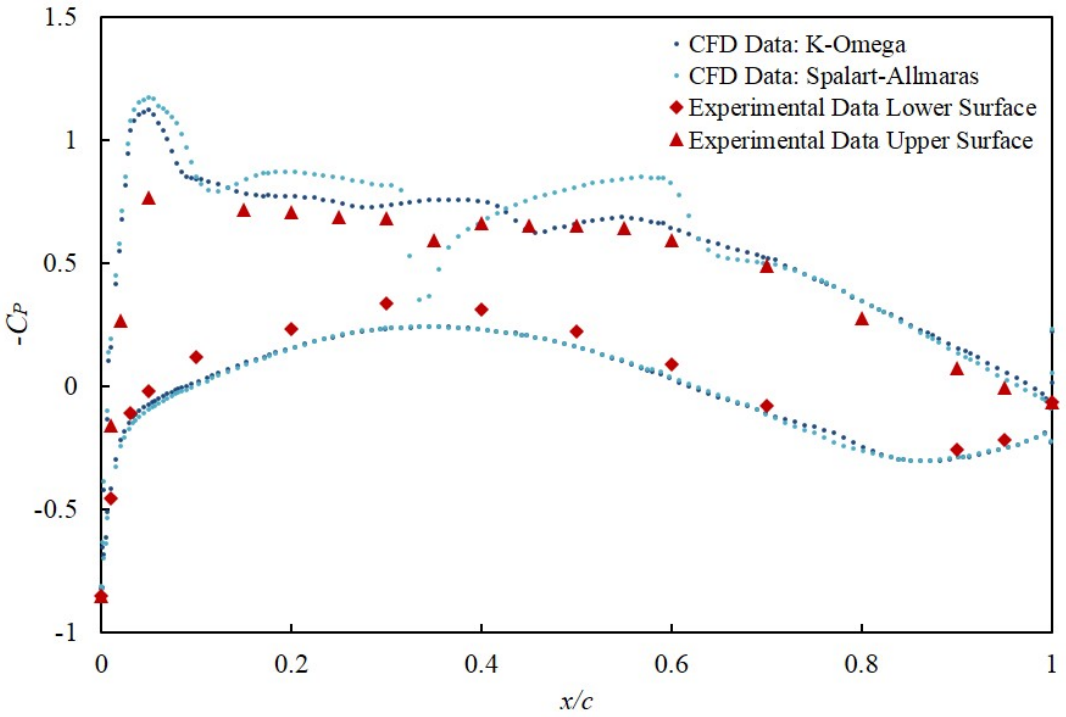

Figure 4.11: Plot showing a comparison of pressure distribution at y/b=0.638 between two CFD results and experimental data. (Experimental error bars were determined to be $\Delta C_{P_{\text{exp}}}$=± 0.01)

For the upper surface, it can be seen that both turbulence models generally produce good accuracy in terms of the predicted pressure distributions for the rear loading, despite the Spalart-Allmaras model wrongly predicting shock wave formation at approximately 70% chord at the wing crank, and 60% chord for outer wing plus an unexpectedly strong shock at roughly 35% chord; this does not match the experimental data in these locations. The suction peak is over-predicted at y/b=0.411 and y/b=0.638 by both turbulence models, while at the inner wing, it is only slightly over-estimated.

For the lower surface, both turbulence models show an acceptable match at the inner-wing station in spite of the small discrepancy between 30% and 50% chord. However, the under-prediction is noticeably worse when it extends to the wing crank and outer wing sections, as the gap between the experimental data and under-estimated C_P values become larger and wider.

4.1.6 Flow Separation Visualisation and Mitigation

In addition to the validation of pressure distributions, the validation case also considers the accuracy of predicting flow separation. During ONERA's wind tunnel test, flow separation was observed across the trailing edge, and the recirculation area was found at the wing root when C_L was fixed at 0.5 (Laflin et al., 2005). To examine the accuracy of the computational solution, it is worth checking whether the extents of flow separation and recirculation occurred in the same regions.

Figure 4.12(a) displays the recirculation observed experimentally at the wing root and flow separation alongside the trailing edge in ONERA's wind tunnel test (Laflin et al., 2005).This is contrasted with CFD results from the present study which shows a plot of the skin friction coefficient on the DLR-F6 WBNP configuration (where the fuselage, nacelle, and pylon were hidden for clear comparison). It can be seen that the contours of skin friction coefficient from CFD simulations visually match the oil-flow patterns from the wind tunnel test. This wing-root recirculation was considered as a "gully" effect at the junction of the wing and fuselage, while the outer wing trailing-edge flow separation was considered as the result of adverse pressure gradients. To mitigate the wing-root recirculation, the FX2B fairing was designed and installed to the original DLR-F6 geometry in DPW3 (Frink, 2006), see Fig. 4.13, with the purpose of reducing the the boundary layer separation region at the wing-body junction.

Following the same meshing strategy and solver physics settings from before, a simulation including the FX2B fairing was run. The comparison of skin friction

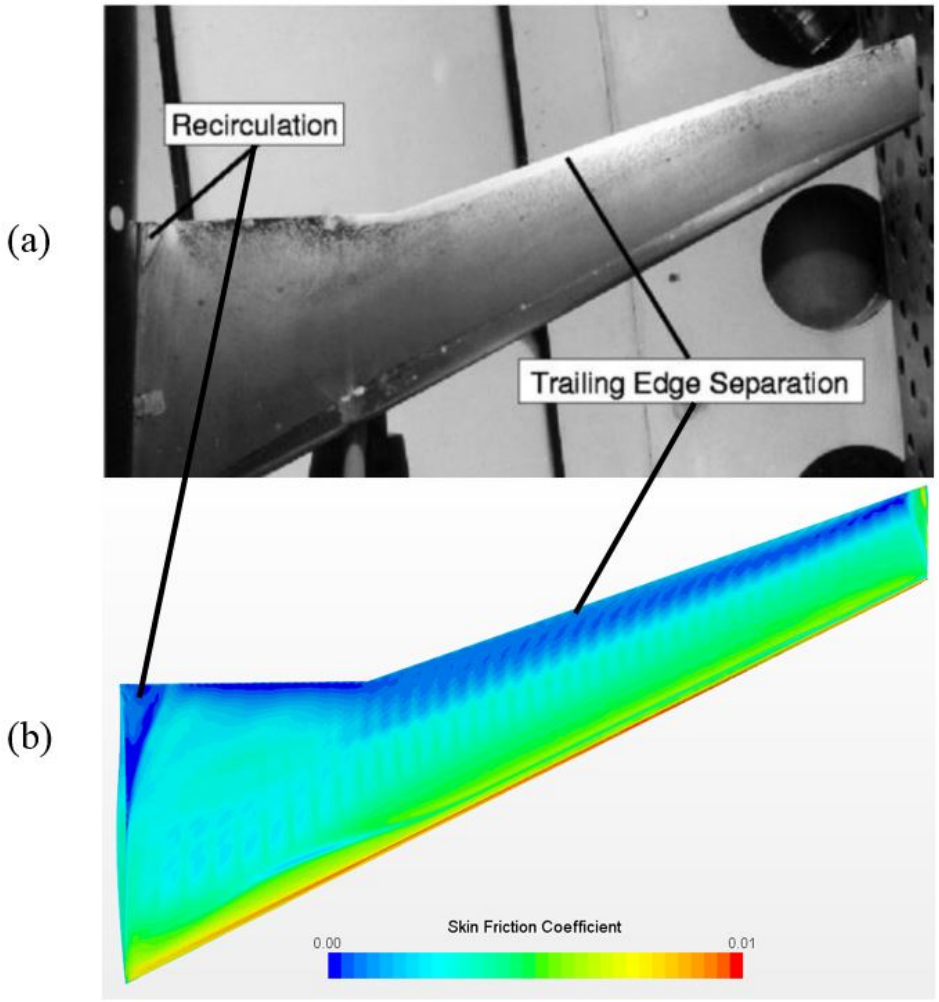

Figure 4.12: Illustration of (a) wing-root recirculation and flow separation from wind tunnel experiment (Laflin et al., 2005) and (b) plot of skin friction coefficient from equivalent CFD simulation.

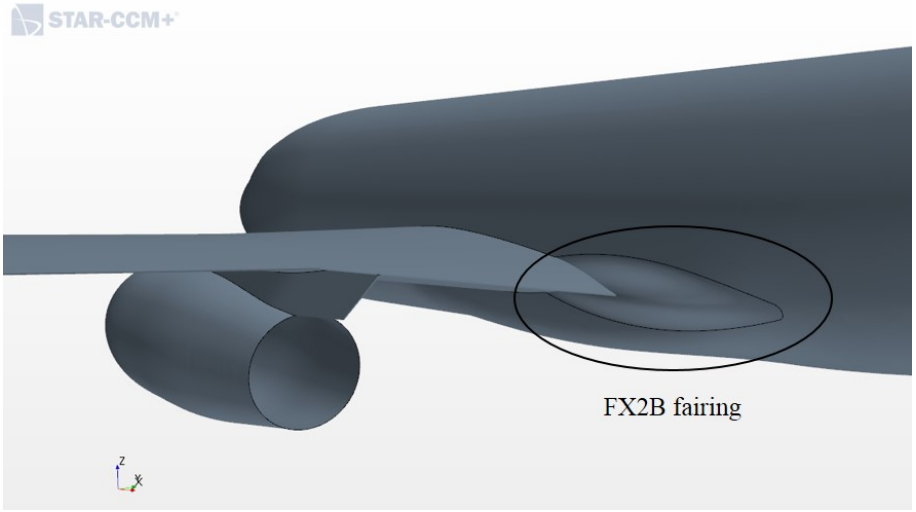

Figure 4.13: FX2B fairing installed at the junction of wing and fuselage to reduce wing-root separation (Frink, 2006).

coefficient focusing on the wing-body junction are shown in Figure 4.14. It can be seen that the separation zone at the wing root was significantly minimised, hence, the fairing did its purpose to reduce boundary layer separation at the wing-fuselage junction.

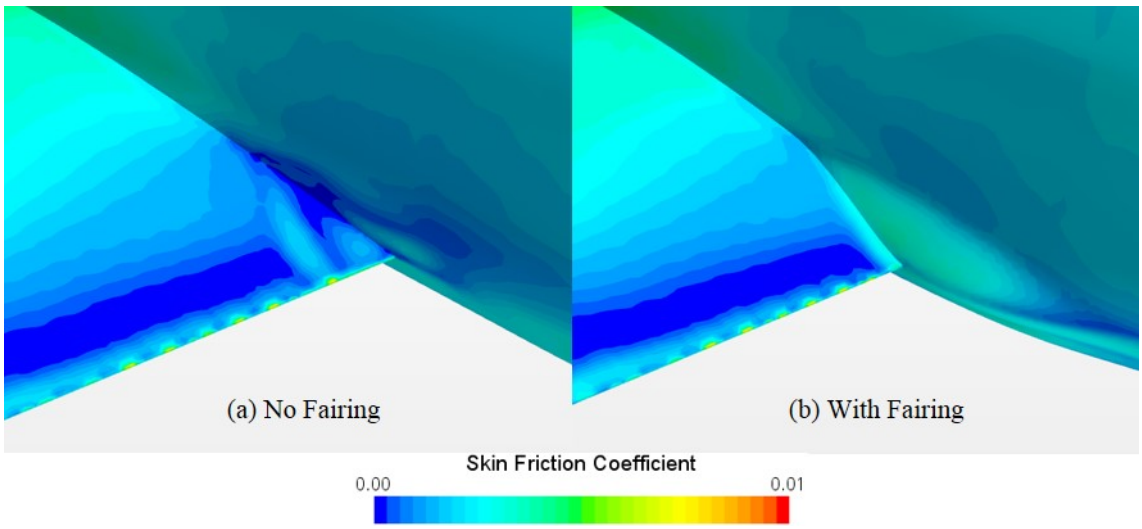

Figure 4.14: Illustration of the reduction of wing-root separation region between (a) no fairing present and (b) after installing the FX2B fairing.

4.1.7 DLR-F6 Summary

In this validation study, by comparing the SST k-ω and Spalart-Allmaras turbulence models, the k-ω SST model prevailed for its enhanced capability to predict the adverse pressure gradient while the Spalart-Allmaras model inaccurately produced shock waves in some locations. It is assumed that the deviations in the prediction of the suction peak and discrepancies at the wing lower surface in both turbulence models are mainly because of insufficient mesh resolution at the leading edge. Whilst the experimental data was subject to experimental error of around $\Delta C_{P_{\text{exp}}} = \pm$ 0.01, this is very small in comparison to the magnitude of the experimental data. Therefore the differences between experimental and CFD data are not affected by these small error bars. If the error bars were, for example, an order of magnitude larger then the discrepancies between CFD and experiments would be within the experimental error, however, this is not the case here. Generally speaking, the SST k-ω turbulence model is more appropriate than the Spalart-Allmaras model at this high-Re condition especially in predicting boundary layers (Cummings et al., 2015). In terms of the mitigation of boundary layer separation, an appropriate fairing design can minimise the risk of separation at "gully" regions, however, wing rear loading still plays a crucial role in boundary layer separation at the trailing

edge, which will be investigated with the NASA Common Research Model in the next section.

4.2 NASA Common Research Model

The NASA Common Research Model (CRM) geometry, developed by Vassberg et al. (2008), is a more complicated geometry than DLR-F6 model, see Fig. 4.15. It comprises of a wing-body-nacelle-pylon-tail (WBNPT) configuration, plus a huge wing root fairing to reduce boundary layer separation; this represents a more current baseline for aerodynamic analysis that has been designed to a high drag standard, similar to the Boeing 777 aircraft. The CRM geometry is publicly available (NASA, 2020) as well as the experimental data obtained from the European Transonic Wind Tunnel. In this case study, the mesh strategy, physical settings, mesh verification, and overall validation strategy are similar to that in the DLR-F6 case study, previously, therefore, the details are only briefly introduced.

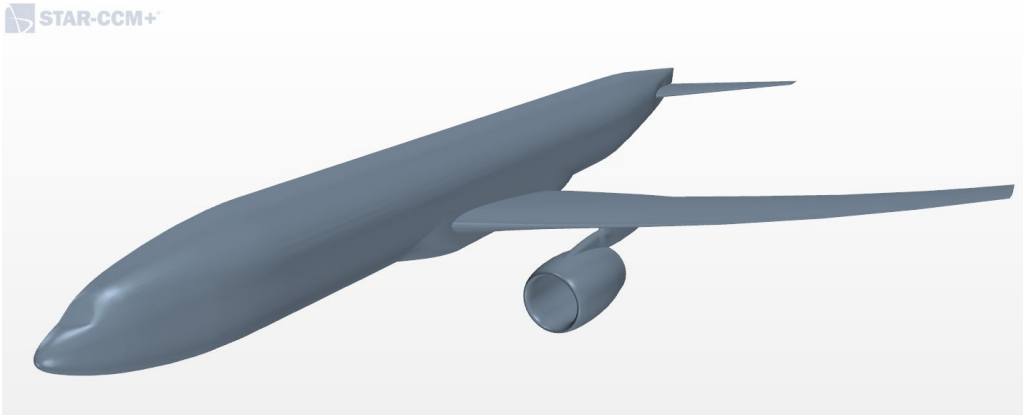

Figure 4.15: NASA Common Research Model with a wing-body-nacelle-pylon-tail configuration (NASA, 2020).

4.2.1 Meshing

As the NASA Common Research Model is more sophisticated than the DLR-F6 geometry due to it having a larger belly-fairing, thin horizontal stabiliser, and a more optimised wing, therefore, a total of ten refinement zones were used in meshing. However, due to more precise control of refinement zones and the advantage of an anisotropic trimmer, which allows the user to specify different mesh sizes in each coordinate direction, the final total number of cells in the mesh is actually less than that in the fully refined mesh of the DLR-F6. Figure 4.16 shows the carefully located volumetric control regions and the fully refined mesh.

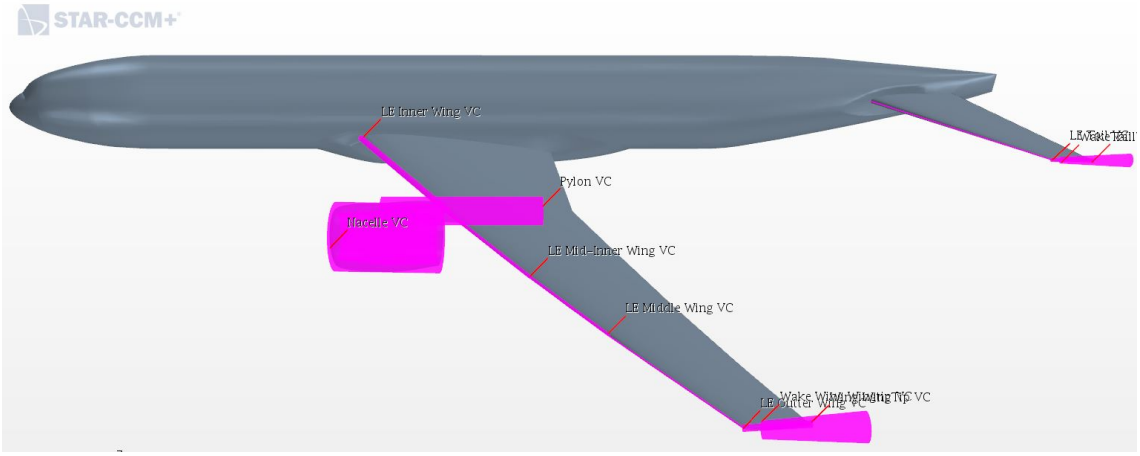

(a) Small refinement zones

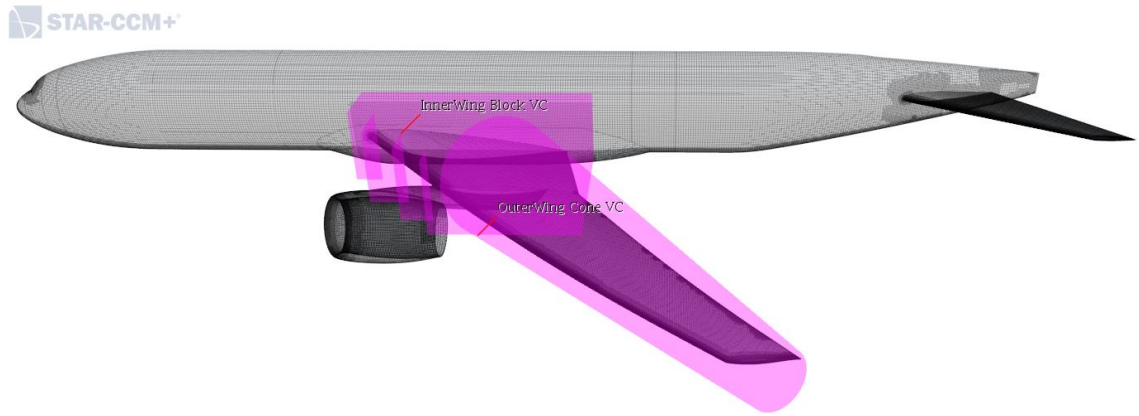

(b) Wing refinement

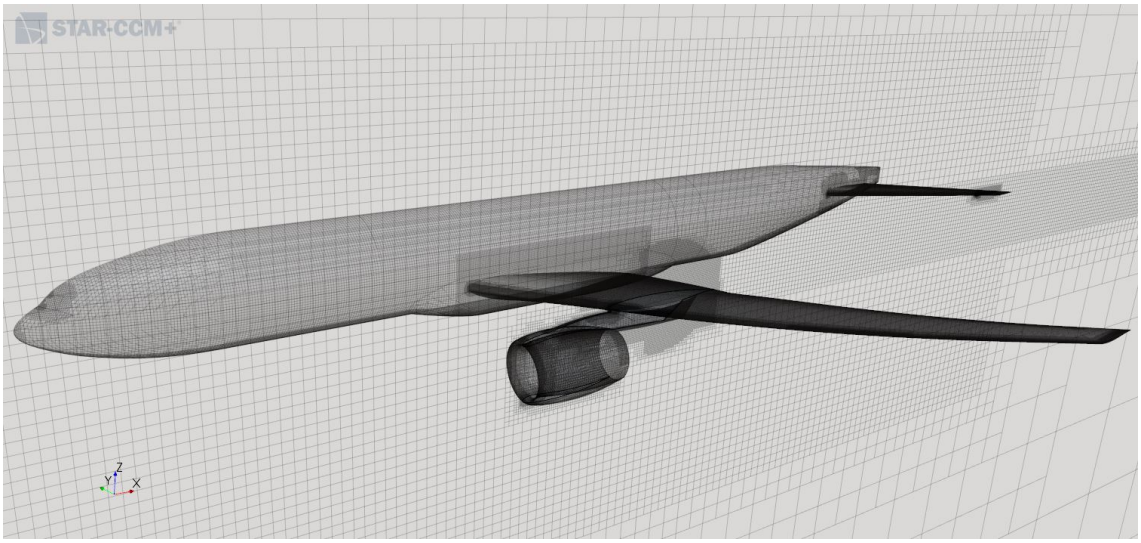

(c) Fully refined mesh

Figure 4.16: Image showing (a) mesh refinement zones at sensitive locations, (b) meshing refinement for inner and outer wing regions, and (c) fully refined mesh (containing 9.30 million cells).

4.2.2 Physics Continuum

Similar to the DLR-F6 case study, to match the European Transonic Wind tunnel test condition, the freestream velocity for domain inlet was set to Mach 0.7, with an

ambient static pressure of P_{static} = 89359.0 Pa for the domain (Rivers, Quest and Rudnik, 2015). The top and bottom surfaces of the domain were both defined as velocity inlets in order to easily conduct simulations of either positive or negative angles of incidence, while left and right surfaces were set as symmetry planes.

The physical settings in this case study were nearly the same as those in the previous study, however, in terms of the selection of turbulence model, only the SST k-ω turbulence model was employed as it has adequate performance for solving complex problems at transonic conditions. Typically, each solution fully converged between 10^{-3} and 10^{-4}, after 2500 iterations.

The mesh verification, including checks of y^+ values and boundary layers, were conducted afterwards and both results were satisfactory, in which the average y^+ value for all walls was 0.87 and a total of 20 prism layers can fully contain the boundary layer.

4.2.3 Grid Independence Study

The grid independence study was similar to the previous one, using the plots of C_L and C_D plots for 6 different-sized meshes (-20%, -10%, -5%, +5%, and +10%) at $AoA_{C_L=0.5}$ = 3.21° to demonstrate that the baseline mesh (9.30 million cells) can efficiently and sufficiently solve the flow problem, see Fig. 4.17 where the C_L and C_D values level off when approaching the baseline mesh density.

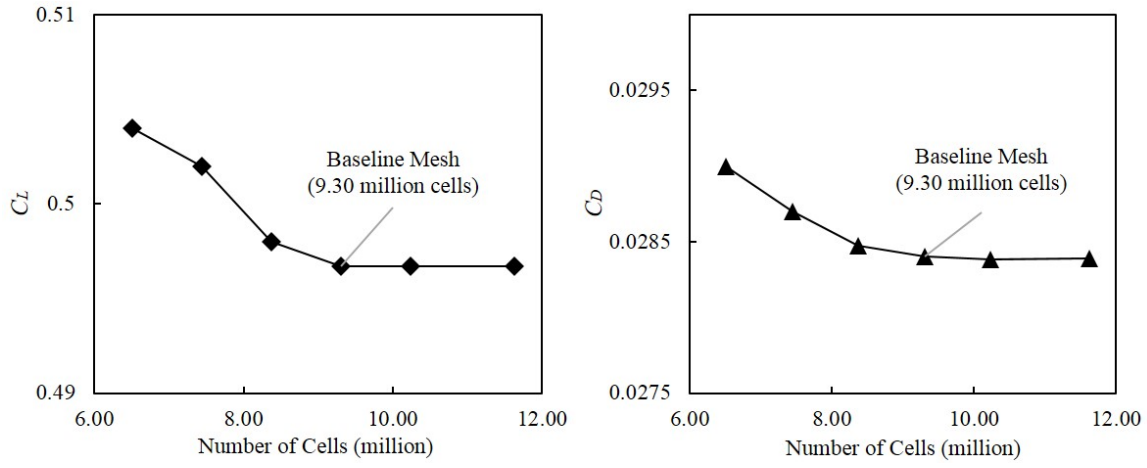

Figure 4.17: Plot showing grid independence study by (a) predicted coefficient of lift and (b) predicted coefficient of drag.

4.2.4 Pressure Distributions

Before the pressure distribution comparison, the Reynolds number, Re_{CFD}=2.96 million and Re_{Exp}=2.93 million, and coefficient of lift, C_L(CFD) = 0.561 and C_L(Wind Tunnel) = 0.560 were matched to ensure each case has the same flow conditions. Figure 4.18 - 4.20 presents the C_P comparisons between CFD results and experimental data at three different stations.

For the upper surface, the suction peak is marginally under-predicted at the inner wing station (y/b=0.201), while a larger discrepancy is shown at the middle wing (y/b=0.502), moreover, at the outer wing, the prediction of suction peak by CFD is slightly over-predicted. The rear loading is very well predicted by CFD against experimental data while the results at the trailing edge are not as accurate for the wing crank and the outer wing due to insufficient mesh resolution and flow separation.

For the lower surface, the results of the wing crank and outer profile show a good match with wind tunnel data, however, for the inner wing, the ΔC_P between CFD and Exp narrows from $\Delta C_P \approx 0.1$ near the leading edge to zero at approximately 35% chord, where the limited mesh density is known to impact results.

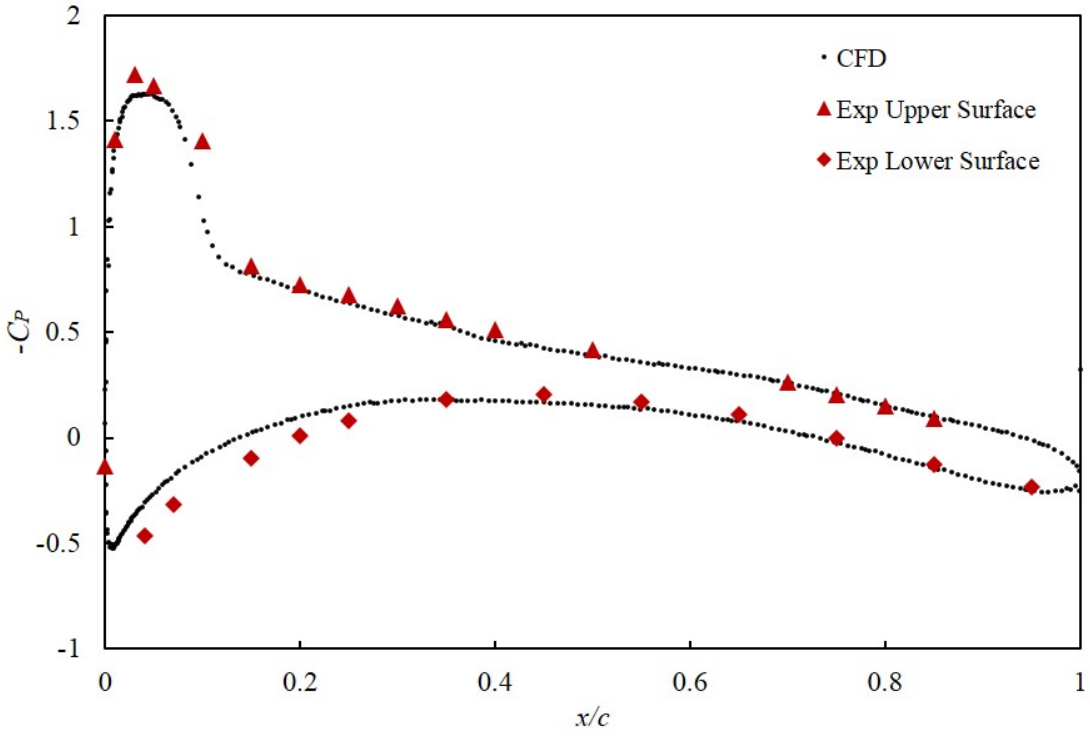

Figure 4.18: Plot showing the comparison of the pressure distributions at y/b=0.201 between the CFD results and experimental data. (Experimental error bars were determined to be $\Delta C_{P_{\text{exp}}}$=± 0.0026)

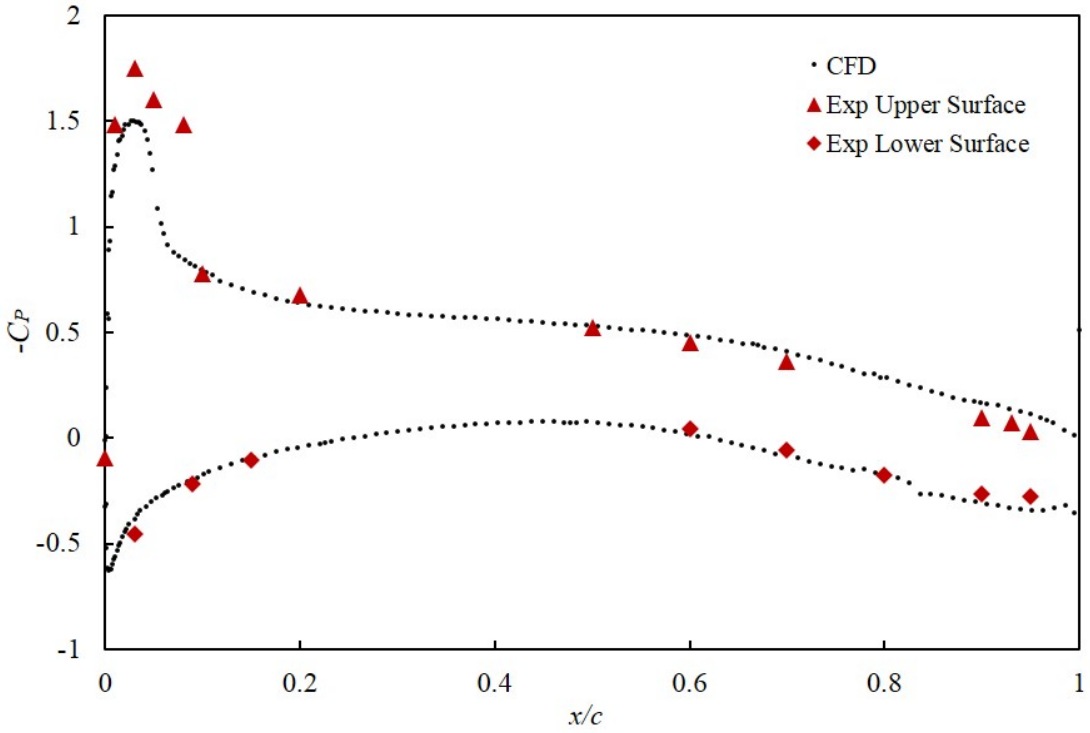

Figure 4.19: Plot showing the comparison of the pressure distributions at y/b=0.502 between the CFD results and experimental data. (Experimental error bars were determined to be $\Delta C_{P_{\text{exp}}}$=± 0.0026)

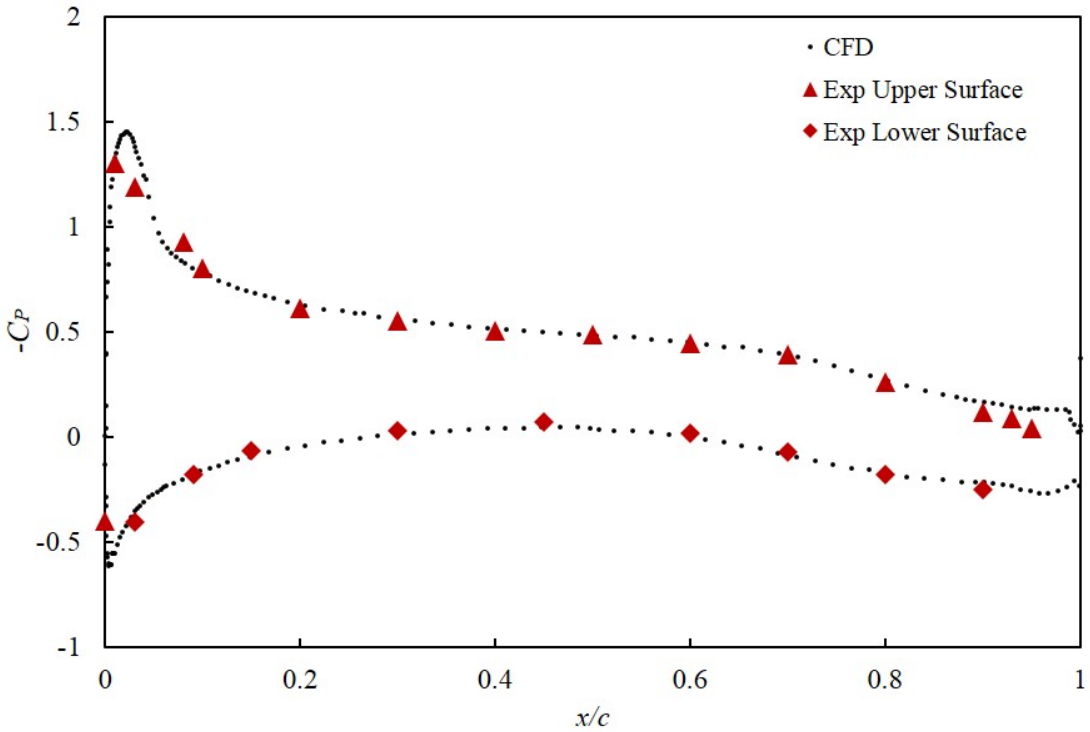

Figure 4.20: Plot showing the comparison of the pressure distributions at y/b=0.846 between the CFD results and experimental data. (Experimental error bars were determined to be $\Delta C_{P_{\text{exp}}}$=± 0.0026)

4.2.5 CRM Powered Nacelle Simulation

As this research will consider utilising powered distributed propulsion systems, in addition to the "flow-through-nacelle" scenario already carried out in both case studies, CFD simulation was also applied to a powered CRM configuration (though no wind tunnel data exists for this configuration). Figure 4.21 shows the concept of the powered nacelle by a sectional view of the mesh through the centre of the nacelle compared to a flow-through nacelle; pressure-outlet and velocity-inlet boundary types are set for the nacelle's intake and exit respectively, to simulate the exhausted jet with appropriate control over the exit velocity.

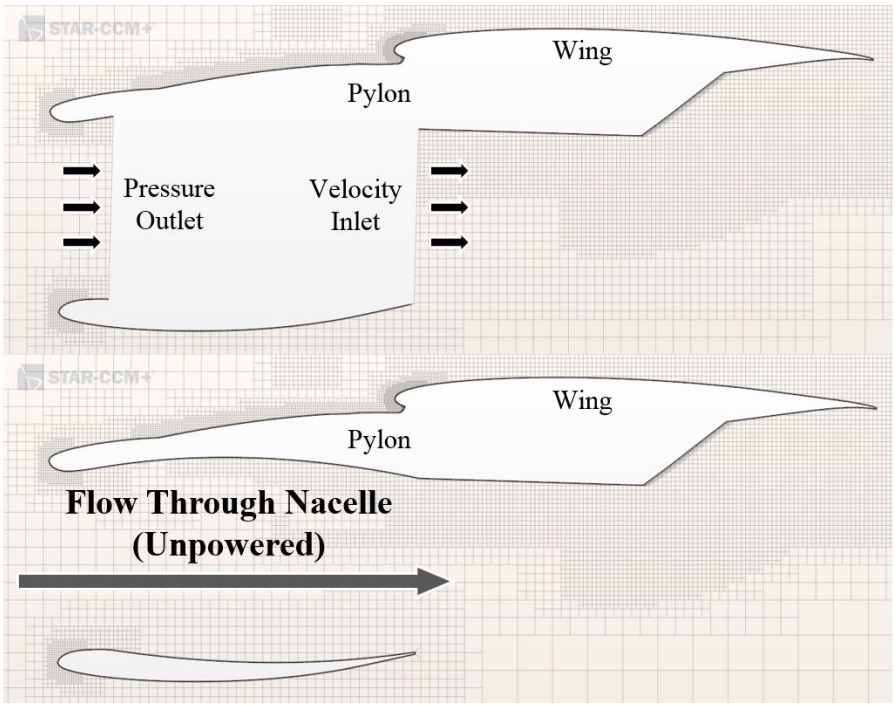

Figure 4.21: Image showing the concept of (a) the powered nacelle and (b) the "flow-through-nacelle" configuration.

As the simulation was simply to explore how the the propulsion influences the flow over the wing, a simplified sea level condition was adopted, with a freestream velocity of Mach 0.7 and an ambient static pressure of P_{static}=101325.0 Pa. Additionally, zero angle of attack was also applied to both cases. For the powered nacelle case, the nacelle exit was set with a velocity of 340.29 m/s. This represents a choked condition for the convergent bypass nozzle with a sonic exit velocity and a maximum mass flow rate. Although the engine core nozzle flow is not included, this simplified model should give a good representation of a powered nacelle on wing performance. Both cases converged after 3500 iterations with all residuals converged with the maximum value of 10^{-4}. Figure 4.22 shows an intuitive view of streamlines going past/through the nacelle, as it can be see that the exhaust jet is accelerated by

the powered nacelle while no velocity changes are seen in the "flow-through-nacelle" case, as expected.

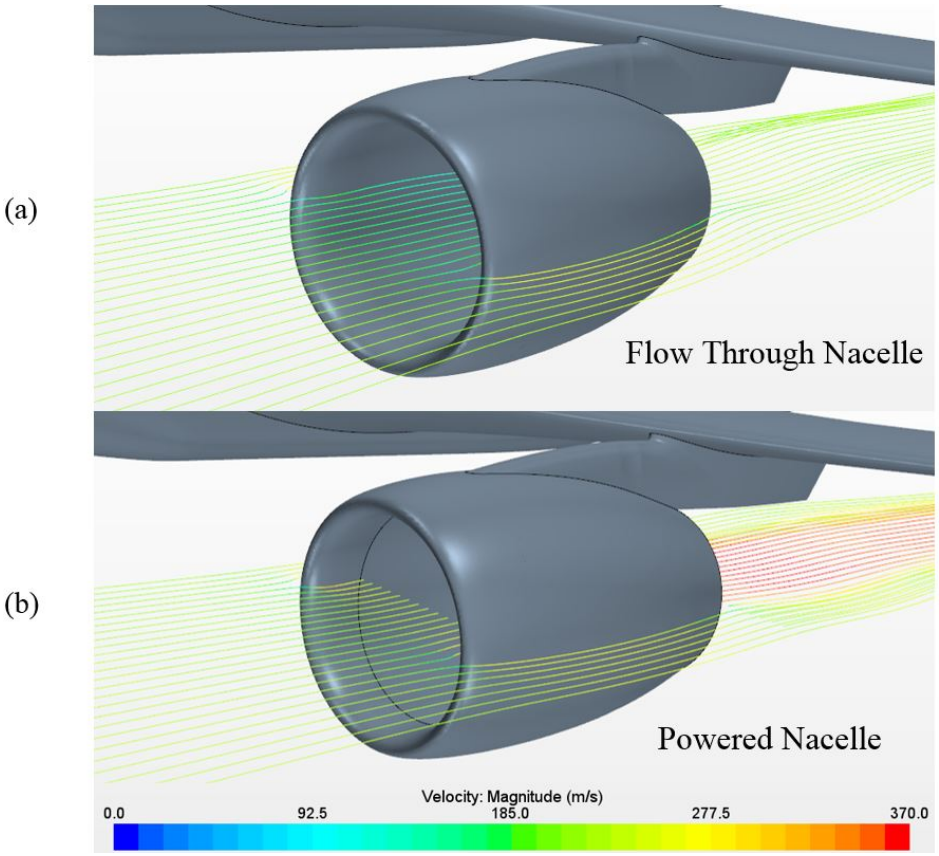

Figure 4.22: Image showing the streamlines going through (a) the flow-through nacelle and (b) streamlines representing the powered nacelle concept.

Analysing the pressure distribution can reveal more information regarding the effect of the powered nacelle. Figures 4.23a and 4.23b show the pressure distribution comparison between the "flow-through-nacelle" and powered nacelle configurations at y/b=0.283, which was slightly off the centreline of the nacelle, and y/b=0.502, where to identify the effect of propulsion at the wing mid-span.

With the presence of the powered nacelle, the most obvious change occurs at the lower surface between 30% and 65% chord at y/b=0.283; the sudden increase of negative C_P values implies flow acceleration produced by the powered nacelle. Interestingly, the remaining C_P profile for the powered nacelle case, including upper and lower surfaces for both stations, was actually lower than "flow-through-nacelle" case, except the front half of the lower surface at y/b=0.502. However, the explanation cannot be simply because of the reduction in velocity, as the propulsion acting, the drag level and cross-flow effect both increase as well. Regardless of these subtleties, this simulation illustrates that propulsion in CFD can be achieved through the combination of appropriate boundary conditions, but it requires careful selection

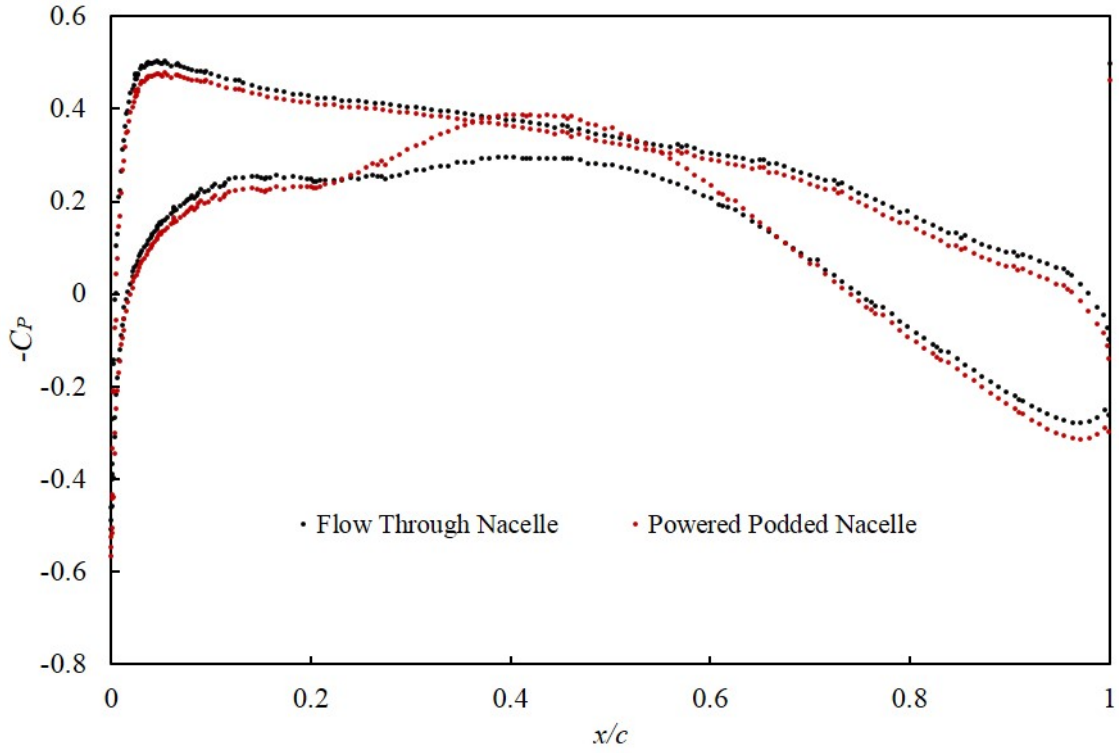

(a) y/b=0.283

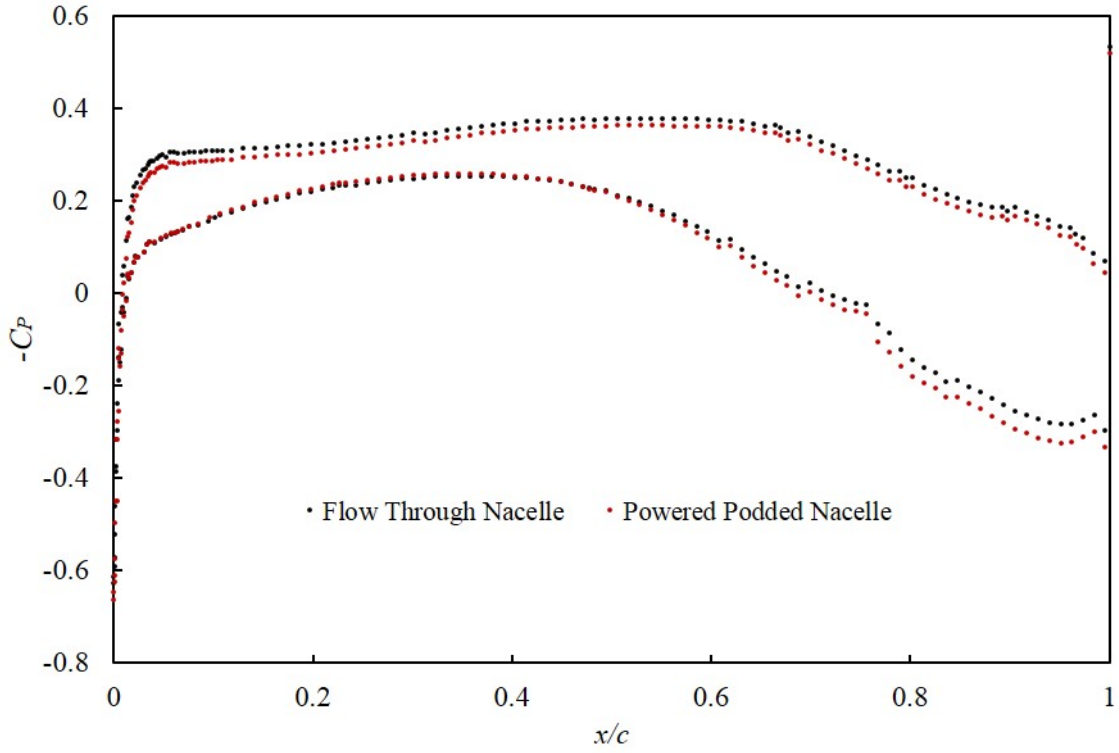

(b) y/b=0.502

Figure 4.23: Plots showing the pressure distribution comparison between "flow-through-nacelle" and powered nacelle configurations at (a) 28.3% span and (b) 50.2% span. (*Centre of engine located at 35% span*)

of boundary types and calculations for boundary condition values to meet different purposes.

4.2.6 NASA CRM Summary

In this case study, the SST k-ω turbulence model was tested again on a more complicated configuration. The increased accumulation of knowledge and experience in CFD, gave results that show good accuracy and efficiency. The consistency in meshing and physics strategy offered a clear and efficient method for the novel part of this research. This case study also suggested a practical method to simulate propulsion in CFD, however, in terms of an electric fan, which will be investigated in next chapters, the simulation of electric propulsion requires further consideration.

4.3 Synthesis

Through two cases, the general conclusions resulting from the CFD method presented in this chapter can be summarised as follows:

- A good general match between CFD computations and wind tunnel tests was observed, and both techniques predicted the same salient features of the flow field surrounding both the DLR-F6 and the NASA Common Research Model geometries.
- In terms of the performance of turbulence models, the SST k-ω turbulence model has preferable capabilities in predicting shock waves than the Spalart-Allmaras turbulence model.
- Effective mesh generation techniques proved to be crucial in CFD, especially in sensitive parts of the research object, such as, leading and trailing edges. Additionally, it is also important to refine the mesh covering small components, i.e. wing tips, to improve the convergence.
- The presence of shock waves and flow separation in both case studies indicates the complexity in high Re flight conditions for simulating the flow around complicated aircraft geometries. As this research will consider even higher Mach numbers, further considerations are required in the areas of meshing and flow physics.
- The fairing test showed that an appropriate fairing design can properly eliminate the wing-root separation, however, it requires careful design to balance the increased weight with drag reduction benefits.

- Results in the NASA CRM case study showed the improvement in knowledge and experience in CFD, plus the sophistication of the CRM geometry, make this suitable to be the baseline aircraft in the next research phase.
- Results from powered CRM simulations showed how propulsion can be simulated by a combination of suitable boundary conditions, and how propulsion can effect the pressure distribution. However, simulating electric ducted fans is different from a gas turbine engine, typically by converting the thrust requirement from a large bypass ratio podded-engine into a smaller distributed bank of electric fans, which will be introduced in Chapter 5.

Two case studies in this chapter were focused on a wind tunnel sized geometry, hence, the focus of subsequent chapters will be on full-scale analysis of more detailed electric distributed propulsion concepts in real flight conditions. Firstly, the modelling of distributed electric fans is introduced and explained in the next chapter. Furthermore, as aerodynamic analysis and performance improvement will be considered, the methodology outlined in this chapter can be extended to investigate the effect of flow conditions on both over and under wing nacelle configurations.

Chapter 5

Electric Ducted Fan Modelling

The results from the validation and verification exercises in the previous chapter represent a first step towards understanding the flow fields around medium-sized aircraft in high Re conditions. The purpose of this chapter is to develop the aforementioned methodology that can address the issues of simulating a simplified electric ducted fan in a commercial CFD package. This is typical of companies and institutes who have their own specifically designed tools for this sort of simulation on either small or medium sized aircraft (Chang and Rajagopalan, 2003; Pandya, Murman and Aftosmis, 2004; Akturk and Camci, 2012; Dillinger et al., 2018). Firstly, a simplified method for sizing a realistic full-scale ducted fan is presented together with detailed step-by-step calculations. Next, the comparison of using different combinations of boundary conditions will be analysed and discussed. Eventually, through the sensitivity study of the most appropriate combination, the final settings for modelling and subsequently improving the aerodynamic performance with distributed electric fans will be determined for the next chapter.

5.1 Modelling Requirements

The nature of a typical electric fan is to accelerate the air and generate thrust without directly involving combustion engine processes, which implies that the mass flow rate at the fan intake and exit must be identical. Despite this, there are numerous distributed electric propulsion concepts for commercial aircraft designs (Brelje and Martins, 2019). This research considers aft embedded propulsion systems to neutralise the nacelle-wing coupling problem, as well as enabling boundary layer ingestion into the fan to maximise overall performance by energising the wake (Steiner

et al., 2012). Therefore, the general requirements for modelling a simplified electric fan in this research are summarised as follows:

- The system must be capable of providing sufficient thrust to propel an Airbus A320-type aircraft.
- Mass flow rates ($\dot{m}$) for fan intake and exit will be identical.
- Fans will only occupy the inner wing, i.e. "inner-wing" distributed propulsion.
- Operating in real flight conditions and the fan exit will have a "just-choked" condition which represents a maximum thrust condition.

5.1.1 Preliminary Design of an Electric Ducted Fan

In this section, the methodology used for sizing an electric ducted fan is introduced. Figure 5.1 illustrates the schematics of a typical electric fan. Given the operating conditions, see Table 5.1, such as flight altitude, target Mach number, thrust requirement, and fan pressure ratio, it is feasible to determine the size of an individual fan.

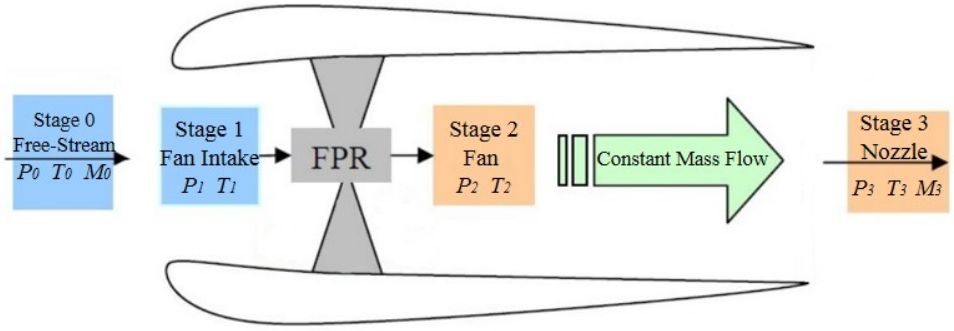

Figure 5.1: Schematics of a simplified electric ducted fan with flow conditions at different stages modified from (Sgueglia et al., 2018).

Parameter	Symbol
Altitude	H
Freestream Mach number	M_0
Fan pressure ratio	FPR
Heat capacity ratio	γ_{cold}
Gas constant	R_{cold}
Thrust Requirement	F_N
Number of fans	N_{fan}

Table 5.1: Initial operating conditions for an electric ducted fan.

The freestream total pressure P_{t0} and total temperature T_{t0} at altitude H can be calculated from isentropic relationships, namely:

$$P_{t0} = P_0\left[1 + \frac{\gamma_{cold} - 1}{2} {M_0}^2\right]^{\frac{\gamma_{cold}}{\gamma_{cold}-1}} \tag{5.1}$$

and,

$$T_{t0} = T_0\left(\frac{P_{t0}}{P_0}\right)^{\frac{\gamma_{cold}-1}{\gamma_{cold}}} \tag{5.2}$$

Assuming the pressure loss in the intake, given the pressure ratio PR_{intake} (100-pressure loss)%, while the total temperature does not change in the intake, the total pressure P_{t1} and total temperature T_{t1} in the intake can be determined from:

$$P_{t1} = PR_{intake} P_{t0} \tag{5.3}$$

and,

$$T_{t1} = T_{t0} \tag{5.4}$$

Assuming no pressure loss at the fan exit, thus, the total pressure after the fan, P_{t2}, and fan exit pressure, P_{t3}, can be determined. From:

$$P_{t3} = P_{t2} = \text{FPR} \times P_{t1} \tag{5.5}$$

The ideal total temperature T'_{t2} is calculated from isentropic relationships, and the actual total temperature T_{t2} is given by the fan isentropic efficiency, η_c.

$$T'_{t2} = T_{t1}\left(\frac{P_{t2}}{P_{t1}}\right)^{\frac{\gamma_{cold}-1}{\gamma_{cold}}} \tag{5.6}$$

and,

$$T_{t2} = \frac{T'_{t2} - T_{t1}}{\eta_c} + T_{t1} \tag{5.7}$$

The nozzle choke test is carried out by comparing the ideal pressure ratio, PR_{ideal}, and the critical pressure ratio, PR_{crit}. The nozzle must be tested to see if the flow is choked at these conditions. As the electric ducted fan does not involve combustion, the air after the fan can still be seen as cold air, therefore:

$$PR_{ideal} = \frac{P_{t3}}{P_0} \tag{5.8}$$

and,

$$PR_{crit} = \frac{P_{t3}}{P} = \left(\frac{\gamma_{cold}+1}{2}\right)^{\frac{\gamma_{cold}}{\gamma_{cold}-1}} \tag{5.9}$$

To ensure the nozzle has a "just-choked" condition ($M_{exit} = 1$), $PR_{ideal} = PR_{crit}$, the FPR must be adjusted to satisfy this criterion. A typical FPR value of FPR=1.35, recommended by Felder, Brown, Kim and Chu (2011); Kim (2010), is used in this thesis. Assuming no changes in the total temperature and the total pressure, this implies that the nozzle static temperature, T_3, and the static pressure, P_3, can be determined from isentropic relationships. They are:

$$T_{t3} = T_{t2} \tag{5.10}$$

$$T_3 = \frac{T_{t3}}{\left(\frac{P_{t3}}{P_0}\right)^{\frac{\gamma_{cold}-1}{\gamma_{cold}}}} \tag{5.11}$$

$$P_{t3} = P_{t2} \tag{5.12}$$

$$P_3 = \frac{P_{t3}}{\left(1+\frac{\gamma_{cold}-1}{2}M_{exit}^2\right)^{\frac{\gamma_{cold}}{\gamma_{cold}-1}}} \tag{5.13}$$

Thus, the local air density at the nozzle is calculated by:

$$\rho_{exit} = \frac{P_3}{T_3 R_{cold}} \tag{5.14}$$

Based on the thrust equation, the thrust is given by:

$$F_N = \dot{m}_{exit}(V_{exit} - V_{in}) + A_{exit}(P_{exit} - P_{in}) \tag{5.15}$$

As $P_3(P_{exit}) = P_0(P_{in})$ for a just choked condition, the thrust can be simplified to:

$$F_N = \dot{m}_{exit}(V_{exit} - V_{in}) \tag{5.16}$$

and the mass flow rate at the exit, $\dot{m}_{exit}$, is given by:

$$\dot{m}_{exit} = \rho_{exit} \cdot V_{exit} \cdot A_{exit} \tag{5.17}$$

Also, the exit velocity, V_{exit}, which equals to local sound speed, a_{exit}, is found from;

$$V_{exit} = a_{exit} = \sqrt{T_3 \cdot \gamma_{cold} \cdot R_0} \tag{5.18}$$

Therefore, the fan total nozzle exit area can be determined for a given thrust (i.e the cruise thrust provided by two CFM56-5A1 engines for an Airbus A320 at an altitude of 10 km is 51020.10 N):

$$A_{exit} = \frac{F_N}{(V_{exit} - V_{in})\rho_{exit} V_{exit}} \tag{5.19}$$

where, V_{in} is normally around Mach 0.5 since a higher inlet Mach number can lead to transonic fan tip speeds and therefore compressibility losses (Ward, 2010). The final fan exit height is 0.595 m, and the length of the distribution system at one side (5 fans) is 2.975 m, which is smaller than the length of the inner wing of A320 (approximately 4.658 m); allowing sufficient space for installation.

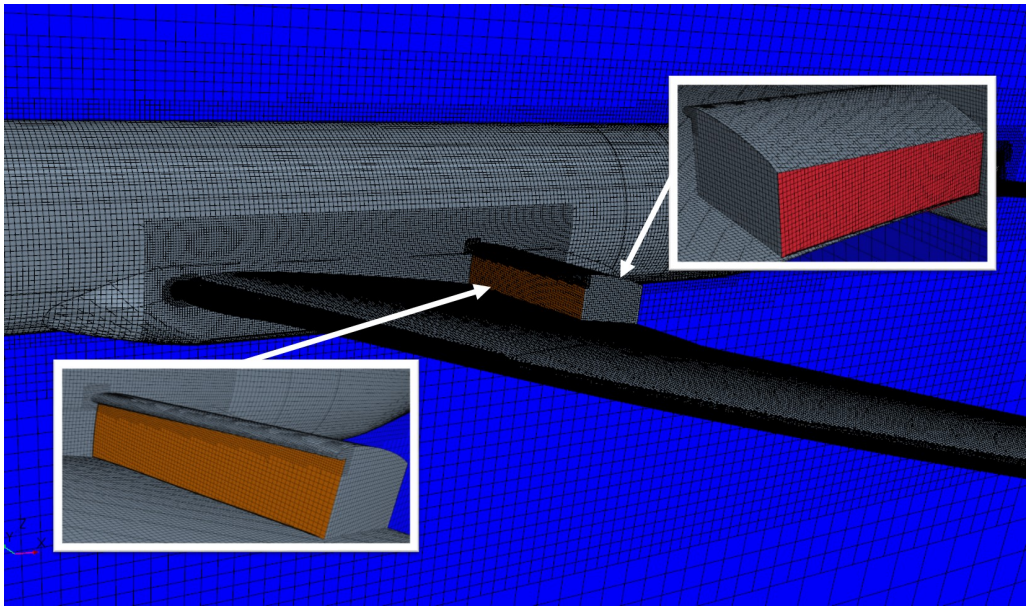

Figure 5.2: Illustration of inner-wing distributed propulsion system investigated in this study.

It is assumed that the distributed ducted fan has a rectangular nozzle exit extending over the full inner wing of the CRM baseline aircraft, i.e. from wing root

to wing crank. Figure 5.2 illustrates the inner-wing distributed electric propulsion system which is investigated in this research. Through this preliminary design process of a simplified electric ducted fan, the size of the rectangular fan exit area can be determined in combination with an appropriate value of the FPR to achieve the same cruise thrust as the baseline A320. As detailed design of an electric ducted fan is not considered in this research, e.g. shape of nozzle and nacelle, the size of the fan intake is determined by the volume ratio of the nacelle used by the NASA Common Research Model.

5.2 Boundary Condition Testing

In CFD simulation, in general, using different combinations of boundary condition types to simulate propulsion has varying impact on final solutions. This section presents three different combinations, (a) pressure-outlet and velocity-inlet, (b) pressure-outlet and mass-flow inlet, and (c) momentum source, to find out the most appropriate combination to be used for the next chapter; as other combinations either had convergence issues or divergence problems.

As this research focuses on an "inner-wing only" aft distributed propulsion concept, see Fig.5.2, the coordinates of a baseline aerofoil were extracted from the middle inner-wing of the NASA CRM model using GEMS, which is a point-based CAD software package. Following a traditional design process, analysis is subsequently based on two-dimensional simulations. Additionally, due to the constant height of fan inlet and exit across the inner-wing span, the 2D simulation of one slice of the propulsion system is considered as an appropriate method to investigate the momentum effect. Naturally, the flow would be 3D in reality with swirl effects, even with this slot-type inlet, however the 2D approximation is considered to be a good first approximation to investigate the overall concept. Further discussion regarding the differences between 2D and 3D simulation results is included in the Discussion and Conclusions chapter later. Hence, the coordinates for the 3D wing section were transformed due to the effects of wing sweep (using the CRM model mean sweep angle 31.5°) to an equivalent two-dimensional design (NASA, 2020) and scaled up to the same chord length as the middle inner-wing on an Airbus A320. The flight altitude was set as 10 km with the corresponding ambient conditions, and the freestream velocity was initially set as Mach 0.725 (equivalent to Mach 0.85 in 3D accounting for sweep) with no angle of incidence. Furthermore, this test adopted a simplified fan shape similar to the design proposed by Wick et al. (2015) and Schmollgruber et al. (2019) having a choked nozzle condition, while the fan size was

still determined through the preliminary design process introduced in Section 5.1.1. It also assumes no distortion losses and no additional viscous losses by using smaller diameter fans to achieve more wetted area for the same inlet area. To simplify the test, only the over wing nacelle configuration was used. Star CCM+ was utilised due to its superior capability for wing design of the distributed electric propulsion aircraft (Deere et al., 2017), however, because of its lack of a pure 2D solver, a 2.5D model (a conventional 2D domain with a relatively small depth in Z direction) was created before cutting a slice through the mesh and proceeding to the solver. The mass flow rate is directly reported by the built-in solver calculation (based on surface integrals), while the inlet and exit velocities are calculated as the average values over the inlet and outlet.

5.2.1 Pressure Outlet-Velocity Inlet

The first hypothesis of the combination of boundary conditions (BC) to simulate an electric ducted fan was a pressure-outlet BC (with the Target Mass Flow option selected) as a fan intake and a velocity-inlet BC as the fan exit, which was previously used to demonstrate the effect of propulsion in Section 4.2.5. Figure 5.3 shows the velocity magnitude contours with additional flow information by using the combination of a pressure outlet, where $P_{initial}$ and $\dot{m}_{target}$ were specified, and a velocity inlet, where velocity was defined as the speed of sound (M_{exit}=1).

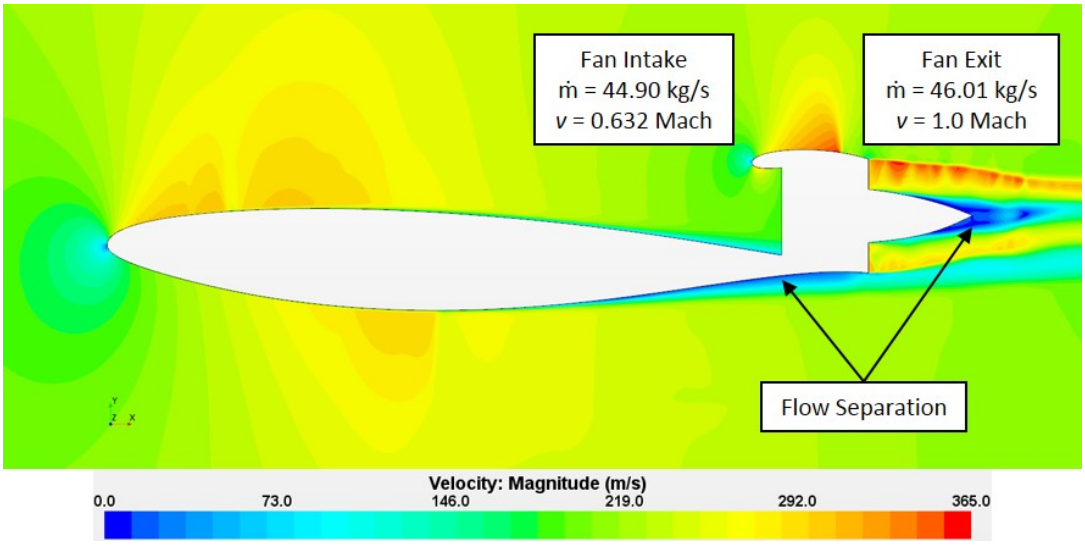

Figure 5.3: Velocity magnitude contours showing the flow field from using the pressure outlet BC (fan intake) and velocity inlet BC (fan exit) combination.

The Target Mass Flow option at the pressure outlet BC was activated to adjust the initial static pressure ($P_{initial}$) in an attempt to yield the specified mass flow rate (CD-adapco, 2016). It was found that although the velocity at the fan intake

and the exit (constant over the exit area) was sensible, the mass flow rates were not perfectly matched, i.e. approximately 2.4% in error. Additionally, this simulation took more than 7500 iterations, while all residuals were level between 10^{-2} and 10^{-3}, which is mainly because of the strong shock on the nacelles and severe separation at the trailing edge and around the nozzle cone.

5.2.2 Pressure Outlet-Mass Flow Rate Inlet

Another combination of BCs for propulsive modelling in CFD was to use a pressure outlet (with the Target Mass Flow option selected) as a fan intake and a mass flow inlet as the fan exit. Figure 5.4 shows the velocity magnitude contours with additional flow information from this BC combination of pressure outlet, where $P_{initial}$ and $\dot{m}_{target}$ were specified, and mass flow inlet, where $\dot{m}_{target}$ and $P_{supersonic}$ were calculated from the preliminary design process in Section 4.2.5.

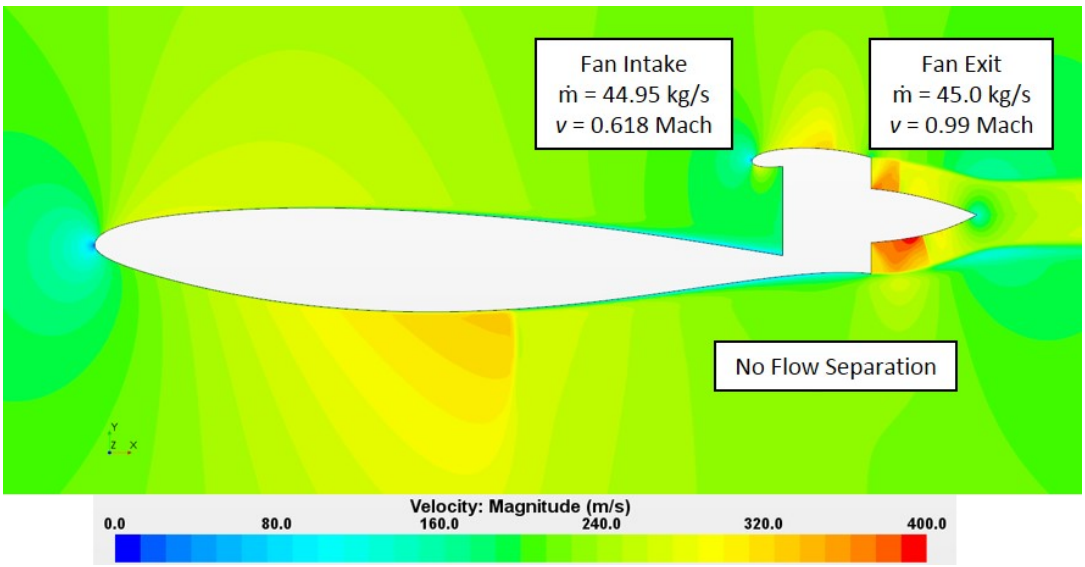

Figure 5.4: Velocity magnitude contour showing the flow field of using pressure outlet BC (fan intake) and mass flow inlet BC (fan exit).

It can be seen that this combination also provided a sensible velocity for the fan intake and exit (constant over the exit area), furthermore, the mass flow rates were acceptably similar (only 0.1% in error), which is clearly better than the previous BC combination. Moreover, this simulation took only 5000 iterations, while all residuals were level at 10^{-4}, which is also an improvement.

5.2.3 Fan Momentum Source

There are two main models in Star CCM+ to simulate fans, i.e. the Fan Interface and the Fan Momentum Source (CD-adapco, 2016). The fan interface simulates the fan by using a simple zero-thickness interface to impose a pressure jump through it, and it is an implicit implementation which allows quicker convergence (CD-adapco, 2016), however, it requires a detailed fan performance curve in which the detailed fan design is not considered. The momentum source requires a 3D region to represent the fan (to be sliced into 2D), while it uses an explicit implementation, which tends to converge more slowly (CD-adapco, 2016). Due to the nature of setting a block of momentum source, the cone was removed. The momentum source uses a source term defined as thrust per volume (unit: N/m^3). As the thrust requirement was given and the fan size was determined from preliminary design, it was easy to define the value of the source term. Figure 5.5 shows the velocity magnitude contours with additional flow information by using the momentum source approach.

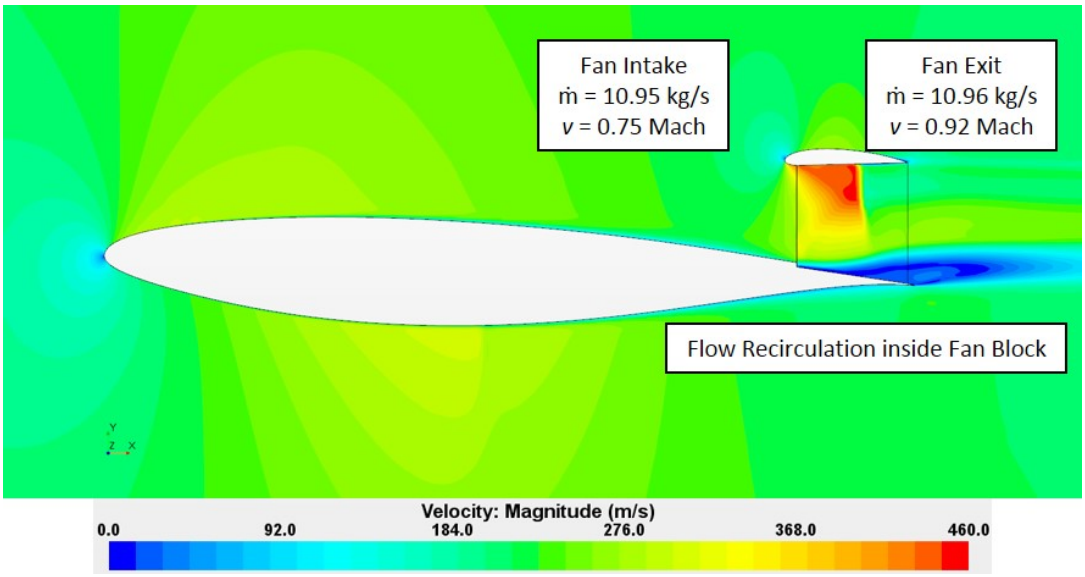

Figure 5.5: Velocity magnitude contour showing the flow field of using momentum source.

In theory, the momentum source is supposed to have advantages, such as delivering an exact value of the target thrust and being capable of adding swirl to the downstream flow. However, after 12000 iterations with all residuals converged to 10^{-3}, the solution bizarrely predicts a strong shock at the top of the fan and numerous flow recirculation zones at the bottom. In spite of the generally sensible velocity for the fan intake and exit , the mass flow rates were only a quarter of the $\dot{m}_{target}$. Unlike the results from previous combinations, the exit velocity is not constant over the exit area. A reasonable explanation for this phenomenon was that the fan momentum source was not suitable in 2D simulation as it is mainly designed for 3D

simulation.

5.2.4 Summary

By analysing the velocity magnitude contours and comparing three combinations of BCs, the "pressure Outlet and Mass Flow Inlet" was chosen as the most appropriate BC combination to simulate an electric ducted fan, due to its ability to produce accurate and reliable results (i.e. identical intake and exit mass flow rates and better solution convergence). Whereas the other two combinations have either poor performance in solving flow gradients or poor convergence. Next, a sensitivity study is proposed for deeper understanding of the best BC combination at different freestream conditions.

5.3 Boundary Condition Sensitivity Study

Since an appropriate combination of the boundary condition had been determined, a sensitivity study was carried out to examine the uncertainty of the outputs as well as improve the understanding of the relationship between the fan intake and exit BCs in different wing-nacelle configurations. In this sensitivity study, both over and under wing nacelle configurations were investigated in 2D simulations, while different Mach numbers were also considered.

5.3.1 Over-Wing Nacelle Configuration

The sensitivity study of over-wing nacelle (OWN) configurations firstly took a lower Mach number of 0.6 and then a higher Mach number of 0.725 into account (both were 2D Mach numbers). To make a fair comparison, all the cases in this sensitivity were C_L-matched at the cruise condition ($C_{L_{2D}} = 0.5$). After running several test cases, a threshold of mass flow rate ($\dot{m}_{threshold}$) was found for each Mach number, as the fan intake can only reach up to $\dot{m}_{threshold}$ while any increase in $\dot{m}$ would not bring it higher. Here, Table 5.2 and 5.3 shows the CFD results of these sensitivity studies at the two Mach numbers.

Clearly, this BC combination did not work perfectly for OWN configuration, as some cases suffered from severe convergence issues. At the lower Mach number study, it was found that the $\dot{m}_{\text{Exit}}$ was constant when $\dot{m}$=36 and 40 kg/s, indicating that the fan size was too large to reach the choked condition at a lower Mach number. For

$\dot{m}_{\text{Target}}$ (kg/s)	$C_{L_{2D}}$	$\dot{m}_{\text{Intake}}$ (kg/s)	$\dot{m}_{\text{Exit}}$ (kg/s)	Intake Velocity (Mach)	Exit Velocity (Mach)
34	Very	Poor	Convergence		
36	0.502	35.98	36	0.508	0.866
38	Very	Poor	Convergence		
40	0.499	39.98	40	0.51	0.866

Table 5.2: Table showing the results of the OWN sensitivity study at Mach=0.6.

$\dot{m}_{\text{Target}}$ (kg/s)	$C_{L_{2D}}$	$\dot{m}_{\text{Intake}}$ (kg/s)	$\dot{m}_{\text{Exit}}$ (kg/s)	Intake Velocity (Mach)	Exit Velocity (Mach)
36	Very	Poor	Convergence		
38	Very	Poor	Convergence		
40	0.501	39.99	40	0.633	0.865
42	0.499	41.98	42	0.631	0.899
45	0.503	44.99	45	0.635	0.947

Table 5.3: Table showing the results of the OWN sensitivity study at Mach=0.725.

the higher Mach number condition, the convergence issue occurred again. However, with higher mass flow rates, the result were acceptable; a relatively constant V_{intake} and nearly choked V_{exit} when the fact that $\dot{m}$=45 kg/s. Additionally, the $\dot{m}_{\text{Intake}}$ and $\dot{m}_{\text{Exit}}$ were acceptably matched. Despite the fact that two cases failed due to either user or numerical errors, it suggested that the BC combination could still be working for OWN at designed Mach number (0.725), as other requirements were achieved.

5.3.2 Under-Wing Nacelle Configuration

Similar to the OWN sensitivity study, an under-wing nacelle (UWN) configuration study also considered the freestream velocity of Mach 0.6 and 0.725. Table 5.4 and 5.5 show the CFD results of sensitivity studies at the two Mach numbers.

In this case, all simulations were successful and fully converged at both Mach numbers, which may suggest that the flow field for the UWN was less challenging for the residuals to converge. Interestingly, the UWN results show consistency of V_{Exit} (unlike OWN results) corresponding to each mass flow rate, which is encouraging for the fan intake, however, the $\dot{m}_{\text{Intake}}$ values were generally slower than for the OWN configuration, which was a promising sign for the fan intake, while V_{Intake} remained at the same level for each configuration, at different Mach numbers. The

$\dot{m}_{\text{Target}}$ (kg/s)	$C_{L_{2D}}$	$\dot{m}_{\text{Intake}}$ (kg/s)	$\dot{m}_{\text{Exit}}$ (kg/s)	Intake Velocity (Mach)	Exit Velocity (Mach)
34	0.508	33.98	34.0	0.424	0.828
36	0.495	35.99	36.0	0.441	0.866
38	0.503	37.96	38.0	0.439	0.866
40	0.501	39.98	40.0	0.440	0.866

Table 5.4: Table showing the results of the UWN sensitivity study at Mach=0.6.

$\dot{m}_{\text{Target}}$ (kg/s)	$C_{L_{2D}}$	$\dot{m}_{\text{Intake}}$ (kg/s)	$\dot{m}_{\text{Exit}}$ (kg/s)	Intake Velocity (Mach)	Exit Velocity (Mach)
36	0.500	35.99	36.0	0.531	0.796
38	0.495	37.99	38.0	0.527	0.831
40	0.494	39.97	40.0	0.525	0.865
42	0.497	41.99	42.0	0.529	0.899
45	0.499	44.98	45.0	0.532	0.947

Table 5.5: Table showing the results of the UWN sensitivity study at Mach=0.725.

other criteria all met the requirements in terms of C_L and $\dot{m}$-matching.

5.3.3 Summary

This sensitivity study demonstrated the capability of "pressure outlet and mass flow intake" BC combination to simulate a simplified electric ducted fan by producing the sensible intake velocity, required exit velocity, and identical mass flow rate for the fan intake and exit at higher Mach numbers. It also suggested that the fan sizing should consider the lower speed condition for higher thrust when needed, which can be solved by fan shape design.

5.4 Synthesis

From the results obtained in this chapter, it is apparent that the method for modelling electric fans can be properly established in a commercial CFD package. The "pressure outlet and mass flow intake" BC combination has full capability to simulate the electric ducted fan with proper mass flow rate settings to meet the thrust requirement.

The pressure distributions of OWN and UWN designs at the same ambient and

fan conditions are seen in Figure 5.6. To achieve the cruise C_L, a higher suction and a stronger shock were observed for the OWN configuration, while the UWN configuration had a more distributed rear loading to compensate the lift. This general observation can be interpreted as the UWN might provide better aerodynamic performance due to its advantage in fan intake design, weaker shock formation, and potential "flow entrainment" to cope with boundary layer separation at the trailing edge. These initial findings will be investigated in Chapter 6 by conducting a parametric study with the aid of a Design of Experiments and a wing parametrisation.

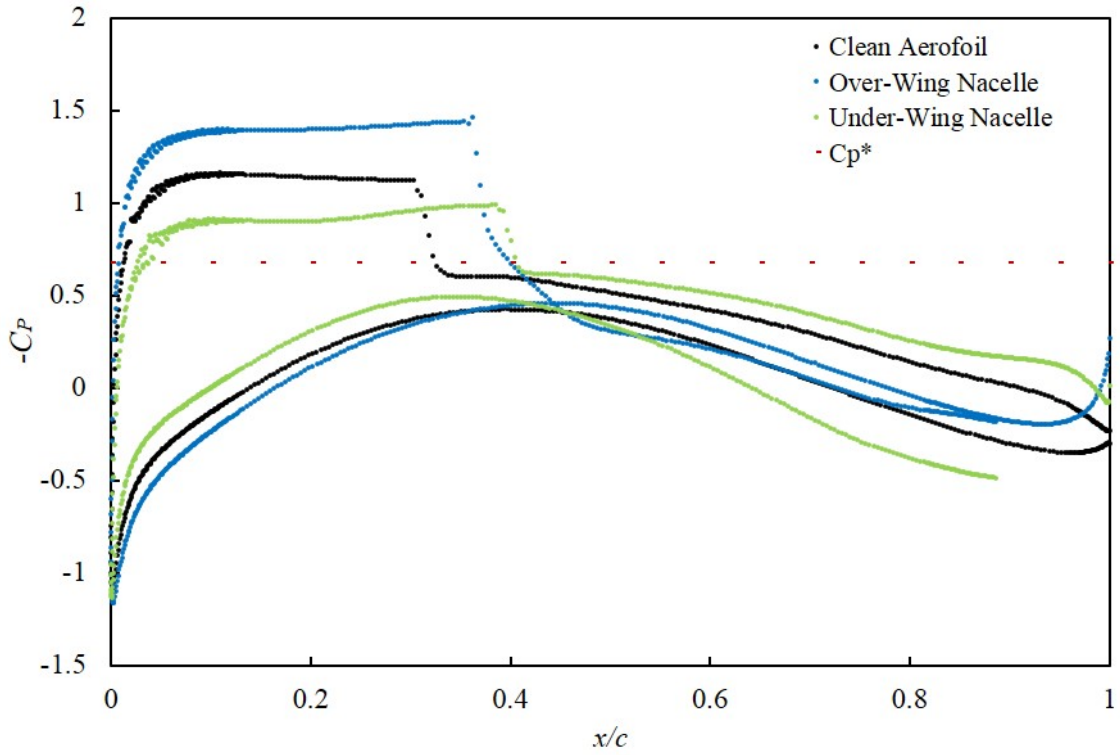

Figure 5.6: Plot showing the comparison of pressure distribution between the clean aerofoil, OWN and UWN configurations at the same lift of $C_{L_{2D}}$=0.5 ±0.25%.

Chapter 6

Aerofoil Performance Analysis

In the CFD validation chapter, the aerodynamic analysis showed that the research methodology and procedures are valid and can be extended to undertake an aerodynamic performance improvement study of an aerofoil with an integrated propulsion system to explore potential benefits in reducing aerodynamic drag and structural weight and improving buffet performance. The focus of this chapter is to extend the method for modelling electric propulsion systems defined in Chapter 5 and couple it with an existing and sophisticated aerofoil parametrisation method (CST) into a design process to investigate the mutual benefits of the electric distributed propulsion concept for both over and under-wing nacelle configurations.

6.1 Problem Definition

Due to the high-Re flight condition and complexity of a typical wing structure, transonic aerofoil design requires important considerations involving highly separated flows, strong shock waves and buffet onset. Moreover, substantial increases in both environmental concerns and flight operation cost also have brought huge demand for minimal aerodynamic drag. Applying a parametric study on a typical supercritical aerofoil shape, coupling with distributed electric fans has the potential to significantly reduce drag compared to conventional podded nacelle configurations, and hence, reducing fuel consumption. The baseline wing from the NASA Common Research Model (CRM) has been highly optimised by a large team of expert engineers at Boeing. Consequently these designs cannot expect to achieve the same drag standard, but need to weaken the shock waves that forms with over and under-wing nacelle configurations. Logic dictates that simply thinning an aerofoil reduces drag,

however, practically, it increases the structural weight. Shape improvements should also consider a sensible range of thickness variations. Therefore, the key consideration in evaluating potential benefits of over and under-wing distributed propulsion concepts are:

- Obtaining a good aerofoil drag standard (indicated by κ_A, see Eq. 2.8) by optimising the aerofoil shape to minimise or eliminate the strength of shock waves;
- Providing Mach flexibility by ensuring that shock strength does not increase significantly off-design which would increase drag and may cause shock-induced separation;
- Controlling the rear adverse pressure gradients to maintain a safe operating margin between cruise and buffet;
- Avoiding "gully" regions that can lead to strong shock waves, and therefore increased drag and possibility of shock-induced separation.

6.1.1 Objective Function

The main objective function of this study is to reduce the drag as well as delay and minimise shock formation by lowering the roof top pressure distribution. This should be at the same lift condition when comparing with a baseline aerofoil. Another objective function is the structural thickness, t_s, defined as the sum of spar thickness at 15% and 75% chord position, which are typically the locations of the front and rear spars of an aerofoil. As has been explained in Section 2.3, reducing the thickness leads to an increase in wing structural weight. It is desirable to increase or maintain the same thickness while minimising aerodynamic drag. The third objective function is to improve the buffet performance by exploring the "flow-entrainment" benefit by aft-embedded distributed propulsion systems to delay buffet at high C_L conditions.

6.1.2 Aerofoil parametrisation and Design of Experiments

Identifying an optimum transonic aerofoil design involves a number of parameters, including the thickness, camber, leading edge radius, etc. Each parameter has its own impact in aerodynamic performance. As a result of Section 3.2, the CST method (Kulfan, 2007) is selected in this study. To fit the baseline transformed aerofoil from the NASA CRM, Matlab scripts were used to derive a set of coefficients to represent the upper and lower surfaces. Based on analysis by Zhu and Qin (2014), a total of 16 CST coefficients (8 for each surface) are used for aerofoil fitting and modification to

ensure the accuracy and complexity of controlling aerofoil parameters. An exception to this is the first sensitivity study using 20 CST coefficients (10 for each surface) for a comprehensive overview of how each coefficient controls the aerofoil shape.

As discussed in Section 3.3, this study employs an Optimal Latin Hypercube (OLH) Design of Experiments (DoE) (Narayanan et al., 2007) to fill the parameter space with adequate selection of aerofoil designs using the combinations of CST coefficients fitting the baseline aerofoil. In order to control the design space and reduce the computational cost, 4 out of 8 coefficients on each surface are sampled, which produces 40 design points for each analysis. Note that this number comes from the generally accepted rule that a design space should have 10D designs, where D is the number of dimensions (in this case, four) (Narayanan et al., 2007). There is no illustration of 40 DoE points filling the parameter space due to the difficulty to create a four-dimensional plot.

6.1.3 Simulation Framework

As shown in Figure 6.1, Star CCM+ provides all essential elements to conduct the aerofoil performance improvement study (i.e. mesh generator, solver, automation of simulation with the aid of Java). Matlab scripts are used to obtain the CST coefficients from the original aerofoil and produce the new sets of CST coefficients for each DoE points. Once all simulations are completed, the objective functions are analysed in Microsoft Excel to find improved design points based on the degrees of reducing drag and structural weight. To validate this framework, a sensitivity study involving the variation of single CST coefficients is implemented, which will be presented in Section 6.2.1.

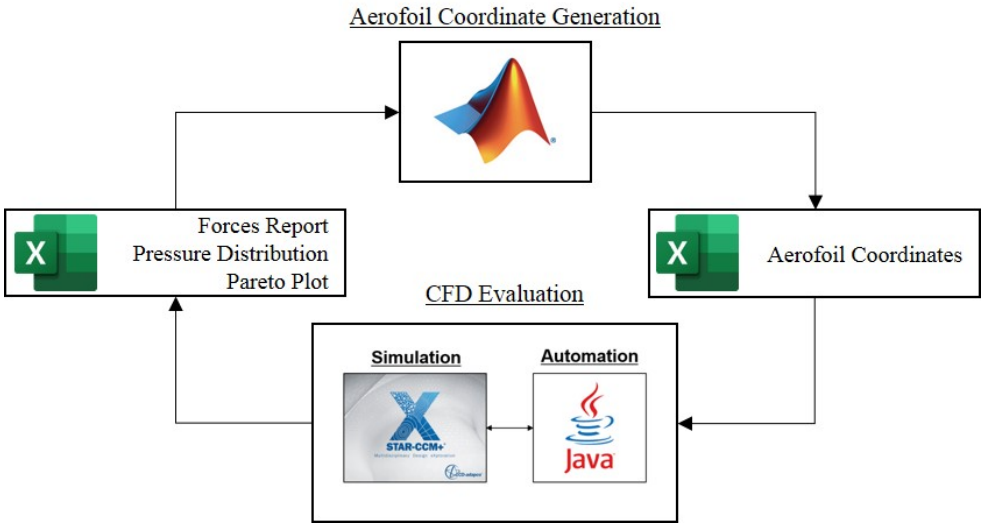

Figure 6.1: Framework of the aerofoil performance improvement study.

6.2 Aerofoil Sensitivity and Parametric Study

This aerofoil sensitivity and parametric study consists of two separate paths by modifying CST coefficients on both upper and lower surfaces for both over and under-wing nacelle configurations. Figure 6.2 shows examples of two-dimensional meshes of both configurations. In the first sensitivity study, only an individual coefficient will be modified at one time to find out the aerodynamic impact of each single CST coefficient, as well as to validate the simulation framework presented in Figure 6.1. The second and third studies demonstrate the suitability of using an OLH DoE to generate 40 aerofoil designs for each design iteration. Also the use of iterative analysis with both over and under-wing nacelle configurations demonstrate potential benefits in order to determine an improved design direction. After the analysis and comparison between results from OWN and UWN studies, an improved aerofoil with better aerodynamic potential will be studied and focused on improving the buffet margin.

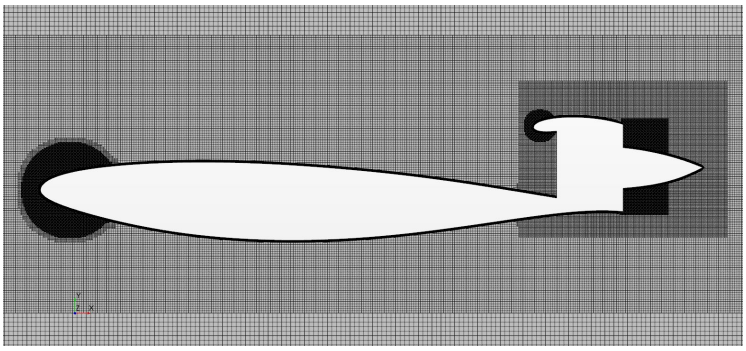

(a) Over-Wing Nacelle

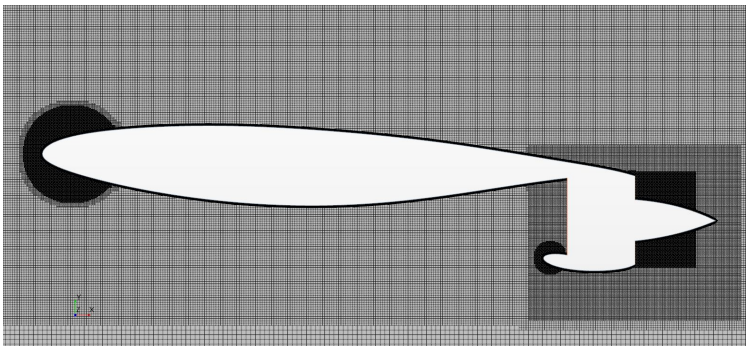

(b) Under-Wing Nacelle

Figure 6.2: Figures showing the two-dimensional meshes for (a) OWN and (b) UWN configurations.

The ambient conditions, simulating a flight altitude of 10 km and Re=75 million, are set as shown below in Table 6.1, which is identical to the flow conditions determined in Chapter 5. Similarly, because this CFD study relies on two-dimensional simulation, the freestream Mach number is set to 0.725, which is equivalent to the

three-dimensional designed Mach number for the NASA Common Research Model of Mach=0.85 due to sweep effect, sweep angle=31.5° (NASA, 2020). The static pressure, static temperature, and air density are determined from isentropic relationships, using the same method outlined in Section 5.1.1.

Freestream Velocity	Static Pressure	Static Temperature	Air Density
0.725 Mach	26436.86 Pa	223.15 K	0.413 kg/m^3

Table 6.1: Table showing the ambient conditions for sensitivity and parametric studies.

Automatic aerofoil generation and C_L matching scripts are employed for the following sensitivity and parametric studies as explained in Section 6.1.3. The Matlab script (Appendix A) for aerofoil generation produces and exports aerofoil coordinates into Star CCM+ by importing the CST coefficients generated by the OLH DoE. Then, the C_L matching Macro script (Appendix B) in Star CCM+ automatically implements geometry creation, mesh generation and boundary condition set-up for imported aerofoil coordinates. It also automatically matches the C_L (fixed at $C_{L_{2D}} = 0.5 \pm 0.25\%$) by extrapolating an angle of attack (AoA) after running two AoAs and obtaining each C_L value. Finally, the script implements simple post-processing, including forces reports, pressure distribution plot, and shock strength (ΔC_P) and position analysis (Georgala, 2002).

6.2.1 Single CST Coefficient Sensitivity Study

This sensitivity study focuses on the general trend of aerodynamic drag and structural thickness by either increasing or decreasing a single CST coefficient out of a set of 20 with a variation of 5% to see an overview of the effect of changing individual coefficients. It aims to validate the framework and identify if any single coefficient potentially influences drag reduction and structural thickness increases. Additionally, through this sensitivity study, the effect of each CST coefficient on aerofoil shape can be understood.

Figure 6.3 shows the distribution of 40 aerofoil samples, modified from the original baseline aerofoil, displayed as coefficient of drag, C_D, against structural thickness, t_s. Clearly, after the first iteration, the U5+5% design point (the 5^{th} coefficient on the upper surface increased by 5%, shortly as U5+5%) is a promising design point as it is the second best in terms of drag reduction and slightly increases the thickness. The U1-5% has the lowest drag, however, it significantly reduces the thickness, which increases the structural weight, therefore, it is not considered as a promising

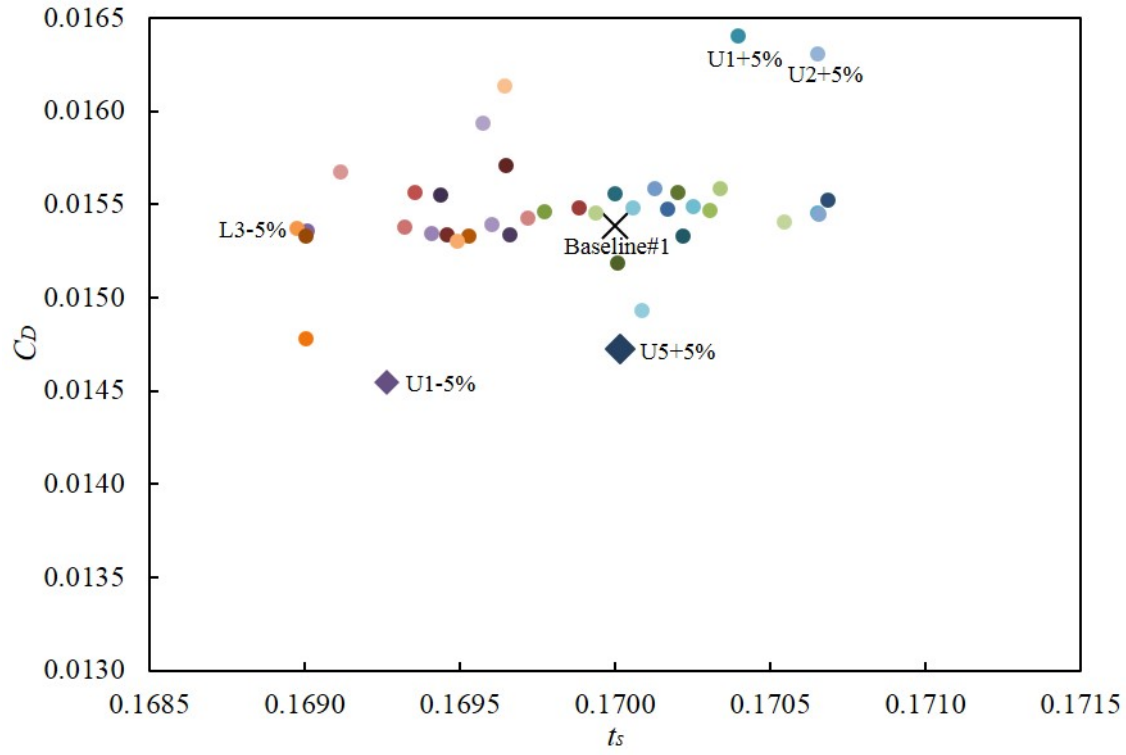

Figure 6.3: Plot showing the distribution of all design points for OWN single CST coefficient sensitivity study after the 1^{st} design iteration.

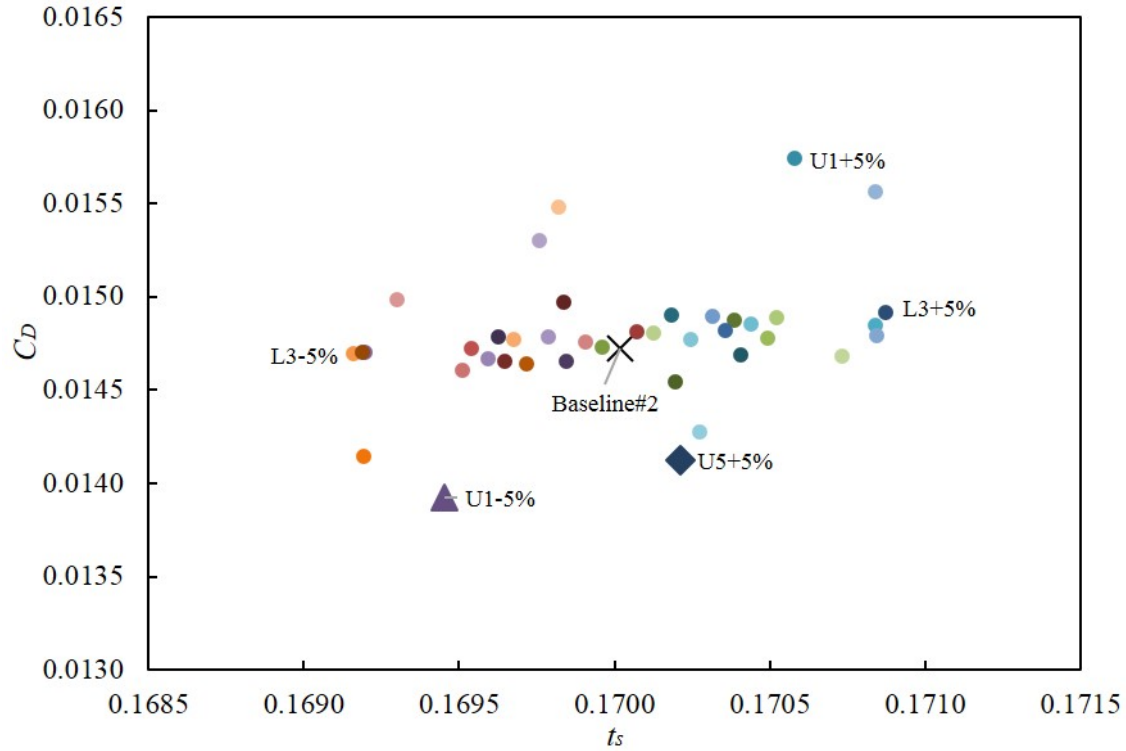

Figure 6.4: Plot showing the distribution of all design points for OWN single CST coefficient sensitivity study after the 2^{nd} design iteration.

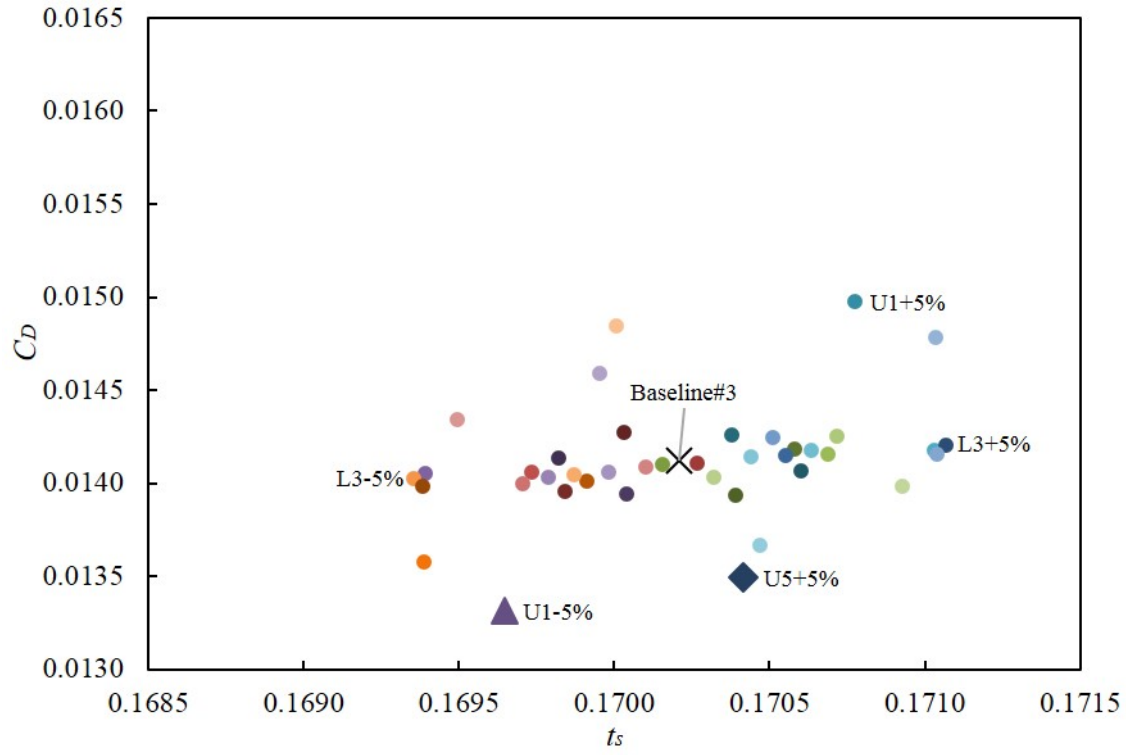

Figure 6.5: Plot showing the distribution of all design points for OWN single CST coefficient sensitivity study after the 3^{rd} design iteration.

design point. The second iteration uses U5+5% from first iteration as the new baseline aerofoil, repeating the same procedures gives the same result as a 5% increase on U5 coefficient continues to produce the best aerofoil design considering the drag reduction and thickness increase, see Fig. 6.4. The third iteration, using the U5+5% from the second iteration, proves that U5+5% is still the most appropriate single coefficient for further iterations, see Fig. 6.5.

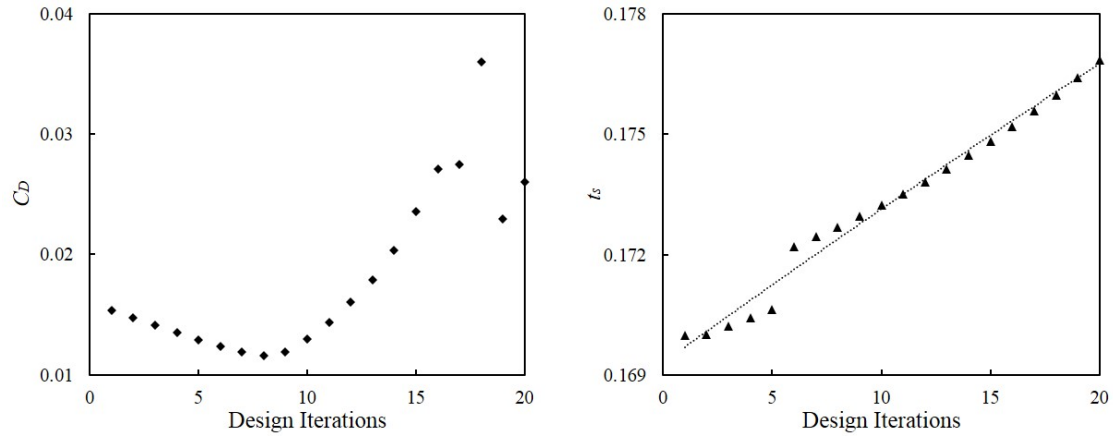

(a) (b)

Figure 6.6: Plot showing the variation of (a) drag coefficient and (b) structural thickness for all 20 design iterations (baseline aerofoil included as the first point).

After three iterations, the most promising single coefficient (the 5^{th} on the upper surface, shortly as U5) has been identified, thus, a total of twenty iterations have been repeated on U5. However, the benefits in drag reduction ends after 7 iterations while structural thickness constantly increases despite a sudden increase between the 5^{th} and 6^{th} iterations, see Fig. 6.6.

Figure 6.7 shows an overview of the parametric study after 7 iterations as no further drag benefits were seen thereafter. It can be seen that drag reduction and structural thickness changes are predicted for the first 4 iterations. However, a sudden increment of structural thickness occurs at the 5^{th} iteration, while the drag reduction still remains proportional.

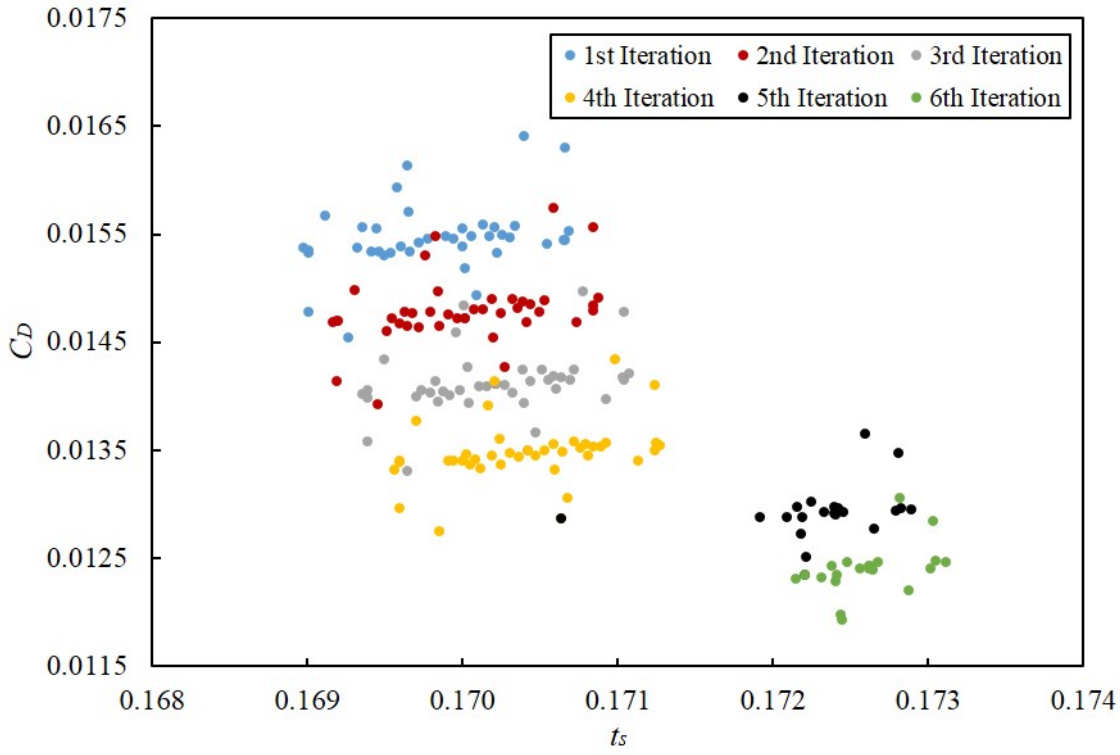

Figure 6.7: Plot showing an overview of single CST coefficient sensitivity analysis after 6 iterations.

As the drag reduction ends at the seventh iteration, analysing velocity contours and pressure distributions gives more insight into why this happens. Figure 6.8 shows the velocity contours for the seventh and later designs, where strong shock waves (and even secondary shocks) and shock-induced separation, start to form before the fan as the shape of upper surface changes. Focusing on the aerofoil shape, the U5 coefficient only affects the location at around 50% chord, which indicates limited control over one region of the aerofoil. For example, the U5 controls the shape at approximately 50% chord upper surface, and L1 (the 1^{st} on the lower surface) controls the shape at 10% chord lower surface based on a total of 20 CST

coefficients representing an aerofoil.

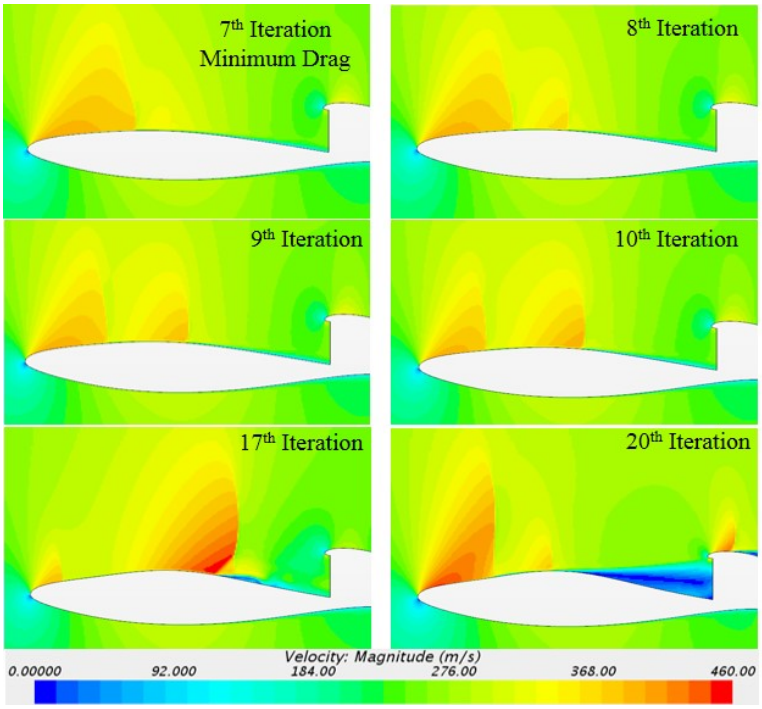

Figure 6.8: Velocity magnitude contour plots for U5 coefficient at 7^{th} (minimum drag), 8^{th}, 9^{th}, 10^{th}, 17^{th}, and 20^{th} iterations.

Figure 6.9 shows the pressure distributions of the baseline aerofoil and some meaningful designs. The benefits of reducing the shock strength can be observed as the roof-top has been lowered, while a more gradual pressure recovery also compensates the loss of lift by lowering the roof-top. Through this sensitivity study, the research outcomes are summarised below:

- Each CST coefficient controls the aerofoil shape only at certain locations, for example, the upper 1^{st} coefficient only influences the very front part of the upper surface.
- The middle CST coefficients provide more promising results rather than the front and rear coefficients, which is important to consider the trade-off of the number of CST coefficients used in a later DoE.
- The upper surface coefficients have more impact than lower surface coefficients in OWN configurations which is expected and explained in Section 2.3.
- The simulation framework shows promise, and it can be implemented for further sensitivity and parametric studies with OWN and UWN configurations.
- This single CST coefficient sensitivity study provides a new baseline aerofoil (at the 7^{th} iteration) for the following OWN study. While the UWN study will start with the original baseline aerofoil as the benefits achieved by modifying the upper surface is not convincingly transferable to the UWN configuration.

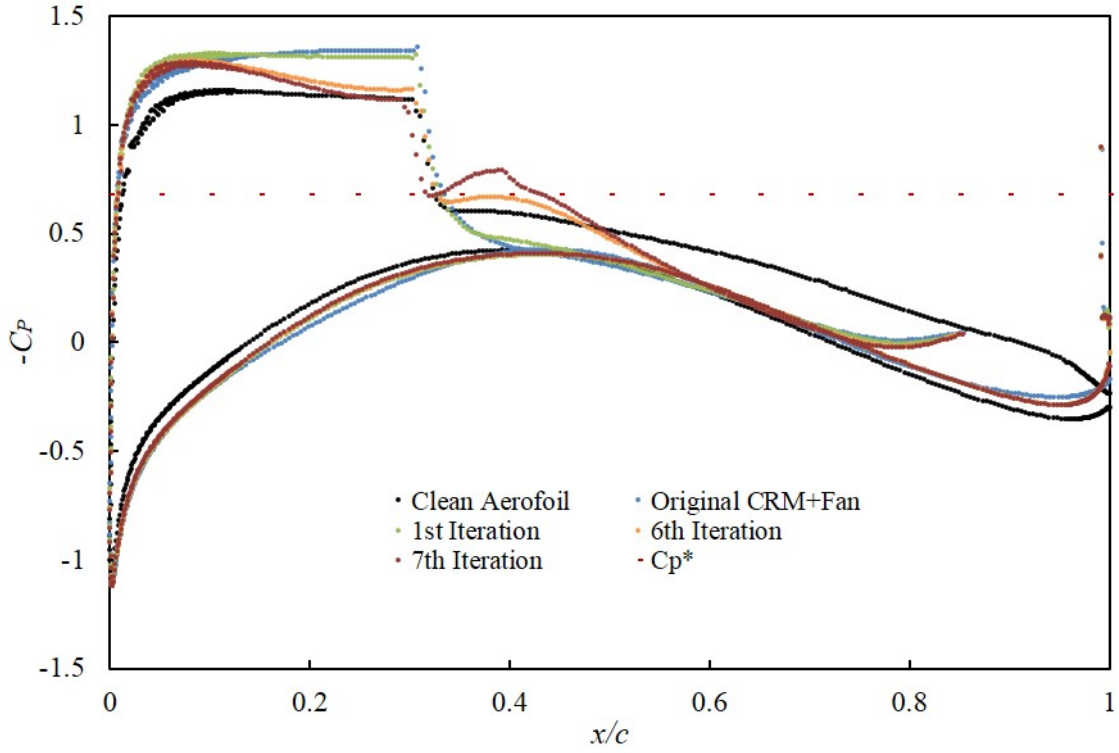

Figure 6.9: Plot showing pressure distribution comparison of original aerofoil, powered original aerofoil, and aerofoil designs after 1^{th}, 6^{th}, and 7^{th} iterations.

6.2.2 OWN Sensitivity and Parametric Study

In this study, a set of 16 CST coefficients (8 coefficients per surface) is employed. In order to control the design space, only the middle four coefficients on either upper or lower surfaces are randomly sampled and adopted in an OLH DoE to obtain a 40-point design space for aerodynamic analysis, based on the research outcomes from the first sensitivity study. Firstly, a sensitivity study is conducted for the OWN configuration. Figure 6.10 shows an overview of drag reduction and thickness variation by varying coefficients by 5%, 10% and 20%, where ranges of variables are -5% to +5%, -10% to +10%, and -20% to +20% respectively (detailed values can be found in Appendix C). Figures 6.11 - 6.13 show the detailed results for each cases, as each point (named from D1 to D40) represents a design point generated by the OLH DoE.

By analysing Figures 6.10 - 6.13, it can be seen that the results are scalable. After considering the extent of drag reduction and thickness increase, the 10% variation is promising because it is more sensitive than the 5% variation and has more precise control than the larger 20% variation. As this sensitivity study suggests, the scalability of applying a DoE to the parametric study allows a new DoE to be used for the OWN configuration, using the best design point (D29) from the 10% study,

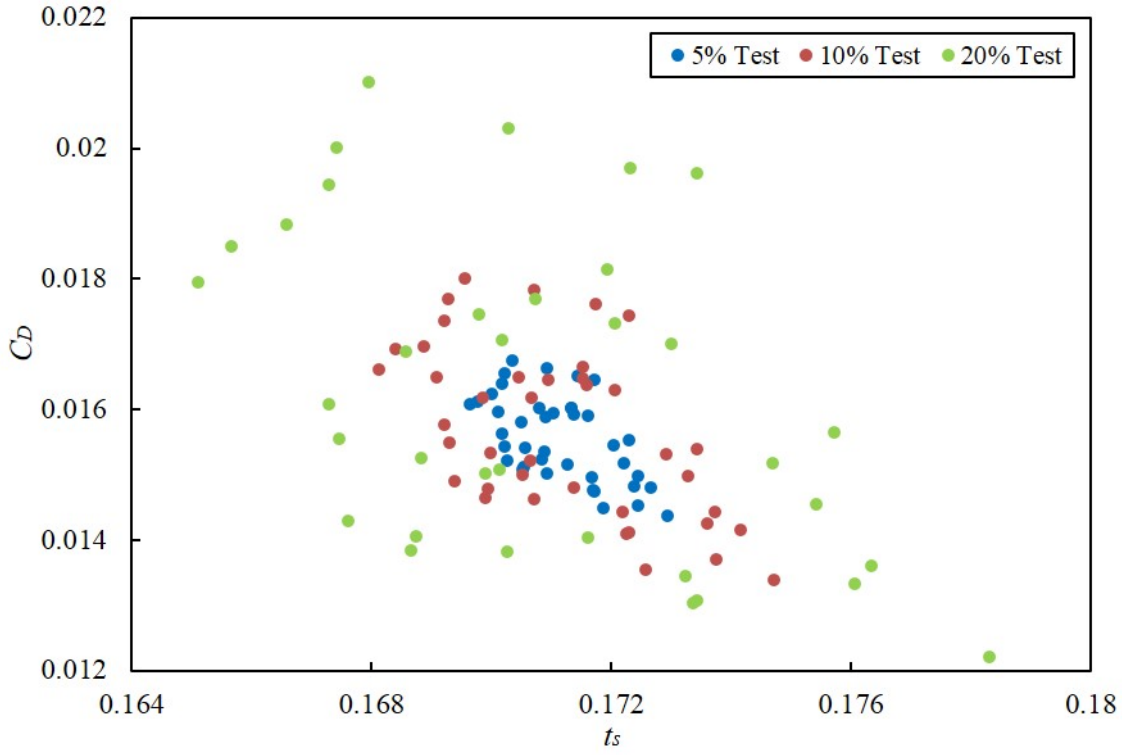

Figure 6.10: Plot showing an overview of distributions of 40 design points with 5%, 10% and 20% variations in coefficients determined by the DoEs.

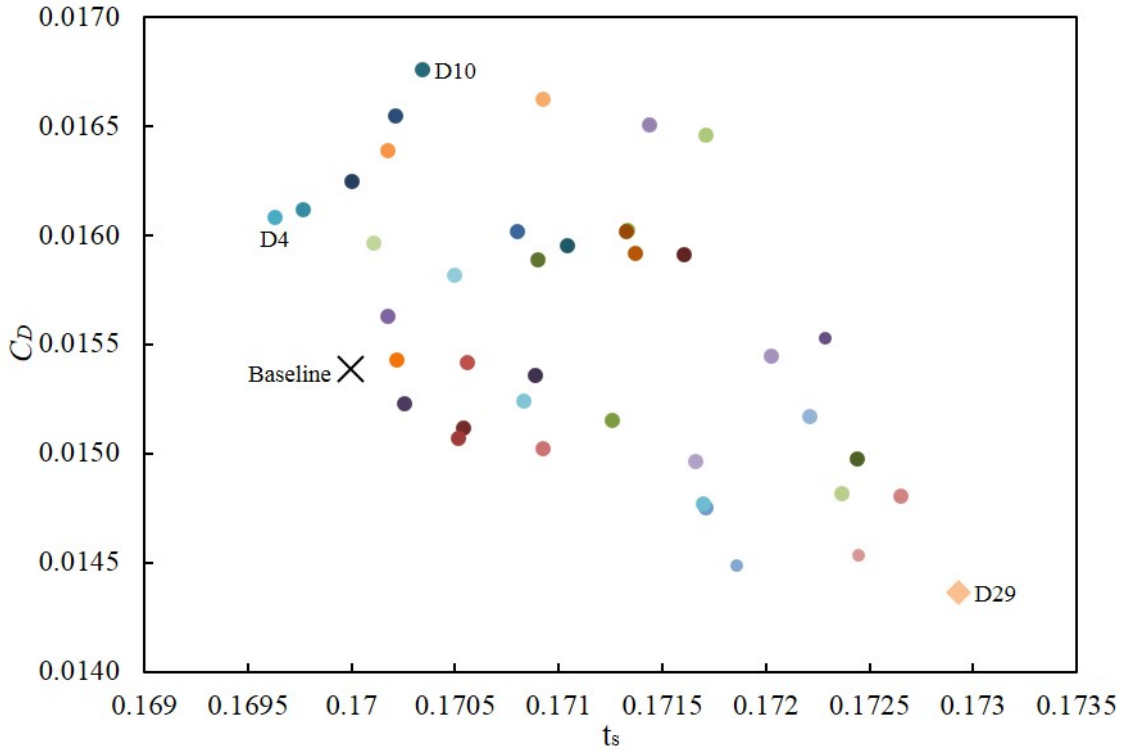

Figure 6.11: Plot showing the distribution of 40 design points for 5% coefficient variations displayed by drag coefficient against structural thickness.

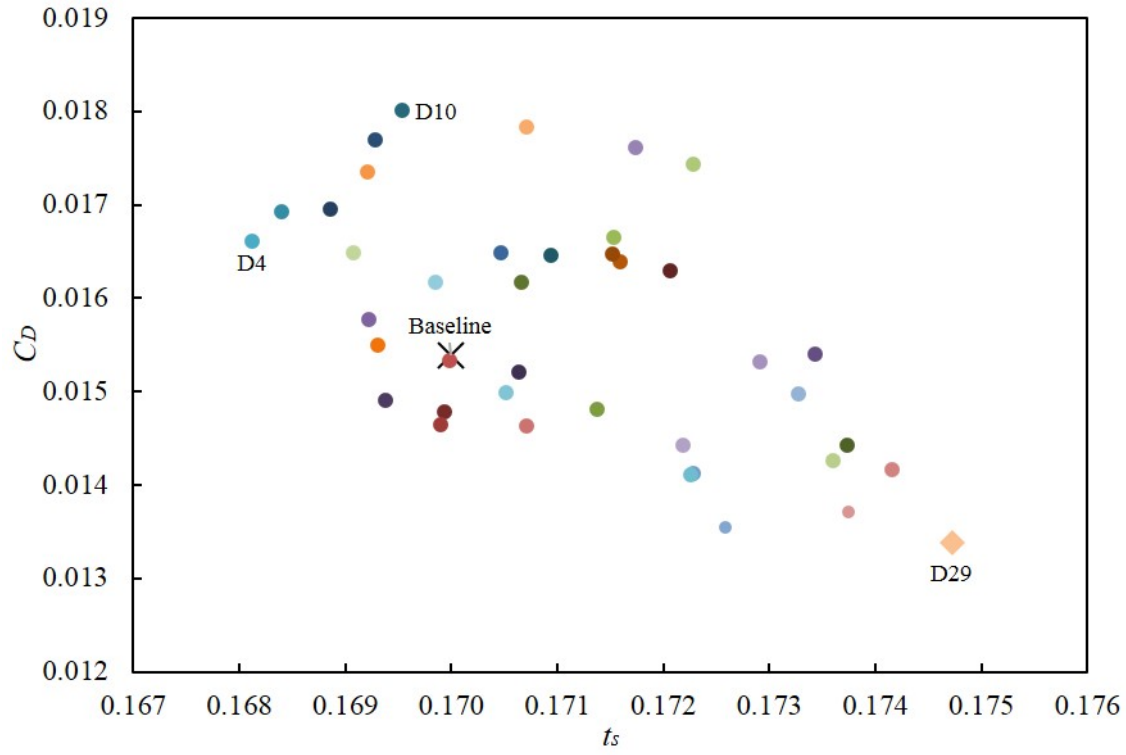

Figure 6.12: Plot showing the distribution of 40 design points in 10% coefficient variations displayed by drag coefficient against structural thickness.

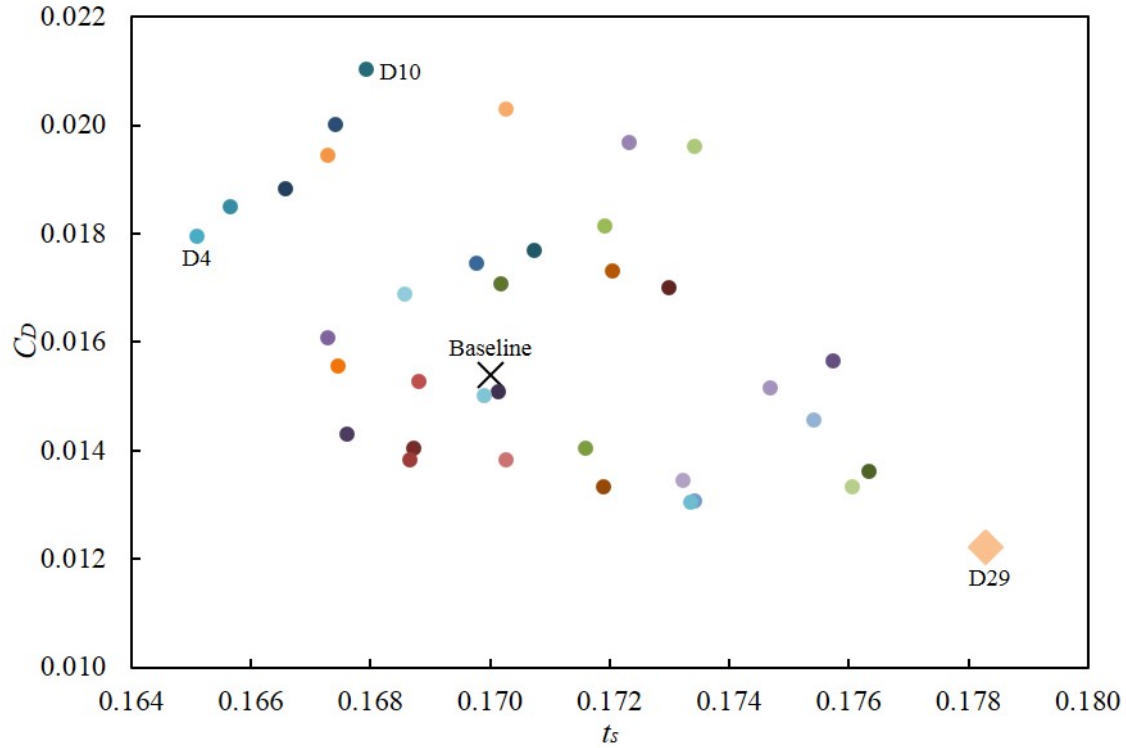

Figure 6.13: Plot showing the distribution of 40 design points in 20% coefficient variations displayed by drag coefficient against structural thickness.

as the new baseline.

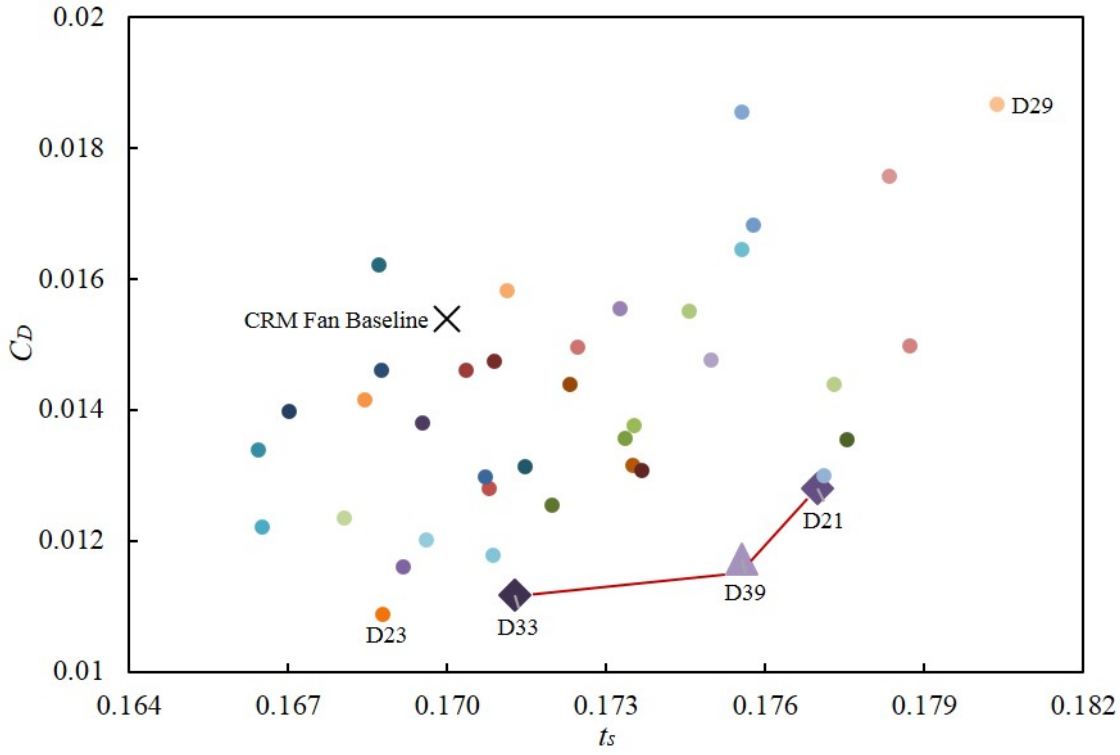

Figure 6.14: "Reversed" Pareto plot showing the CFD results from the OWN configuration on the upper surface from the DoE on the new baseline (D29).

Figure 6.14 shows the distribution of all 40 design points by conducting the DoE on the upper surface of the new baseline aerofoil (D29) for the OWN configuration. Considering the objective functions, there are three promising design points (D33, D39, and D21), which can be spotted in this "reversed" Pareto front. Figure 6.15 shows the comparison of velocity contours between those design points and the clean baseline aerofoil. It can be observed that a secondary shock forms in D21 and D39, while D33 does not show this sign but a secondary shock is potentially possible, which explains why D33 has the minimum drag.

In Figure 6.16, 6.17, and 6.18, the pressure distributions are presented separately for a clearer comparison with the clean original CRM aerofoil, original powered OWN CRM aerofoil, and the powered OWN baseline aerofoil. It can be seen that all three design points lower the roof-top, with evidence of reduced shock strength, compared with the powered original aerofoil, see Figs 6.16 - 6.18. Whilst D33, the minimum drag design, delays the primary shock, with an indication of secondary shock at 40% chord, it loses some lift during the pressure recovery. The D39 design also slightly delays the shock, Figure 6.17, while losing lift which is similar to D33. The D21 design, lowest drag reduction of all three designs, actually brings the shock forward, however, it has a less steep adverse pressure gradient to compensate for the lost lift.

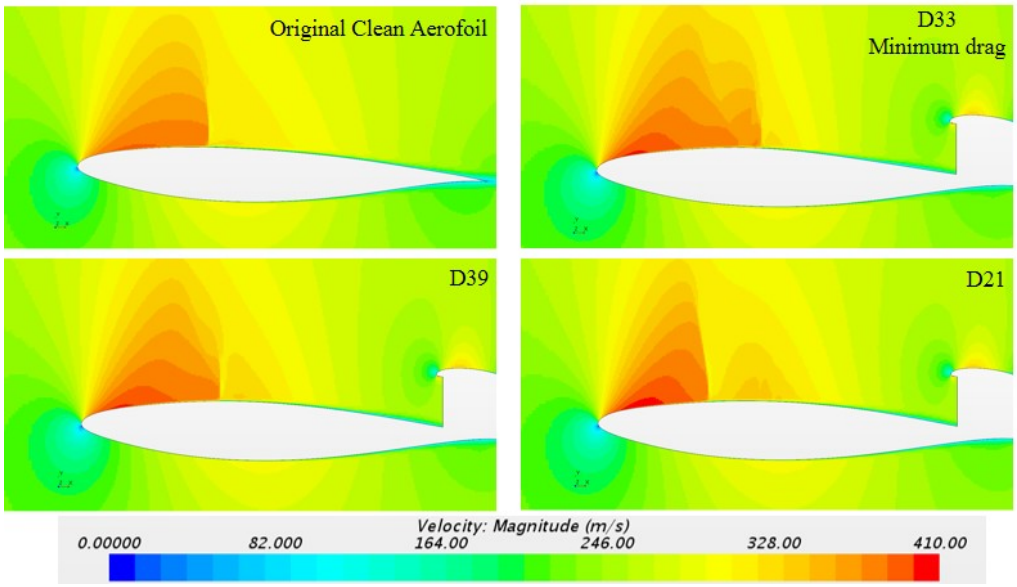

Figure 6.15: Velocity magnitude contour plots for clean baseline aerofoil, D33, D39, and D21.

Additionally, all OWN cases have reduced rear loading compared with the clean aerofoil, due to the acceleration of flow by the powered nacelle.

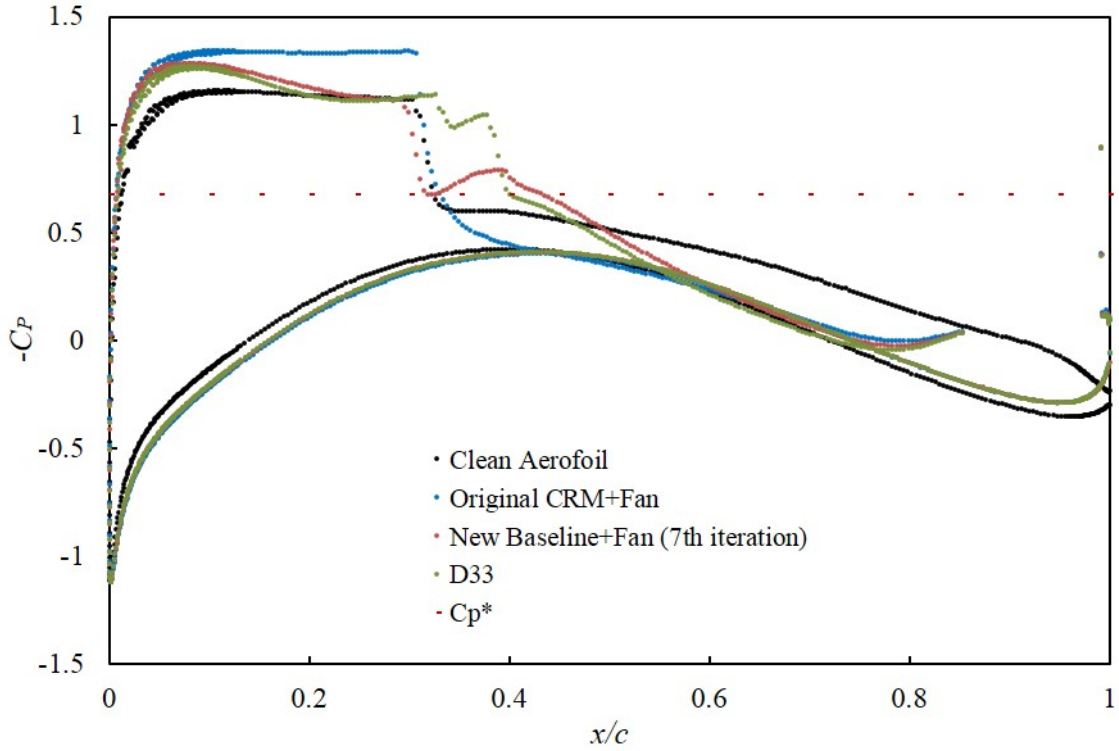

Figure 6.16: Plot showing the pressure distribution comparison between the D33 and the baseline aerofoils.

Once the design study on the upper surface is complete, the parametric study is extended to the lower surface. Accordingly, Figure 6.19 shows the distribution

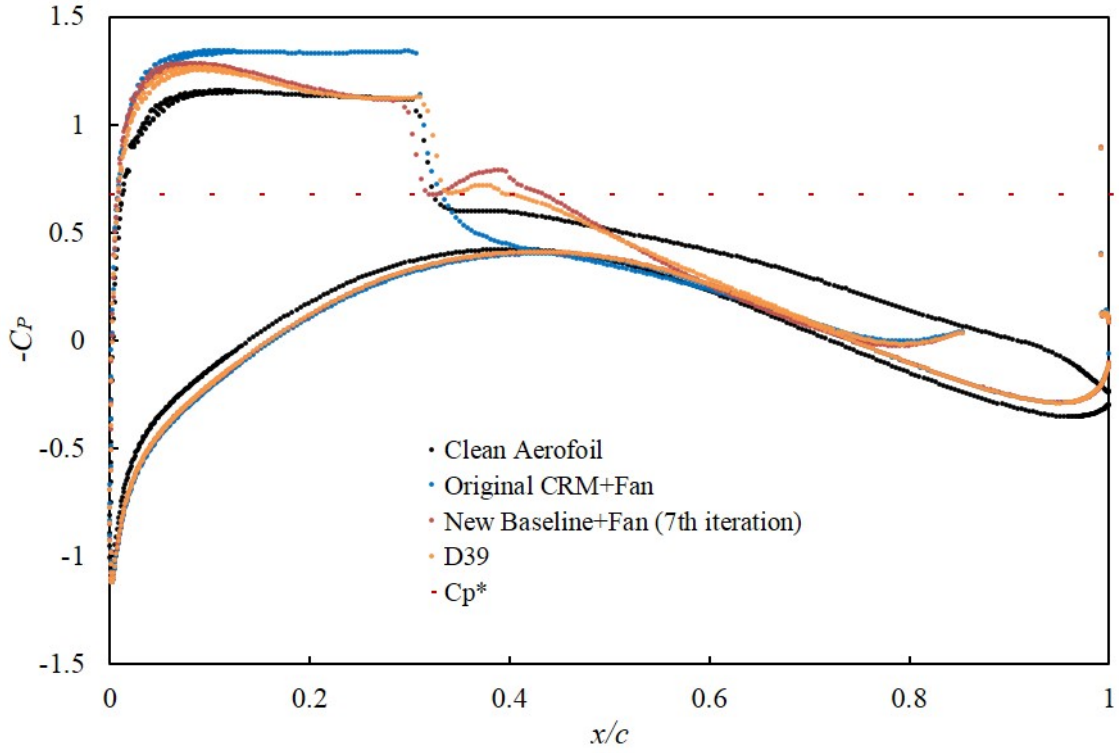

Figure 6.17: Plot showing the pressure distribution comparison between the D39 and the baseline aerofoils.

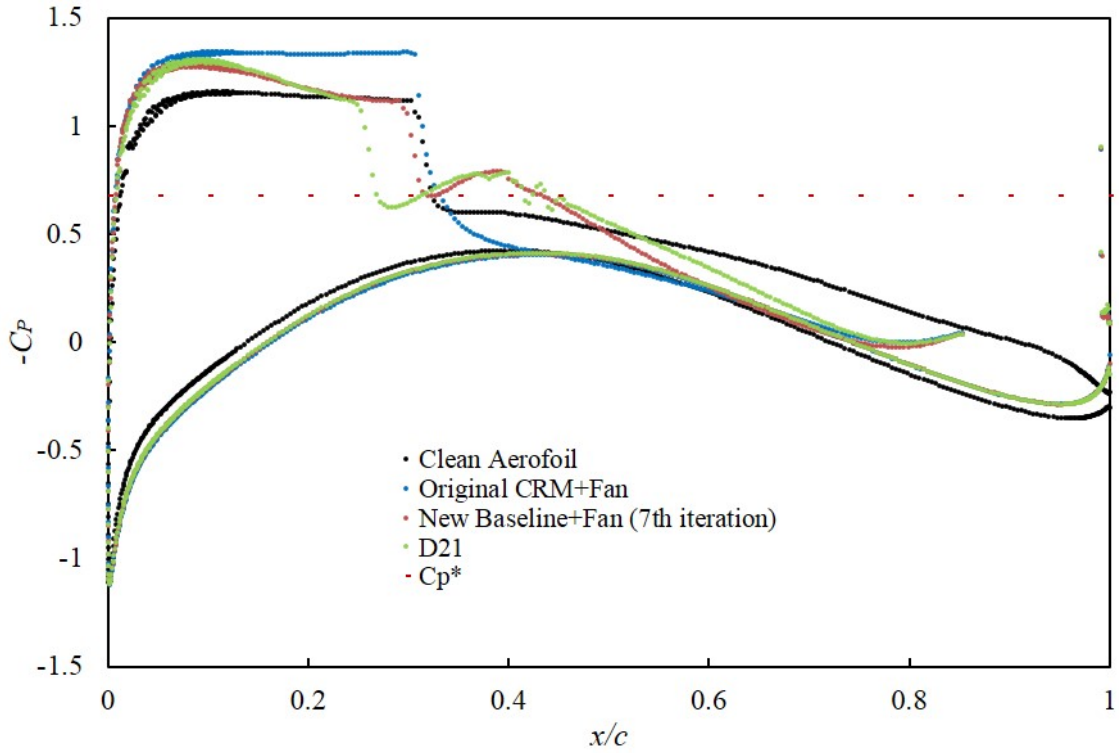

Figure 6.18: Plot showing the pressure distribution comparison between the D21 and the baseline aerofoils.

of 40 design points by re-sampling the lower surface of the aerofoil for the OWN configuration. Interestingly, the result presents a simple trend of aerofoil design, as thinning the aerofoil reduces the drag. Additionally, the drag reduction achieved is much less than the results on the upper surface. Therefore, it is unnecessary to discuss the results of the OWN for lower surface, because no obvious benefits are seen.

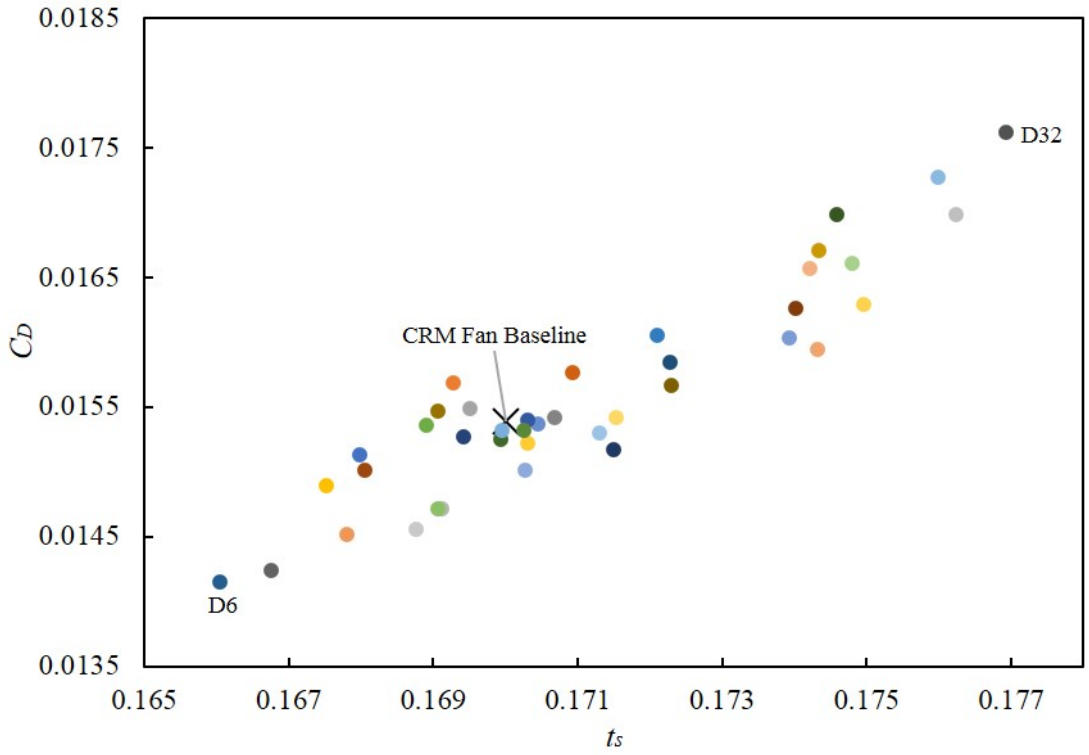

Figure 6.19: The Pareto plot of the OWN configuration for lower surface aerofoil changes.

Through this sensitivity and parametric study on the OWN configuration, research outcomes are summarised below:

- DoE is applicable in this sensitivity and parametric study.
- The CFD results are scalable through different percentage variations in coefficients which determine aerofoil shape.
- It is impossible to achieve a shock-free aerofoil design with the OWN configuration, based on the design changes used.
- As explained in Section 2.3.5.1, the drag reduction is relatively small unless a more comprehensive shape optimisation can be conducted to deal with the shock on the upper surface.
- All three promising aerofoil designs from the OWN configuration show some evidence of drag reduction, however, it is necessary to conduct an UWN study

to evaluate this configuration as well.

- The rear loading of all OWN cases are limited which is not in favour of minimising the risk of boundary layer separation for higher C_L conditions.

6.2.3 UWN Sensitivity and Parametric Study

Based on the results from the OWN parametric study (and indeed the baseline aerofoil), a reasonably strong shock exists on the upper surface that is weakened by the OWN parametric study but not eliminated, that deteriorates the aerodynamic performance, as explained in Section 2.3. As the UWN is less sensitive than OWN in terms of shock formation on upper surface, it is worth implementing another sensitivity and parametric study on the UWN configuration. As before, a sensitivity study is carried out on the upper surface. Figure 6.20 shows an overview of the 10% and 20% aerofoil parameter variations for the UWN configuration and Figure 6.21 and 6.22 present the details of distributions of all 40 design points in each sensitivity study.

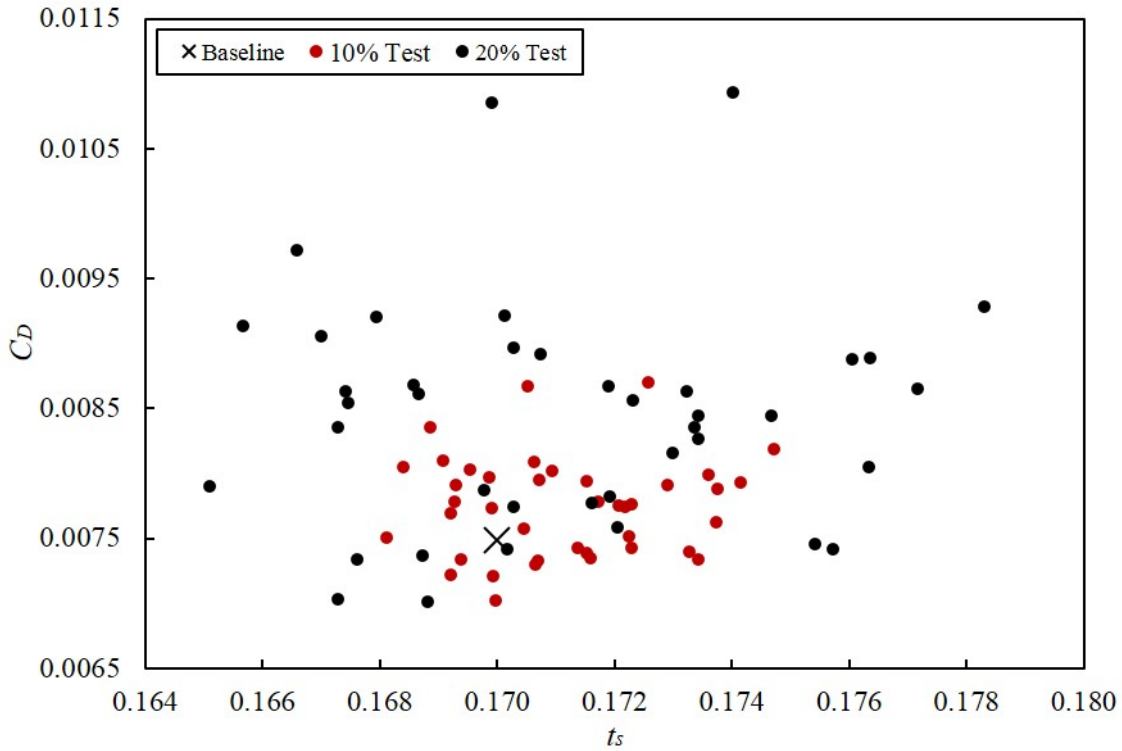

Figure 6.20: Plot showing the general overview of all design points with 10% and 20% variations in coefficient variations for the UWN configuration.

Similar to the sensitivity study on the OWN configuration, the pattern of results is also repeatable for the UWN configuration, and a 10% variation is sensible for the following parametric study. By analysing Figure 6.21, the D1 design is seen to

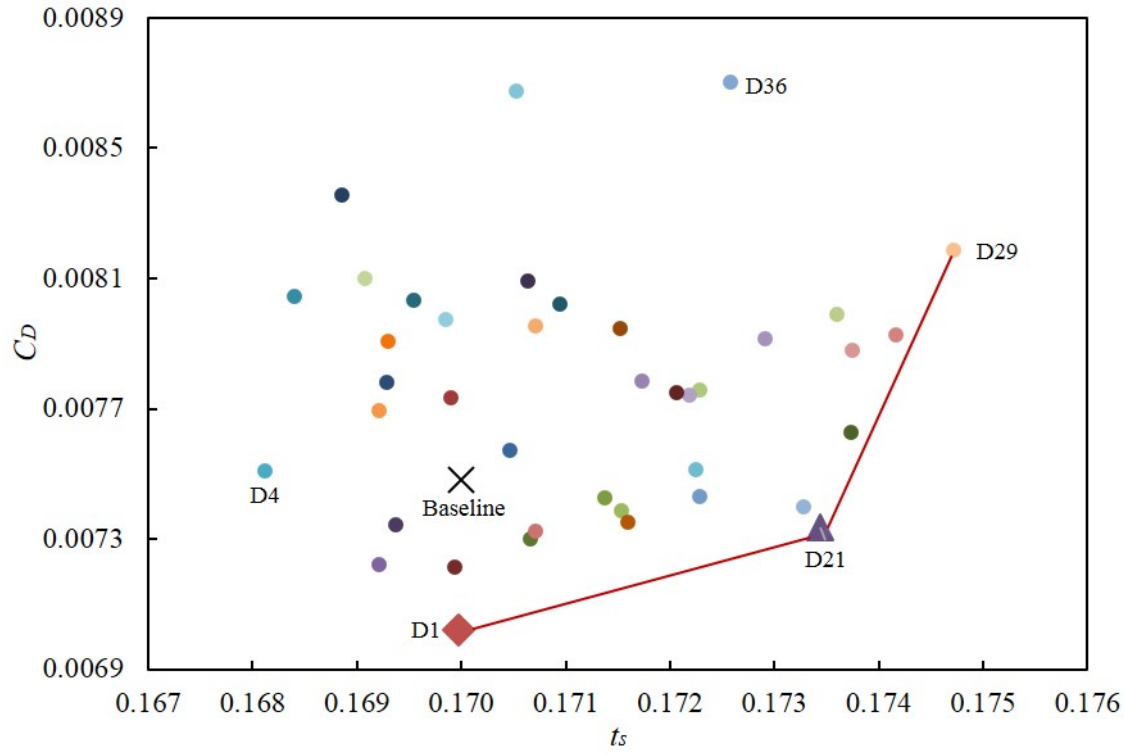

Figure 6.21: 'Reversed' Pareto plot showing the distribution of 40 design points for the 10% aerofoil coefficient variation, displayed by drag coefficient against structural thickness.

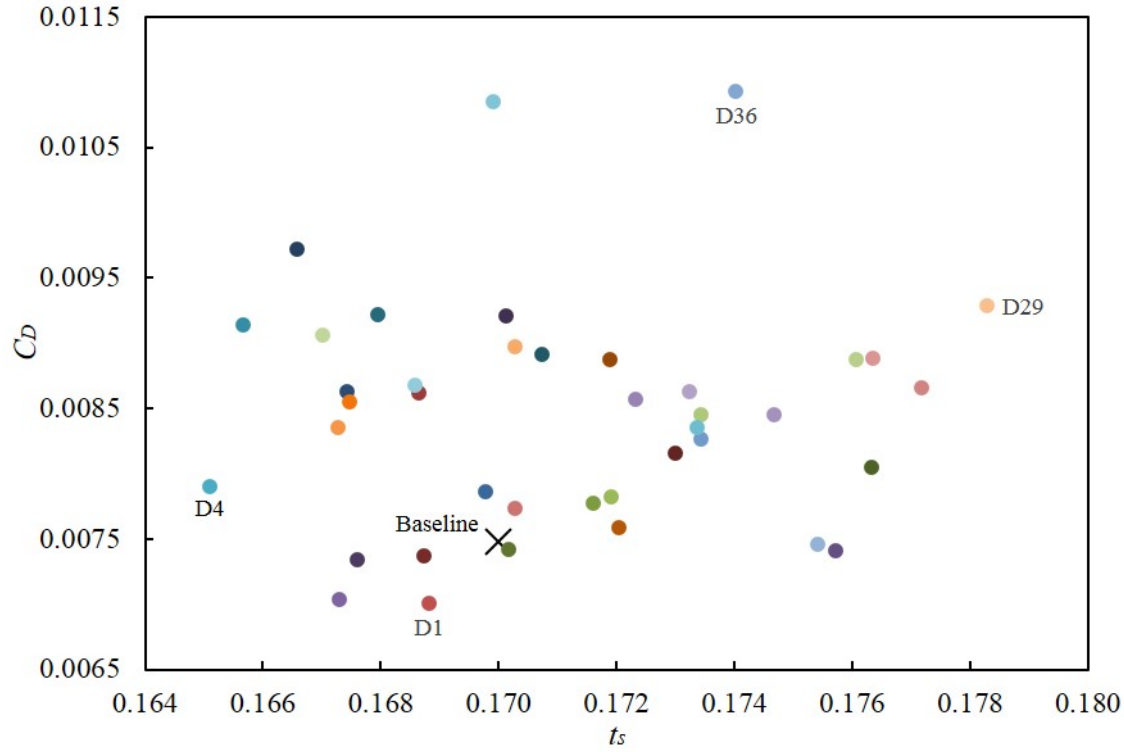

Figure 6.22: Plot showing the distribution of 40 design points with 20% aerofoil coefficient variation, displayed by drag coefficient against structural thickness.

be the best design point despite the fact that it reduces the structural thickness by 0.000118%, which is acceptable considering the significant drag reduction achieved. The D21 design point, another strong candidate, is also selected for further analysis of the pressure distribution, see Fig. 6.23. It can be observed from the pressure distribution plot that the D1 design pushes the suction peak slightly higher than both the powered baseline aerofoil and D21, however, it lowers the roof-top and brings the shock position forwards with a more gradual adverse pressure gradient compared to the powered baseline aerofoil. The D21 design also lowers the roof-top without a higher suction peak, compared to the D1 design, and it brings the shock position further towards the leading edge, however, the lift is compensated during a gradual pressure recovery. Both cases produce a less constrained rear loading compared to the OWN cases, which indicates the potential benefit of suppressed boundary layer separation and a delayed buffet onset.

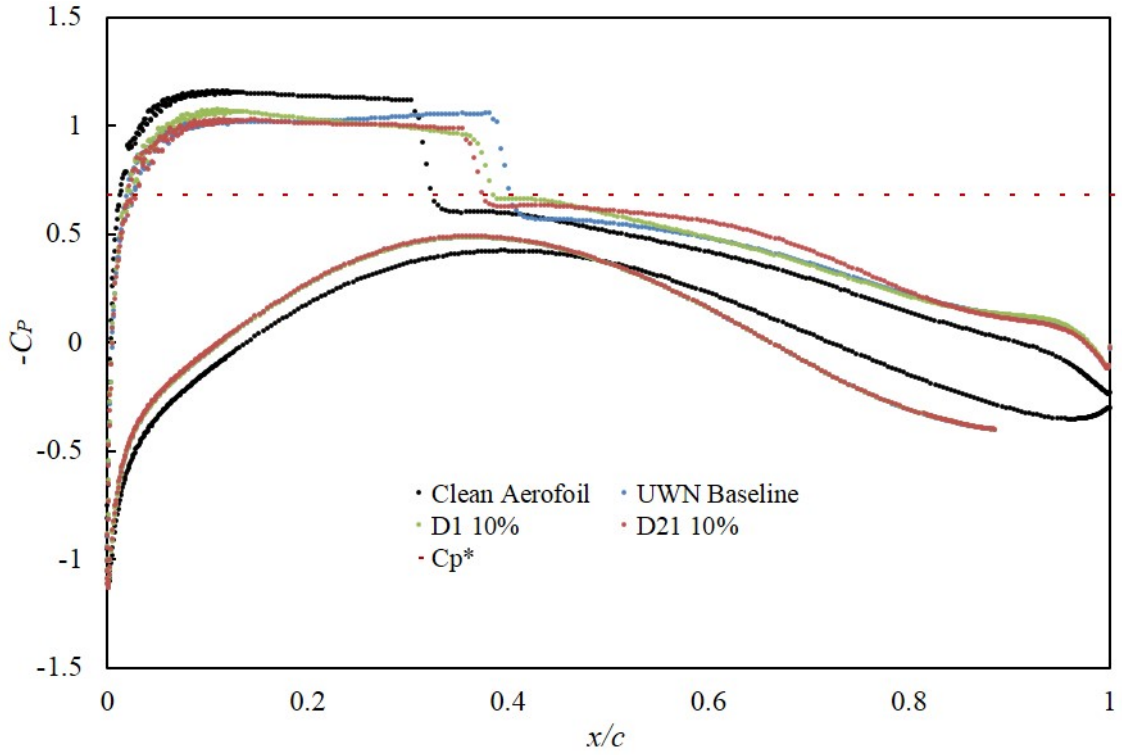

Figure 6.23: Plot showing the pressure distribution comparison between the clean and powered baseline aerofoils, D1 and D21 design points.

The parametric study is also carried out on the lower surface of the baseline aerofoil with a 10% coefficient variation, Figure 6.24 shows a "reversed" Pareto plot of the CFD results while both D26 and D28 design points (highlighted) are selected for pressure distribution analysis, shown in Figure 6.25. It can be seen that the difference between D26 and D28 is subtle in spite of the lowered roof-top, however, the similarity of both designs is that they accelerate the flow between 12% and 35% chord and retard it immediately downstream to make up the lift between 35% and

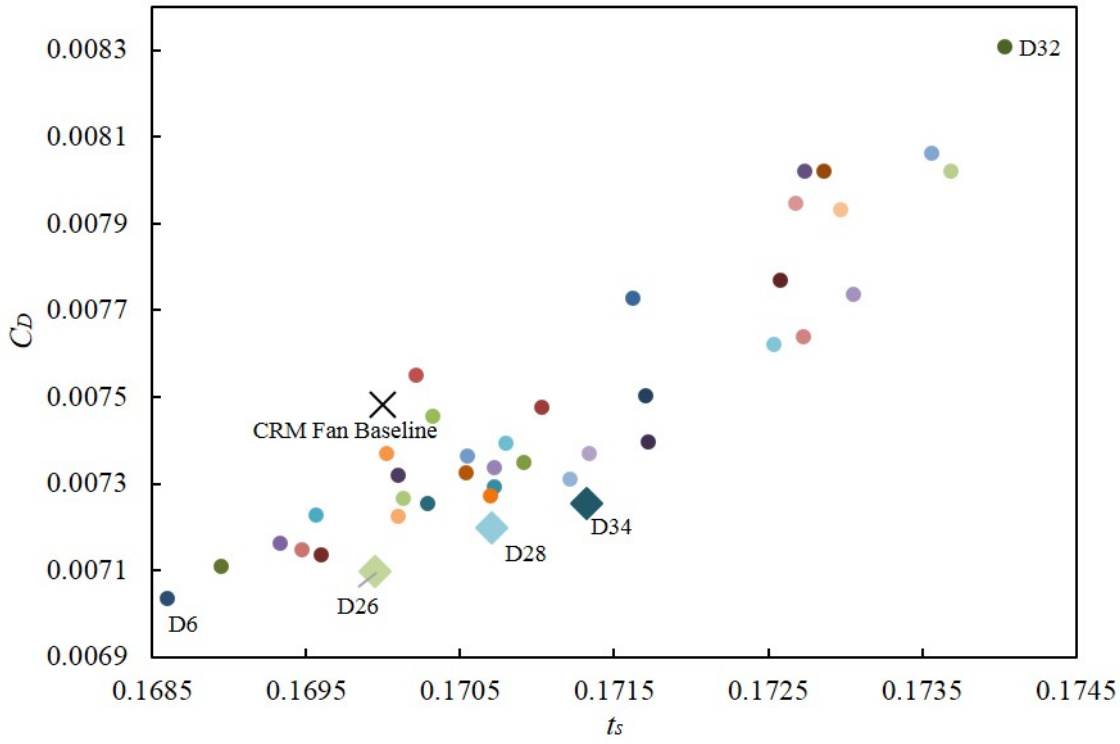

Figure 6.24: "Reversed" Pareto plot showing the distribution of 40 design points for 10% parameter variation on the lower surface of the baseline aerofoil, displayed by drag coefficient against structural thickness

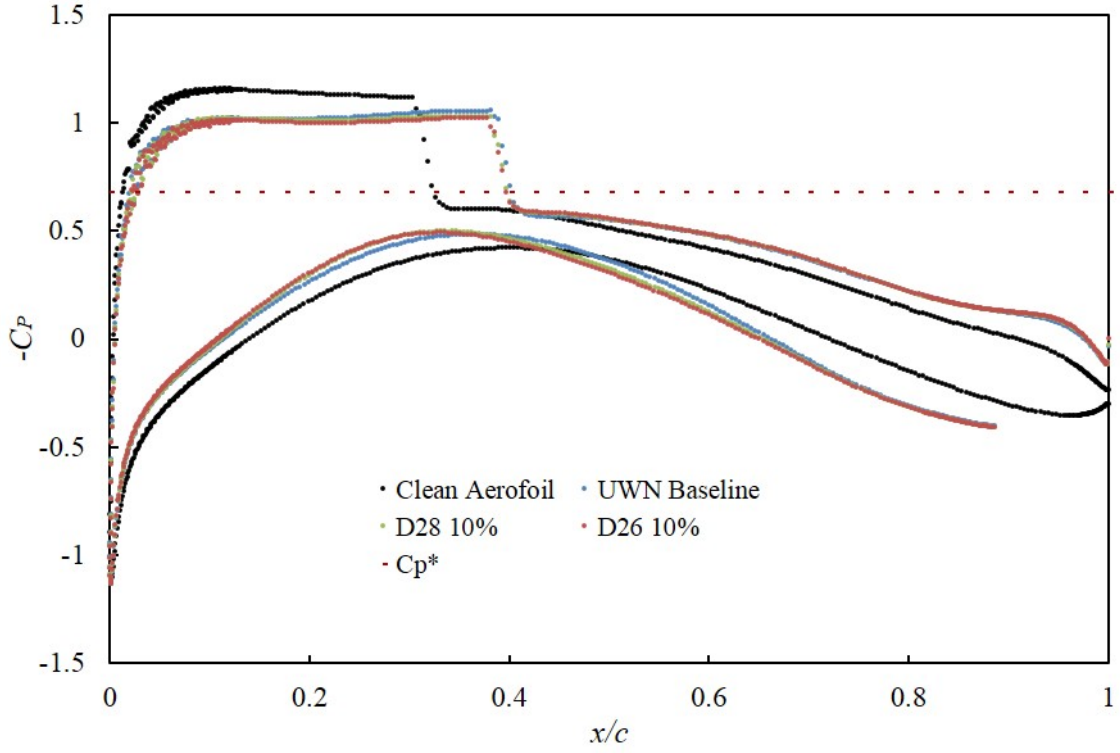

Figure 6.25: Plot showing the pressure distribution comparison between the clean and powered baseline aerofoils, D26 and D28 design points.

70% chord.

After conducting two parametric studies on the upper and lower surfaces of the baseline aerofoil, the D1 design point from the upper surface study has been considered the best design point due to its drag reduction (6.17% drag reduction compared to the baseline aerofoil) and an acceptable decrease in structural thickness (0.01% thickness decrease compared to the baseline aerofoil). The same procedure from Section 6.2.2 has been applied to the D1 design as the new baseline aerofoil. The results of both DoEs are shown in Figure 6.26 and 6.27, and the x and y-axis in both plots use the same scale for clearer comparison.

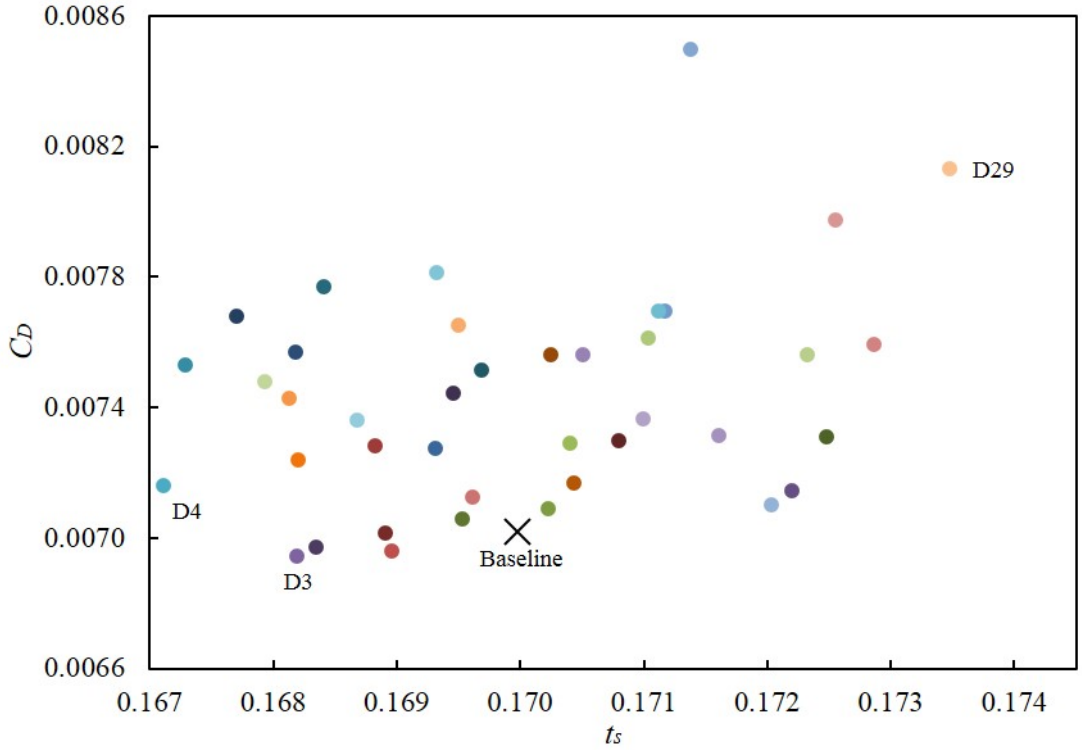

Figure 6.26: Plot showing the DoE results for the UWN configuration on the upper surface for the new baseline (D1).

It is clear that there is no notable design point in Figure 6.26 worth investigating (compared to the baseline), while in Figure 6.27, the D34 design (highlighted) is considered a promising design point despite the relatively small drag reduction and thickness increase improvement. The pressure distribution plot also illustrates the marginal improvement in drag, and a similar effect of manipulating the flow at the lower surface, shown in Figure 6.28.

In Figure 6.29, it can also be seen that the formation of the shock has been delayed with the difference in velocity contours at 40% chord upper surface, which is the aerodynamic evidence to explain the improvement for the same lift condition. Through this sensitivity and parametric study on the UWN configuration, research

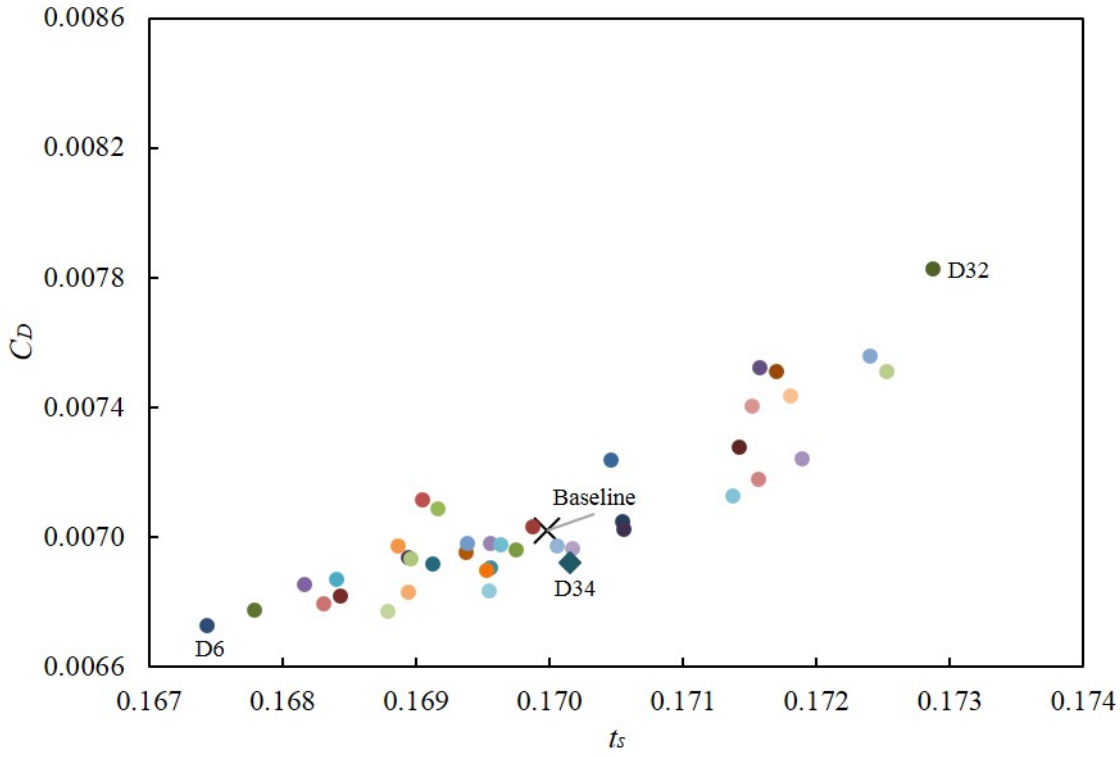

Figure 6.27: Plot showing the DoE results for the UWN configuration on the lower surface for the new baseline (D1).

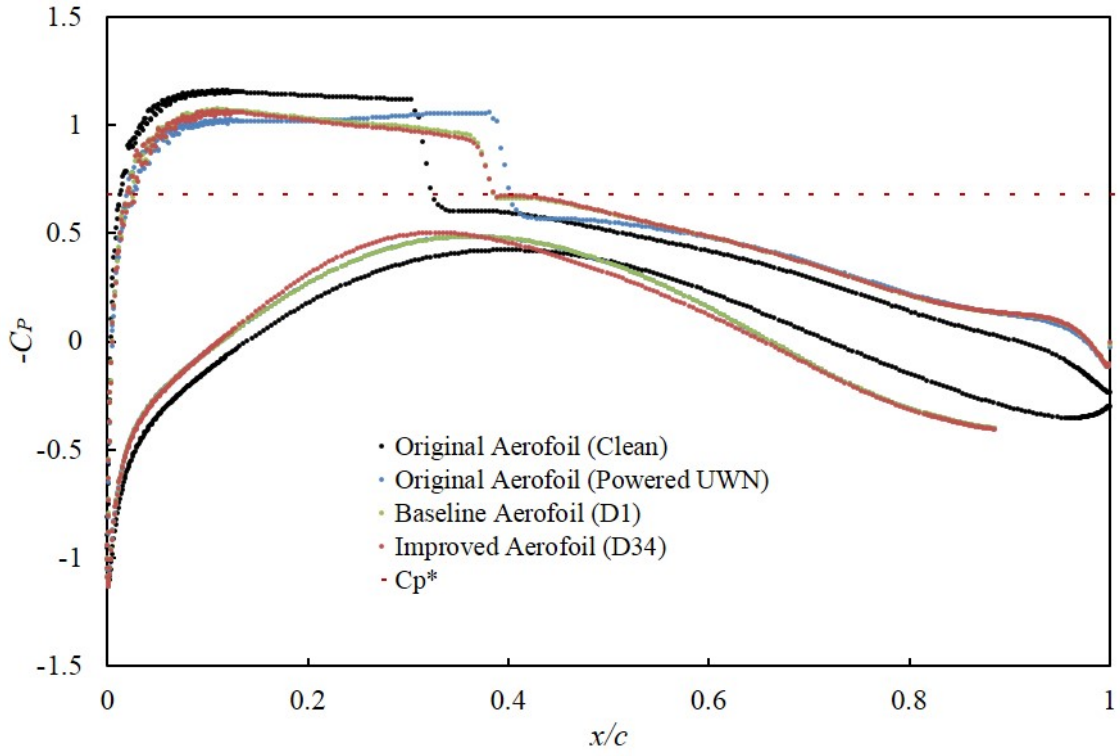

Figure 6.28: Plot showing the pressure distribution comparison between the original aerofoils, baseline aerofoil (D1) and the D34 design point.

outcomes are summarised below:

- The best aerofoil design (D34) provides greater drag reduction ($C_{D_{\mathrm{UWN}}} = 0.00692$) compared to the best design point in the OWN study ($C_{D_{\mathrm{OWN}}} = 0.01116$), for the same cruise lift condition ($C_{L_{2D}} = 0.5$).
- The relatively low fan inlet velocity creates a compression zone on the lower surface upstream of the fan, which consequently relieves the upper surface suction level at the same lift condition, and therefore weakens the shock wave. The fan exit flow also has a beneficial "flow entrainment", giving a more adverse pressure recovery to increase aft suction levels, further helping to reduce suction levels at the leading edge and weaken the shock wave.

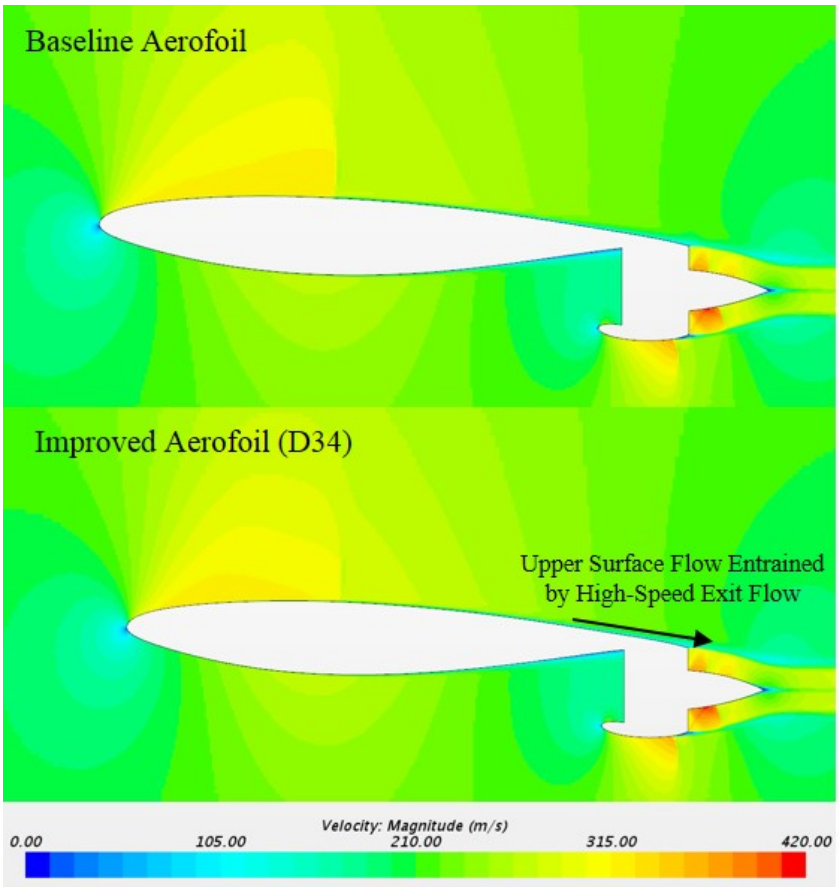

Figure 6.29: Velocity magnitude contour plot comparison between the baseline aerofoil (D1) and the D34 design point.

6.3 Buffet Onset Analysis

The previous section has highlighted that the UWN configuration increases the rear adverse pressure gradient due to the fan exit entraining the upper surface flow. Due

to these increased pressure gradients it is important to determine whether this has a detrimental or beneficial effect on trailing edge boundary layer separation and buffet onset.

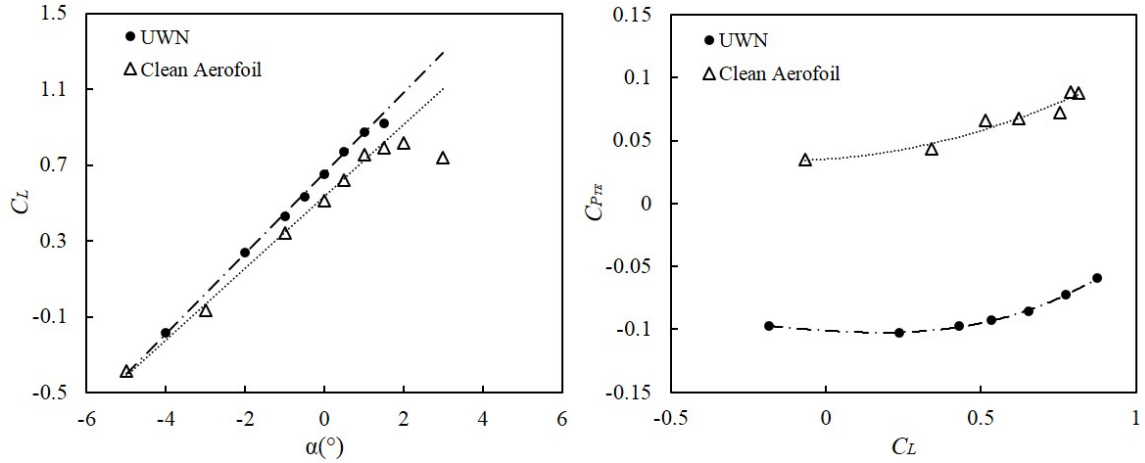

(a) Lift curve slope (b) $C_{P_{TE}}$ versus C_L

Figure 6.30: Plot showing (a) the lift curve slopes of the clean aerofoil and the powered UWN configuration, (b) $C_{P_{TE}}$ vs C_L at 95% chord on the upper surface, at a freestream velocity of Mach number 0.725.

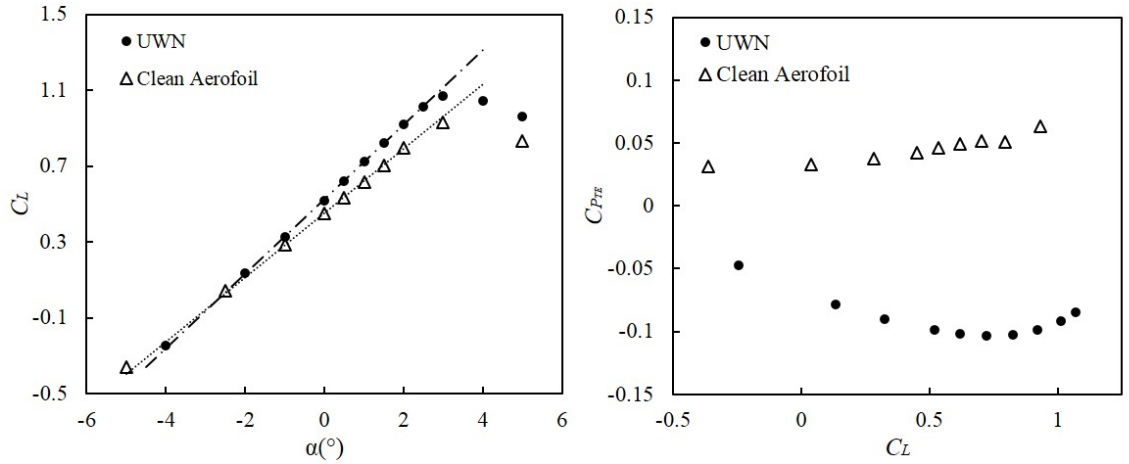

(a) Lift curve slope (b) $C_{P_{TE}}$ versus C_L

Figure 6.31: Plot showing (a) the lift curve slopes of the clean aerofoil and the powered UWN configuration, (b) $C_{P_{TE}}$ vs C_L at 95% chord on the upper surface, at a freestream velocity of Mach number 0.65.

In this section, the D34 design point from the UWN parametric study is set as the baseline UWN aerofoil. The lift curve slope for both the clean aerofoil and the powered UWN configuration is constructed at different 2D Mach numbers, see Figs 6.30 - 6.32. In addition, plots of the coefficient of pressure, $C_{P_{TE}}$, at the trailing edge upper surface against the coefficient of lift, C_L, are presented. For an attached boundary layer the $C_{P_{TE}}$ would be expected to increase gradually with increasing

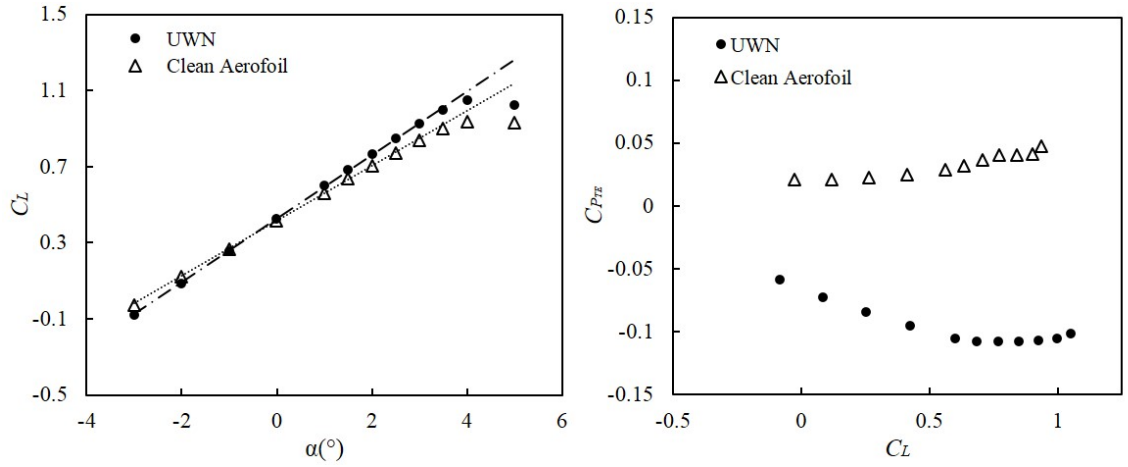

(a) Lift curve slope (b) $C_{P_{TE}}$ versus C_L

Figure 6.32: Plot showing (a) the lift curve slopes of the clean aerofoil and the powered UWN configuration, (b) $C_{P_{TE}}$ vs C_L at 95% chord on the upper surface, at a freestream velocity of Mach number 0.60.

lift coefficient. At the point of boundary layer separation there is a departure from this trend with an observed increase in $C_{P_{TE}}$. Consequently this can be used as a means of determining the C_L corresponding to buffet-onset (Hackett, 2020).

At higher Mach numbers, this trend is not so noticeable however. The C_L-alpha plots show that a higher $C_{L_{max}}$ is achieved with the UWN configuration relative to the baseline aerofoil. However, in these cases flow breakdown is instigated by a shock-induced boundary-layer separation and not by the aft pressure gradient. Therefore, the trend in $C_{P_{TE}}$ corresponding to buffet is not observed. The plots do however highlight the significantly reduced suction levels for the UWN configuration due to the entrained flow.

To investigate the influence of the UWN configuration on trailing edge boundary layer separation (due to adverse pressure gradients), rather than a shock-induced separation, which occurs at higher Mach numbers ($0.6<M_{2D}<0.725$), a lift curve slope is also drawn for M_{2D}=0.5, where no shock-induced separation occurs, as evidenced from Figure 6.33. It can be seen that the two C_L polars overlap before buffet-onset points, i.e. at AoA=4.5°, where the powered UWN configuration still has a higher $C_{L_{max}}$, see Fig. 6.33a. Additionally, Figure 6.33b also indicates that when the $C_{P_{TE}}$ of the clean aerofoil starts to increase, this does not occur in the UWN case, as desired.

To investigate the reason why the UWN configuration achieves a delayed buffet-onset, the flow entrainment concept is considered whereby the acceleration at the fan exit also increase the momentum of the upper surface flow. Figure 6.34 illustrates the comparisons of boundary layer velocity profiles of the UWN configuration

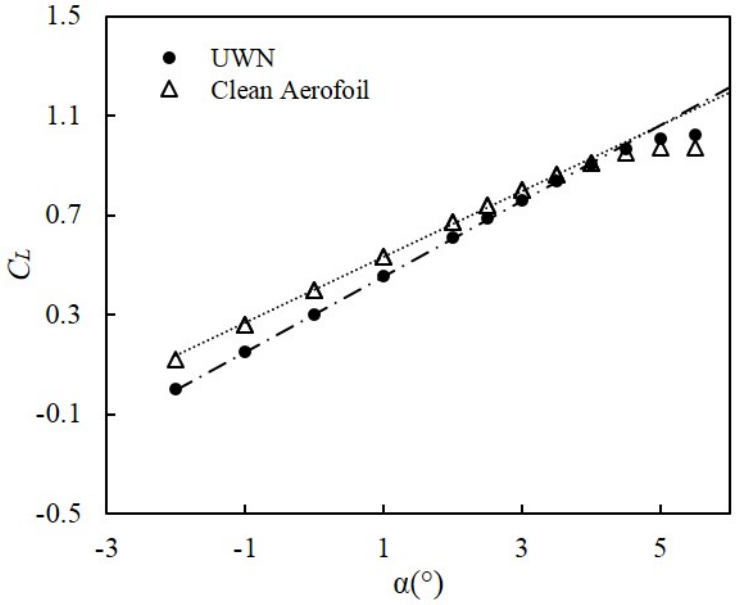

(a) Lift curve slope

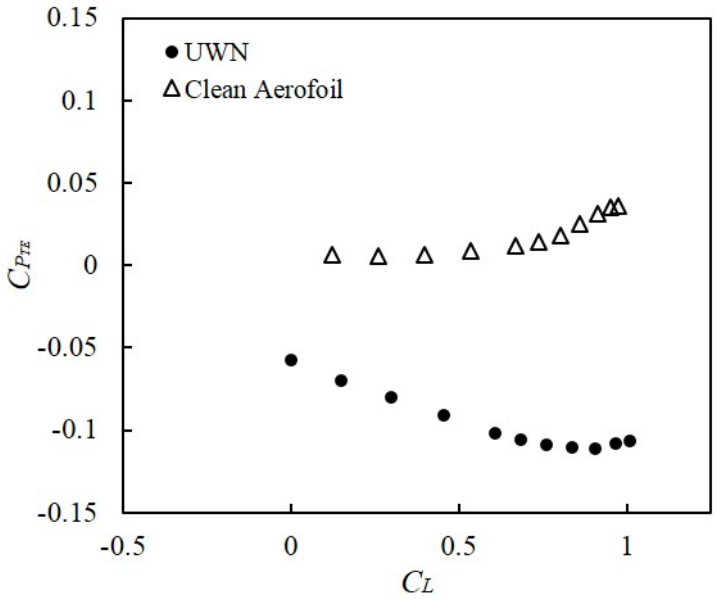

(b) $C_{P_{TE}}$ versus C_L

Figure 6.33: Plot showing (a) the lift curve slopes of the clean aerofoil and the powered UWN configuration, (b) $C_{P_{TE}}$ vs C_L at 95% chord on the upper surface, at a freestream velocity of Mach number 0.50.

and the clean aerofoil for a cruise condition ($C_L = 0.5$) and a high lift condition ($C_{L_{2D}} = 0.85$), both at 95% chords on the upper surface when the freestream velocity is M_{2D}=0.725. No reversed flow is observed in both plots, however, comparing the gradient of the velocity profile, the UWN design consistently has a higher near-wall velocity gradient compared to that for the clean aerofoil, which demonstrates that the flow entrainment is achieved by the powered UWN configuration; the flow is energised to resist flow reversal, which normally results in boundary layer breakdown.

The velocity profiles of M_{2D}=0.65, 0.6, and 0.5 show the same flow physics.

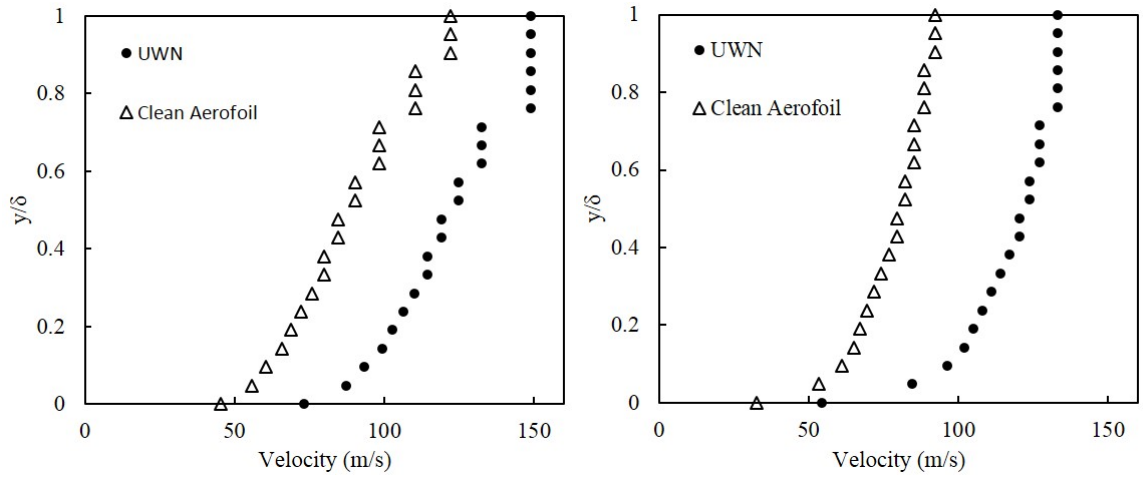

Figure 6.34: Plot showing the comparison of boundary layer velocity profiles at 95% chord on the upper surface at (a) Cruise ($C_L = 0.5$) and (b) in High lift ($C_{L_{2D}} = 0.85$) conditions, at a freestream velocity of M_{2D}=0.725.

After the analysis of the lift curve slopes and velocity profiles, a new set of DoEs is set up with a higher coefficient of lift of $C_{L_{2D}} = 0.9$ in the Star CCM+ Macro script to improve transonic aerofoil performance at buffet-onset. This DoE is applied to both upper and lower surfaces and the results are shown in Figure 6.35, which produces a better design point (D29) for upper-surface change at this higher C_L condition. Clearly, the D29 design offers the largest improvement, see Fig. 6.35a, as it has both minimum drag and maximum structural thickness. While the lower surface variation produces less benefits due to the smaller data spread.

When analysing the pressure distribution of the improved D29 design, see Fig. 6.36, a lowered roof-top and delayed shock is observed, showing weaker shock strength and aft shock position. By comparing the velocity magnitude contours, it can be seen that the separation region is dramatically reduced in size, as well as a visible weakened shock and delayed shock position at the same lift condition ($C_{L_{2D}} = 0.9$). Although the AoA for these two cases are different, achieving this high lift condition at lower angles still indicates the potential of combining DoE and CST methods for mitigating the shock-induced separation. Through this buffet-onset analysis, research outcomes are summarised below:

- Lift curve slopes of the powered UWN and clean aerofoils show a limited operational range of the improved UWN aerofoil design at a real flight altitude. It can be explained that the angle of attack needs to remain in a very small range during cruise.

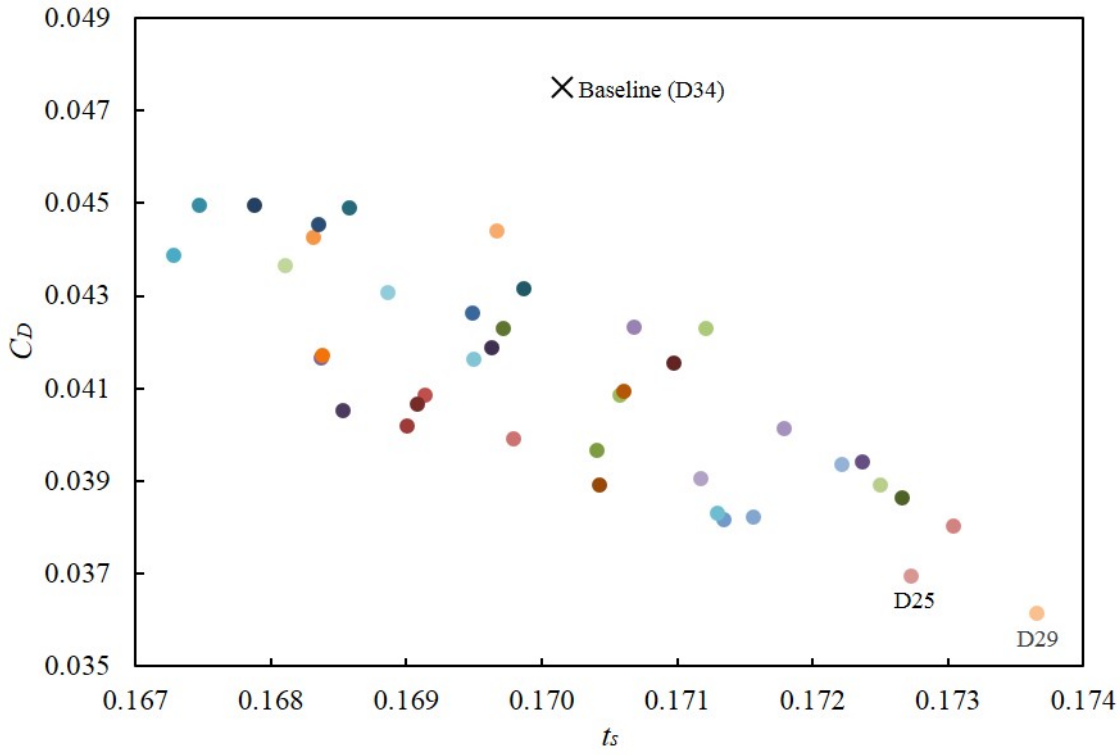

(a) Upper Surface

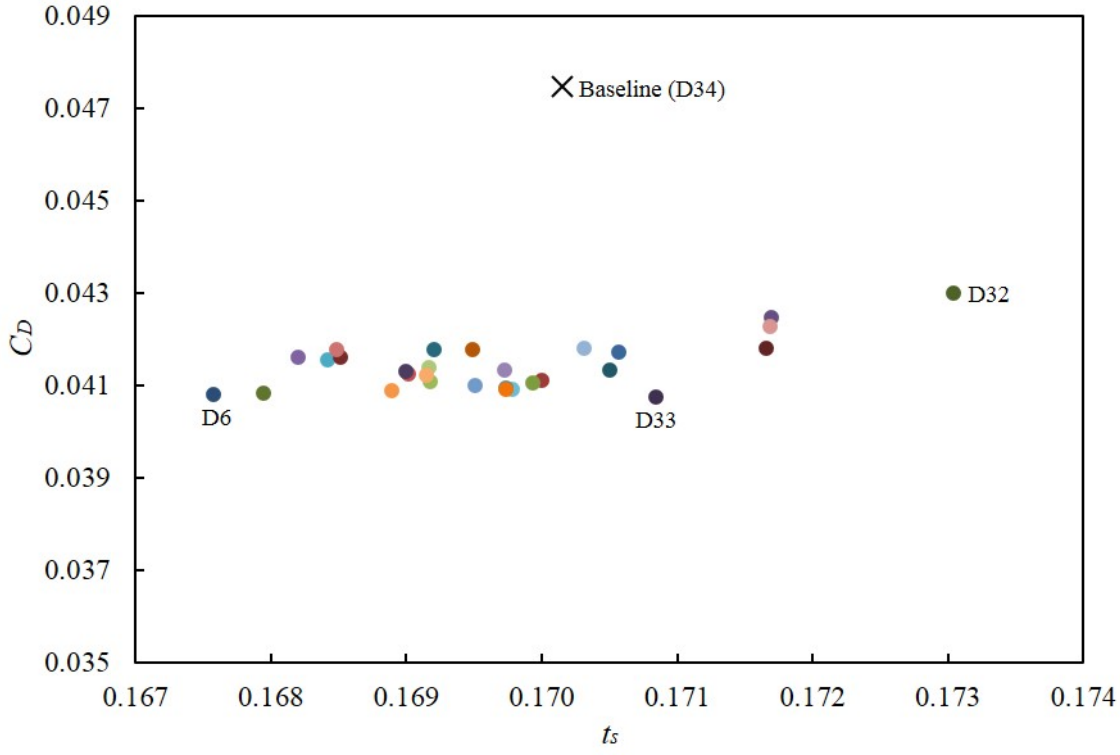

(b) Lower Surface

Figure 6.35: Plot showing the distribution of 40 DoE points by resampling (a) Upper surface and (b) Lower surface. *(All cases have same lift conditions of* $C_{L_{2D}}$*=0.9* $\pm$*0.25%.)*

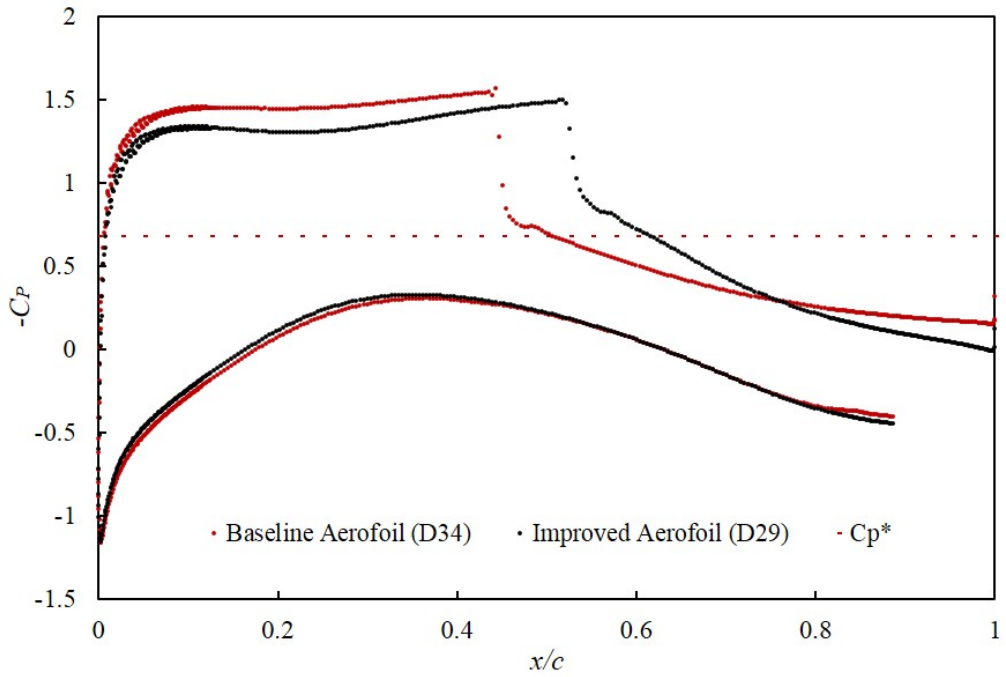

Figure 6.36: Plot showing the pressure distribution comparison between the improved aerofoil (D29) and baseline aerofoil (D34)

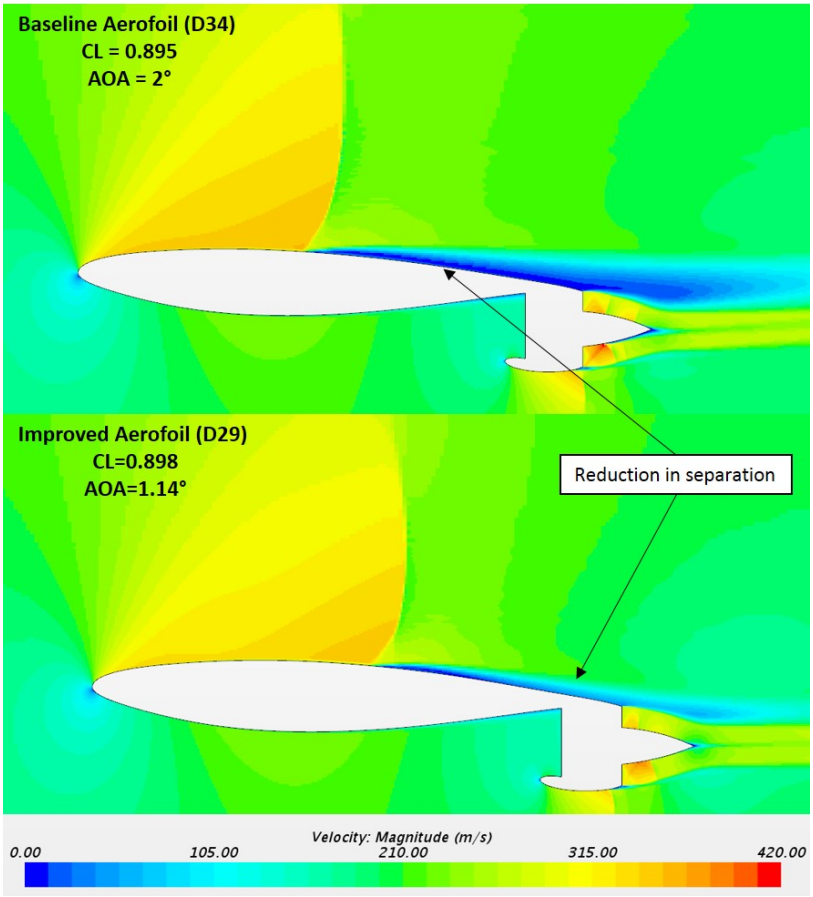

Figure 6.37: Velocity magnitude illustrating the separation reduction when compare the improved aerofoil (D29) with baseline aerofoil (D34) at high lift condition

- The UWN configuration provides the opportunity to delay buffet compared with the clean aerofoil.
- The UWN configuration enables flow entrainment to energise the boundary layer at the trailing edge on the upper surface to resist boundary layer separation, which is proven by a higher C_L value at buffet-onset and a more gradual velocity gradient in the boundary layer.
- Using the DoE has shown the capability to produce an improved aerofoil (D29) at a high lift condition ($C_{L_{2D}}$=0.9) compared to the baseline aerofoil design (D34), which indicates the potential of using CST and DoE in future buffet-onset optimisation.

6.4 Engineering Insight

The advantage of a low-drag and weight has been discussed in detail in previous sections. An improved aerofoil design, which either lowers the drag and shock strength or increases the structural thickness for lower weight, is challenging to find in a comprehensively covered design and optimisation process. However, deriving engineering insight from the large quantity of data generated by the high-fidelity CFD simulations in this study can still offer practical and tangible benefits for aerospace vehicle design.

6.4.1 Design Space Analysis

Analysing the correlations between the design variables and the objective functions is one of the easiest ways to derive engineering insights. In this analysis, R^2, which is a statistical measure representing the degree of variance for a dependent variable in a regression model, is used to explore the correlation between each design variable and objective functions. The formula for R^2 is given by:

$$R^2 = \left(\frac{n(\sum xy) - (\sum x)(\sum y)}{\sqrt{[n\sum x^2 - (\sum x)^2][n\sum y^2 - (\sum y)^2]}} \right)^2 \tag{6.1}$$

where, n is the number in the given dataset, x is the value of design variable, and y is the value of objective function.

Because the UWN configuration provides better aerodynamic performance than the OWN design, the following analysis is based on the UWN configuration by plotting the percentage of drag reduction and structural thickness increase against

changes in each design variable used in the previous parametric study (plots shown in Appendix D). All objective functions are presented with the same scale and each design variable is normalised from 0 to 1 for clearer comparison. Table 6.2 presents the R^2 values of each design variable and objective function for both upper and lower surfaces, based on analysis of all data sets presented in Figs D.2 - D.5.

For upper surface aerofoil shape changes, the design variable D1* has the highest influence on C_D reduction ($R^2 = 0.5138$), and D4* has the largest impact on structural thickness ($R^2 = 0.8459$). A general trend is observed that when D1* decreases, more drag reduction can be achieved, while, the decrease of D4* results in an increase of structural thickness. Considering that each design variable only influences the shape at a certain aerofoil location, it can be assumed that D1* leads to control of the shock formation area, which is the most sensitive part on the aerofoil in terms of drag. The R^2 values of D2*, D3*, and D4* for drag reduction are relatively small, indicating a fairly small direct correlation between drag reduction with those design variables. In terms of structural thickness, D1* has a small effect on this parameter, while D2* and D3* only have a further-reduced influence.

Upper Surface	D1*	D2*	D3*	D4*
$C_{D_{2D}}$	0.5138	0.0564	0.0001	0.0127
Structural Thickness	0.2215	0.1128	0.0258	0.8459
Lower Surface	D1*	D2*	D3*	D4*
$C_{D_{2D}}$	0.3164	0.0539	0.2535	0.2559
Structural Thickness	0.6841	0.0223	0.0833	0.2165

Table 6.2: Table showing the R^2 values of each design variable against objective functions for upper and lower surfaces.

For lower surface aerofoil shape changes, D1* has the most influence on both drag ($R^2 = 0.3164$) and structural thickness ($R^2 = 0.6841$); as it increases, there is a general tendency for C_D to increase, but the effect is not pronounced on the upper surface, and the structural thickness also notably increases. D3* and D4* have nearly the same weight of influence on C_D, as increasing their values both reduce the drag level. For structural thickness, D4* has far less impact on the lower surface than the upper one, while D2* and D3*'s effects are very weak.

In conclusion, D1* is the most influential design variable in achieving a low-drag and weight aerofoil design, with a similar impact on both upper and lower surfaces. D4* plays an important role on the upper surface in terms of structural thickness, and a relatively small role on the lower surface for both objective functions. The tendency of how objective functions are behaving by increasing each design variable

are summarised in Table 6.3.

Upper Surface	D1* (↑)	D2* (↑)	D3* (↑)	D4* (↑)
C_D	↑	-	-	-
Structural Thickness	↓	↓	-	↓
Lower Surface	D1* (↑)	D2* (↑)	D3* (↑)	D4* (↑)
C_D	↑	-	↑	↑
Structural Thickness	↓	-	-	↓

Table 6.3: Table showing the general tendency of both objective functions by increasing values of each design variable.

6.4.2 Engineering Implications

Analysing the design space reveals the correlations between each design variable and objective functions. Besides reducing the aerodynamic drag, there are some other important aspects worthy of consideration which can be transferred into practical implications in engineering. Table 6.4 presents the improvements in drag reduction and structural thickness increase achieved throughout this study. The aerofoil (podded nacelle) is a two-dimensional representation of a powered conventional high bypass ratio engine, illustrated in Figure 6.38.

	Aerofoil (Clean)	Aerofoil (Podded Nacelle)	OWN	UWN
C_D(Baseline)	0.00921	0.05519	0.01539	0.00748
C_D(Improved)	-	-	0.01172	0.00692
Drag Reduction	-	-	23.84%	7.51%
Thickness Increase	-	-	3.16%	0.09%

Table 6.4: Table showing the percentage drag reduction and thickness increase after improvements achieved compared to the baseline OWN and UWN configurations. *(All cases have same lift conditions of $C_{L_{2D}}$=0.5 ±0.25%.)*

Comparing the C_D between over and under-wing nacelle configurations with the baseline aerofoil powered by a podded nacelle at the same lift condition, it can be found that both OWN and UWN baseline configurations improve the performance of the podded baseline configuration, however, the UWN configuration gives the lowest C_D when coupled with a distributed propulsion system. Furthermore, after DoE parametric studies, the improved UWN and OWN configurations achieve further drag reduction of 7.51% and 23.84% respectively, in addition to structural thickness increases with improvement of 0.09% and 3.16% for each configuration, implying that

the distributed OWN has more potential if the shock formation on the upper surface can be properly managed, which has been discussed in Section 2.3.5.1. To determine if a 2D simulation of a typical podded nacelle configuration is representative, and why the C_D is high relative to the clean aerofoil, 2D and 3D simulations are compared in Figure 6.38. The 2D simulation was performed at a transformed freestream Mach number due to sweep effects (Mach 0.725) and so is equivalent to a 3D Mach number of 0.85.

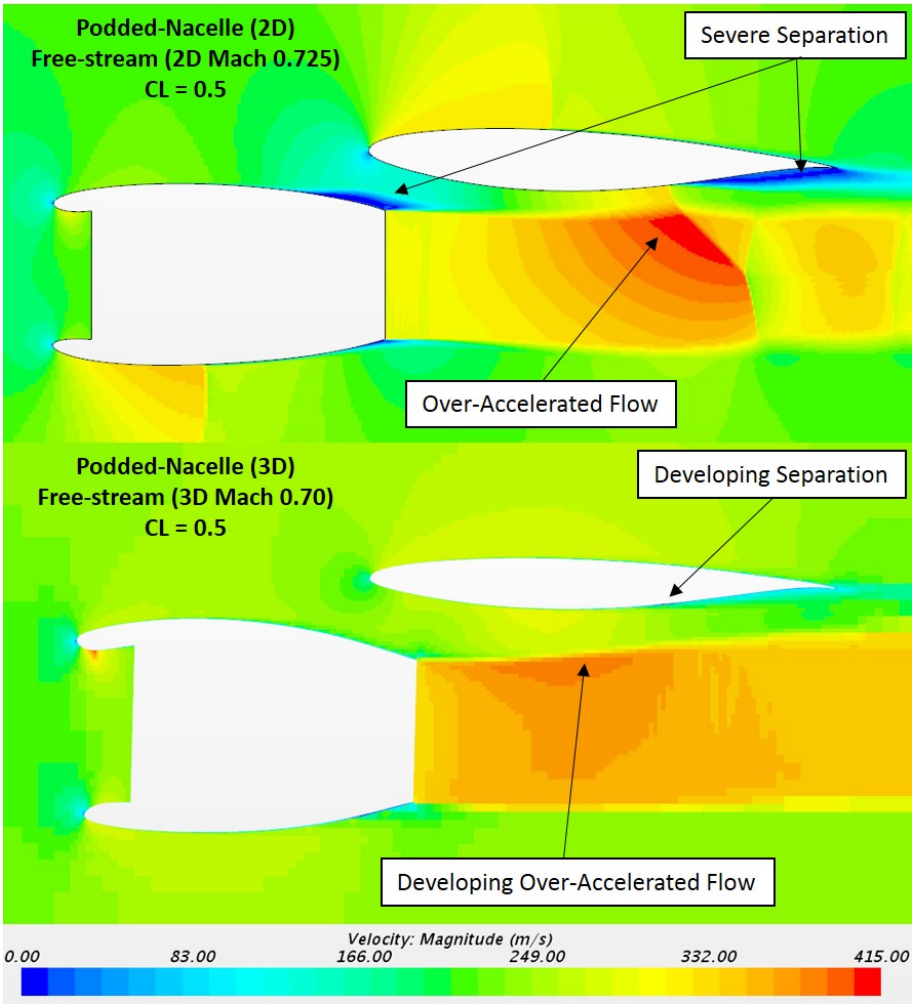

Figure 6.38: Velocity magnitude comparison between two-dimensional and three dimensional powered podded-nacelle configurations with same lift conditions ($C_{L_{2D}}$=0.5 ±0.25%).

The jet exhausted from the fan exit is expanded due to the shape of the lower aerofoil surface resulting in an acceleration of the flow. In 2D, this is terminated by a reasonably strong shock wave that causes a shock-induced separation of the aerofoil lower surface boundary-layer. In 3D, the velocity magnitude plot is a sectional slice view just off the pylon close to the fuselage from the simulation of a powered and fully configured Common Research Model (consisting of fuselage, wing, powered nacelle, pylon, and tail). In 3D, the flow can expand in three dimensions, and so

the flow expansion is not as significant as the 2D case with no evidence of a shock induced separation. Consequently the 2D podded case is not that representative of the real world 3D flow and caution needs to exercised in comparing with the 2D distributed propulsion cases. This does however highlight the advantage of a distributed UWN configuration that eliminates the potential for a "gully shock" forming with an integrated nacelle.

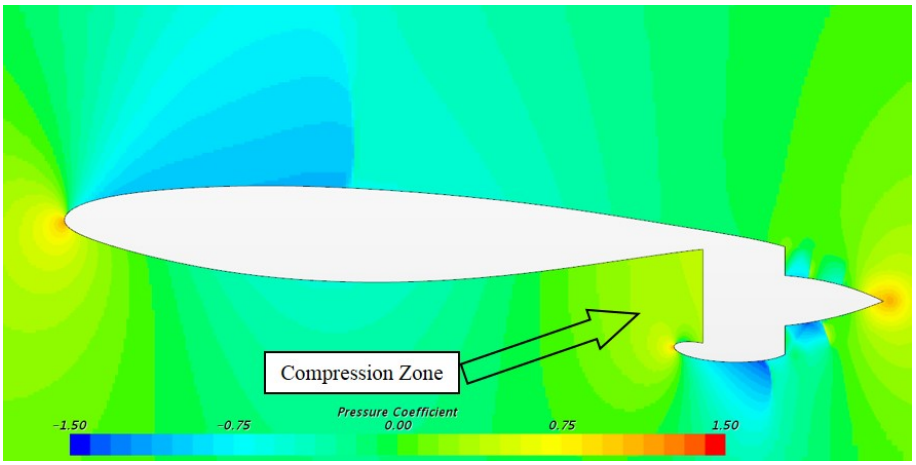

Figure 6.39: Pressure coefficient plot illustrating the compression zone to help the flow naturally slow down for fan intake.

Another potential advantage offered by the distributed UWN configuration is that a compression zone occurs upstream of the fan inlet as the flow decelerates, see Fig. 6.39. This is opposite to the flow expansion observed over the same region for the podded cases (both 2D and 3D) and the distributed OWN configuration. The compression zone helps to re-distribute the aerofoil pressure distribution, reducing the leading-edge suction levels and therefore helping to minimise wave drag. The UWN configuration therefore provides some inherent design benefits for the wing due to its intake design.

6.5 Synthesis

The purpose of this chapter has been to establish whether the concept of combining the strengths of CFD automation, CST aerofoil parametrisation and DoE methods for aerodynamic shape optimisation is feasible and practical for different distributed propulsion concepts. Although this design strategy is capable of providing an improved aerofoil design compared to the original aerofoil, it still requires three-dimensional and experimental validation and proof. The aerodynamic performance for either cruise condition ($C_{L_{2D}} = 0.5$) or high lift condition ($C_{L_{2D}} = 0.85$) can be improved by the combination of those methods. The simplicity of the CST

method using coefficients rather than conventional parameters makes the design and improvement process much easier as all the change can be intuitively observed without considering more than a dozen shape parameters, such as in the PARSEC method (Sobieczky, 1999).

The improvement in drag reduction in percentage terms is significant for the OWN configuration, 23.84%, and a 3.16% increase in structural thickness, but these are relative to the 2D podded case which is not truly representative of the real world 3D flow. The UWN configuration achieves smaller percentage benefits, but the starting point for the UWN was a better drag standard. Considering the final drag and structural thickness results, the UWN configuration provides significantly better aerodynamic performance at the same lift condition. This highlights the benefits of the UWN design; the combination of a compression zone ahead of the intake and an entrainment of the upper surface flow help to redistribute the pressure distribution to reduce upper surface suction levels and the potential for shock waves to form. There may be potential for further benefits to the OWN configuration by weakening the upper-surface shock wave but fundamentally the UWN configuration appears better for transonic conditions. Comparing the final improved design, OWN has significantly stronger shock strength than UWN, 20.51% in terms of ΔC_P for the same lift condition.

Another point of discussion is that this study also establishes that the distributed UWN configuration can benefit more in terms of buffet-onset than the distributed OWN configuration to cope with boundary layer separation. Obviously, the improved aerofoil (D34) has suffered a strong shock-induced separation at relatively high Mach numbers (Mach_{2D}=0.725, 0.65 and 0.6) and because of that, a final aerofoil design will go through shock-free optimisation, which was beyond the scope of this study. However, for Mach_{2D}=0.5, the shock-induced separation has been eliminated, therefore, a fair comparison of lift curve slope and trailing edge pressure coefficients between the clean aerofoil and the powered UWN configuration was made to detect the evidence of resisting buffet at high angles of attack. Clearly, in the UWN plot, the $C_{P_{TE}}$ remains relatively flat, see Fig. 6.33b, whereas the $C_{P_{TE}}$ of the clean aerofoil starts to increase. The boundary layer velocity profile plot, Figure 6.34, also proves the "flow entrainment" energised the boundary layer in the UWN configuration. Additionally, the relatively low-velocity compression zone observed in the distributed UWN configuration, Figure 6.39, potentially offers intake design relief for nacelles.

Last but not least, the numerical noise during the CFD simulation has a marked effect on the auto-C_L Macro scripts as producing each solution with an acceptable tolerance of C_L by varying the boundary conditions is crucial in this study. Thank-

fully, all the scripts are tuned into a perfectly stable working state which ensures the accuracy of the improvements seen.

Chapter 7

Discussion and Conclusions

The focus of the research reported in this thesis is a detailed analysis of the aerodynamic characteristics of both over and under wing nacelle configurations, assuming a distributed propulsion system, with the aim of improving the design and examining how an integrated nacelle configuration might provide benefits in terms of reduced shock strength and improved buffet margins. This was achieved by using computational techniques to reveal the flow characteristics in different configurations. The main findings of this research are summarised below together with closing remarks and recommendations for future work.

7.1 Computational Fluid Dynamics

Through the CFD preliminary study, two generic representative aircraft geometries, the DLR-F6 and NASA Common Research Model, were analysed using RANS turbulence models (i.e. SST k-ω and Spalart-Allmaras models) to predict the pressure distributions and flow visualisations against wind tunnel test information. Additionally, the preliminary simulation of a powered nacelle was also conducted to explore the effect of propulsion over a typical wing, which illustrated the effect of cross-flow over it and the importance of conducting research in 3D. Numerical solutions from two case studies showed good agreement with experimental data in terms of predicting wing pressure distributions at transonic speeds. The first case study also presented the influence of the FX2B fairing to mitigate wing root separation, which was validated by flow visualisation from wind tunnel tests. Comparing the performance of two turbulence models, the SST k-ω showed enhanced capability of predicting the adverse pressure gradient and boundary-layer separation, while the

Spalart-Allmaras model over-estimated the shock strength for rear loading, which is crucial for supercritical aerofoil performance.

Another important lesson learnt from this CFD study was the meshing strategy. A well balanced mesh can effectively discretise the flow domain for optimal solutions, whereas an overly-fine mesh may cause huge computational cost or deteriorate the solution with diverging issues (both occurred in 2D and 3D cases) and a coarse mesh will result in an unreliable result since flow features will not be resolved. That makes the grid independence study imperative in CFD applications. Using an appropriate meshing strategy is also important due to the complexity of aircraft geometries and the flow characteristics around it at transonic speeds. It is also necessary to control the mesh refinement method over certain regions, e.g. the pylon region, wing tips, and the leading and trailing edges. Using anisotropic cell clustering is a good example to coarsen the mesh along the span-wise direction, which led to great acceleration of convergence without comprising accuracy.

Utilising High Performance Computing (HPC) has made all simulations in this research more efficient and less time-consuming. However, to determine a suitable usage of nodes and RAM was found to be important, as too much resource can significantly speed up the calculations but it will lead to excessively long queuing times. Therefore a good guess of the computational resources can also benefit the simulation throughput.

7.1.1 Validation and Verification

In this CFD validation and verification (V&V) study, the good agreement of pressure distributions between CFD results and experimental data was achieved in relatively high freestream speeds (e.g. Mach 0.7 and 0.75). For both case studies, discrepancies of predicting the suction peak were observed due to the insufficient mesh resolution at the leading edge, which is one of the difficulties in the preliminary study. As the refinement zone at the leading edge was set to the finest refinement ratio (0.05% of the base size), any increase in either refinement volume or ratio can result in significantly rising the mesh size which could cause tremendous computational cost.

To minimise the discretisation errors, one of the best ways is to improve the mesh quality, especially in the regions containing shock waves and separation, which typically occurs at "gully" regions, wing upper surface and trailing edge, for example; indicting the importance of grid independence study in CFD. Actually, grid independence was observed for all of the computations in this study. In the DLR-F6 case study, the smallest discretisation errors were attributable to the SST k-ω model,

with less than 1.5% for the drag and lift predictions when compared the baseline mesh to the finer mesh. Lastly, setting the suitable thickness of prism layer to represent the boundary layer is also critical, as a small y^+ value can significantly slow down or deteriorate the convergence. A good practice is to obtain an approximate thickness value from a y^+ wall distance estimator. Then, adjusting the height of first cell from the number and expansion ratio of prism layer with a spreadsheet can efficiently give an accurate value for the prism layer setting.

The convergence errors were properly dealt with in this study (i.e. all residuals in all cases were down by 3.5 or higher orders of magnitude). Allowing sufficient iterations of simulation to be running can minimise the convergence errors. For instance, the initial running steps for the powered NASA CRM were set to 3000 in Section 4.2.5, all residuals were dropping by around 3.5 orders of magnitude but still showing a decreasing trend. After another 500 iterations, all residuals were down to 4 orders of magnitude which provided a better solution.

7.2 Electric Ducted Fan Modelling

Developing a method for modelling electric ducted fans assuming a choked nozzle exit condition was one of the most challenging parts is this research, as it requires identical mass flow rates for fan intake and exit. The research carried out by Berguin et al. (2018) offered great help in over-wing engine integration in Chapter 2, however, their method compromised the mass flow rate because even the conventional turbofan engines should also consider the balance of mass flow rates for nacelle intake and exit as the mass flow rate of fuel is only a fraction of the whole mass of the jet exhausted from the nozzle. As it has been mentioned in Chapter 5, companies and research institutes have their own specifically designed tools (Dillinger et al., 2018), and these are worth investigating if a suitable combination of boundary conditions (BC) can properly model the electric ducted fan in commercial CFD packages.

In this method, the fan pressure ratio (FPR), suggested by Felder, Kim and Brown (2009) and Kim (2010), is the most crucial parameter as it determines the total pressure at the nozzle. Besides, it is also the only parameter to determine whether the choked condition can be achieved at different cruise speeds and altitudes. Thereafter, BC studies showed that it is feasible to model a choked electric ducted fan with a pressure outlet (target mass flow rate option selected) and mass flow inlet with good $\dot{m}$-matching and faster convergence. However, using this combination of boundary conditions requires careful calculation of the fan size, to ensure that the intake and exit areas (in 2D) are compatible with the desired mass flow rate and

with a choked nozzle condition. Moreover, using the inlet/outlet BCs to simulate electric ducted fans in this research was not tested in proper 3D cases, only a simple 3D cylinder test was conducted to validate the mass flow rate and thus the feasibility of achieving the choked condition. In this research, the ideal momentum source BC failed due to its limitations in 2D, but this could still be an appropriate BC for 3D distributed UWN or OWN simulations, but careful definition of source term is still required. Another BC to model a fan in Star CCM+ is the fan interface, which is mainly designed for 3D cases and requires a specific fan performance curve (not considered in this research). However, it is recommended this is considered for future work if the study involves detailed 3D design for electric ducted fans.

7.3 Aerofoil Performance Improvement

The parametric study presented in Chapter 6 is not as comprehensive as doing an aerofoil optimisation, which can involve full analysis of aerodynamic performance for the variations of each individual or group of CST coefficients. Due to the scope of this project and the consideration of computational cost, using an initial sensitivity study to identify a group of promising coefficients for the later parametric study was deemed to be sensible. Considering the design space and the results from the sensitivity, 4 out of 8 coefficients in the middle location of the baseline aerofoil was found to partially represent the most sensitive part of the aerofoil, where the shock-induced separation occurs. A 40-point Optimal Latin Hypercube (OLH) Design of Experiments (DoE) was found to be sufficient to fully cover the design space (Narayanan et al., 2007). Another limitation of this study is not considering the 3D effects (e.g. cross flow over the wing and swirls). However, design from 2D aerofoils is the start of the traditional design process. Additionally, considering the complexity of 3D simulations (tens of millions of cells in each mesh) this was prohibitive and beyond the scope of this research.

The general outcomes from each parametric study were established in detail in Chapter 6. Interestingly, the UWN configuration achieves better performance than the OWN configuration for the "aft-embedded and inner-wing only" distributed propulsion concept with 8.7% more drag reduction achieved compared to the 2D podded nacelle configuration for the same lift condition. However, it is also important to note that the 2D podded nacelle simulation is not truly representative of the 3D podded nacelle flow development. Despite the fact that the UWN prevails the drag contest, as reported in Table 6.4, the OWN configuration still improves the sectional C_D by 78.76% from the 2D podded nacelle configuration. However, one reason that

the OWN configurations is worse than the UWN configuration in this study is that the OWN configuration has to operate at higher AoA to achieve the same lift condition, which results in higher upper surface suction levels and a strong shock wave on the upper surface. There may be further potential to decrease drag for the OWN configuration through a more detailed design, but it will be difficult to eliminate the upper surface shock wave. Among those limitations and benefits, if more CST coefficients and 3D effects are considered in a larger and more densely populated design space, then the future of extending the methods from the parametric study in combination with sophisticated optimisation methods, could provide limited improvements. It was also noted that the correlation between objective functions and single CST coefficient may be small in terms of R^2, but the effect of the combination of multiple CST coefficients for the objective functions is worth investigating due to the nature of class and shape functions employed in the CST method (Kulfan, 2007).

Fundamentally, the UWN represents a better configuration for transonic flows, giving a significantly better aerodynamic performance at the same lift condition in this study. The benefits are derived as follows;

1) Since the flow must decelerate into the intake (to Mach 0.5 approximately), to avoid transonic tip losses in the fan, a compression zone forms ahead of the intake, increasing the aft lower surface static pressure.

2) The upper surface flow would normally decelerate over the aft region of the aerofoil, with velocity reducing towards the freestream velocity at the trailing-edge. However, due to the presence of the under-wing fan, the high velocity fan exhaust (Mach 1 approximately) entrains the upper surface flow maintaining a relatively high velocity in this region and consequently reducing the aft upper surface static pressure.

3) Both of the above effects contribute to a significant increase in aft loading of the aerofoil.

4) As a consequence the forward (rooftop) suction levels can be reduced, by operating at a lower angle of attack, to meet the same Lift condition.

5) A reduced rooftop suction level will weaken or eliminate the shock wave, reducing or eliminating wave drag at cruise.

6) At off-design conditions, this should also provide better Mach flexibility and limit the possibility of shock-induced boundary-layer separation.

7.4 Buffet Onset Analysis

The importance of detecting buffet onset for transonic designs, especially for low C_L conditions, is to control the rear adverse pressure gradients to maintain a safe operating margin between cruise and buffet, as either boundary layer separation or shock-induced separation can cause significant drag rise, which can deteriorate the aerodynamic performance. One method for buffet detection is to observe the lift curve slope, as the buffet onset point is where the C_L point starts to deviate from the linear relationship. Therefore, buffet detection must take possible shock-induced separation into consideration, as both of them will impact the lift curve slope. Observing the velocity magnitude contours and plot of skin coefficient is important to find the presence of shock waves and separation bubbles.

Another method to detect buffet onset due to strong adverse pressure gradients is to plot the coefficient of pressure on the upper surface at the trailing edge, $C_{P_{TE}}$, against the C_L (Hackett, 2020), which should be close to the trailing edge (e.g. 95% chord). At the onset of buffet (i.e. trailing-edge boundary-layer separation), the $C_{P_{TE}}$ trend will increase from a linear relationship. This was observed for the clean aerofoil to occur around $C_{L_{2D}}$=0.7 at the lowest freestream Mach number of 0.5. At all higher freestream Mach numbers buffet was caused by a shock-induced separation rather than by aft adverse pressure gradients. In this research, the plot of $C_{P_{TE}}$ versus C_L for the UWN configuration at this low freestream Mach number shows a continuously decreasing trend due to the entrainment effects previously mentioned. A sudden increase in $C_{P_{TE}}$ is not observed for this configuration suggesting that it has a better buffet performance at low speeds (Schmollgruber et al., 2019).

7.5 Distributed Propulsion Concept

The advantages of hybrid distributed propulsion can be summarised as: lower emission, lower fuel consumption and lower noise. Incorporating this technology with the embedded wing-nacelle integration eliminates the risks of gully shocks due to conventional engine integration if a proper nacelle or fairing design can be achieved. Otherwise, a higher standard for the strength of nacelle may be required in case fan blade failure damages the wing structure and other fans, which may cause additional weight. Another prominent disadvantage of distributed propulsion is the complexity of the electrical architecture (Schmollgruber et al., 2019), which can result in a challenging trade-off study during conceptual design, including the selection and location of power units. After the aerofoil performance improvement study and buffet

onset analysis in this thesis, the advantages and disadvantages of distributed OWN and UWN configurations have been understood.

7.5.1 Over Wing Nacelle Configuration

Compared to the conventional podded engine integration, the recent CFD research by Hooker et al. (2013) and Hooker and Wick (2014) proved that the single OWN configuration has the advantage of improving the aerodynamic efficiency, reducing the wing weight and mitigating the community noise levels compared to a single UWN configuration. However, the OWN configuration has a major disadvantage in that it can easily induce strong shock waves on the upper surface by over-accelerating the flow. Utilising the aft-embedded OWN configuration in this study is based on the results provided by Berguin et al. (2018) to extend the roof-top and reduce the rear wing loading. However, a strong shock (even a secondary shock wave) is inevitable after the shape improvement, which significantly increases the drag. The results from Chapter 6 suggest that the distributed OWN configuration is unsuitable for distributed propulsion at transonic speeds based on the wing geometry considered in this thesis. There may well be other potential wing designs, possibly found through design optimisation, which could realise a better drag standard but eliminating the shock wave will be challenging.

7.5.2 Under Wing Nacelle Configuration

The natural advantages of the UWN configuration are easier maintenance access and cabin noise shielding. In terms of aerodynamic performance, the distributed UWN configuration in this study showed dominant drag reduction compared to the distributed OWN configuration, at transonic speeds. Unlike the OWN configuration, the shock wave strength on the upper surface is much weaker. A similar result to (Wick et al., 2015) demonstrated that the relatively low speed (below transonic) inlet velocity of the fan creates a compression zone on the lower surface, upstream of the fan. This consequently relieves the upper surface suction level at the same lift condition, and consequently weakens the shock wave. The relatively high speed flow from the fan exit also has a beneficial effect by entraining the upper surface flow providing a more adverse pressure recovery (compared with the baseline and OWN configuration), that increases aft suction levels, further helping to reduce leading suction levels and then weaken the shock wave. The combination of those phenomena makes the UWN configuration more favourable in transonic wing design. However, the inner-wing-only distributed UWN configuration also has challenges in

terms of the position and design of landing gear, as the traditional tri-cycle landing gear configuration occupies the inner wing space, close to the belly fairing. In this case, the distributed UWNs have to extend to the outer wing by sacrificing part of the inner wing space to landing gear, which would also increase the complexity of designs.

7.6 Recommendations for Future Work

A number of areas for future investigation have been identified throughout this research project. These areas are either beyond the scope of this work or would require additional experimental tests and evaluations that were not feasible due to time constraints and restrictions on equipment or resource. Suggestions for future work are as follows:

- Using the fan interface for modelling the electric ducted fan if a fan performance curve is made available in the public literature;
- Investigating the optimum size and number of distributed fans on a transonic civil aircraft;
- Increasing the number of CST coefficients used in the parametric study to develop a more extensive optimisation method for the aerofoil performance improvement study;
- Conducting 3D simulations to explore 3D flow effects and the effect of swirl from the electric ducted fans;
- Optimising the aerofoil shape in both 2D and 3D to achieve a shock-free design for the UWN configurations in order to fully realise trade-offs and the potential benefits;
- Implementing the UWN configuration for different sized aircraft to explore the degree of aerodynamic improvements.
- Developing an understanding of how boundary-layer ingestion in the fan intake influences the dynamic performance of an electric fan at transonic speeds.

7.7 Conclusions

The present study demonstrates that the hybrid electric distributed propulsion concept, either with the OWN or UWN configurations, is an advanced technical concept that can be potentially beneficial for future design of large transonic transport

aircraft, compared to the conventional engine integration. The distributed UWN configuration offers a significantly better drag standard than the distributed OWN configuration after a limited performance improvement study.

The improvement achieved by the aerofoil performance study consisting of the CST parametrisation method and a Design of Experiments (DoE) study also indicates the potential to establish a more comprehensive aerofoil optimisation method in future for the distributed propulsion concept if more CST coefficients and 3D simulations are involved. This research also shows that the modelling method for an electric ducted fan can be established using a commercial CFD package with careful fan sizing.

Finally, the distributed UWN configuration offers some inherent performance advantages at cruise due to the increased aft loading of the wing section, as well as at off-design conditions with an increased buffet margin due to both a delay in shock-induced separation and in boundary-layer separation caused by aft adverse pressure gradients.

References

AIAA. 1998. "Guide for the Verification and Validation of Computational Fluid Dynamics Simulations." *AIAA G-077-1998* .

Airbus Group. 2014. "Aircraft Characteristics for Airport and Maintenance Planning-A380 Guide Book.".

Airbus Group Innovations and Rolls-Royce. 2014. "E-Thrust Electrical distributed propulsion system concept for lower fuel consumption, fewer emissions and less noise.".
URL: *www.airbusgroup.com*

Akturk, Ali and Cengiz Camci. 2012. "Experimental and computational assessment of a ducted-fan rotor flow model." *Journal of Aircraft* 49(3):885–897.

Amadori, Kristian, Christopher Jouannet and Petter Krus. 2008. Aircraft Conceptual Design Optimization. In *26th International Congress of the Aeronautical Sciences*. Anchorage: pp. 1–12.

Anderson, John D. 1995. *Computational Fluid Dynamics, The Basics with Applications*. McGraw-Hill.

Anderson, John D. 2004. *The Wright Brothers and Their Predecessors: Inventing Flight*. 1st ed. John Hopkins University Press.

Anderson, John D. 2005. *Introduction to Flight*. 3rd ed. New York: McGraw-Hill.

Anderson, John D. 2011. *Fundamentals of Aerodynamics*. 5th ed. Boston: McGraw-Hill.

ANSYS Fluent. 2018. "ANSYS Fluent User Guide, Version 18, Fluent Incorporated, Lebanon, USA.".

Argüelles, Pedro, John Lumsden, Manfred Bischoff, Denis Ranque, Philippe Busquin, Søren Rasmussen, B.A.C. Droste, Paul Reutlinger, Richard Evans, Ralph Robins, Walter Kröll, Helena Terho, Jean-Luc Lagardère, Arne Wittlöv and Alberto Lina. 2001. European Aeronautics: A Vision for 2020. Technical report European Commission.

Ashill, P. 1995. Modern Wing Aerodynamic Design. Technical report Defence Research Agency, Bedford.

Bagassi, S, G Bertini, D Francia and F Persiani. 2012. Design Analysis for Hybrid Propulsion. In *28th International Congress of the Aeronautical Sciences*. Brisbane: pp. 1–7.

Bardina, J. E., P. G. Huang and T. J. Coakley. 1997. "Turbulence Modeling Validation, Testing, and Development." *NASA Technical Memorandum 110446* .

Barlow, J. B, W. H Rae Jr. and A. Pope. 1999. *Low-Speed Wind Tunnel Testing*. 3rd ed. John Wiley & Sons.

Barnard, R. H. 2000. *Aircraft Flight: A Description of the Physical Principles of Aircraft Flight*. 2nd ed. Longman.

Barnard, R. H. 2001. *Road Vehicle Aerodynamic Design, An Introduction*. 2nd ed. MechAero Publishing.

Batchelor, George Keith. 2000. *An Introduction to fluid dynamics*. Cambridge University Press.

Becker, K. 2003. "Perspectives for CFD." *DGLR-2002-013, DGLR Jahrbuch 2002, Band III, Germany* .

Berguin, Steven H., Sudharshan Ashwin Renganathan, Jai Ahuja, Mengzhen Chen, Christian Perron, Jimmy Tai and Dimitri N Mavris. 2018. "CFD Study of an Over-Wing Nacelle Configuration.".

Bertin, J. J. and M. L. Smith. 1989. *Aerodynamics for Engineers*. 2nd ed. New Jersey: Prentice Hall, Inc.

Berton, J J. 2002. "Advanced Engine Cycles Analyzed for Turbofans With Variable-Area Fan Nozzles Actuated by a Shape Memory Alloy." *Programs/Projects: UEET, Revolutionary Concepts in Aeronautics* .

Binder, R. C. 1958. *Advanced Fluid Mechanics: Volume II*. Prentice Hall.

Birajdar, Mahasidha R and Sandip A Kale. 2015. "Effect of Leading Edge Radius and Blending Distance from Leading Edge on the Aerodynamic Performance of Small Wind Turbine Blade Airfoils." *International Journal of Energy and Power Engineering* 4(5-1):54–58.

Birckelbaw, Larry D. 1992. "High Speed Aerodynamics of Upper Surface Blowing Aircraft Configuration." *AIAA paper 92-2611* .

Botti, Jean. 2016. "Airbus group: A story of continuous innovation." *Aeronautical Journal* 120(1223):3–12.

Bradshaw, P. 1964. *Experimental Fluid Mechanics*. 1st ed. Pergammon Press.

Brelje, Benjamin J. and Joaquim R.R.A. Martins. 2019. "Electric, hybrid, and turboelectric fixed-wing aircraft: A review of concepts, models, and design approaches." *Progress in Aerospace Sciences* 104:1–19.

CD-adapco. 2016. "Star CCM+ User's Guide.".
URL: *http://www.cd-adapco.com/products/star-ccm/*

Chang, I. Chung and R. G. Rajagopalan. 2003. CFD Analysis for Ducted Fans with Validation. In *21st AIAA Applied Aerodynamics Conference*. Orlando, Florida: AIAA.

Chau, K.T and Y.S Wong. 2002. "Overview of power management in hybrid electric vehicles." *Energy Conversion and Management* 43:1953–1968.

Chaudhry, Imran Ali and Ali Ahmed. 2014. "Preliminary Aircraft Design Optimization Using Genetic Algorithms." *Journal of Scientific & Industrial Research* 73:302–307.

Clancy, L.J. 1975. *Aerodynamics*. New York: John Wiley & Sons.

Climate Change Act. 2008.

Cummings, Russell M., William H. Manson, Scott A. Morton and David R. McDaniel. 2015. *Applied Computational Aerodynamics*. New York: Cambridge University Press.

Deere, Karen A., Sally A. Viken, Melissa B. Carter, Jeffrey K. Viken, Joseph M. Derlaga and Alex M. Stoll. 2017. Comparison of high-fidelity computational tools for wing design of a distributed electric propulsion aircraft. In *35th AIAA Applied Aerodynamics Conference*.

Dehpanah, Payam and Amir Nejat. 2015. "The aerodynamic design evaluation of a blended-wing-body configuration." *Aerospace Science and Technology* 43:96–110.

Della Vecchia, Pierluigi, Elia Daniele and Egidio D'Amato. 2014. "An airfoil shape optimization technique coupling PARSEC parameterization and evolutionary algorithm." *Aerospace Science and Technology* 32(1):103–110.

Dillinger, E, R Liaboeuf, C Toussaint, J Hermetz and M Ridel. 2018. Handling Qualities of Onera's Small Business Concept Plane With Distributed Electric Propulsion. In *31st Congress of the International Concil of the Aeronautical Science*.

Durbin, Paul A. and Gorazd Medic. 2007. *Fluid Dynamics with a Computational Perspective*. Cambridge: Cambridge University Press.

Felder, J. L., Hyun Dae Kim and G. V. Brown. 2009. "Turboelectric Distributed Propulsion Engine Cycle Analysis for Hybrid-Wing-Body Aircraft." *AIAA-2009-1132* .

Felder, James L., Gerald V. Brown, Hyun Dae Kim and Julio Chu. 2011. Turboelectric Distributed Propulsion in a Hybrid Wing Body Aircraft. In *20th International Symposium on Air Breathing Engines*.

Felder, James L, Hyun Dae Kim, Gerald V Brown and Julio Chu. 2011. "An Examination of the Effect of Boundary Layer Ingestion on Turboelectric Distributed Propulsion Systems." *AIAA-2011-300* pp. 1–26.

Friedrich, C. and P.A. Robertson. 2015. "Hybrid-Electric Propulsion for Aircraft." *Journal of Aircraft* 52(1):176–189.

Frink, Neal T. 2003. "2nd AIAA CFD Drag Prediction Workshop.".
URL: *https://aiaa-dpw.larc.nasa.gov/Workshop2/workshop2.html*

Frink, Neal T. 2006. "3rd AIAA CFD Drag Prediction Workshop.".
URL: *https://aiaa-dpw.larc.nasa.gov/Workshop3/workshop3.html*

Fujino, Michimasa. 2005. "Design and development of the HondaJet." *Journal of Aircraft* 42(3):755–764.

Fujino, Michimasa and Yuichi Kawamura. 2003. "Wave-Drag Characteristics of an Over-the-Wing Nacelle Business-Jet Configuration." *Journal of Aircraft* 40(6):1177–1184.

Georgala, J.M. 2002. SAUNA User Guide - Chapter 12 - User Guide for FIELDPP the Field Mesg and Flowfield Post-Processor. Technical report ARA Ltd.

Ghoreyshi, Mehdi and Russell M. Cummings. 2014. "From Spreadsheets to Simulation-Based Aircraft Conceptual Design." *Applied Physics Research* 6(3):1–19.

Goodyer, M. J. 1992. "The cryogenic wind tunnel." *Progress in Aerospace Sciences* 29(3):193–220.

Graham, Donald J. 1947. "High-speed Tests of an Airfoil Section Cambered to Have Critical Mach Numbers Higher than Those Attainable with a Uniform-load Mean Line, NACA-TN-1396.".

Green, John E. 2008. Laminar Flow Control - Back to the Future? In *38th Fluid Dynamics Conference and Exhibit*. Seattle, Washington: AIAA.

Green, William. 1976. *The Observer's Book of Aircraft*. F Warne Publishers Ltd.

Hackett, Kevin. 2020. "Viscous full-potential (VFP) method for three dimensional wings and wing-body combinations. Part 4: VFP analysis program for flow breakdown and forces and loads." *ESDU T1026C* .

Harris, Charles D. 1990. "NASA Supercritical Airfoils, NASA Technical paper 2969.".

Hirsch, C. 2007. *Numerical Computation of Internal and External Flows*. 2nd ed. Butterworth-Heinemann.

Hooker, John R. and Andrew Wick. 2014. Design of the hybrid wing body for fuel efficient air mobility operations at Transonic Flight Conditions. In *52nd AIAA Aerospace Sciences Meeting - AIAA Science and Technology Forum and Exposition, SciTech 2014*.

Hooker, John R., Andrew Wick, Cale Zeune and Anthony Agelastos. 2013. Over wing nacelle installations for improved energy efficiency. In *31st AIAA Applied Aerodynamics Conference*.

Hung, J. Y. and L. F. Gonzalez. 2012. "On parallel hybrid-electric propulsion system for unmanned aerial vehicles." *Progress in Aerospace Sciences* 51:1–17.

Hutton, A. G. 2009. "The emerging role of large eddy simulation in industrial practice: Challenges and opportunities." *Philosophical Transactions of the Royal Society A: Mathematical, Physical and Engineering Sciences* 367:2819–2826.

ICAO. 1999. "ICAO Aerodrome Standards.".
URL: *http://www.icao.int/safety/implementation/library/manual_aerodrome_stds.pdf*

Isikveren, A. T., A. Seitz, J. Bijewitz, A. Mirzoyan, A. Isyanov, R. Grenon, O. Atinault, J. L. Godard and S. Stückl. 2015. "Distributed propulsion and ultra-high by-pass rotor study at aircraft level." *Aeronautical Journal* 119(1221):1327–1376.

Jeong, Woowon and Jaehoon Seong. 2014. "Comparison of effects on technical variances of computational fluid dynamics (CFD) software based on finite element and finite volume methods." *International Journal of Mechanical Sciences* 78:19–26.

Johnson, Forrester T., Edward N. Tinoco and N. Jong Yu. 2005. "Thirty years of development and application of CFD at Boeing Commercial Airplanes, Seattle." *Computers and Fluids* 34(10):1115–1151.

Joslin, Ronald D. and D Miller. 2009. *Fundamentals and Applications of Modern Flow Control, Aeronautics and Astronautics series Vol 231.* AIAA.

Jupp, J. A. 2016. "The design of future passenger aircraft - the environmental and fuel price challenges." *The Aeronautical Journal* 120(1223):37–60.

Kawaguti, M. 1953. "Numerical Solution of the Navier-Stoke Equations for the Flow Around a Circular Cylinder at Reynolds Number 40." *Journal of the Physical Society of Japan* 8(6):747–757.

Keith, Arvid L. Jr. 1975. A Brief Study of the Effects of Turbofan-Engine Bypass Ratio on Short- and Long-Haul Cruise Aircraft. Technical report NASA Lungley Reseurch Center.

Kemp, M. 2006. *Leonardo Da Vinci Experience, Experiment and Design.* V&A Publications.

Kim, Hyun Dae. 2010. Distributed Propulsion Vehicles. In *27th International Congress of the Aeronautical Sciences.* Nice, France: pp. 1–11.

Kim, Hyun Dae, Aaron T. Perry and Phillip J. Ansell. 2018. A Review of Distributed Electric Propulsion Concepts for Air Vehicle Technology. In *AIAA Propulsion and Energy Forum, 2018 AIAA/IEEE Electric Aircraft Technologies Symposium.* Cincinnati, Ohio: AIAA.

Kirby, M. and D. Mavris. 2008. The Environmental Design Space. In *26th International Congress of the Aeronautical Sciences.*

Ko, Andy, J. A. Schetz and William H. Manson. 2003. Assessment of the Potential Advantages of Distributed-Propulsion for Aircraft. In *16th International Symposium on Air Breathing Engines.* Cleveland, Ohio: AIAA.

Korn, David G. 1968. *Computation of Shock-Free Transonic Flows for Airfoil Design.* Courant Institute of Mathematical Sciences, New York University.

Krajnovic, Sinisa. 2009. "Large eddy simulation of flows around ground vehicles and other bluff bodies." *Philosophical Transactions of the Royal Society A: Mathematical, Physical and Engineering Sciences* .

Kroo, Ilan M. and Nicolas E. Antoine. 2005. "Framework for Aircraft Conceptual Design and Environmental Performance Studies." *AIAA Journal* 43(10):2100–2109.

Kulfan, Brenda M. 2007. A Universal Parametric Geometry Representation Method - "CST". In *45th AIAA Aerospace Sciences Meeting and Exhibit.* Reno, Nevada: AIAA.

Kulfan, Brenda M. and John E. Bussoletti. 2006. "Fundamental" parametric geometry representations for aircraft component shapes. In *11th AIAA/ISSMO Multidisciplinary Analysis and Optimization Conference: The Modeling and Simulation Frontier for Multidisciplinary Design Optimization.* Vol. 1 Portsmouth, USA: pp. 547–591.

Laflin, Kelly R., Steven M. Klausmeyer, Tom Zickuhr, John C. Vassberg, Richard A. Wahls, Joseph H. Morrison, Olaf P. Brodersen, Mark E. Rakowitz, Edward N. Tinoco and Jean-Luc Godard. 2005. "Data Summary from the Second AIAA Computational Fluid Dynamics Drag Prediction Workshop." *Journal of Aircraft* 42(5):1165–1178.

Lane, Kevin A and David D Marshall. 2009. A Surface Parameterization Method for Airfoil Optimization and High Lift 2D Geometries Utilizing the CST Methodology. In *47th AIAA Aerospace Sciences Meeting Including The New Horizons Forum and Aerospace Exposition.* Orlando, Florida: AIAA.

Lane, Kevin A. and David D. Marshall. 2010. "Inverse airfoil design utilizing CST parameterization." *AIAA 2010-1228, 48th AIAA Aerospace Sciences Meeting Including the New Horizons Forum and Aerospace Exposition* .

Launder, B. E. and D. B. Spalding. 1974. "The numerical computation of turbulent flows." *Computer Methods in Applied Mechanics and Engineering* 3:269–289.

Lieh, J., E. Spahr, Alireza Behbahani and John Hoying. 2011. Design of Hybrid Propulsion Systems for Unmanned Aerial Vehicles. In *47th AIAA/ASME/SAE/ASEE Joint Propulsion Conference & Exhibit.* San Diego: pp. 1–14.

Lock, C. N. H. 1945. The Ideal Drag Due to a Shock Wave, ARC/R&M-2512. Technical report Aeronautical Research Council.

Loftin, Laurance K. Jr. 1985. Quest for Performance: The Evolution of Modern Aircraft, NASA SP-468. Technical report NASA.

Longley, J.P. and E.M. Greitzer. 1992. Inlet distortion effects in aircraft propulsion system integration. In *Steady and transient performance prediction of gas turbine engines. AGARD Lecture Series, 183.* AGARD.

Massey, B. 1998. *Mechanics of Fluids.* 7th ed. Stanley Thrones Publisher Ltd.

Masters, D. A., N. J. Taylor, T. C.S. Rendall, C. B. Allen and D. J. Poole. 2017. "Geometric comparison of aerofoil shape parameterization methods." *AIAA Journal* 55(5):1575–1589.

Masters, D. A., N. J. Taylory, T. C.S. Rendall, C. B. Allen and D. J. Poole. 2015. Review of aerofoil parameterisation methods for aerodynamic shape optimisation. In *53rd AIAA Aerospace Sciences Meeting.* Kissimmee, Florida: AIAA.

Menter, F. R. 1993. "Zonal Two Equation k-ω Turbulence Models for Aerodynamic Flows." *AIAA 93-2906* .

Menter, F. R. 1994. "Two-Equation Eddy-Viscosity Turbulence Models for Engineering Applications." *AIAA Journal* 32(8):1598–1605.

Miller, John M. 2008. *Propulsion systems for hybrid vehicles.* London: Institution of Engineering and Technology.

Moore, Mark D. 2012. Distibuted Electric Propulsion (DEP) Aircraft. Technical report NASA Langley Research Center.

Munjulury, Raghu Chaitanya, Ingo Staack, Patrick Berry and Petter Krus. 2016. "A knowledge-based integrated aircraft conceptual design framework." *CEAS Aeronautical Journal* 7(1):95–105.

Narayanan, A., V. V. Toropov, A. S Wood and I. F Campean. 2007. "Simultaneous Model Building and Validation with Uniform Designs of Experiments." *Engineering Optimization* 39(5):497–512.

NASA. 2014. "NASA Armstrong Fact Sheet: F-8 Supercritical Wing.".
URL: *https://www.nasa.gov/centers/armstrong/news/FactSheets/FS-044-DFRC.html*

NASA. 2020. "NASA Common Research Model.".
URL: *https://commonresearchmodel.larc.nasa.gov/crm-nlf/crm-nlf-geometry/*

Oberkampf, William L. and Timothy G. Trucano. 2002. "Verification and validation in computational fluid dynamics." *Progress in Aerospace Sciences* 38:209–272.

Obert, Ed. 2009. *Aerodynamic Design of Transport Aircraft.* Amsterdam: IOS Press BV.

Pandya, Shishir, Scott Murman and Michael Aftosmis. 2004. "Validation of Inlet and Exhaust Boundary Conditions for a Cartesian Method." *American Institute of Aeronautics and Astronautics Paper 2004-4837* .

Patankar, S. V. 1980. *Numerical heat transfer and fluid flow.* Hemisphere Publishing Corporation.

Pornet, C. and A. T. Isikveren. 2015. "Conceptual Design of Hybrid-Electric Transport Aircraft." *Progress in Aerospace Sciences* 79:114–135.

Prandtl, Ludwig. 1952. *Essentials of fluid dynamics: With applications to hydraulics aeronautics, meteorology, and other subjects.* Hafner Pub. Co.

Queipo, V. N, R. T Haftka, W. Shyy, T Goel, R Vaidyanathan and K Tucker. 2005. "Surrogate-based Analysis and Optimization." *Progress in Aerospace Sciences* 41:1–28.

Randle, William E, Cesare A Hall and Maria Vera-Morales. 2011. "Improved Range Equation Based on Aircraft Flight Data." *Journal of Aircraft* 48(4):1291–1298.

Raymer, Daniel P. 1989. *Aircraft Design A Conceptual Approach.* 2nd ed. Washington, DC: AIAA Inc.

Reynolds, Osborne. 1883. "An experimental investigation of the circumstances which determine whether the motion of water shall be direct or sinuous, and of the law of resistance in parallel channels." *Philosophical Transactions of the Royal Society* 174(0):935–982.

Rivers, Melissa B., Jürgen Quest and Ralf Rudnik. 2015. Comparison of the NASA Common Research Model European Transonic Wind Tunnel Test Data to NASA Test Data (Invited). In *53rd AIAA Aerospace Sciences Meeting.* Kissimmee, Florida: AIAA.

Roache, P. J. 1994. "Perspective: A Method for Uniform Reporting of Grid Refinement Studies." *Journal of Fluids Engineering* 116:405–413.

Roache, Patrick J. 1998. "Verification of codes and calculations." *AIAA Journal* 36(5):696–702.

Roberts, J. 1989. *Leonardo Da Vinci*. Yale University Press.

Rolt, Andrew and John Whurr. 2015. Distributed Propulsion Systems to Maximize the Benefits of Boundary Layer Ingestion. In *22nd International Symposium on Air Breathing Engines*. Phoenix, USA: pp. 1–10.

Roskam, J. 1997. *Airplane Design*. Lawrence: Design, Analysis and Research Corporation.

Sasaki, Daisuke and Kazuhiro Nakahashi. 2011. "Aerodynamic optimization of an over-the-wing-nacelle-mount configuration." *Modelling and Simulation in Engineering* 2011.

Schlichting, Hermann and K. Gersten. 2000. *Boundary-Layer Theory*. 8th ed. New York: Springer.

Schmollgruber, P., C. Döll, Jean Hermetz, R. Liaboeuf, M. Ridel, I. Cafarelli, O. Atinault, C. François and B. Paluch. 2019. Multidisciplinary exploration of dragon: An onera hybrid electric distributed propulsion concept. In *AIAA Scitech 2019*. San Diego: AIAA.

Schoemann, J. 2012. Modeling of Hybrid-Electric Propulsion Systems for Small Unmanned Aerial Vehicles. In *2th AIAA Aviation Technology, Integration and Operations and 14th AIAA/ISSMO Multidisciplinary Analysis and Optimization Conference*. Indianapolis: AIAA.

Schoemann, J and M Hornung. 2013. Design of hybrid-electric propulsion systems for small unmanned aerial vehicles. In *5th European Conference for Aeronautics and Space Sciences*.

Schrauf, Géza. 2006. Key Aerodynamic Technologies for Aircraft Performance Improvement. In *5th Community Aeronautical Days*.

Sforza, Pasquale M. 2014. *Commercial Airplane Design Principles*. Butterworth-Heinemann.

Sgueglia, Alessandro, Peter Schmollgruber, Nathalie Bartoli, Olivier Atinault, Emmanuel Benard and Joseph Morlier. 2018. Exploration and Sizing of a Large Passenger Aircraft with Distributed Ducted Electric Fans. In *2018 AIAA Aerospace Sciences Meeting*. Kissimmee: AIAA.

Sobieczky, Helmut. 1999. *Parametric Airfoils and Wings, Recent Development of Aerodynamic Design Methodologies*. Springer.

Spalart, P. R. and S. R. Allmaras. 1992. "A One-Equation Turbulence Model for Aerodynamic Flows." *AIAA Paper 92-0439* .

Spalart, P. R., W.-H. Jou, M. Stretlets and S. R. Allmaras. 1997. Comments on the Feasibility of LES for Wings and on the Hybrid RANS/LES Approach, Advances in DNS/LES. In *Proceedings of the First AFOSR International Conference on DNS/LES*.

Spalart, Philippe R. 2000. "Strategies for Turbulence Modelling and Simulations." *International Journal of Heat and Fluid Flow* 21:252–263.

Steiner, Hans-Jörg, Arne Seitz, Kerstin Wieczorek, K Plötner, Askin T. Isikveren, Mirko Hornung and Bauhaus Luftfahrt. 2012. "Multi-disciplinary design and feasibility study of distributed propulsion systems." *28th Congress of the International Council of the Aeronautical Sciences 2012, ICAS 2012* 1:403–414.

Sun, Xiaoqian. 2014. "Incorporating Multicriteria Decision Analysis Techniques in Aircraft Conceptual Design Process." *Journal of Aircraft* 51(3):861–869.

Tennekes, Hendrik and John Leask Lumley. 1972. *A First Course in Turbulence*. MIT Press.

Thom, A. 1933. "The Flow Past Circular Cylinders at Low Speeds." *Proceedings of the Royal Society of London, Series A. Containing Papers of a Mathematical and Physical Character* 141(845):651–669.

Tinoco, Edward N. 1991. "CFD codes and applications at Boeing." *Sadhana* 16(2):141–163.

Torenbeek, Egbert. 1997. "Cruise Performance and Range Prediction Reconsidered." *Progress in Aerospace Sciences* 33:285–321.

Tu, Jiyuan, Guan-Heng Yeoh and Chaoqun Liu. 2018. *Computational Fluid Dynamics A Practical Approach*. 3rd ed. Butterworth-Heinemann.

Vassberg, John C., Mark A. DeHaan, S. Melissa Rivers and Richard A. Wahls. 2008. Development of a common research model for applied CFD validation studies. In *Collection of Technical Papers - AIAA Applied Aerodynamics Conference*.

Versteeg, H.K. and W. Malalasekera. 2007. *An Introduction of Computational Fluid Dynamics: The Finite Volume Method*. 2nd ed. New York: Pearson Education Limited.

Vos, Roelof and Saeed Farokhi. 2015. *Introduction to Transonic Aerodynamics*. Springer.

Ward, Thomas A. 2010. *Aerospace Propulsion Systems.* John Wiley & Sons (Asia) Pte Ltd.

Whitcomb, Richard T. and L. R. Clark. 1965. An Airfoil Shape for Efficient Flight at Supercritical Mach Numbers. Technical report NASA Langley Research Center.

Wick, Andrew T., John R. Hooker, Christopher J. Hardin and Cale H. Zeune. 2015. "Integrated aerodynamic benefits of distributed propulsion." *AIAA 2015-1500* .

Wilcox, David C. 1998. *Turbulence Modeling for CFD.* 2nd ed. Anaheim: DCW Industries.

Wolfshtein, Micha. 2009. "Some comments on turbulence modelling." *International Journal of Heat and Mass Transfer* 52:4103–4107.

Zhu, Feng and Ning Qin. 2014. "Intuitive class/shape function parameterization for airfoils." *AIAA Journal* 52(1):17–25.

Appendices

Appendix A

Matlab Scripts for CST Method

Aerofoil Fitting

```
% Load exsiting aerofoil
load CRM_NB
% Provide initial weights
% 8 initial coefficient for each surfaces
Win = [-1 -1 -1 -1 -1 -1 -1 -1  1 1 1 1 1 1 1 1];
% Use fmincon to find the minimum error compared with
    original aerofoil
[Wout]=fmincon(@(W) CST_AerofoilFit(W,yt,XL,XU,-0.036869),
    Win,[],[],[],[],ones(1,8)*-1,ones(1,8),[]);
% Generate aerofoil with optimised CST weights
[ycoord] = CST_FitGenerate(Wout,XL,XU,-0.036869);
% Plot and compare CST and target aerofoils
figure
plot(xcoord,ycoord,'b--')
hold on
```

```
14 plot(xcoord,yt,'r')
15 legend('CST','Target')
16 set(gcf,'color','w')
17 title('CST Aerofoil Fitting Comparison')
18
19 %Determine the error (in a separate file)
20 function error = CST_AerofoilFit(W,yt,xl,xu,dz)
21 % W: CST weights
22 % yt: y-coordinates of target airfoil
23 % xl: x-coordinates of lower surface
24 % xu: x-coordinates of upper surface
25 % dz: y-coordinate of trailing edge
26 % Aerofoil generated by CST
27 yp = CST_FitGenerate(W,xl,xu,dz);
28 % Minimise the error
29 error = mean(abs(yt-yp));
```

Aerofoil Generation

```
1 function [xycoord] = CST(wl,wu,dz,N);
2 % Input: wl = CST coefficients of lower surface
3 %        wu = CST coefficients of upper surface
4 %        dz = trailing edge thickness
5 % Output: xycoord = set of x-y coordinates of airfoil
      generated by CST method
6 % Create x coordinate
7 x=ones(N+1,1);y=zeros(N+1,1);zeta=zeros(N+1,1);
8 for i=1:N+1
9     zeta(i)=2*pi/N*(i-1);
```

```
10      x(i)=0.5*(cos(zeta(i))+1);
11  end
12  % N1 and N2 parameters (N1 = 0.5 and N2 = 1 for airfoil
        shape)
13  N1 = 0.5;
14  N2 = 1;
15  % Used to separate upper and lower surfaces
16  zerind = find(x(:,1) == 0);
17  xl= x(1:zerind-1); % Lower surface x-coordinates
18  xu = x(zerind:end); % Upper surface x-coordinates
19  % Call ClassShape function to determine lower surface y-
        coordinates
20  [yl] = ClassShape(wl,xl,N1,N2,dz);
21  % Call ClassShape function to determine upper surface y-
        coordinates
22  [yu] = ClassShape(wu,xu,N1,N2,dz);
23  % Combine upper and lower y coordinates
24  y = [yl;yu];
25  % Combine x and y into single output
26  xycoord = [x y];
27  % Function to calculate class and shape function
28  function [y] = ClassShape(w,x,N1,N2,dz);
29  % Class function; taking input of N1 and N2
30  for i = 1:size(x,1)
31      C(i,1) = x(i)^N1*((1-x(i))^N2);
32  end
33  % Shape function; using Bernstein Polynomials
34  n = size(w,2)-1; % Order of Bernstein polynomials
35
```

```
36 for i = 1:n+1
37       K(i) = factorial(n)/(factorial(i-1)*(factorial((n)-(i
             -1))));
38 end
39
40 for i = 1:size(x,1)
41     S(i,1) = 0;
42     for j = 1:n+1
43         S(i,1) = S(i,1) + w(j)*K(j)*x(i)^(j-1)*((1-x(i))^(n
               -(j-1)));
44     end
45 end
46 % Calculate y output
47 for i = 1:size(x,1)
48    y(i,1) = C(i,1)*S(i,1) + x(i)*dz;
49 end
```

Appendix B

Star CCM+ C_L-matching Script

```
//Scripts for geometry creation, mesh generation,
//and some boundary condition settings are hidden to save the space
//Velocity setting for Domain inlet
velocityProfile_0.getMethod(ConstantVectorProfileMethod.class).getQuantity().setComponents(217.0759332, 3.789074, 0.0);
//Velocity setting for Domain bottom surface
velocityProfile_1.getMethod(ConstantVectorProfileMethod.class).getQuantity().setComponents(217.0759332, 3.789074, 0.0);
//Velocity setting for Domain top surface
velocityProfile_2.getMethod(ConstantVectorProfileMethod.class).getQuantity().setComponents(217.0759332, 3.789074, 0.0);
//Report of coefficient of drag
forceCoefficientReport_0.setPresentationName("CD");
```

```
11 forceCoefficientReport_0.getDirection().setComponents
       (0.9998476952, 0.01745240644, 0.0);
12 forceCoefficientReport_0.getReferenceDensity().setValue
       (0.4127);
13 forceCoefficientReport_0.getReferenceVelocity().setValue
       (217.109);
14 //Report of coefficient of lift
15 forceCoefficientReport_1.getDirection().setComponents
       (0.01745240644, 0.9998476952, 0.0);
16 forceCoefficientReport_1.getReferenceDensity().setValue
       (0.4127);
17 forceCoefficientReport_1.getReferenceVelocity().setValue
       (217.109);
18 forceCoefficientReport_1.getParts().setObjects(boundary_17);
19 stepStoppingCriterion_0.setMaximumNumberSteps(20000); //
       running steps for AoA=1degree case
20 simulation_0.getSimulationIterator().run();
21 //Declare variables
22 double CL1, CL2, Newalpha, Velocitycos, Velocitysin;
23 //Assign the value of the report to a double precision
       variable
24 CL1 = forceCoefficientReport_1.getReportMonitorValue();
25 //Start of AoA=2 case
26 velocityProfile_0.getMethod(ConstantVectorProfileMethod.
       class).getQuantity().setComponents(216.9767431,
       7.57699483, 0.0);
27 velocityProfile_1.getMethod(ConstantVectorProfileMethod.
       class).getQuantity().setComponents(216.9767431,
       7.57699483, 0.0);
```

```
28 velocityProfile_2.getMethod(ConstantVectorProfileMethod.
       class).getQuantity().setComponents(216.9767431,
       7.57699483, 0.0);
29 forceCoefficientReport_0.getDirection().setComponents
       (0.999390827, 0.0348994967, 0.0); //CD report
30 forceCoefficientReport_1.getDirection().setComponents
       (0.0348994967, 0.999390827, 0.0); //CL report
31 stepStoppingCriterion_0.setMaximumNumberSteps(40000); //
       running steps for 2nd case
32 simulation_0.getSimulationIterator().run();
33 //Assign the value of the report to a double precision
       variable
34 CL2 = forceCoefficientReport_1.getReportMonitorValue();
35 //Calculate the alpha for CL=0.5
36 Newalpha=(0.5-(2+CL1+CL1))/(CL2-CL1); //Alpha slope
37 Velocitycos=Math.cos(Math.toRadians(Newalpha)); //cos(new
       alpha)
38 Velocitysin=Math.sin(Math.toRadians(Newalpha)); //sin(new
       alpha)
39 //Start of CL=0.5 case
40 velocityProfile_0.getMethod(ConstantVectorProfileMethod.
       class).getQuantity().setComponents((217.109*Velocitycos),
        (217.109*Velocitysin), 0.0);
41 velocityProfile_1.getMethod(ConstantVectorProfileMethod.
       class).getQuantity().setComponents((217.109*Velocitycos),
        (217.109*Velocitysin), 0.0);
42 velocityProfile_2.getMethod(ConstantVectorProfileMethod.
       class).getQuantity().setComponents((217.109*Velocitycos),
        (217.109*Velocitysin), 0.0);
```

```
43 stepStoppingCriterion_0.setMaximumNumberSteps(60000); //
       running steps for CL-matched case
44 simulation_0.getSimulationIterator().run();
45 simulation_0.saveState(resolvePath("C:\CLMATCHED.sim"));
```

Appendix C

Examples of 40 Design Points for OWN Sensitivity and Parametric Study

---

Tables C.1 - C.3 here present all 40 design points with 5%, 10% and 20% variations in coefficients determined by the DoEs, where ranges of variables are -5% to +5%, -10% to +10%, and -20% to +20% respectively. These CST coefficients were taken from the upper surface and used for the OWN sensitivity and parametric studies in Section 6.2.2.

D1	D2	D3	D4
0.120873051	0.242869114	0.02173557	0.330161016
0.121199294	0.234379308	0.021415537	0.344796576
0.121525537	0.240443455	0.020988826	0.32585644
0.12185178	0.235592137	0.021575553	0.319830033
0.122178023	0.230740819	0.021682231	0.329300101
0.122504266	0.22952799	0.020188744	0.331021931
0.122830509	0.245294774	0.020615454	0.32757827
0.123156752	0.236198552	0.019815372	0.337048338
0.123482995	0.244081944	0.021148843	0.323273694
0.123809238	0.225283086	0.021522214	0.332743762
0.124135481	0.233772893	0.020882149	0.343074746
0.124461724	0.247720433	0.02034876	0.341352915
0.124787967	0.244688359	0.019762033	0.331882847
0.125114211	0.226495916	0.020135405	0.350822983
0.125440454	0.225889501	0.02082881	0.346518407
0.125766697	0.246507603	0.020295422	0.340492
0.12609294	0.224676671	0.020402099	0.339631084
0.126419183	0.231347234	0.021788908	0.333604677
0.126745426	0.243475529	0.021095504	0.324134609
0.127071669	0.241656285	0.020455438	0.335326508
0.127397912	0.234985722	0.021628892	0.351683898
0.127724155	0.230134404	0.02125552	0.318969117
0.128050398	0.238017796	0.020722132	0.321551863
0.128376641	0.238624211	0.019868711	0.349101153
0.128702884	0.247114018	0.020935487	0.347379322
0.129029127	0.231953649	0.01992205	0.322412778
0.12935537	0.2422627	0.020028727	0.338770169
0.129681613	0.232560063	0.020242083	0.326717355
0.130007856	0.248326847	0.020562116	0.352544814
0.130334099	0.227708745	0.021468876	0.320690948
0.130660342	0.228921575	0.021202181	0.34221383
0.130986585	0.239230626	0.021842247	0.348240237
0.131312829	0.236804967	0.020508777	0.328439185
0.131639072	0.22831516	0.020082066	0.334465593
0.131965315	0.227102331	0.021362198	0.337909254
0.132291558	0.245901188	0.021308859	0.336187423
0.132617801	0.24104987	0.019975389	0.349962068
0.132944044	0.239837041	0.021042165	0.345657491
0.133270287	0.233166478	0.020668793	0.343935661
0.13359653	0.237411382	0.020775471	0.324995524

Table C.1: Table showing all 40 design points for 5% sensitivity study.

D1	D2	D3	D4
0.114511311	0.24923647	0.022668999	0.324565067
0.115163797	0.232256856	0.022028933	0.353836187
0.115816284	0.244385151	0.021175512	0.315955914
0.11646877	0.234682515	0.022348966	0.3039031
0.117121256	0.224979879	0.022562321	0.322843236
0.117773742	0.22255422	0.019575347	0.326286897
0.118426228	0.254087788	0.020428769	0.319399575
0.119078714	0.235895345	0.018828604	0.338339711
0.1197312	0.251662129	0.021495545	0.310790422
0.120383686	0.214064413	0.022242288	0.329730558
0.121036172	0.231044026	0.020962157	0.350392526
0.121688658	0.258939106	0.01989538	0.346948864
0.122341145	0.252874958	0.018721926	0.328008728
0.122993631	0.216490072	0.01946867	0.365889001
0.123646117	0.215277243	0.020855479	0.357279848
0.124298603	0.256513447	0.019788703	0.345227034
0.124951089	0.212851583	0.020002058	0.343505203
0.125603575	0.226192708	0.022775677	0.331452389
0.126256061	0.250449299	0.021388867	0.312512252
0.126908547	0.24681081	0.020108736	0.33489605
0.127561033	0.233469686	0.022455644	0.367610831
0.12821352	0.223767049	0.0217089	0.302181269
0.128866006	0.239533833	0.020642124	0.307346761
0.129518492	0.240746663	0.018935282	0.36244534
0.130170978	0.257726276	0.021068834	0.359001678
0.130823464	0.227405538	0.019041959	0.309068591
0.13147595	0.24802364	0.019255314	0.341783373
0.132128436	0.228618367	0.019682025	0.317677744
0.132780922	0.260151935	0.020322091	0.369332662
0.133433408	0.218915731	0.022135611	0.30562493
0.134085894	0.22134139	0.021602223	0.348670695
0.134738381	0.241959492	0.022882354	0.360723509
0.135390867	0.237108174	0.020215413	0.321121405
0.136043353	0.220128561	0.019361992	0.33317422
0.136695839	0.217702902	0.021922256	0.340061542
0.137348325	0.255300617	0.021815578	0.336617881
0.138000811	0.245597981	0.019148637	0.36416717
0.138653297	0.243172322	0.02128219	0.355558017
0.139305783	0.229831197	0.020535446	0.352114356
0.139958269	0.238321004	0.020748801	0.314234083

Table C.2: Table showing all 40 design points for 10% sensitivity study.

D1	D2	D3	D4
0.101787832	0.26197118	0.024535858	0.313373168
0.103092804	0.228011953	0.023255726	0.371915408
0.104397777	0.252268543	0.021548884	0.296154862
0.105702749	0.232863271	0.023895792	0.272049234
0.107007721	0.213457998	0.024322503	0.309929507
0.108312693	0.20860668	0.018348555	0.316816829
0.109617666	0.271673816	0.020055397	0.303042184
0.110922638	0.23528893	0.016855068	0.340922457
0.11222761	0.266822498	0.02218895	0.285823878
0.113532582	0.191627067	0.023682437	0.323704151
0.114837554	0.225586294	0.021122173	0.365028086
0.116142527	0.281376452	0.01898862	0.358140763
0.117447499	0.269248157	0.016641712	0.32026049
0.118752471	0.196478385	0.018135199	0.396021036
0.120057443	0.194052726	0.020908818	0.37880273
0.121362415	0.276525134	0.018775265	0.354697102
0.122667388	0.189201408	0.019201976	0.351253441
0.12397236	0.215883657	0.024749213	0.327147813
0.125277332	0.264396839	0.021975594	0.28926754
0.126582304	0.257119862	0.019415331	0.334035135
0.127887276	0.230437612	0.024109147	0.399464697
0.129192249	0.211032339	0.02261566	0.268605572
0.130497221	0.242565907	0.020482107	0.278936556
0.131802193	0.244991566	0.017068423	0.389133714
0.133107165	0.278950793	0.021335529	0.382246391
0.134412138	0.218309316	0.017281778	0.282380217
0.13571711	0.259545521	0.017708489	0.34780978
0.137022082	0.220734975	0.01856191	0.299598523
0.138327054	0.283802111	0.019842042	0.402908359
0.139632026	0.201329703	0.023469081	0.275492895
0.140936999	0.206181021	0.022402305	0.361584424
0.142241971	0.247417225	0.024962568	0.385690053
0.143546943	0.237714589	0.019628686	0.306485845
0.144851915	0.203755362	0.017921844	0.330591474
0.146156887	0.198904044	0.023042371	0.344366118
0.14746186	0.274099475	0.022829016	0.337478796
0.148766832	0.254694202	0.017495133	0.392577375
0.150071804	0.249842884	0.021762239	0.375359069
0.151376776	0.223160635	0.020268752	0.368471747
0.152681748	0.240140248	0.020695463	0.292711201

Table C.3: Table showing all 40 design points for 20% sensitivity study.

Appendix D

Correlation bewteen Design Variables and Objective Functions

Figures D.2 - D.5 show how each design variable influences C_D and t_s on both upper and lower surfaces. To help interpret the correlations, Figure D.1 is drawn to illustrate the locations controlled by each design variable, which is corresponding to the design variables used in sensitivity and parametric studies.

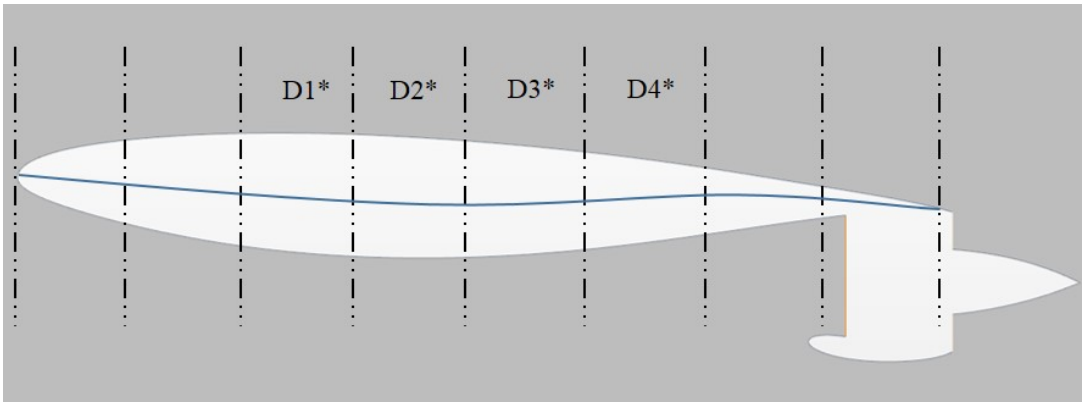

Figure D.1: Schematics illustrating the location on the aerofoil controlled by each design variable.

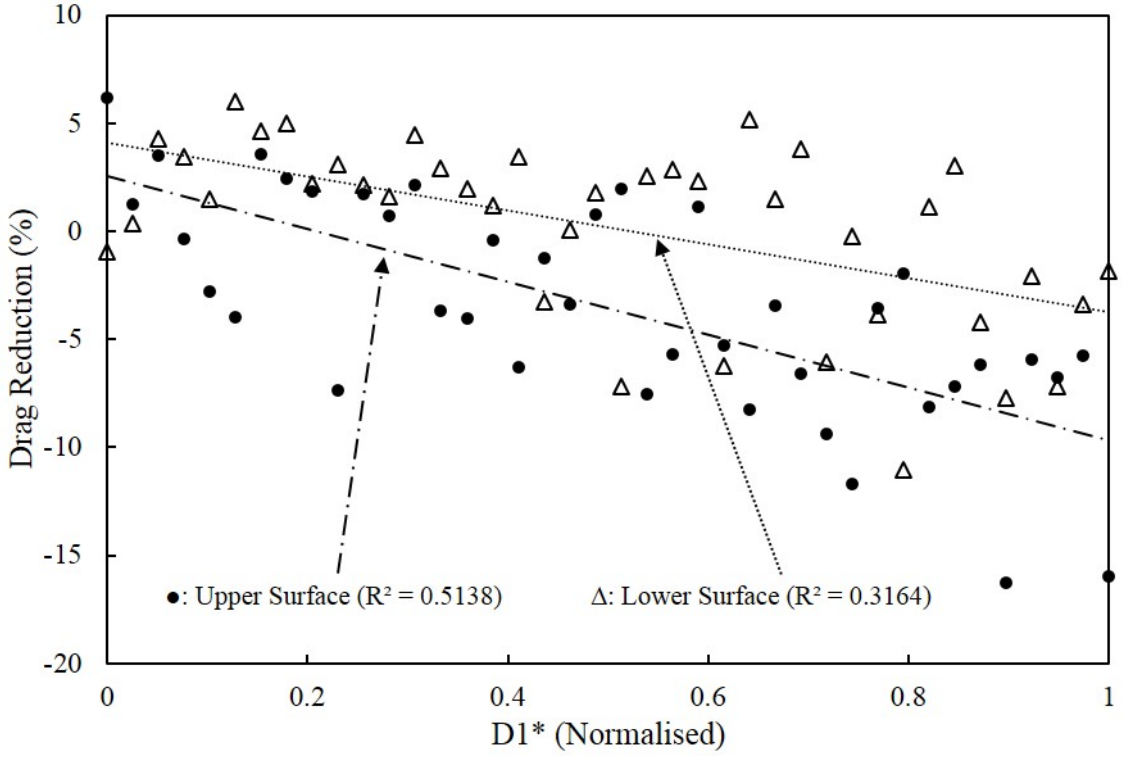

(a)

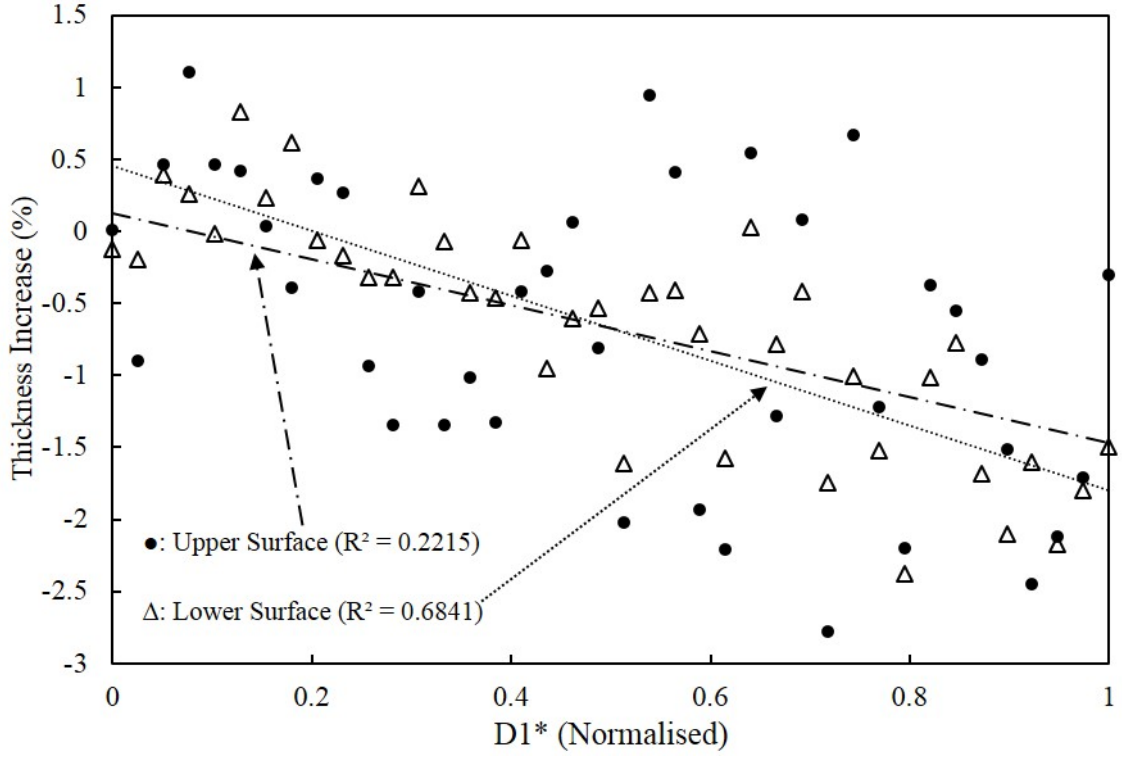

(b)

Figure D.2: Plot showing the correlation between design variable D1 (upper and lower surfaces) and (a) C_D and (b) t_s, for the 40-point DoE results.

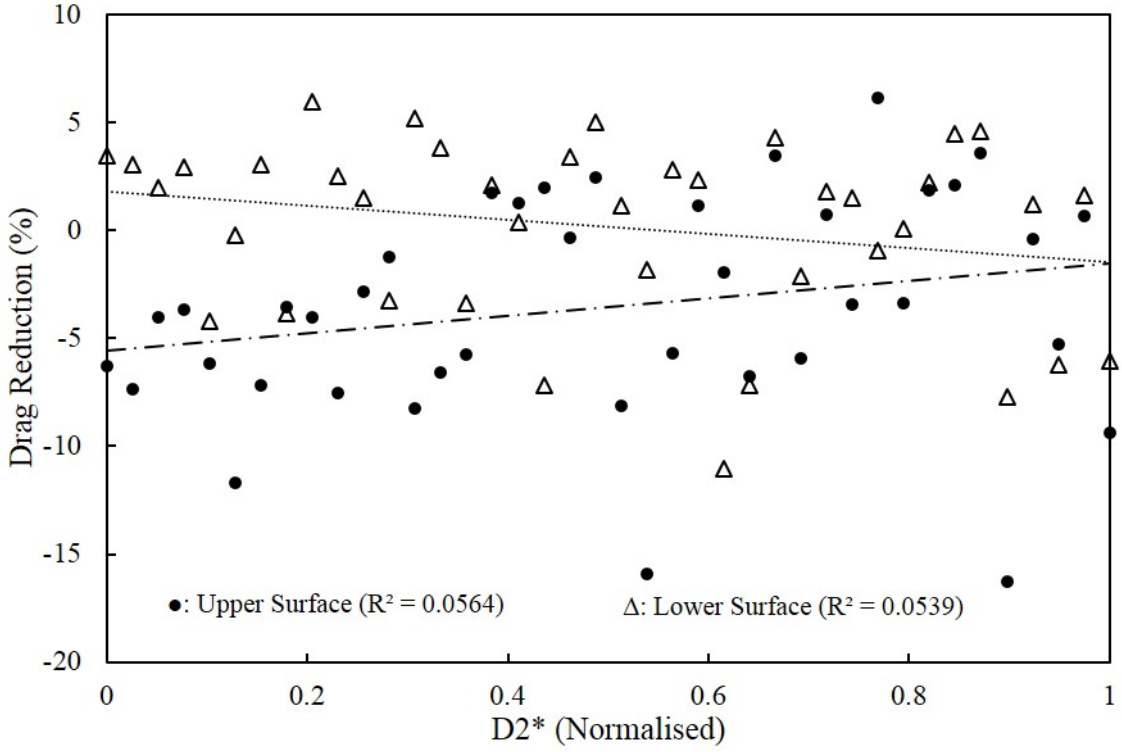

(a)

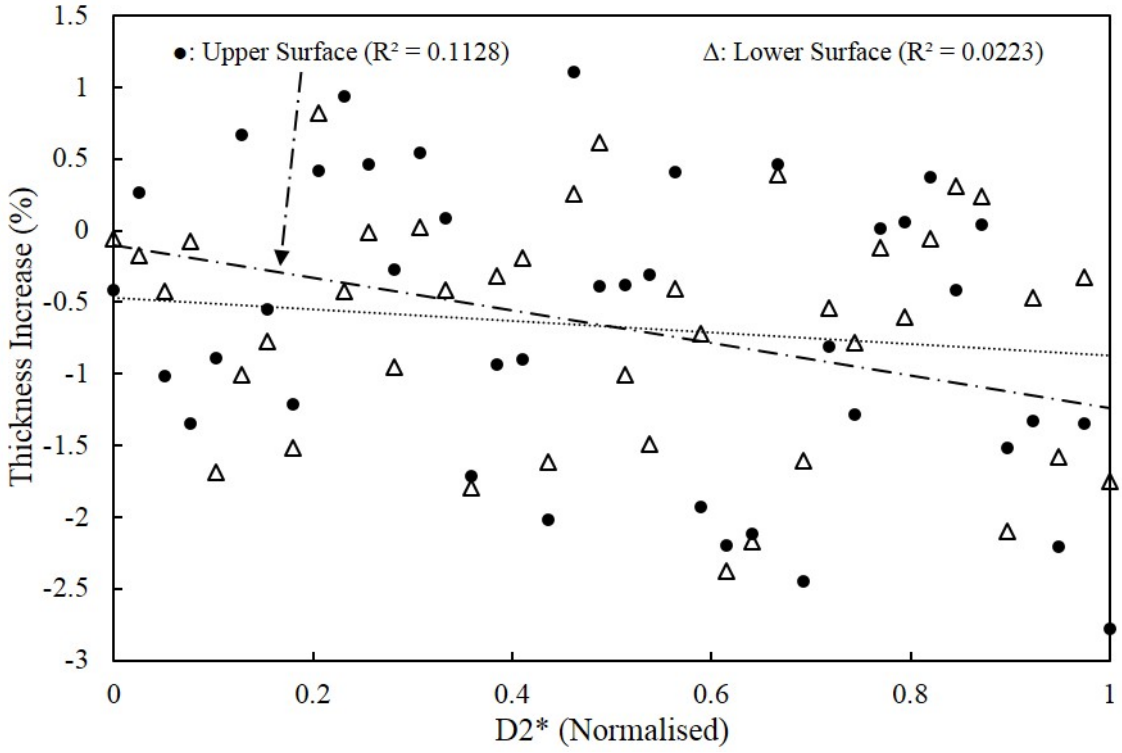

(b)

Figure D.3: Plot showing the correlation between design variable D2 (upper and lower surfaces) and (a) C_D and (b) t_s, for the 40-point DoE results.

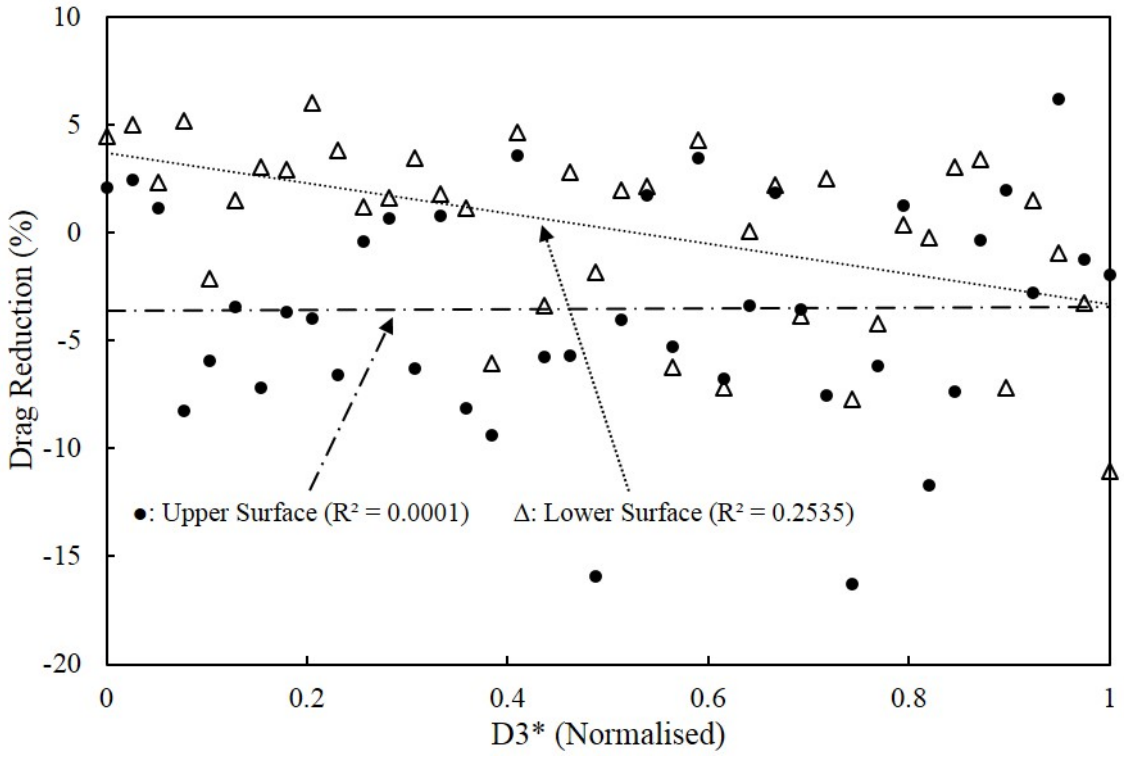

(a)

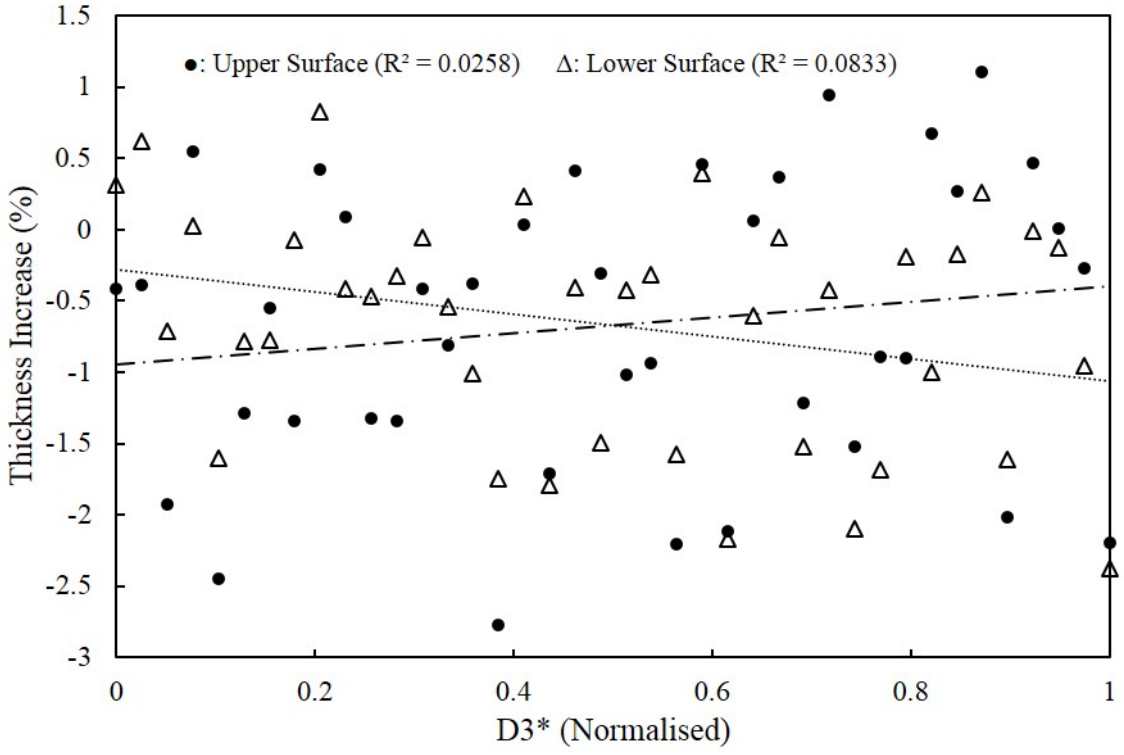

(b)

Figure D.4: Plot showing the correlation between design variable D3 (upper and lower surfaces) and (a) C_D and (b) t_s, for the 40-point DoE results.

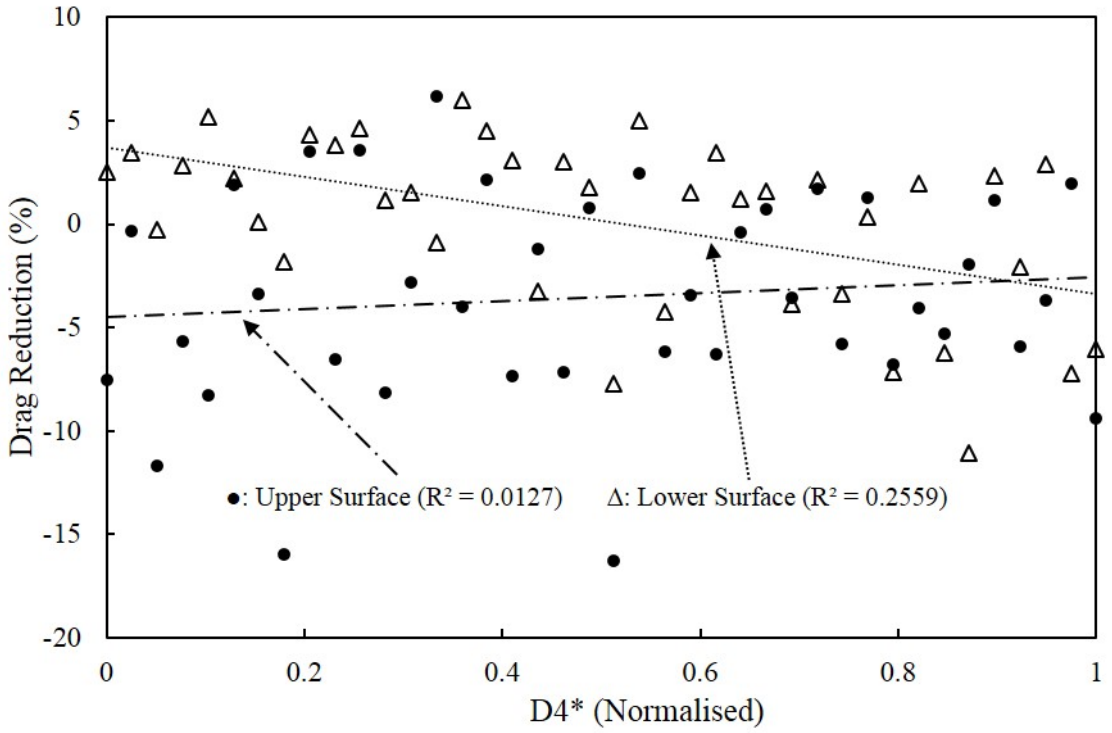

(a)

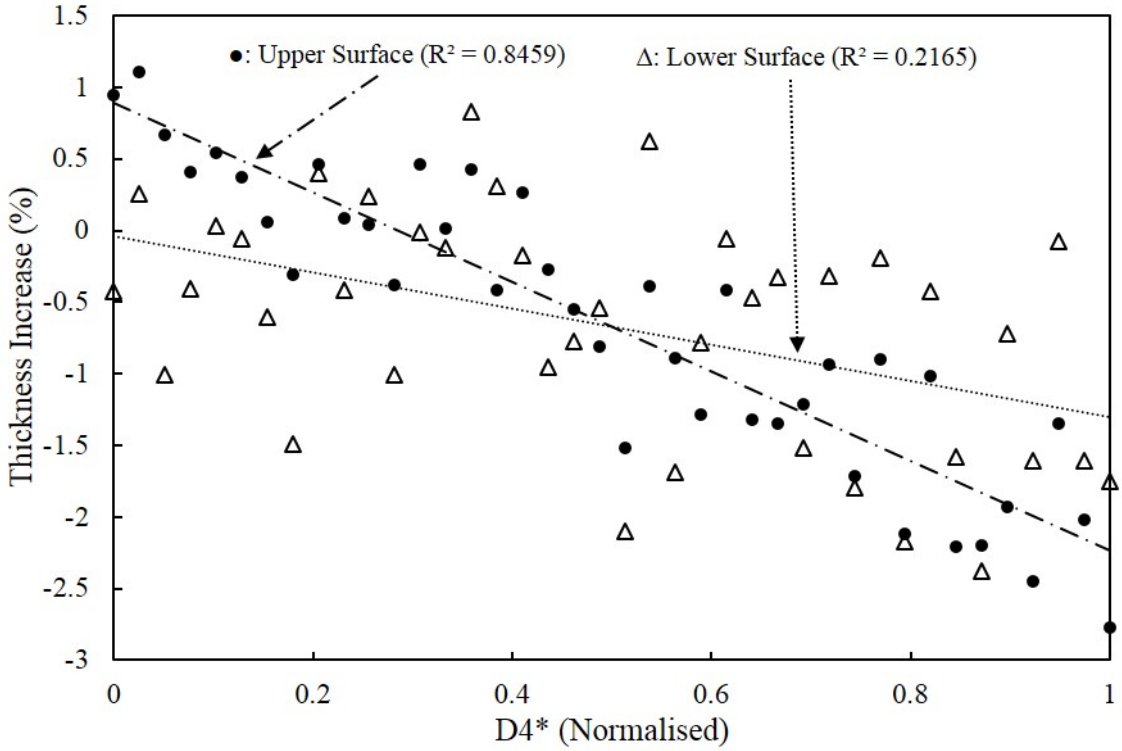

(b)

Figure D.5: Plot showing the correlation between design variable D4 (upper and lower surfaces) and (a) C_D and (b) t_s, for the 40-point DoE results.